On Buckling, Kink Boundaries and Kinking Nonlinear Elastic Solids

A thesis

Submitted to the Faculty

of

Drexel University

by

Mohamed Shamma

in partial fulfillment of the

requirements for the degree

of

Doctor of Philosophy

Fall 2014

UMI Number: 3672082

All rights reserved

INFORMATION TO ALL USERS
The quality of this reproduction is dependent upon the quality of the copy submitted.

In the unlikely event that the author did not send a complete manuscript
and there are missing pages, these will be noted. Also, if material had to be removed,
a note will indicate the deletion.

UMI 3672082

Published by ProQuest LLC (2015). Copyright in the Dissertation held by the Author.

Microform Edition © ProQuest LLC.
All rights reserved. This work is protected against
unauthorized copying under Title 17, United States Code

ProQuest LLC.
789 East Eisenhower Parkway
P.O. Box 1346
Ann Arbor, MI 48106 - 1346

Table of Contents

List of Tables iv
List of Figures vi
Chapter 1: Introduction to Deformation Mechanisms 1
1.1 Background 1
1.2 Goals and Motivation 6
Chapter 2: Evolution of buckling features observed in materials 7
2.1 Physical and Phenomenological Features of Buckling 7
2.2 Dislocations and Mosaic Walls 12
2.3 Buckling and Surrounding Support 22
2.3.1 Multiple Buckling Features in Layered Solids 29
2.4 Deformation of Geological Layered Structures 34
2.4.1 Kink Bands in Geological Structures 38
2.4.2 Modeling Kink Bands 40
2.5 Summary and Conclusions 43
Chapter 3: Normal and Shear Stresses on Layered Solids 45
3.1 Resolved Shear and Normal Stresses Extended in 3D 51
3.2 Summary and Conclusions 61
Chapter 4: Single Crystal Buckling Dislocation Mechanism 62
4.1 Carpet-like edge dislocation configuration in layered structures 62
4.2 Pseudo-Single Crystal Layered Structure Buckling Dislocation Mechanisms 69
4.3 Buckling dislocation stages analogy to extrusion and indentation 89
4.4 Inverse Expansion Effect 96
4.5 Summary & Conclusion 98
Chapter 5: MAX Phases Sample Fabrication & Characterization 119
5.1 MAX phases mechanical behavior 123
5.2 Summary and Conclusions 125
Chapter 6: In situ Experimental Techniques Used 126
6.1 In situ Neutron Diffraction (ND) 127
6.1.1 Elasto-Plastic Self-Consistent Model (EPSC) 131
6.1.2 Experimental Details 131

Chapter 7: Linear Elastic & Textured MAX Phases In situ ND and EPSC Results 137
7.1 Linear Elastic Ti_2SC In situ Neutron Diffraction Results 137
7.1.1 Conclusions 144
7.2 Textured Ti_2AlC In situ Neutron Diffraction Results 146
7.2.1 Summary and Conclusions 170
7.3 Effect of Grain Size 172
7.3.1 Random Textured Polycrystalline FG Ti_3SiC_2 179
7.3.2 Random Textured Polycrystalline CG and Porous Ti_3SiC_2 187
7.3.1 Summary & Conclusions 191
Chapter 8: Conclusions and Proposed Future Work 192
Appendix 195
A: EPSC fitting of stress- strain curve on CG, FG and porous Ti_3SiC_2 196
B: Nonlinear Strains and Dislocation Densities 204
C: Ultrasonic Bias Stress (UBS) in situ characterization technique 206
C1: UBS in situ characterization technique theory 206
C2: UBS Results of Selected Linear Elastic Ceramics 224
C3: UBS Results of MAX phases 240
References 280

List of Tables

Table 4-1: Dislocation evolution of KNE layered structured materials employing a pseudo-single crystal PP setup with P-sample texture. (i) In-plane forces, (ii) Normal forces, (iii) DIC displacement snapshots of the A4 PP experiment made from Dodwell *et al.* video, (iv) Schematic evolution of DWs as function of loading, (v) Representation of the resolved forces acting at different locations of the layered structure pseudo-single crystal resulting in the dislocations evolution observed in (iv)……..…99

Table 4-2: Dislocation evolution of KNE layered structured materials employing a pseudo-single crystal PP setup with P-sample texture. (i) In-plane forces, (ii) Normal forces, (iii) Deformation evolution of the A4 paper sheets in Fig. 4-8, (iv) Representation of the resolved forces acting at different locations of the layered structure pseudo-single crystal resulting in the dislocations evolution observed in (iii)……117

Table 6-1: Angles between selected planes investigated in Ti_2AlC and Ti_3SiC_2 and basal plane…….137

Table 7-1: Elastic constants, C_{ij} (in GPa) for Ti_2SC used in the EPSC model……....140

Table 7-2: Summary of sound velocities (m/s) and elastic moduli (GPa) in Ti_2SC and those predicted from the elastic constants listed in Table 7-1. Also shown are the values measured in this and previous work…….140

Table 7-3: Ti_2AlC elastic constants from *ab initio* calculations……..152

Table 7-4: Parameters used in the EPSC calculations. TwinVF is the Twin Volume Fraction; # of Twins is the value at the maximum strain; Max # Twins/Grain is the value at the maximum strain; Gradual is the range (in MPa) after the corresponding TTS, or CRSS where the HR changes linearily from HR1 to HR2. As an example, for Basal slip in Parallel, the HR changes

from 23 MPa to 9.5 MPa in the RSS range of 35 MPa – 50 MPa……..152

Table 7-5: Comparison of measured ND elastic moduli (in GPa) versus those calculated from the ESPC model using *ab initio* calculated elastic constants, viz. c_{11} = 307.5; c_{12} = 61.7; c_{13} = 66.5; c_{33} = 282.3; c_{44} = 117.5 (see Table 7-4). ND results are obtained from single peak-fit to data measured on SMARTS longitudinal bank upon loading of either the N- or P-samples. The EPSC calculations account for samples' texture. Standard deviations are given in brackets……....158

List of Figures

Figure 1-1: The mechanical behavior of the three classes of materials: ceramics, metals and polymers indicating their general mechanical characteristics[1]. 2

Figure 1-2: Comparison of SiC linear elastic response to the KNE response of Ti_3SiC_2 during cyclic loading. Arrows indicate the loading/unloading for each material. 4

Figure 1-3: Scaling of kinks observed in nature: (a) Kink folding at Millook Haven[3], (b) Cliff on north east side of Millook Haven[4], (c) Compression test of a stack of paper with foam side supports[5] , (d) Post-test observation with SEM of kink bands in curipixa wood[6], (e) High magnification optical micrograph of Ti_3SiC_2 cube were the basal plane is parallel to loading direction and subjected to 6 % compressive strain that kinked at lower left-hand corner[7], (f) First SEM image of Ti_3SiC_2 kinking boundary illustrating Orowan's concept[7, 8], (g)&(h) are SEM images for a $(V_{0.6}Cr_{0.4})_2GeC$ MAX phase solid solution that shows kinking after microhardness indentations. 5

Figure 2-1: Kinking deformation mechanism. (a) Photograph of kinks in originally cylindrical cadmium single-crystal wires of 1mm diameter[8], (b) Structure of kinking in (a); Thin parallel lines, denote glide planes. Dotted red lines denote, boundaries of the wedge-shaped regions of flexural glide. Dotted green lines, *k* and *k′*, denote planes of kinking. Solid blue lines outline a kinked band. The dotted red, green and solid blue lines were added to the schematic to mark different regions of kinking deformation [8]. 7

Figure 2-2: Difference between ideal (a), and observed (b) morphology of kink band where glide planes are tilted at an angle[11]. 8

Figure 2-3: Schematics of kink band formation (a) elastic buckling, (b) corresponding shear diagram, (c) initiation of pairs of dislocations in locations of maximum shear, (d) kink band and kink boundaries composed of oppositely signed edge-dislocations[12]..... 10

Figure 2-4: Schematics of successive stages for kink formation by dislocations. The stages develop gradually from (a) - (c). Each dislocation is marked by a T with the extra plane of atoms indicated by the stem of the T.[12] 10

Figure 2-5: Schematics of dislocations arrangements on basal plane layers. (a) Dislocation pile-ups on a basal plane. (b) Dislocations Walls across the basal plane layers (typically found in layered structured materials deformation). 11

Figure 2-6: (a) Vickers Projection Microscope image of deformed single crystal zinc showing two narrow twins (T) and two DWs (K) (X165),(b) Talysurf surface profile record at same location[15]. 13

Figure 2-7: (a) Schematic representation of lattice DWs caused by twinning[15, 16], (b) Sectional optical photomicrograph image of a twin and DWs of single crystal zinc[17]. 14

Figure 2-8: (a) Sectional optical photomicrograph image of a twin and two DWs of the same sign, (b) Reflection electron micrograph of twin with an oppositely signed DWs (shown by arrows) half-way across the accommodation region. Both images are of single crystal zinc[17].14

Figure 2-9: Schematic representation of twin and DWs growth and movement at different stages of loading in a single grain lattice (a) Initial twin, (b) Growth of twin in length and thickness, and principal DWs at twin tip, (c) Additional growth of twin two more steps and principal DWs moving to a new position. (d) Twin growth by increase in thickness results in an oppositely signed secondary DWs, (e) Twin growth by increase in length results in same signed secondary DWs as the principal DWs [17]. 16

Figure 2-10: SEM images of a Zn single crystal under successive stress increments, showing the increase in the mosaic wall angle (indicated by darkness change) and movement of mosaic boundary. Two main boundary lines AB and AC are labeled on the images [18]. 18

Figure 2-11: Plot of C_{44} versus c/a ratio for hexagonal materials. The vertical line at c/a = 1.4 is the boundary between KNE (right side) and non-KNE (left side) solids [19]..... 19

Figure 2-12: Pseudo-single crystal setup of layered structured material setup (a), horizontal displacement measurement (b), (c) DIC snapshot after completion of buckling across the paper pile layers length[5, 20, 21]. 20

Figure 2-13: (a) Basic pinned column before and after buckling, (b) Load-Deflection diagram for column buckling, (c) First three column buckling modes [24]..... 24

Figure 2-14: Different premature buckling modes:(a) Effect of loading angle relative to column center line, (b) Effect of shift in loading direction from column center line, (c) Effect of tilt in column; (a)(ii), (b)(ii) & (c)(ii) are the same as (a)(i) (b)(i) & (c)(i) respectively illustrating the lateral deflection direction relative to the loading angle, loading shift direction and tilt direction respectively; α is considered negative in (c)(i) and in positive (c)(ii) .[25]..... 26

Figure 2-15: Schematic of buckled structures showing the regions under tension and compression split by the neutral plane, (a) Left buckle, (b) Right buckle[26]. 27

Figure 2-16: Schematic of buckled slinky showing the wide and narrow regions within the structure corresponding to slinky sections under tension and compression. Red dashed line indicates the general curvature affecting the features observed in different regions. The dashed red circles designate the locations of interest in the buckled slinky marked by various letters [27]. 28

Figure 2-17: Illustration of kinks and ridges formation after buckling deformation. (a) Photograph of cadmium single-crystal after extensive buckling [8]. Locations of the ridges formed are marked. (b) Schematic demonstrating edge dislocations arrangement proposed by H&B causing ridge formation. Translucent green and red colors are added to differentiate between the DWs nucleated at different stages. Translucent green color represents DWs resulting

from the primary buckle, while the translucent red color represents a secondary DW formed as a result of secondary buckling within the DW region [12]. 31

Figure 2-18: (a) Bright-field image of Ti_3SiC_2 bent region delaminated in three slices S1 through S3 and containing primary and secondary DWs; (b) Schematic of S2 showing primary and secondary DWs. The DW region, secondary buckles in the DW region and kink bands are marked. The distance between A-A represent the basal plane layers, the dots ● represent atoms in the basal planes, green edge dislocations, ⊥, are the primary DWs and red edge dislocations, ⊥, are the secondary DWs. The green and red edge dislocations where added to the schematic to differentiate between primary and secondary DWs. (c) Bright-field image of an area containing dislocation arrays. The specimen is close to the orientation where basal planes are in an edge-on position [13]. 31

Figure 2-19: (a) TEM bright-field image of Ti_3SiC_2, and adjacent schematic of a region containing two kink bands denoted as i and ii and the DW regions neighboring them. The crystal is close to the edge-on position for the basal planes. The numbers show the measured rotation angles between the blocks of the crystal around $<11\bar{1}00>$ directions provided, mostly, by the DWs; (b) Schematic showing DWs, DWs and kink bands. The red arrows surrounding the basal plane material layers represent the forces exerted by the neighboring grains on this grain[13]. . 33

Figure 2-20: SEM micrograph of a fractured surface of a Ti_2AlC sample held at 1100ºC and 30 MPa for 3 h. Sample failed at a tensile strain of 16%. This micrograph emphasizes the profusion of kink boundaries formed as a result of the deformation. Inset shows a fractured surface of the grip area where no kink boundaries are present. Note grain refinement resulting from deformation[28]. 33

Figure 2-21: Schematic representation of (a) pure shear, and (b) simple shear [30]. 35

Figure 2-22: Schematic representation defining different parts of a folded layer [31]. 36

Figure 2-23: Fold profile classification based on angle between fold layers' limbs [31]. 36

Figure 2-24: Ramsay's classification of folds based on curvature of the inner and outer lines of a fold, and the behavior of the dip isogons [33]. 37

Figure 2-25: Lenticular lens shape of kink bands observed at all scale sizes [36]. 39

Figure 2-26: Schematic side elevation of the experimental rig. Displacement control via two screw jacks can be applied both axially and transversely. The rig can accommodate paper of size A4 (210 mm ×297 mm) and a sample height of 150 mm [48]. 41

Figure 2-27: Schematic of two kink band configurations observed in layered solids at all size scales [36]. 43

Figure 3-1: The final stage of buckled paper pile experiment by Dodwell *et al*.; arrows indicate lateral displacement of a group of layers, red arrows to the right and purple arrow to the left. [5, 20, 21, 24]. 45

Figure 3-2: Forces and moment created during buckling of an inclined column. 46

Figure 3-3: Traction applied in all directions on a layered structure in a matrix when a compressive load along z is applied. 47

Figure 3-4: Schematic of possible slip directions in a material. Thick red arrows represent compressive load, light blue plane is the slip plane, thin red arrows are the possible slip directions on the slip plane; χ represents the angle between the loading direction and the slip plane, black dashed arrows represent the angle between the loading direction and slip direction λ on the slip plane, Z' is the vector normal to the slip plane. ϕ represents the angle between the loading direction and slip plane normal Z'. Note that angles ϕ and χ are complementary. 48

Figure 3-5: Schematic of possible slip directions (and/or shear stress vectors) in, a) N-sample and, b) P-sample, assuming tilts of 1º from horizontal or vertical, respectively. 49

Figure 3-6: Possible variations of the Schmid factor for the, a) N-sample and, b) P-sample; and c) both samples together (red line N-sample, blue line P-sample), for λ range from 0-180º and, d) λ range from 91-89º. The dashed line corresponds to a RSS of ±0.01, above which slip is assumed to be activated. In other words, at values > 0.01, slip is possible. The corresponding ranges of λ from 89.45-89.00º & 90.55-91.00º in which the dislocations will be activated. Note that under those conditions, no dislocations can be activated in the P-sample..... 50

Figure 3-7: (a) Schematic of resolved components X, Y, and Z of shear vector given by solid red line. The thin solid red arrow is the shear stress vector and the thin dashed red arrows are the RSS components in 3D; (b) on the active slip plane, in addition to the infinite number of imaginary planes, (inactive slip planes shown as transparent light blue planes) whose RSS components can also contribute to that of the active slip plane..... 52

Figure 3-8: 3D Schmid factor of each layer under loading. The lines shown are from values obtained from inactive planes, rotated 5º each from the loading direction..... 53

Figure 3-9: Schematic of layered structure of N-sample loaded in compression, and the resulting RSS components acting on the layers. The red half arrows designate the stresses normal to, and along the layers. 54

Figure 3-10: Plot of, (a) normal forces to the XY plane, and, (b) shear forces on the XY plane; both plots are for the N-sample configuration. 55

Figure 3-11: Plots of normal forces onto the XY plane, (a) X-View, (b) Y-View and, (c) XY-View (forces are acting normal to the page). All plots are for N-sample configuration. 57

Figure 3-12: Schematic of layered structure under compressive loading, P-sample texture, and the resulting RSS components acting on the layered structure. The red half arrows designate the shear stresses applied. 58

Figure 3-13: Plot of, a) normal force to the XZ plane, and (b) shear force on XZ plane. Both are for the P-sample configuration..... 59

Figure 3-14: Plots of normal forces onto the XZ plane, (a) X-View (b) Z-View and, (c) XZ-View (forces are acting normal to the page). All plots are for a P-sample configuration. 61

Figure 4-1: The 'carpet' analogy for the motion of an edge dislocation [49]..... 63

Figure 4-2: Experimental arrangement of 800 sheets of A4 paper loaded in a pseudo-single crystal P-sample texture. Foam is used as the supporting medium. (a) Initial state before deformation, (b) & (c) show progress in the paper sheets' buckling, demonstrating changes in the carpet-like dislocation intensity shown on the figures, (d) Final state after deformation by compression, with highest carpet-like dislocation intensity at the kink edges, (e) Zoomed in view of the buckled paper sheets in (d). The black lines are for illustrative purposes, and were produced by inserting a single black layer of paper between every 25 layers of white sheets [5]. 64

Figure 4-3: Pseudo-single crystal setup of a layered material (a). Initial configuration (b), (c) DIC snapshot after completion of the 3rd harmonic buckling mode across the PP layers length [5, 20, 21]. 67

Figure 4-4: Translation of the pseudo-single crystal DIC horizontal displacement measurements to carpet-like configuration dislocations. (a) video snapshot of the DIC horizontal displacement measurement before any deformation, (b) schematic representation of the paper layers of (a); (c) DIC video snapshot after completion of the 3rd harmonic buckling mode [5, 20, 21]; (d) schematic representation of PP layers with resulting carpet-like dislocations reflecting localized displacements in (c). 68

Figure 4-5: In plane shear forces acting on layers tilted 1° about the X-axis for P-sample texture (2D view of XZ-component forces acting parallel to XZ-plane is on the left)..... 69

Figure 4-6: Forces acting normal to the layers tilted about the X-axis for a P-sample texture; (a) 3D view, (b) 2D Z-axis view and, (c) XZ-view of normal forces acting on to XZ-plane. The maximum forces T and T' correlate in (a), (b) and (c). 75

Figure 4-7: Forces acting normal to the layers tilted about the Z-axis for a P-sample texture; (a) 3D view, (b) 2D X-axis view and (c) XZ-view of normal forces acting on to XZ-plane. The maximum forces T and T' correlate in (a), (b) and (c). 79

Figure 4-8: Forces acting parallel to sheets tilted about the Z-axis for a P-sample texture. 2D view of XZ-component forces acting parallel to XZ-plane is depicted on the left..... 79

Figure 4-9: Built-in column setup under compressive loading after deforming under the 1st order buckling harmonic mode [50]. 88

Figure 4-10: Extrusion configuration comparable to stage I buckling in the PP experiment by Dodwell *et al.* [5, 20, 21]; (a) Initial situation; (b) Edges of the orifice are highly stressed (red nodes) (c) Red dashed line represents the U-shapes DWs that nucleated at the boundaries of the layers that buckled locally, d) Configuration at end of stage 1 where the buckling has swept across the layers. Note that at this step, the U shape transforms into two near parallel DWs of the *same* sign. 90

Figure 4-11: Indentation configuration comparable to stage II and III buckling in the PP experiment by Dodwell *et al.* [5, 20, 21]; (a). (b) After indentation two DWs nucleated at an inclined angle and the layers buckled out to the left. The two DWs are not nucleated simultaneouslty, but sequentially. 91

Figure 4-12: a) Extrusion and, (b), indentation, symbols with their corresponding resulting DWs applied to a stack of paper. 92

Figure 4-13: Application of the extrusion and indentation symbols to the buckled PP experiment by Dodwell *et al.* [5, 20, 21]. 93

Figure 4-14: (a) Photograph of Zn single crystal after buckling deformation indicating nucleation of a single DW as indicated by ridge. Schematic representation of single DW after buckling. [8, 12] 93

Figure 4-15: Development of a 2nd harmonic buckling mode – or classic kink boundary - for the deformation of the Zn [12]. Extrusion symbols added at corresponding locations where they may have taken place. 94

Figure 4-16: TEM bright-field images and corresponding schematics of fractured Ti_3SiC_2 by Barsoum *et al*. [13]. Extrusion and indentation symbols are marked in the possible locations on schematics (a) DWs in different directions with possible extrusion and indentation processes, (b) All DWs in one direction with no surface support on sample indicating extrusion process for all DWs nucleated. 95

Figure 4-17: Buckling of A4 paper sheets loaded in a P-sample orientation (i.e. vertical) with foam used as the supporting medium (Table 4-2). (a) Initial stage before deformation, and (b) & (c) after deformation. (b) shows the changes in heights while, (c) shows the changes in widths of the paper stack after deformation. 96

Figure 4-18: The initial and final stage of the development of A4 paper sheets buckling starting from a P-sample orientation but horizontally inclined with foam used as the supporting medium (Table 4-2). (a) Initial stage before any deformation, (b) & (c) are the final stage, (b) is for comparison of width while (c) for length. 97

Figure 5-1: Microstructures of the MAX phases used in this study: (a) FG Ti_2SC, (b) CG Ti_2SC, (c) FG Ti_3SiC_2, (d) CG Ti_3SiC_2, (e) Porous Ti_3SiC_2, (f) CG Textured Ti_2AlC, (g) FG Alumina, (h) CG Alumina. 122

Figure 5-2: Stress-strain curves for: (a) CG Ti_2SC. (b) FG & CG Ti_3SiC_2. (c) Ti_2AlC N-texture (blue circles) and P-texture (red circles) samples. Both stress and strain axes are reversed to

render the plots similar to conventional tensile stress-strain curves. (d) Schematic representation of a sample whose majority of grains have their basal planes i) normal “N” or ii) parallel “P” to the compressive loading direction. 124

Figure 6-1: Schematic of sample configuration relative to incident neutron beam, detectors (Bank 1 - Transverse; Bank 2 - Longitudinal), and loading direction in SMARTS. Q_L is the longitudinal scattering vector resulting from the diffraction beam directed to the longitudinal bank, and Q_T is the transverse scattering vector resulting from the diffraction beam directed to the transverse bank. 129

Figure 6-2: Schematic of a series of IKBs formed on basal planes[2]. 135

Figure 7-1: Stress–strain curves of Ti_3SiC_2 and Ti_2SC. The macroscopic stress–strain curve for the latter, on loading and unloading, is depicted as a thick gray line. The results of the EPSC model using the results of Bouhemadou and Khenata [66], Du et al.[67] , Cover et al. and Scabarozi et al.[68, 69] are plotted, respectively, as dashed line, open squares, filled diamonds and blue crosses. Inset shows an etched optical micrograph of the sample used. 138

Figure 7-2: Stress-strain response along the (a) longitudinal and, (b) transverse directions to the compressive loading axis assuming linear elastic behavior given for the 0001, $10\bar{1}1$, and $10\bar{1}0$ reflections. The ND results are shown as data points; the EPSC model, as solid lines. The results are shifted for clarity. The results on loading are in blue while unloading in red. 141

Figure 7-3: Variations in the lattice parameters, normalized by the values without load, as a function of compressive stresses on both loading and unloading. 142

Figure 7-4: Spherical nanoindentation stress-strain of polycrystalline Ti_2SC of cyclic indents on the same location. The values given next to the stress-strain curves correspond to the maximum applied stress. 143

Figure 7-5: Stress-strain curves: (a) schematic showing the various parameters used in IKB model. The non-linear energy stored, U_{nl} at the maximum stress is given by hatched area; the linear elastic energy, U_{el} is given by blue triangle. Lower right corner inset shows schematic of prolate spheroid IKB formed on the parallel basal planes with D spacing between them assumed herein. (b) Stress-strain curves for "N" (blue circles) and "P" (red circles) samples and corresponding EPSC model prediction fits assuming either a purely linear elastic response (dashed line), or by activating basal slip, (solid black lines). Both stress and strain axes are reversed to render the plots similar to conventional tensile stress-strain curves. (c) Plot of U_{nl}/U_{el} for both loops shown in (b), using the same color code. 147

Figure 7-6: (a) Pole figures for (i) {0002}, and ii) $\{10\bar{1}5\}$ planes for N-sample. (b) same as (a) for P-sample..... 150

Figure 7-7: Rietveld analysis of powder ND data of the CG-N Ti_2AlC sample as measured on the SMARTS diffractometer, under a minimal compressive stress of 5.0 MPa load. The data presented here was collected using bank 2, configured to measure the longitudinal stress direction (Fig. 7-5(c)). Open circles, solid line, and dashed line in the bottom, represent the measured data, refined model, and the difference between the two, respectively. The three rows of vertical tags represent the calculated Bragg reflections' positions of the major Ti_2AlC (1st row), and the minor Ti_3AlC_2 (2nd), and $Ti_5Al_2C_3$ (3rd) phases. The strong preferred orientation of the {000l} reflections is marked for the major Ti_2AlC phase. In this fit χ^2=2.489. 153

Figure 7-8: Ti_2AlC stress–strain curves: (a) bulk N- (blue), P- (red) samples and solid black lines are EPSC fits assuming DPs activity; (b) transverse and, (c) longitudinal directions for the N-sample; (d) transverse and (e) longitudinal directions for the P-sample. The experimental results, derived from ND data, taken on SMARTS, on loading (unloading) are represented by red circles (blue squares). The EPSC model results, assuming linear elastic behavior (green dash lines), and DP (black solid lines) are shown. Both axes are reversed to render the plots similar to conventional tensile stress-strain curves. 154

Figure 7-9: Ti_2AlC stress–strain curves: (a) bulk N- (blue) and P- (red) samples and solid black lines are EPSC fits assuming $\{11\bar{2}1\}$ twin activity; (b) transverse and, (c) longitudinal directions for the N-sample; (d) transverse and (e) longitudinal directions for the P-sample. The experimental results, derived from ND data, taken on SMARTS, on loading (unloading) are represented by red circles (blue squares). The EPSC model results, assuming linear elastic behavior (dash lines), and $\{11\bar{2}1\}$ twin (solid lines) are shown. Both axes are reversed to render the plots similar to conventional tensile stress-strain curves. 155

Figure 7-10: Ti_2AlC stress–strain curves: (a) bulk N- (blue) and P- (red) samples and solid black lines are EPSC fits assuming DPs + $\{11\bar{2}1\}$ twin activity ; (b) transverse and, (c) longitudinal directions for the N-sample; (d) transverse and (e) longitudinal directions for the P-sample. The experimental results, derived from ND data, taken on SMARTS, on loading (unloading) are represented by red circles (blue squares). The EPSC model results, assuming linear elastic behavior (dash lines), and DPs + $\{11\bar{2}1\}$ twin (solid lines) are shown. Both axes are reversed to render the plots similar to conventional tensile stress-strain curves. 156

Figure 7-11: Stress–strain response of selected $\{10\bar{1}l\}$ planes along transverse (a) and, longitudinal (b) directions for the N-sample. The experimental results, derived from single peak fit to the ND data, taken on SMARTS. The EPSC model results, assuming linear elastic behavior are also presented (solid lines) 158

Figure 7-12: Stress–strain response of selected $\{10\bar{1}l\}$ planes along transverse (a) and, longitudinal (b) directions for the P-sample. The experimental results, derived from single peak fit to the ND data, taken on SMARTS. The EPSC model results, assuming linear elastic behavior are also presented (solid lines). 158

Figure 7-13: Stress–strain response of individual reflections obtained from single peak fits of the ND results of the N-sample. (a) Longitudinal $10\bar{1}1$ and $10\bar{1}5$; (b) N-sample 0004 in longitudinal (right hand side curve) and P-sample on transverse bank (left hand side). The EPSC results, where basal slip is activated are depicted by dotted black lines. The linear elastic EPSC results are depicted by green dashed lines. The elastic strains on loading are represented by open

symbols; those on unloading by solid symbols with the same shape. Both axes are reversed to render the plots similar to conventional tensile stress-strain curves. 163

Figure 7-14: Stress–strain response along longitudinal and transverse direction for the N- and P-sample. 166

Figure 7-15: Full width at half maximum (FWHM) of the N-sample {0004} ND reflection on the longitudinal bank as a function of stress. Note hysteresis. Inset shows FWHM for the $\{10\bar{1}0\}$ reflections in the P-sample. 168

Figure 7-16: Difference between FG & CG layered structured materials in terms of buckling (a) Five of HCP crystals stacked together; (b) Top view of the five stacked crystals in (a); (c) The five HCP crystals constituting one fine grain (d) Top view of multiple (75) HCP crystals stacked together (e) The multiple HCP crystals in (d) constituting one coarse grain [97, 98]. 174

Figure 7-17: Effect of favorable growth on basal plane layers rather than formation of new basal planes during grain coarsening on grain texture; (a) Fine grain; (b) Coarse grain. 178

Figure 7-18: Optical micrographs of Ti_3SiC_2 samples HIPed at 1450ºC for (a) 8 , (b) 16 , (c) 24h. 178

Fig. 7-19: Microstructure of CG Ti_3SiC_2 polycrystalline sample deformed at 1300ºC in compression. Compression direction is vertical. Grain denoted by black arrow buckled and delaminated into voids that formed to its right due to its presence at the sample surface[99]. .. 179

Figure 7-20: (a) Macroscopic stress-strain curve of FG & CG Ti_3SiC_2 **for comparison**. The coarse sample was annealed from the sample bulk (microstructures are in Fig. 5-1). 179

Figure 7-21: (a) Macroscopic stress-strain curve of FG Ti_3SiC_2. Complementary stress–strain response of selected $\{10\bar{1}l\}$ and basal planes along transverse (b) and, longitudinal (c) directions. The experimental results, derived from single peak fit to the ND data, taken on SMARTS. 181

Figure 7-22: Zoom of figure 7-21(c) showing the complementary FG Ti_3SiC_2 stress–strain response of selected $\{10\bar{1}l\}$ along longitudinal direction. The dashed lines are the corresponding linear elastic response prediction obtained from EPSC calculations. 182

Figure 7-23: (a) Macroscopic stress-strain curve of FG & CG Ti_3SiC_2 **for comparison**. Complementary stress–strain response **for** CG Ti_3SiC_2 of selected $\{10\bar{1}l\}$ and basal planes along transverse (b) and, longitudinal (c) directions. The experimental results, derived from single peak fit to the ND data, taken on SMARTS. 188

Figure 7-24: Zoom of figure 7-23 (c) showing the complementary CG Ti_3SiC_2 stress–strain response of selected $\{10\bar{1}l\}$ along longitudinal direction. The dashed lines are the corresponding linear elastic response prediction obtained from EPSC calculations. 189

Figure 7-25: (a) Macroscopic stress-strain curve of Porous, FG & CG Ti_3SiC_2 for comparison. Complementary stress–strain response of Porous Ti_3SiC_2 for selected $\{10\bar{1}l\}$ and basal planes along transverse (b) and, longitudinal (c) directions. The experimental results are derived from single peak fits of the in situ ND diffractograms. 190

Figure 7-26: Zoom of figure 7-25(c) showing the complementary Porous Ti_3SiC_2 stress–strain response of selected $\{10\bar{1}l\}$ along longitudinal direction. The dashed lines are the corresponding linear elastic response prediction obtained from EPSC calculations. 191

ABSTRACT

The mechanical behavior of materials has been under investigation for decades. However, there is always unknown information to be researched and characterized. Extensive research has been performed on materials deforming by slip and twin mechanisms due to their presence in a lot of materials used in practical applications. Conversely, much less attention was directed to investigating the dislocation mechanism responsible for the fully reversible energy dissipating mechanical response of Kinking Nonlinear Elastic (KNE) solids.

Herein, the buckling dislocation mechanism responsible for the KNE mechanical behavior of MAX phases is investigated. The main features of the buckling dislocation mechanism are identified that are globally applicable for layered structured materials as well. This was done by analyzing the deformation of a single crystal layered structure. The single crystal layered structure is a setup consisting of a pile of paper supported by sponge and ply wood in which paper buckles during compression. The displacement of the paper layers is studied in relation to dislocation nucleation across the layers called dislocation walls (DW). Schmid factor maps where developed that recognize the shape and progress of traction applied on the layers during deformation. Hence, the evolution of buckling dislocation mechanism that occurs in layered structures has been discovered distinguishing between two possible buckling modes (extrusion and indentation) that depend on the layered structure surrounding support and constraints.

In situ neutron diffraction and ultrasonic bias stress techniques were used to perform in situ experiments on selected MAX phases to obtain information about the dislocation mechanism during its activity. Linear elastic Ti_2SC was investigated as well for comparison with Ti_3SiC_2 and Ti_2AlC MAX phases which demonstrate KNE mechanical response in bulk. The in situ ND

results of textured Ti_2AlC showed typical results except for the (0004) grains which demonstrated an almost linear elastic response however for the first time a reversible loop is observed on microstrain measurements at the crystal level. The $\{10\bar{1}5\}$ grains inclined at 45º showed a reversible loop as well. The results indicate that dislocation pile-ups are undoubtedly not the active dislocation mechanism. All of the features observed prove that buckling is the dislocation mechanism taking place in KNE materials. The reversibility of mechanism is believed to originate from the bonds within and between the layers, however, this aspect needs further investigation.

Counterintuitive features in the mechanical response of textured Ti_2AlC are explained. The higher strain accommodation and energy dissipation of the N- relative (loading direction with respect to basal plane) to the P-orientation is explained through schmid factor analysis. In addition, the inverse expansion that occurs during buckling of layered structures in the N-sample orientation explains the grains expansion that occurs along the compressive axis.

In summary, this work demonstrates the evolution of the buckling dislocation mechanism taking place in layered structured materials, and the normal and shear traction applied on the layers that govern the behavior. The in situ ND results eliminate the possible activity of slip and/or twin and support the buckling dislocation activity.

Chapter 1: Introduction to Deformation Mechanisms

1.1 Background

The mechanical behavior of materials is an important topic to be studied for the advancement of mankind. Extensive research must be accomplished to gain enough knowledge about a materials' performance under various loading conditions (e.g. tension, compression, fatigue etc…) and operating environments (e.g. temperature, humidity, acidity etc…). The mechanical behavior of materials is initially linear elastic, where the amount of resulting strains depends on the materials' structure bond strengths. If the load exceeds the elastic regime, plastic deformation proceeds. The shape of the plastic regime curve is governed by the possible deformation mechanisms and their interactions in the material during loading. The materials' mechanical behavior differs based on the mode of loading, whether tension or compression, cyclic loading, fatigue, bending, torsion…etc.

Figure 1-1 shows the general mechanical behavior, at room temperature, for the main three classes of materials: polymers, metals and ceramics. Thermoplastic polymers are generally made from covalently bonded chains with weak Van der Waal's forces between them. Hence, during mechanical loading, the chains slide easily against each other resulting in a limited elastic regime and an extended plastic strain as shown in Fig. 1-1 (thermoset polymers, not shown in Fig. 1-1, have a higher strength and limited ductility compared to thermoplastics due to their cross-liked structure).

On the other hand, ceramics have strong and stable structures composed of ionic and covalent bonds. This results in small elastic strains, however a large stress could be carried until catastrophic failure is reached since dislocation slip is limited. The metallic bonds found in metals represent a "sea of electrons" shared among all atoms uniting them

together. Some metals are strong and express considerable ductility during plastic deformation. Metals are widely used in our lives, especially iron due to its abundance and relative low cost.

Research and investigation of the deformation mechanisms in various materials started since the existence of mankind when cavemen used wood and, stones to make knifes, spears and axes to cut plants and hunt animals for food. Today modern technologies use waterjets for cutting masses of slaughtered chicken and very hard materials like diamond for machining hard materials with high precision.

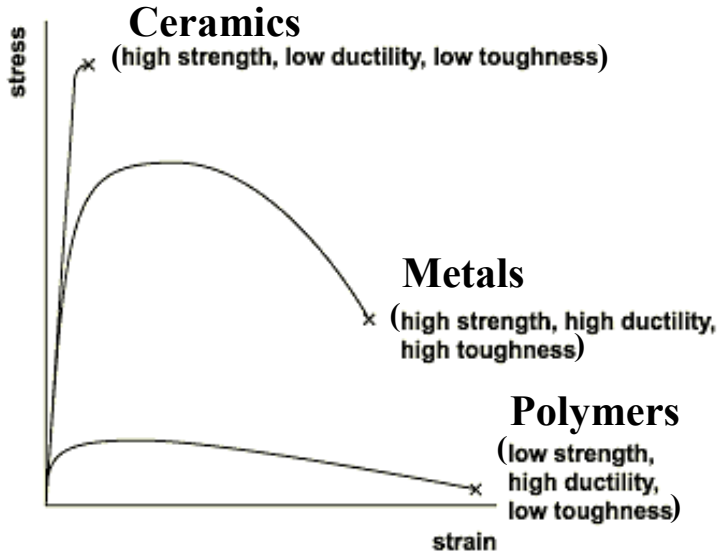

Figure 1-1: The mechanical behavior of the three classes of materials: ceramics, metals and polymers indicating their general mechanical characteristics[1].

During the 20th century until today, significant discoveries and findings were reached about materials deformation mechanisms. Dislocation motion by slip and twinning were found to be the two main material deformation mechanisms responsible for accommodating strain resulting from applied loads in the plastic regime. Much attention was directed by researchers into obtaining detailed information about the activity of these mechanisms in the past decades. Slip and twinning are the deformation

mechanisms taking place in the three main classes of materials in Fig. 1-1. Deformation by slip or twin always result in permanent plastic deformation even when the material is subjected to cyclic loading.

However, much less work was directed in investigation of a principal mechanical response observed in Kinking Nonlinear Elastic (KNE) solids where fully reversible mechanical response takes place. Figure 1-2 illustrates the difference in mechanical response between the linear elastic regime of SiC and the KNE behavior of Ti_3SiC_2 during cyclic loading. In KNE materials the number of slip systems is limited to two independent slip systems. The unique feature in these solids is the spontaneous, fully reversible hysteretic stress-strain loops obtained upon cyclic loading, whether during tensile or compressive loading. Hence, during unloading, the strain returns back to zero displaying a closed stress-strain loop. Fine grained Ti_3SiC_2 was cycled 100 times at a compressive stress of 700MPa with no change in the resulting stress-strain loop[2]. In addition, these structures are capable of dissipating a considerable amount of energy during cyclic loading[2]. This distinct mechanical response has been investigated for a decade; however, the active dislocation mechanisms have not been fully understood. Polycrystalline layered structured materials like MAX phases and some hexagonal closed packed metals like Mg and Co respond in a KNE manner during mechanical cyclic loading. The observation of kinks is the common feature found in all KNE materials. However, kinks are observed during deformation of layered structures that range in size scaling from geological earth layers, stacks of paper to wood fibers. Figure 1-3 shows images of different sizes of kinks observed in nature.

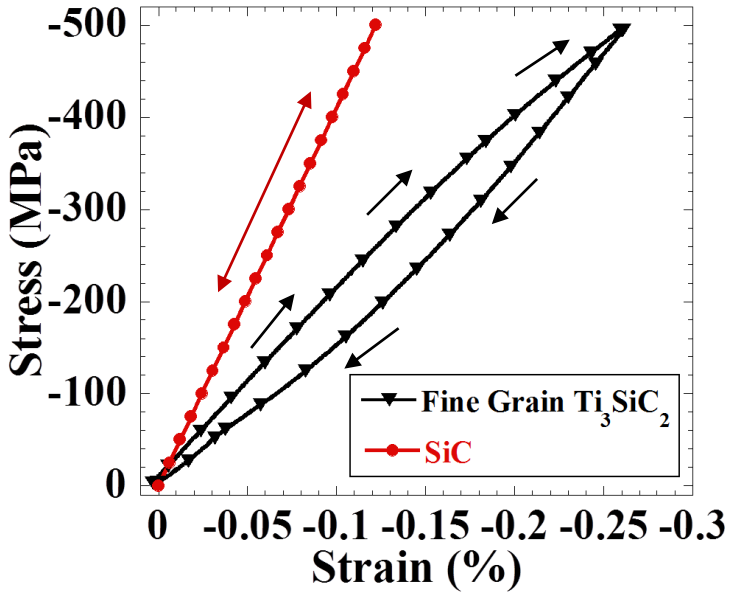

Figure 1-2: Comparison of SiC linear elastic response to the KNE response of Ti_3SiC_2 during cyclic loading. Arrows indicate the loading/unloading for each material.

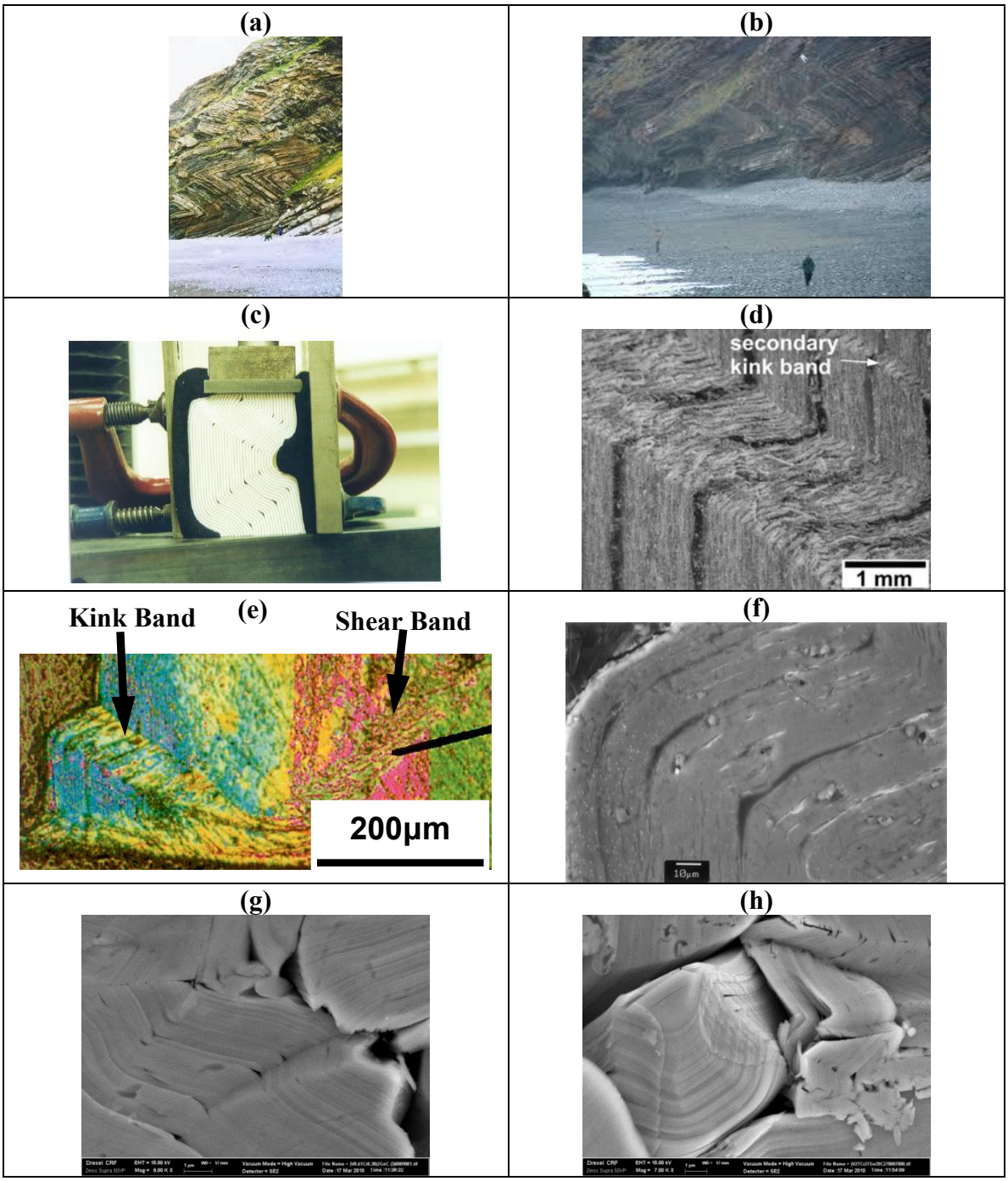

Figure 1-3: Scaling of kinks observed in nature: (a) Kink folding at Millook Haven[3], (b) Cliff on north east side of Millook Haven[4], (c) Compression test of a stack of paper with foam side supports[5] , (d) Post-test observation with SEM of kink bands in curipixa wood[6], (e) High magnification optical micrograph of Ti_3SiC_2 cube were the basal plane is parallel to loading direction and subjected to 6 % compressive strain that kinked at lower left-hand corner[7], (f) First SEM image of Ti_3SiC_2 kinking boundary illustrating Orowan's concept[7, 8], (g)&(h) are SEM images for a $(V_{0.6}Cr_{0.4})_2GeC$ MAX phase solid solution that shows kinking after microhardness indentations.

1.2 Goals and Motivation

The main goal of this thesis is to provide a better understanding of the dislocation-based deformation mechanism occurring in KNE materials during cyclic loading. The scientific community has been in a dilemma concerning this topic for decades and did not reach a final model describing the active mechanism. This is due to the insufficient single crystal size of layered structured crystalline materials that could be fabricated to experiment. In addition, the fully reversible hysteretic mechanism taking place during cyclic loading of KNE materials reduces the credibility of post mortem characterization due to the non-permanent deformation (unlike slip and twin mechanisms). Materials with such mechanical behavior would have practical applications once the active dislocation deformation mechanisms is better understood. This thesis is an attempt to provide additional information about the mechanical behavior of KNE solids by experimenting, investigating and explaining the reversible dislocation mechanism in layered structural materials.

Reversible dislocations are active during cyclic loading of MAX phases, therefore, the characterization techniques used must be *in situ* in order to capture the dislocations behavior. Two *in situ* characterization techniques used herein are: (1) *In situ* Neutron Diffraction (ND) and (2) Ultrasonic Bias Stress (UBS) technique. Experiments performed by researchers in the literature are also used for analyzing the active reversible dislocation mechanism. The shear and normal forces/stresses acting on layered solids are quantified as well.

Chapter 2: Evolution of buckling features observed in materials

2.1 Physical and Phenomenological Features of Buckling

Kink bands and folds in geological formations were observed and described since ancient history. For example, Mugge[9] showed kinks while describing the behavior of disthene and stibnite crystals when compressed parallel to their glide planes. In 1942, Orowan[8] was the first to describe the kinking deformation mechanism of single crystal Zn and Cd. He was the first to report on kinking in metals. He reported the following features: (1) kinking occurs when the only possible glide plane (0001) is near edge-on to the loading direction, (2) abrupt changes occur when the loading forms kinks with sharp ridges and regular curvatures, (3) kink orientation is non-crystallographic, where "local symmetry" is valid only within a "limited volume" [10], and (4) characteristic physical features illustrate that the deformation cannot be dislocation glide or twinning; a new kinking phenomenon is observed. Figure 2-1 shows Orowan's photograph and schematic of kinks formed in Cd upon deformation.

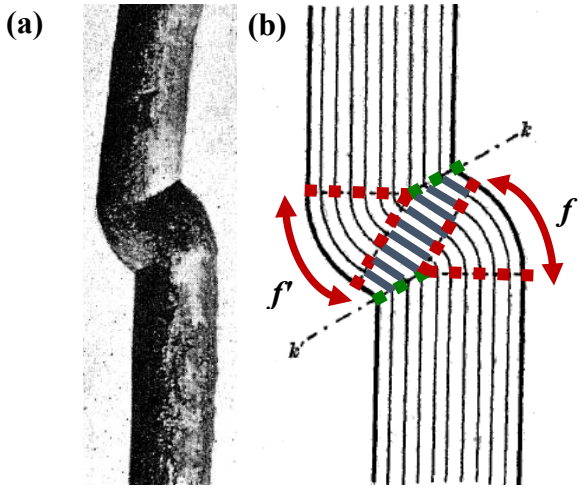

Figure 2-1: Kinking deformation mechanism. (a) Photograph of kinks in originally cylindrical cadmium single-crystal wires of 1mm diameter[8], (b) Structure of kinking in (a); Thin parallel lines, denote glide planes. Dotted red lines denote, boundaries of the wedge-shaped regions of flexural glide. Dotted green lines, *k* and *k′*, denote planes of kinking. Solid blue lines outline a kinked band. The dotted red, green and solid blue lines were added to the schematic to mark different regions of kinking deformation [8].

The schematic representation of kinking in Fig. 2-1(b) shows a continuous bend of the basal plane lamellae known as "flexural glide" ***f*** & ***f'*** regions. The non-crystallographic kink planes, ***k*** & ***k'***, are boundaries forming sharp edges along the glide plane lamellae. It is clearly observed that the lattice constants are different in the flexural glide regions (between the red dashed lines) from the kink band (the solid blue lines). Ideal kinking would occur without the flexural glide region in which "the glide lamellae remain practically planar within a certain distance from the kinking plane. In other words, the amount of glide between neighboring lamellae must be an integral multiple of the lattice period in the direction of glide"[8]. Figure 2-2a and b compares the idealized and observed kinking schematics, respectively.

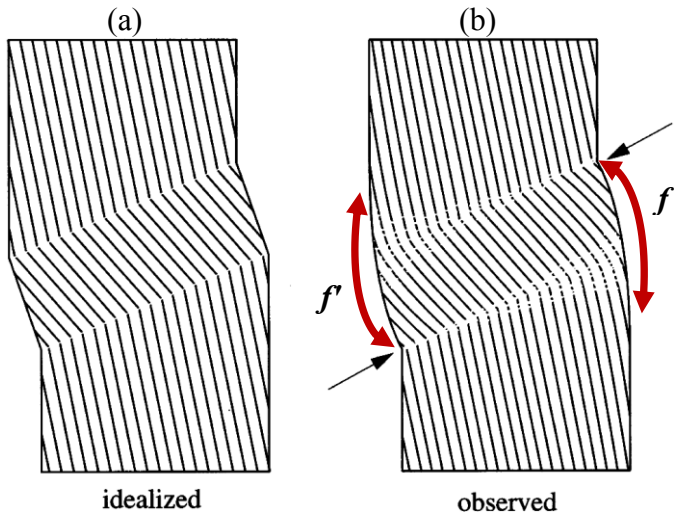

Figure 2-2: Difference between ideal (a), and observed (b) morphology of kink band where glide planes are tilted at an angle[11].

The features observed in Figs. 2-1 & 2-2 indicate that the initial event necessary for kink band formation occurs at opposite sides of the specimen's surface and propagate through the specimens' cross-section[11]. Note the tensile stresses at the flexural region surfaces ***f*** & ***f'*** (Figs. 2-1 & 2-2(b)) which diminish across the specimen until ideal kink

follows (at intersection of broken red lines with green lines in Fig. 2-1(b)) at the kink planes ***k*** & ***k'*** forming a ridge at the surface.

To conclude that there is a new deformation mechanism forming the observed kinks, Hess and Barrett[12] (H&B) in 1949 went further and explained the developments of the various features observed during kinking of zinc single crystal loaded such that the basal planes were parallel to the loading direction. They related the phenomenon to the appropriate shear diagrams and Euler's elastic buckling of rods. The effect of different single crystal lengths and thicknesses in addition to using sample support setups were investigated. The main outcome of their study was that kink bands form by standard dislocation slip. However, depending on the local stress conditions at various locations in the sample, edge dislocations would develop in an orderly manner. Figure 2-3 shows the main phenomena H&B proposed to be responsible for kink band formation. Initially the rod is under Euler's elastic buckling condition (Fig. 2-3(a)) in which maximum shear occurs at L/4 and 3L/4 (Fig. 2-3(b)). In the region between those locations, the oppositely signed shear stresses in the basal planes enforce opposite dislocation slip motion resulting in two flip-sided ridge and groove forming on the opposite sides of the sample surface (Fig. 2-3(c)). Hence, oppositely signed edge-dislocations are aligned at locations L/4 and 3L/4 forming the kink plane boundaries BC and DE (Fig. 2-3(d)) creating the rotated crystal lattice kink in between[12-14]. H&B elaborated even more into the stages of kink formation by dislocations as shown in Fig. 2-4[12].

As mentioned previously, as soon as the load exceeds the elastic region, plastic deformation proceeds depending on the materials' possible deformation mechanism. Figure 2-4(a) shows the stages of kinking plastic deformation in layered solids. The first

stage of kinking is when the initial oppositely signed pair of edge dislocations form at the maximum shear stress locations (Fig. 2-3(b), Fig. 2-4(a)). While the compressive load keeps increasing, the kink band is the weakest location in the sample. In this state, excessive deformation continues in the kink band through the development of more oppositely signed edge dislocations to accommodate the resulting strain (Fig. 2-4(b)). This phenomenon continues as the loading increases explaining the flexural glide region observed by Orowan[8] in Fig. 2-1.

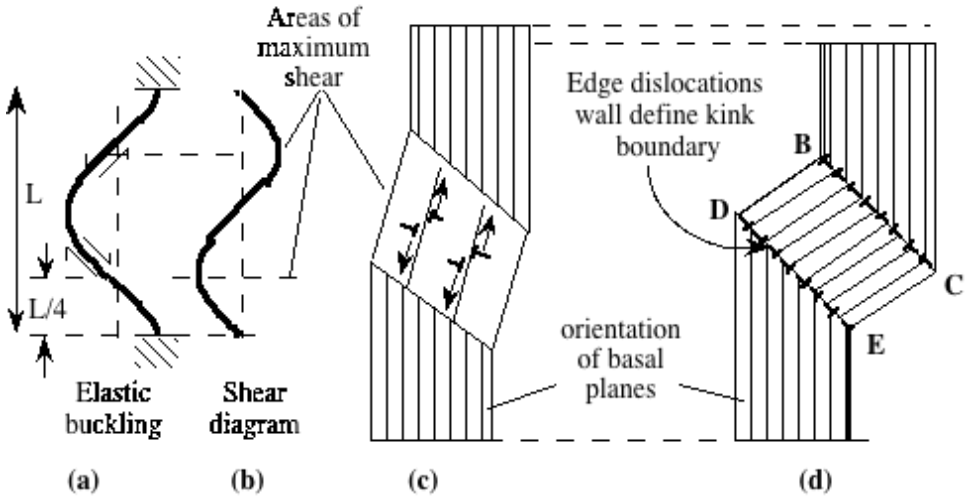

Figure 2-3: Schematics of kink band formation (a) elastic buckling, (b) corresponding shear diagram, (c) initiation of pairs of dislocations in locations of maximum shear, (d) kink band and kink boundaries composed of oppositely signed edge-dislocations[12].

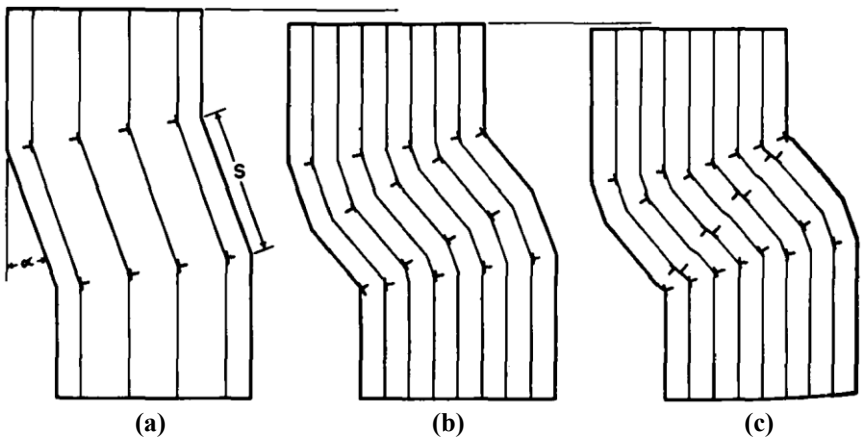

Figure 2-4: Schematics of successive stages for kink formation by dislocations. The stages develop gradually from (a) - (c). Each dislocation is marked by a T with the extra plane of atoms indicated by the stem of the T.[12]

Figures 2-3 and 2-4 show dislocations of opposite signs that result in the kinks observed. This deformation could be classified as pure kinking, in which the glide planes are initially nearly parallel to the loading direction and there is a free boundary surface that could adapt to stress conditions and deform easily. However, not all layered solids are bounded by these conditions. The layered solids could have a random or oriented texture. It becomes even more complex in polycrystalline layered solids which are not perfectly textured. In that case, kinking would depend on each grains' orientation and the surrounding forces applied on it. A remarkable feature noted is the ordered alignment of dislocations across the layers, called dislocations walls (Fig. 2-5(b)). This arrangement is observed during deformation of layered materials. Also quite commonly observed after the deformation of layered solids are dislocation pile-ups (Fig. 2-5(a)).

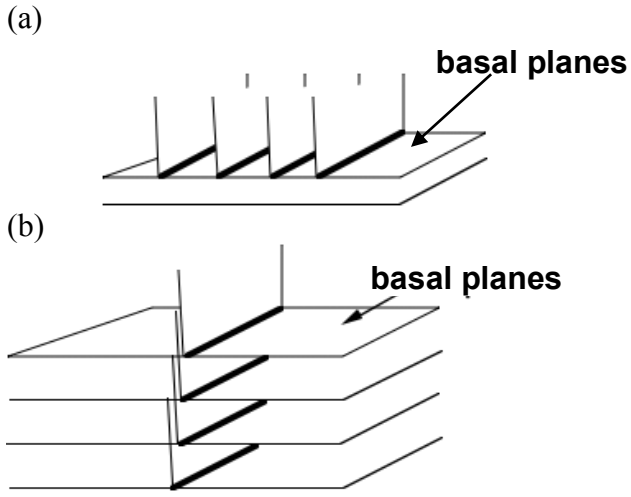

Figure 2-5: Schematics of dislocations arrangements on basal plane layers. (a) Dislocation pile-ups on a basal plane. (b) Dislocations Walls across the basal plane layers (typically found in layered structured materials deformation).

2.2 Dislocations and Mosaic Walls

Dislocations walls have been observed by several researchers after the deformation of single crystal Zn. The significance of their observations is the presence of dislocation walls in a singular dislocation sign. These dislocation walls will henceforth be referred to as Dislocation Walls (DW) since they accommodate strain by nucleation of edge dislocations. The sign of the DWs depends on the strain applied on a grain.

In polycrystalline materials, the deformation is usually inhomogeneous and twins that form lenticular shapes not extending across the grain have been observed. Hence, there is a high shear strain adjacent to the lenticular twins. DWs adjacent to twins were found to accommodate the shear strain in the untwined region in the grain. Moore [15] (1955) experimented on single crystal zinc after tensile loading and investigated the DWs parallel to the twins. He observed the twins and DWs using a Vickers Projection Microscope and measured the small changes of the surface slopes using a Talysurf needle-type profilometer recorder. Figure 2-6 shows the image taken of the deformed zinc single crystal. A clear distinction could be made between the twins and DWs due to the high reflectivity and flatness of the cleaved surface. The horizontal fine lines across the image in Fig. 2-6(a) are abrupt cleavage steps made on the sample.

In addition to the apparent difference observed microscopically in Fig. 2-6(a), the Talysurf measurement of the twin slopes from horizontal are 4º 16’ and 3º 32’ respectively, while the DW zones are about 0º 22’ and 0º 12’. The amount of shear strain a twin accommodates is quantified and depends on the active twin. In the single crystal zinc samples investigated the $\{10\bar{1}2\}$ twin is the active twin system. The theoretical slope value is 3º 58’. The deviation from the theoretical value is due to the precision of the

measuring technique. The twins are probably narrower than observed and their boundaries cannot be determined accurately. However, the DWs lie on a larger surface on the sample and the error is comparatively reduced. In addition, the DWs slope measurements are the mean values. It is noticed that the DWs slopes decrease gradually from the highest near the twin boundary to the lowest at the DWs at the opposite end.

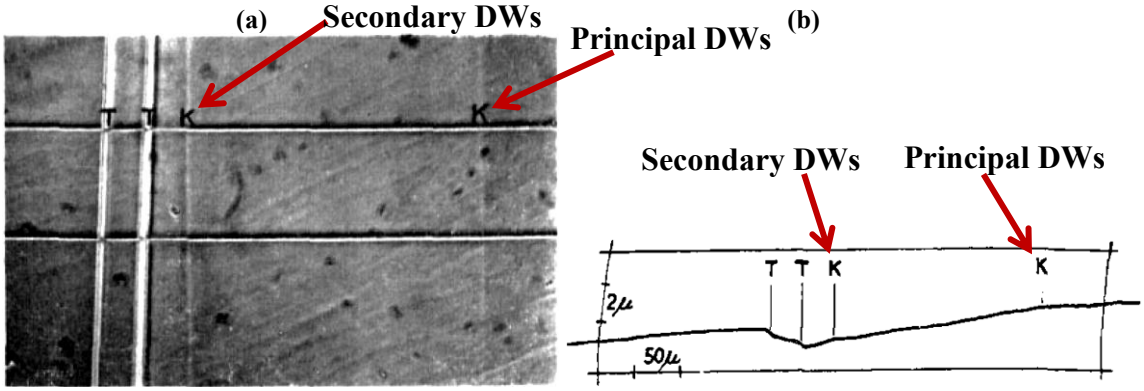

Figure 2-6: (a) Vickers Projection Microscope image of deformed single crystal zinc showing two narrow twins (T) and two DWs (K) (X165),(b) Talysurf surface profile record at same location[15].

Figure 2-7(a) shows Jillson's [16] schematic representation of how DWs can form parallel to twins. The schematic shows a lenticular twin that does not go through a grains' cross-section. Therefore, the lattice has remaining strain that has not been accommodated. There is thus a high stress concentration at the edge of the twin, hence the adjacent lattice basal planes bend at a larger scale to accommodate the required deformation strain. A sectioned optical photomicrograph image of a twin and a DW in single crystal zinc are shown in Fig. 2-7(b). There are several parameters that affect the shape, size, DWs angle and number of DWs that form parallel to the twin. The additional DWs that form between the principal DWs and the twin boundary are termed secondary DWs. Figure 2-6 illustrates the existence of a principal and a secondary DWs of the same sign when shear stress spreads across the grain lattice.

Moore [17] elaborated on the investigation of DWs in single crystal zinc by studying the relationship between twin shape and the adjacent DWs. Moore [17] proposed an angular expression between the twin and DWs, and clarified a lot of interesting features observed in twins and DWs. He showed optical and electron microscope images where secondary DWs could be of the same or opposite sign of the principal DWs (Figs. 2-7(b) & 2-8).

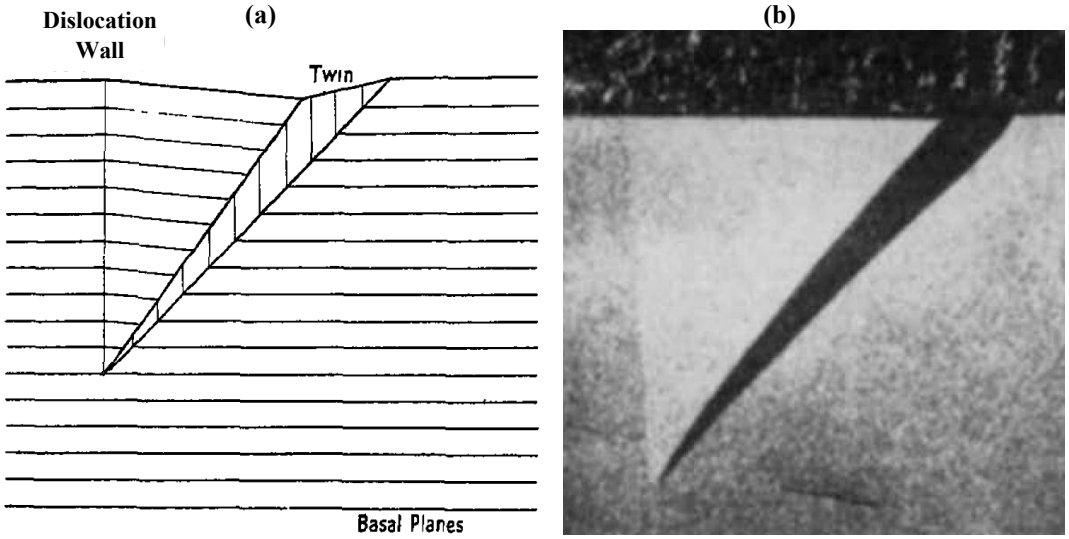

Figure 2-7: (a) Schematic representation of lattice DWs caused by twinning[15, 16], (b) Sectional optical photomicrograph image of a twin and DWs of single crystal zinc[17].

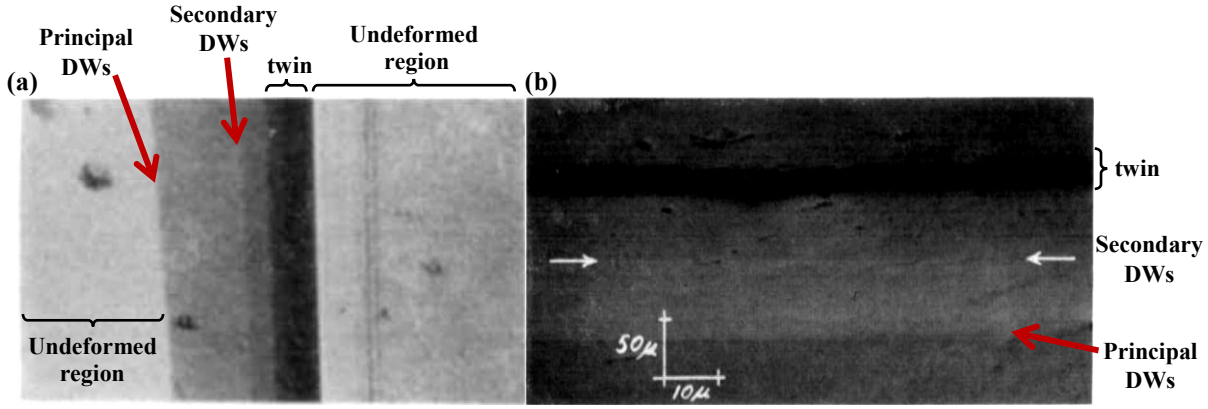

Figure 2-8: (a) Sectional optical photomicrograph image of a twin and two DWs of the same sign, (b) Reflection electron micrograph of twin with an oppositely signed DWs (shown by arrows) half-way across the accommodation region. Both images are of single crystal zinc[17].

Figure 2-8(a) shows an optical microscope, OM, micrograph of the top view of a deformed Zn single crystal where the dark strip is the thickness of the lenticular twin and

the large wide, light regions, on the left and right sides of the image are undeformed. Between the twin and undeformed regions, there are two grey scale colored strips bordered by principal DWs, secondary DWs and twin boundaries. The gradual decrease in intensity from the twin, to the secondary DWs, to the principal DWs, and finally to the undeformed region indicate that both DWs are of the same signs. However, the intensity differences in the reflection electron micrograph shown in Fig. 2-8(b) show that the secondary DWs is of an opposite sign to the principal DWs.

Moore [17] presented a schematic representation of the twin and DWs growth stages shown in Fig. 2-9. At low stress, a small twin AB forms with a DW C (Fig. 2-9a). As the stress increases, the twin grows in length and thickness by the formation of a parallel twin DE and movement of the principal DWs to location F (Fig. 2-9b). More twin steps form and the principal DWs follows the movement of the twin tip with growth (Fig. 2-9(c)) and loading. However, Moore's [17] study observed an interesting feature about secondary DWs. The edge dislocation sign of the secondary DWs is opposite to that of the principal DWs when the twin growth expands in thickness as shown in Fig. 2-9d. On the other hand, secondary DWs are of the same sign if the twin grows in length relative to its thickness Fig. 2-9e.

The oppositely signed secondary DWs is a very important observation by Moore [17]. Figures 2-9(a)-(c) show that when the shear stress is low, the twin develops and the adjacent lattice basal planes form a principal DW. As the twin extends in length into the grain, the principal DW follow, starting from the lenticular twin tip to the sample surface. A secondary DW of the same sign would develop if the shear stress is spread across the grain lattice and the twin size elongates in the same proportions. However, if the shear

stress applied on the grain lattice increases but is localized in the same region, i.e. due to the lenticular twin growing in thickness more than in length, then the secondary DWs would form in an opposite sign to the principal DWs. The DWs develop because the shear stress is not above the twin threshold stress for twin nucleation or growth to accommodate all of the strain required. The principal and secondary DWs, whether of the same edge dislocation sign or opposite, are to make a gradual change in the strain field and basal plane angles between the highly strained lenticular twin and the undeformed surrounding lattice in the grain.

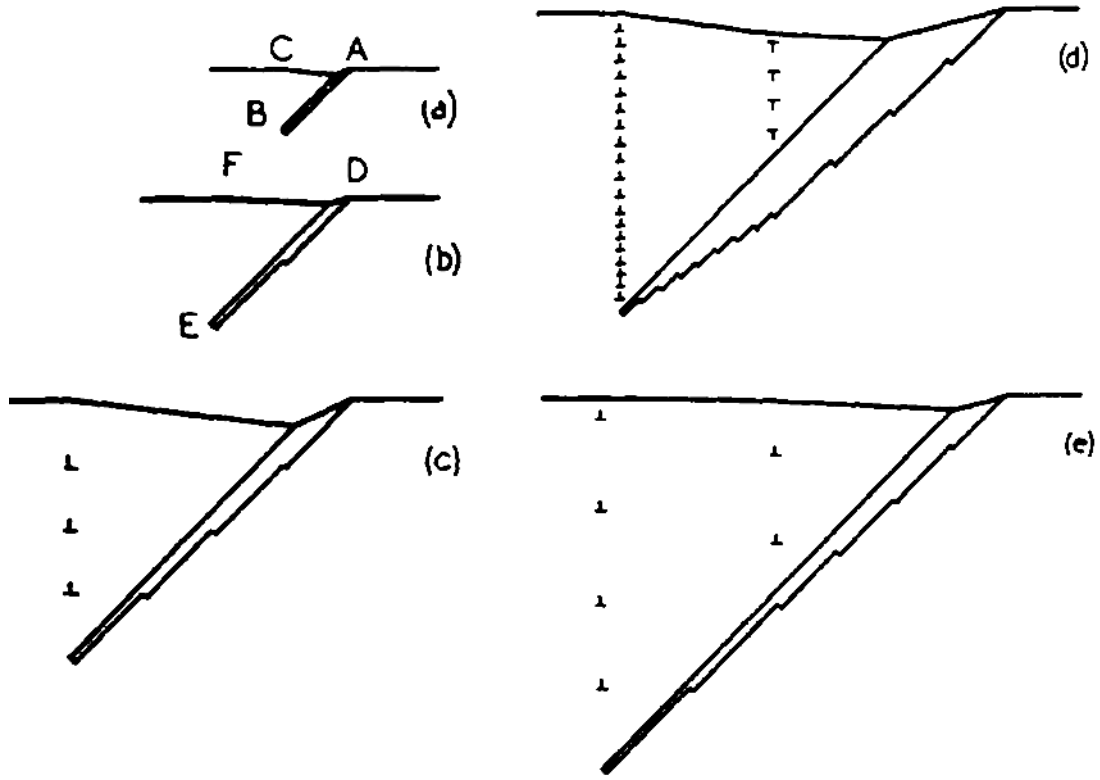

Figure 2-9: Schematic representation of twin and DWs growth and movement at different stages of loading in a single grain lattice (a) Initial twin, (b) Growth of twin in length and thickness, and principal DWs at twin tip, (c) Additional growth of twin two more steps and principal DWs moving to a new position. (d) Twin growth by increase in thickness results in an oppositely signed secondary DWs, (e) Twin growth by increase in length results in same signed secondary DWs as the principal DWs [17].

In addition, Pratt & Pugh [18] (1953) progressively strained zinc single crystals where they managed to control twin growth and shape, and observed the movements and change in angles of the DWs called mosaic walls due to their curved nature. Figure 2-10 shows scanning electron microscope (SEM) images of single crystal zinc showing the increase in the mosaic angle (indicated by darkness change) and the movement of mosaic boundaries as the stress increases. After each successive strain step, the sample was placed in the SEM to observe the same location. The deformation markings and DWs mosaic boundaries between location A-B and A-C can be seen in Fig. 2-10(a). The increase in the mosaic boundary angle is observed between A-C in Fig. 2-10(b) and the movement of A-B in Fig. 2-10(c).

The existence of kinks and DWs have been observed in layered materials and HCP solids like zinc, cadmium, magnesium, titanium and others. In layered solids like mountain cliffs, geological earth layers, wood, paper stacks etc… kinking is the only possible deformation mechanism since twinning is not possible. However, in HCP materials depending on the orientation of the grain and magnitude of shear stress applied, the lattice would twin only, twin and form DWs or might only form DWs to accommodate the required strain. It was found that materials that form DWs have a KNE mechanical behavior.

After extensive research, Barsoum *et al.* [19] identified Fig. 2-11 which developed a criteria for identifying various KNE versus Non-KNE HCP materials. They postulated that as c/a ratios > 1.4, solids will tend to be KNE. Note that there is an overlap of twin and DWs formation in materials having c/a ratio close to ~ 1.4 like beryllium, zinc, cadmium, magnesium etc…

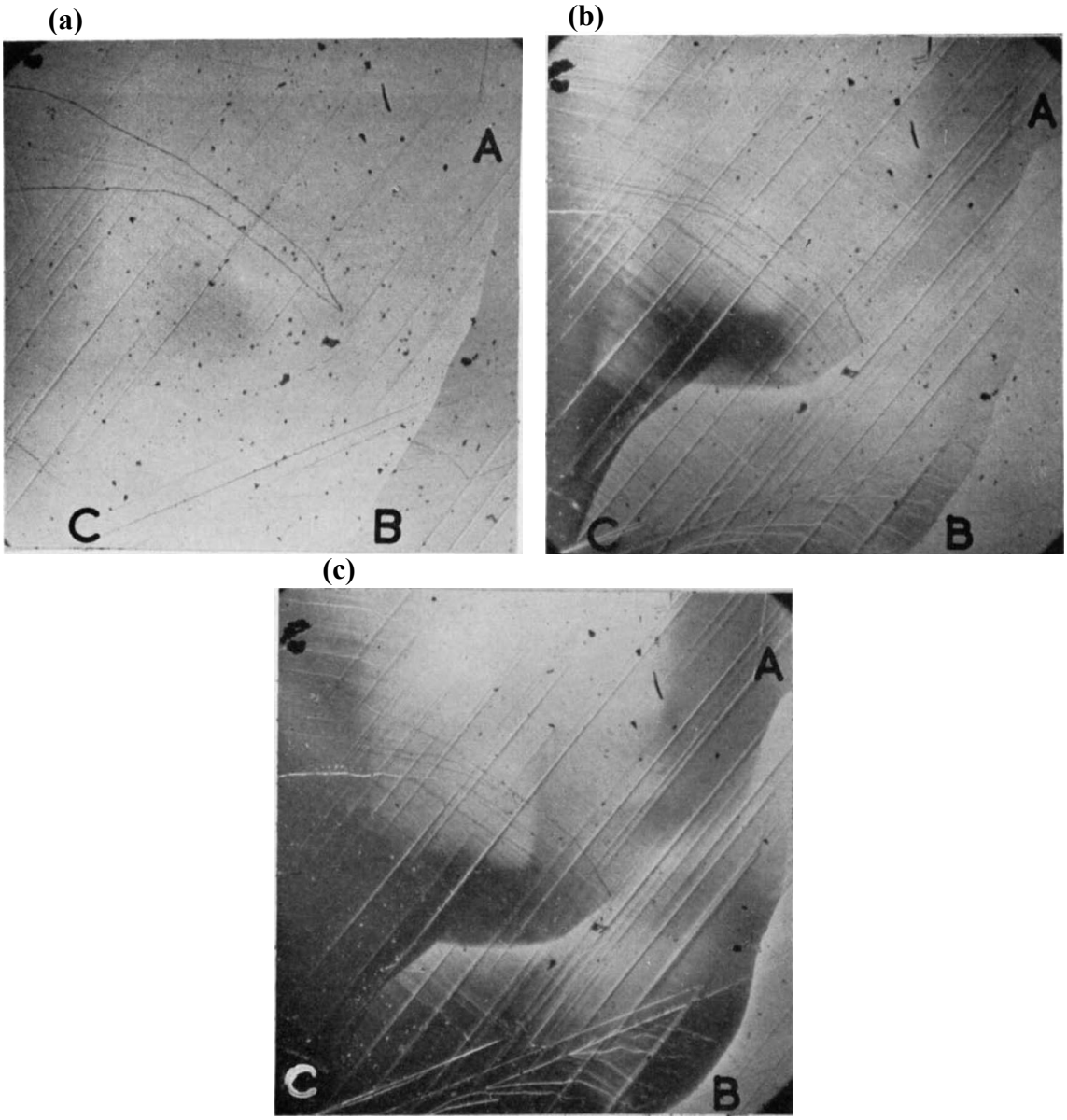

Figure 2-10: SEM images of a Zn single crystal under successive stress increments, showing the increase in the mosaic wall angle (indicated by darkness change) and movement of mosaic boundary. Two main boundary lines AB and AC are labeled on the images [18].

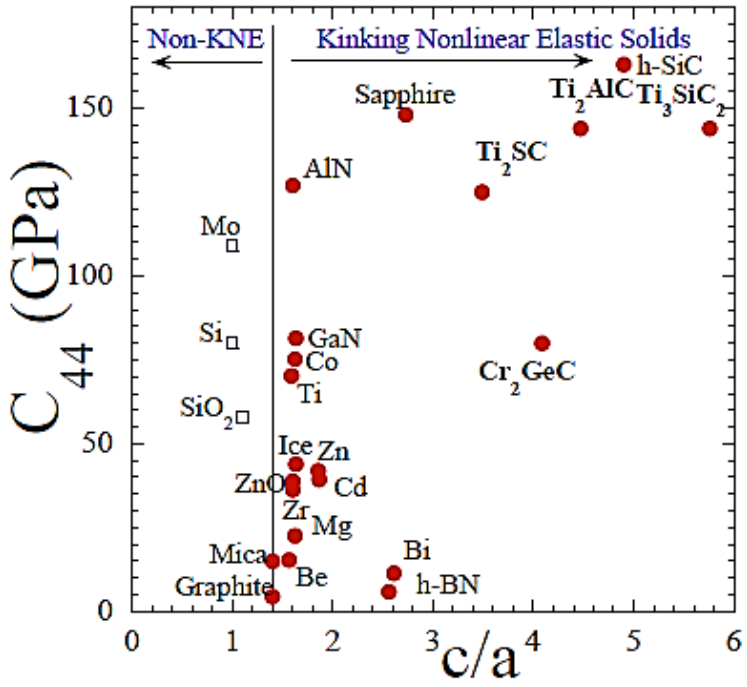

Figure 2-11: Plot of C_{44} versus c/a ratio for hexagonal materials. The vertical line at c/a = 1.4 is the boundary between KNE (right side) and non-KNE (left side) solids [19].

Dodwell *et al*.[5, 20, 21] performed extensive studies on deformation of single and multi-layered folds of rocks and paper. Their studies indicate apparently that buckling takes place during deformation of layered structured materials, confirming Orowan and H&B's schematic features findings. In addition, they uploaded a video showing the displacement of 1000 vertical A4 half sheet papers under compression using Digital Imaging Correlation (DIC) technology [20]. The video indicates the paper layers buckling at different locations and development of different signed edge dislocation-like walls at different deformation stages. Figure 2-12 shows a schematic of the paper pile setup supported by sponge and ply wood made by Dodwell *et al* [5, 20, 21]. Fig 2-12(a) shows a video snapshot of the DIC horizontal displacement measurement before any deformation occurs. Figure 2-12c shows the entire DIC color spectrum "correspond to global horizontal displacement, red right to purple left" [5, 20, 21] after the whole paper

pile length has buckled, with all color gradients in between, in which green represents the neutral state, with zero horizontal displacement (Figs. 2-12(b) & (c)). Based on the developments that occur in the DIC experiment video it is obvious that the paper pile 1st buckle starts at the bottom right corner, with a right buckle. As deformation develops, a 2nd left buckle is established, and finally a 3rd right buckle in the remaining top section of the paper pile setup is observed. It is deduced from Fig. 2-12(c) that kink bands occur between every two opposite direction buckled regions.

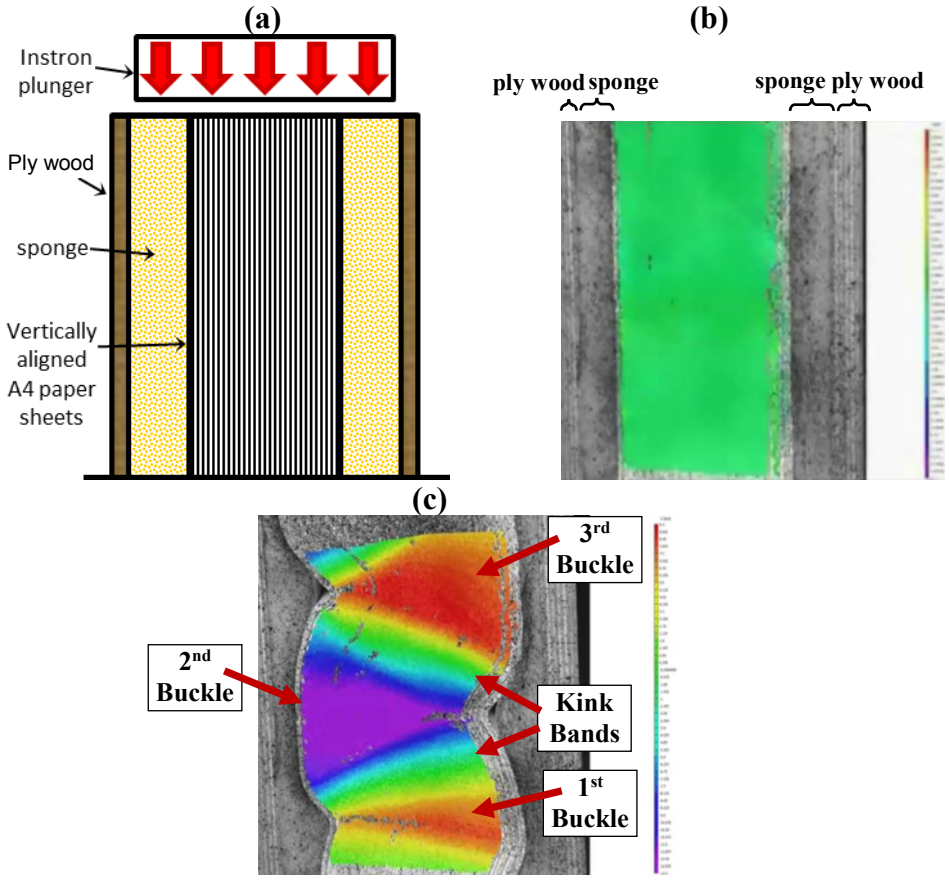

Figure 2-12: Pseudo-single crystal setup of layered structured material setup (a), horizontal displacement measurement (b), (c) DIC snapshot after completion of buckling across the paper pile layers length[5, 20, 21].

A closer look at the development of the edge dislocation-like walls in Fig. 2-12 and the theoretical explanation by H&B in Fig. 2-4, one can conclude that their

hypothesis is correct in that edge dislocations and edge dislocation-like features are active on the layers (or basal planes in crystalline materials).

Considerable studies were performed in the current era investigating slip and twin dislocation mechanisms. However, limited information is known concerning edge dislocation-like walls nucleation, angle, strain accommodation, morphology etc… that occur during buckling of layered structures. The dynamic behavior of edge dislocation-like walls to accommodate strain during mechanical loading starting from their formation, growth and rotation makes the numerical modeling of DWs during layers buckling a challenge. Layers buckling in Fig. 2-12(c) shows edge dislocations-like walls aligned at the maximum shear regions (Fig. 2-3(b) & (c)), then symmetric localized bending of the buckled region occurs "about an axis that lies in the slip plane and normal to the slip direction"[22]. However, at different stages of the layers buckling in Fig. 2-12(c) the plane of symmetry changes and flexural regions develop as shown in Figs. 2-1, 2-2 & 2-4. When a plane or set of planes (region) buckles, the plane(s) rotate. This would result in an increase in the resolved shear stress (RSS) on the plane(s) (due to the tilt of the layers); explaining the progressive increase and localized systematic deformation in the buckled region. The edge dislocation-like walls adapt themselves to accommodate more strain as the deformation develops in the buckled region, therefore, the amount of shear the edge dislocation-like walls could accommodate is not fixed as in twins [22, 23].

The number of possible buckles in the paper pack is governed by Euler's elastic buckling condition. The next section discusses buckling deformation of members and describes the various conditions that affect the buckling behavior that are observed in layered solids as well.

2.3 Buckling and Surrounding Support

A preliminary background about Euler's buckling equation needs to be explained before exploring the deformation of layered structures in detail. For any structure, or structural component, under compressive loading, a sudden change in its geometry, resulting in a loss of its ability to resist further loading is defined as an “instability”. This phenomenon is a strength-related limiting state and must be accounted for in designing structures since it can lead to catastrophic failure. Buckling is a deformation mechanism in which the structure transfers to an unstable state when a critical compressive load limit is surpassed. The type of structure (i.e. cross-sectional shape and moment of inertia), condition of support, kind of loading and the material used all affect the critical load limit and resulting buckling modes.

Consider a column structure under compressive load (P) where its length is an order of magnitude larger than either of its other dimensions (Fig. 2-13(a)). The column will buckle when the load reaches a critical value (P_{cr}). At this load, the column deflects significantly in the lateral direction (V in Fig. 2-13(b)(i)) compared to the axial displacement. The column in this state cannot sustain additional load (P_{cr}) and the lateral deflection increases (Fig. 2-13(b)(ii)). Columns, sheets, plates, shells and other shape configurations can buckle. Premature buckling occurs in real life due to loading misalignment, material imperfections/defects and variations in structural dimensions. Nevertheless, in imperfect systems, buckling can occur at a significantly lower uniaxial stress than a material's compressive yield stress. The drawbacks of buckling are a considerable lateral deflection (V) and an inability to maintain additional load (P_{cr}).

Buckling does not occur until P_{cr} is reached. The theoretical buckling load, P_{cr}, for a basic column is given by Euler's formula, Eq. (1)

$$P_{cr} = \frac{n^2\pi^2EI}{L^2} \quad (1)$$

where P_{cr} = critical axial force needed for buckling to occur, n = buckling mode, could be 1, 2, 3….etc, E = Young's modulus, I = second moment of area for the column's cross-sectional area (i.e. moment of inertia) and L = length of column.

Figure 2-13(c) illustrates the first three harmonic buckling modes. The first buckling mode, where n = 1, is the lowest value of critical force, P_{cr1}. The critical loads needed for the different buckling harmonics increase progressively with "n", such that $P_{cr1} < P_{cr2} < P_{cr3}$. Note that modes higher than n = 1 do not occur unless bracing is placed at locations where V = 0 (lateral deflection, Fig. 2-13(c)),

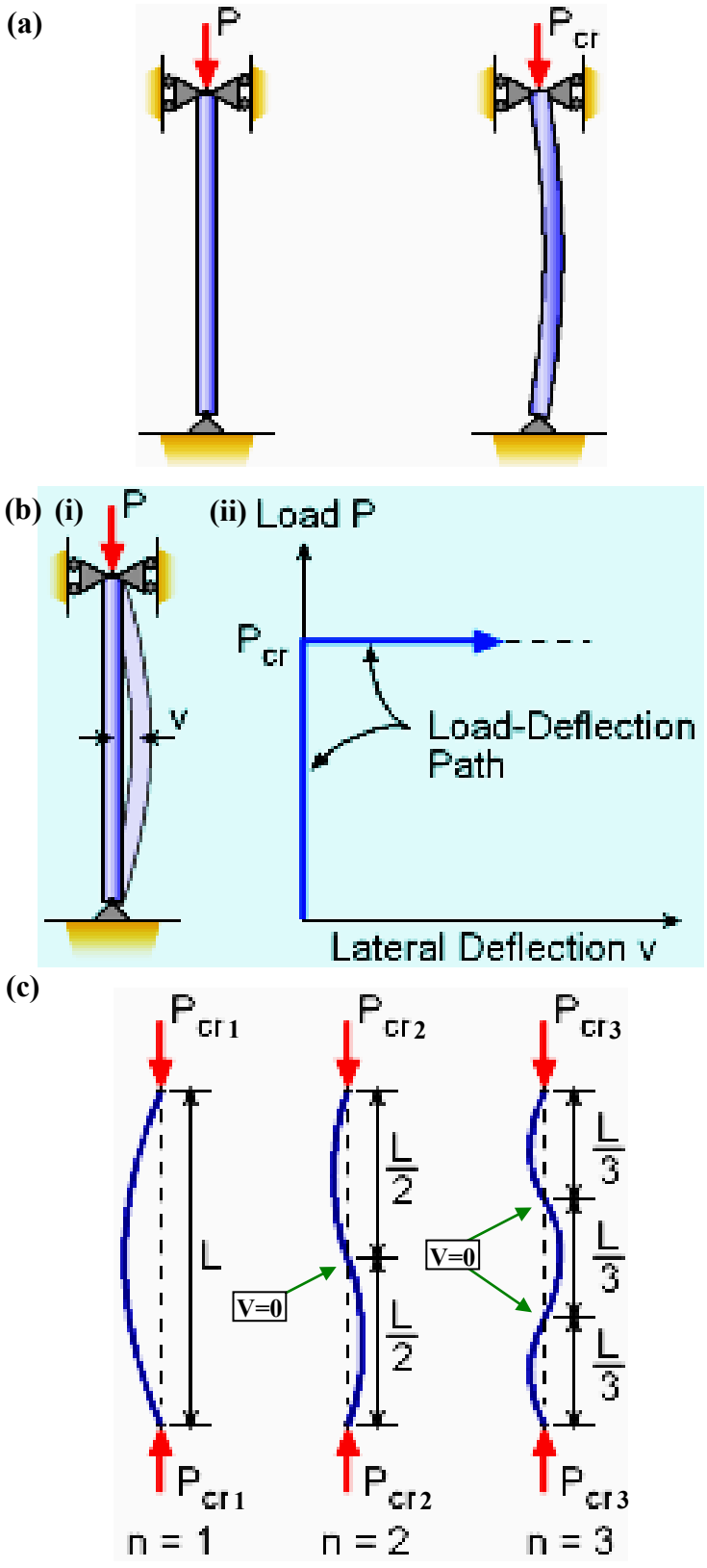

Figure 2-13: (a) Basic pinned column before and after buckling, (b) Load-Deflection diagram for column buckling, (c) First three column buckling modes [24].

In addition, as stated previously, loading misalignment and structure tilt can trigger premature buckling. The direction of the resulting column lateral deflection is governed by these two factors, and is illustrated in Fig. 2-14. The misalignment can occur when a columns is: i) perfectly vertical and the loading direction is at an angle, θ, (Fig. 2-14(a)); ii) the load is shifted from the columns centerline (Fig. 2-14(b)); or iii) the columns structure is tilted at an angle, α, while the load is perfectly aligned (Fig. 2-14(c)). Under these conditions premature buckling of the column can result. Figures 2-14(a)(ii), (b)(ii) & (c)(ii) are the same as Figs. 2-14(a)(i) (b)(i) & (c)(i), respectively illustrating the lateral deflection direction relative to the loading angle, loading shift direction and tilt direction, respectively. The difference between columns (i) & (ii) in Fig 2-14 is the deflection direction, (i) is to the left while (ii) is to the right. An important feature that needs to be considered in the buckled structure is the stretch in the outerside of the column and squeeze on the innerside (Fig. 2-15) resulting in tension and compression at two regions in the structure. There is only one plane that is neither longer nor shorter than it was before buckling, called the “neutral plane”. Figure 2-15(a) & (b) shows the stress distribution of symmetric structures that buckled in two different lateral deflection directions. For explanatory purposes, buckled structures resembling Figs. 2-14(a)(ii), (b)(ii), (c)(ii) and 2-15(b) will be termed “right buckle” since the lateral deflection direction is to the right; consequently, Figs. 2-14(a)(i), (b)(i), (c)(i) and 2-15(a) represent a “left buckle”.

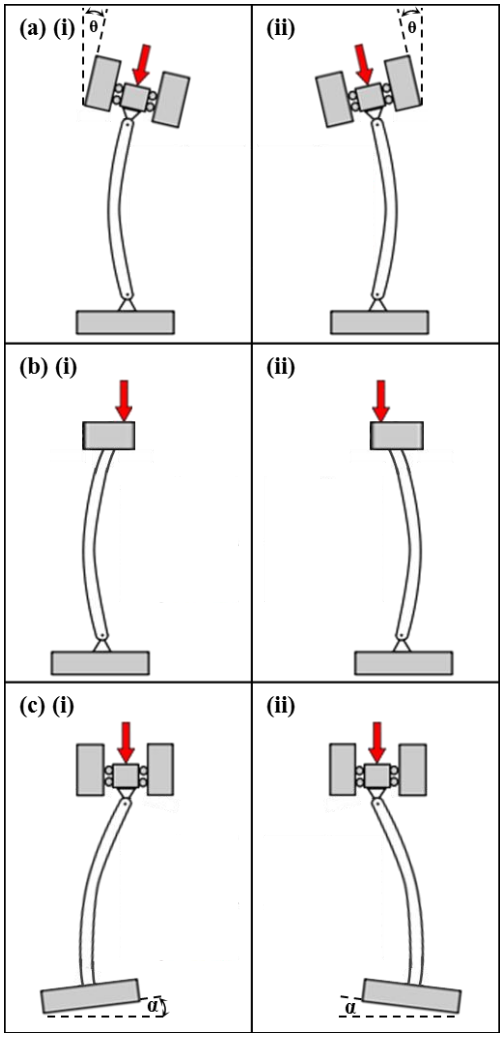

Figure 2-14: Different premature buckling modes:(a) Effect of loading angle relative to column center line, (b) Effect of shift in loading direction from column center line, (c) Effect of tilt in column; (a)(ii), (b)(ii) & (c)(ii) are the same as (a)(i) (b)(i) & (c)(i) respectively illustrating the lateral deflection direction relative to the loading angle, loading shift direction and tilt direction respectively; α is considered negative in (c)(i) and in positive (c)(ii) .[25]

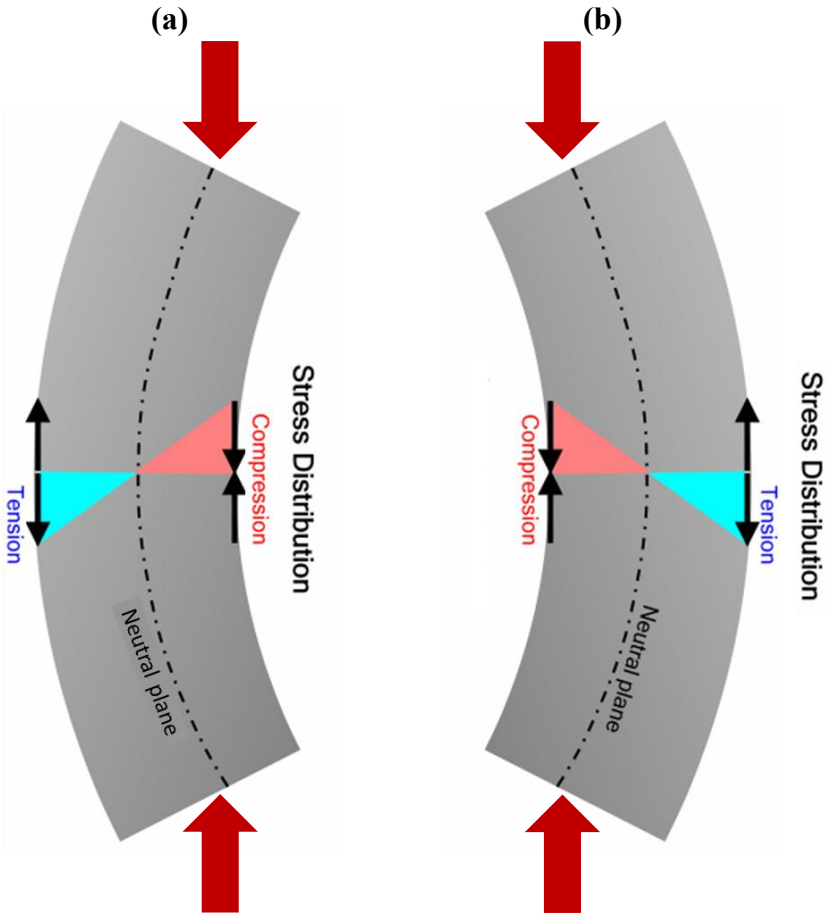

Figure 2-15: Schematic of buckled structures showing the regions under tension and compression split by the neutral plane, (a) Left buckle, (b) Right buckle[26].

Figure 2-16 shows the 3rd harmonic mode of a buckled slinky. The wide and narrow regions and variations in the slinky parts that are under tension and compression are clearly observed. Despite the 3rd harmonic buckling mode displayed by the buckled slinky (Fig. 2-16) there is always a general curvature for the whole structure affecting the stress distribution details in the different parts. The slinky curvature results directly from the stress distribution of Fig. 2-15(b). The wide and narrow regions illustrate the extension and contraction of the gaps between the buckled slinky exemplifying general tensile and compressive sections on the right and left hand sides, respectively. Note, the red dashed curved line represents the neutral plane where neither stresses exist. In

addition, certain parts in the slinky itself are under tension or compression depending on their location. For example, locations A, D & E are in tension, while B, C, & F are in compression. However, due to the buckled slinky strips between A-B and E-F located in the compression contraction section, the gaps between the slinky strips at A & E are equivalent, but smaller than those at location D. Furthermore, the number of slinky strips touching each other at location C is larger than those at B & F. This is due to the higher compressive stresses in the slinky at C and is due to the narrow region and angle of the buckle C-D than A-B and E-F. Thus, the 3rd harmonic buckling mode of the slinky in Fig. 2-16 illustrates a multiple buckling harmonic mode with a right buckle where the general lateral buckling deflection is to the right (red dashed line in Fig. 2-16).

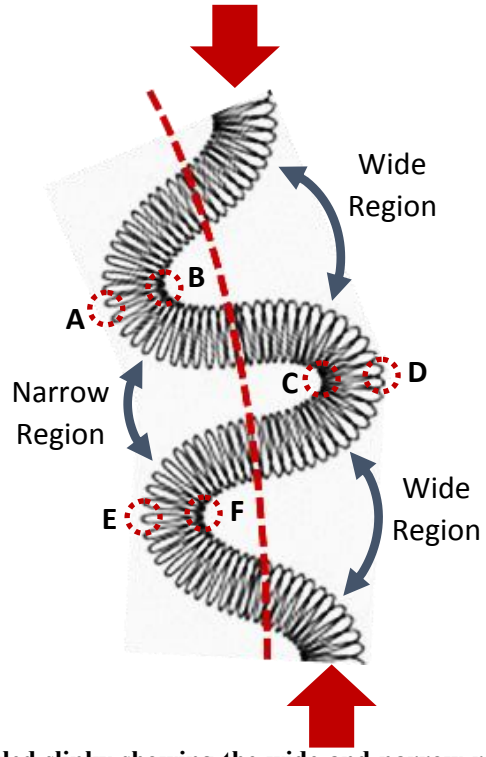

Figure 2-16: Schematic of buckled slinky showing the wide and narrow regions within the structure corresponding to slinky sections under tension and compression. Red dashed line indicates the general curvature affecting the features observed in different regions. The dashed red circles designate the locations of interest in the buckled slinky marked by various letters [27].

2.3.1 Multiple Buckling Features in Layered Solids

The paper pile experiment by Dodwell *et al.* [5, 20, 21], clearly demonstrate the importance of the surrounding support on the behavior of the paper pile during deformation. The sponge and ply wood support are the reason for occurrence of the 2nd and 3rd harmonic buckling mode observed.

Figure 2-17 shows the formation of ridges after extensive buckling deformation of cadmium single-crystal wire [8]. A schematic demonstrating the edge dislocations arrangement causing ridge formation proposed by H&B is shown in Fig. 2-17(b) [12]. It is predicted that the primary DWs (marked as green translucent lines) nucleated first in the primary buckle, followed by the secondary DWs (marked as red translucent line) within a DW region of the buckled layered structure schematic [12]. A DW region is the region in the primary buckle (i.e. between two primary DWs of the same sign) where secondary DWs of the same sign can nucleate. Nevertheless, multiple secondary DWs could nucleate in a DW region as observed in the TEM bright-field image and the representative schematics in Fig. 2-18. It is not necessary that one secondary DWs wall be nucleated from one secondary buckle within the DW region. Two secondary DWs could nucleate from one secondary buckle, depending on the flexural strength of the layers in the DW region after the dimensional changes that occur.

Figure 2-18(a) displays a TEM bright-field image of a bent region that is delaminated in three slices (designated as S1 through S3) [13]. The dislocation walls observed indicate the presence of multiple secondary buckles within the DW region nucleating several secondary DWs. Figure 2-18(b) shows a schematic representation of S2 marking the primary DWs, secondary DWs, secondary buckles & kink bands [13].

The schematic is a cross-sectional view of S2 through the material depth normal to the basal plane layers A-A. It is assumed that the ends of the DW region are the green DWs (Fig. 2-18(b)) since this is the field of view that could be observed in Fig. 2-18(a). The width of the kink band is not defined since the whole crystal periphery is not identified. The multiple secondary DWs resulting from multiple secondary buckles in the DW region is evident in Fig. 2-18(a) represented by the red edge dislocations in Fig. 2-18(b). The green and red edge dislocations added to the schematic is a possible combination of primary and secondary DWs resulting from the multiple buckles that occurred in S2. However, the material properties and the local changes in layers dimension plays a major role in deciding how and where these secondary DWs would nucleate and move until they reach the final state of S2 in Figs. 2-18(a) & (b). Figures 2-17 & 2-18 are examples of layered buckling where secondary buckles are of the same direction due to the lack of support. Unlike the paper pile 3rd harmonic buckling (Fig. 2-12) where each adjacent buckle occurs in an opposite direction to the one before it.

It is crucial to note that for buckling of layered structures to take place, relative motion between the layers is imperative. Therefore, dislocation pile-ups is essential for buckling of layered grains as shown in Fig. 2-18(c) where dislocation arrays are observed on the basal planes of Ti_3SiC_2 [13].

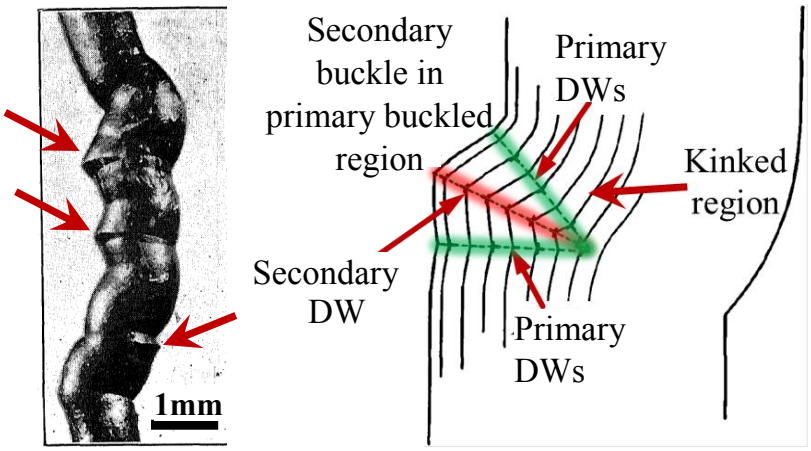

Figure 2-17: Illustration of kinks and ridges formation after buckling deformation. (a) Photograph of cadmium single-crystal after extensive buckling [8]. Locations of the ridges formed are marked. (b) Schematic demonstrating edge dislocations arrangement proposed by H&B causing ridge formation. Translucent green and red colors are added to differentiate between the DWs nucleated at different stages. Translucent green color represents DWs resulting from the primary buckle, while the translucent red color represents a secondary DW formed as a result of secondary buckling within the DW region [12].

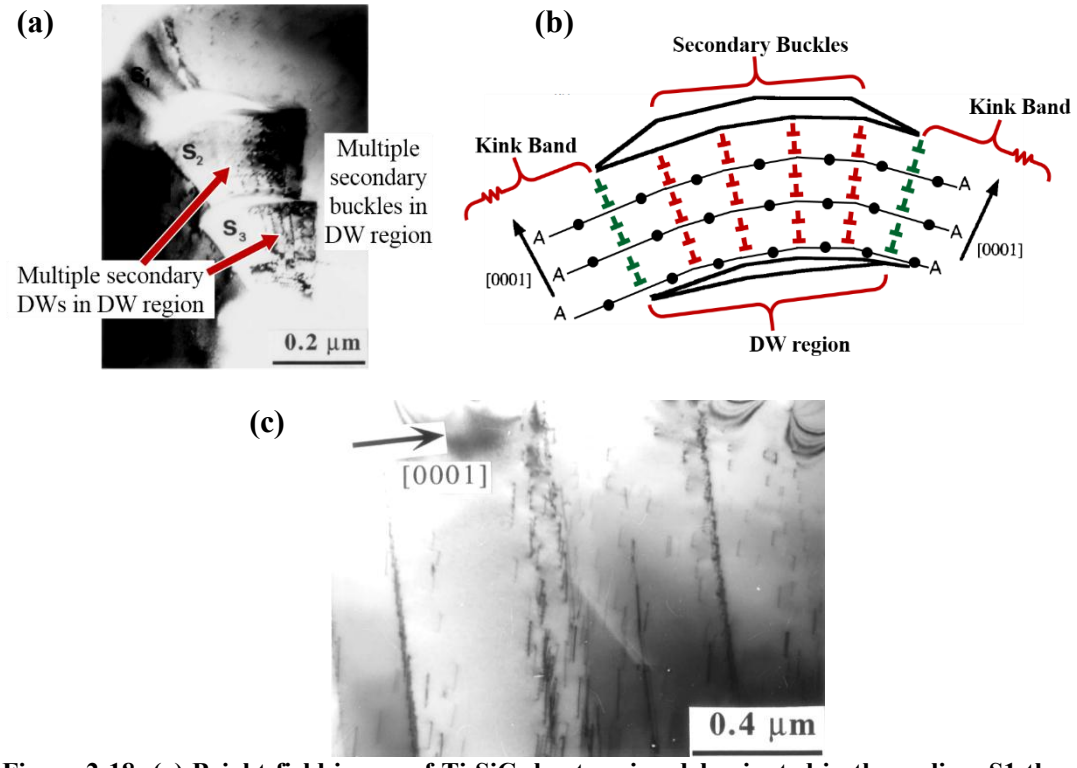

Figure 2-18: (a) Bright-field image of Ti_3SiC_2 bent region delaminated in three slices S1 through S3 and containing primary and secondary DWs; (b) Schematic of S2 showing primary and secondary DWs. The DW region, secondary buckles in the DW region and kink bands are marked. The distance between A-A represent the basal plane layers, the dots ● represent atoms in the basal planes, green edge dislocations, ⊥, are the primary DWs and red edge dislocations, ⊥, are the secondary DWs. The green and red edge dislocations where added to the schematic to differentiate between primary and secondary DWs. (c) Bright-field image of an area containing dislocation arrays. The specimen is close to the orientation where basal planes are in an edge-on position [13].

Euler's elastic buckling formula (Eq. (1)) and rules apply on the layered structured grains in polycrystalline materials, however, the effect of a materials' crystalline nature needs to be taken into account. In polycrystalline materials, the surrounding grains and grain boundaries provide the bracing required for the layered structured grains to deform in multiple buckling harmonic modes. The elastic moduli of the surrounding grains will determine the buckling harmonic mode and location of the possible DWs, DW & kink bands. However, the orientation of the surrounding grains will affect the magnitude and direction of the surrounding forces exerted on a layered grain. Figure 2-19 shows a schematic adjacent to the bright field TEM images of a fractured Ti_3SiC_2 crystal showing the basal planes, the corresponding DWs, and DW & kink bands [13]. The red arrows in the schematic (Fig. 2-19(b)) surrounding the grain's basal planes represent the forces exerted by the neighboring grains on the grain of interest in the TEM image. The orientation of the neighboring grains, and the amount of deformation they will experience during deformation will determine the magnitude and direction of the forces applied on each grain. Figure 2-20 displays a SEM micrograph fracture surface of a Ti_2AlC sample. This image shows DWs in different locations with various angles on the fractured surface. Hence, the deformation of any grain is related to its neighbors and therefore, there is an interconnection between all grains' deformation since all of them affect each other. This fact illuminates the reality of the 3D effect of all grains in a polycrystalline material on each other and the resultant macroscopic stress-strain of the whole system.

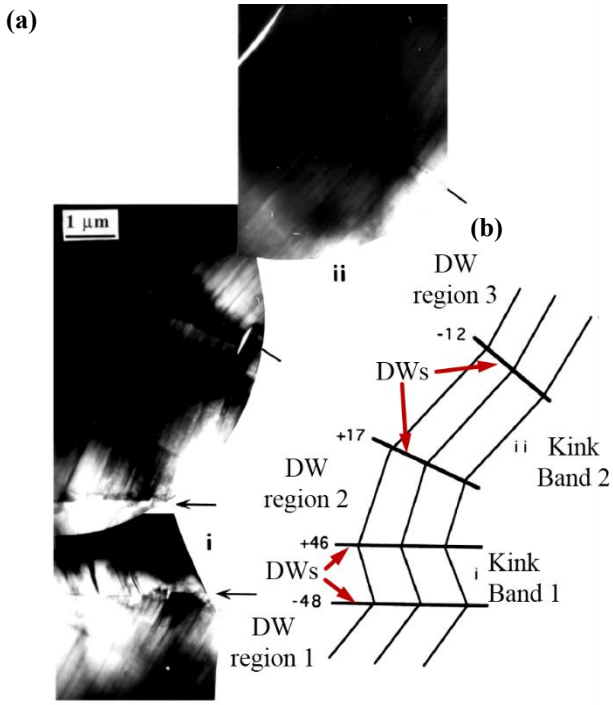

Figure 2-19: (a) TEM bright-field image of Ti_3SiC_2, and adjacent schematic of a region containing two kink bands denoted as i and ii and the DW regions neighboring them. The crystal is close to the edge-on position for the basal planes. The numbers show the measured rotation angles between the blocks of the crystal around <11$\bar{2}$0> directions provided, mostly, by the DWs; (b) Schematic showing DWs, DWs and kink bands. The red arrows surrounding the basal plane material layers represent the forces exerted by the neighboring grains on this grain[13].

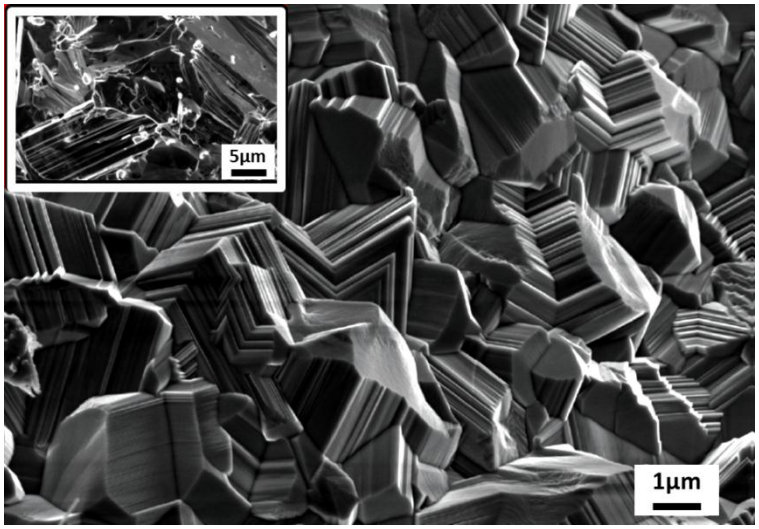

Figure 2-20: SEM micrograph of a fractured surface of a Ti_2AlC sample held at 1100ºC and 30 MPa for 3 h. Sample failed at a tensile strain of 16%. This micrograph emphasizes the profusion of kink boundaries formed as a result of the deformation. Inset shows a fractured surface of the grip area where no kink boundaries are present. Note grain refinement resulting from deformation[28].

2.4 Deformation of Geological Layered Structures

Deformation of the earths' geological layers takes a lot of different forms like folds, faults, cleavage, foliation and joints. The deformation rate in addition to the physical properties of the layers is very crucial in dictating the deformation mechanisms taking place, since earth layers and rocks can behave in a ductile or brittle fashion depending on the speed of the deformation. Small structures are a key to and mimic the styles and orientations of larger structures of the same generation within a particular area. This relationships was first stated by the Raphael Pumpelly and is known among geologist as the Pumpelly's rule [29]. Therefore, the geological layers deformation features can be observed at the micro, meso and macroscopic scales.

Faults that occur as a result of the earth's seismic activity are fractures with considerable movement parallel to the layers. This type of geological deformation is possible in crystalline layered solids. Folding is the geological deformation mechanism of interest since it is observed in all post mortem images of KNE materials; Figs. 1-3, 2-1, 2-2, 2-3, 2-4, 2-6, 2-7, 2-8, 2-10, 2-12, 2-17, 2-18, 2-19 & 2-20. They form in all deformation rates in ductile and brittle materials. Relative motion between the layers is necessary for folding to take place. Therefore, during layer folding both pure and simple shear types (Fig. 2-21) are needed for the deformation to take place. Pure shear (Fig. 2-21(a)) results in distortion by homogeneous deformation in which a body is elongated in one direction and shortened perpendicularly while the principle axes remain unchanged [30]. However, in simple shear, the lengths parallel to the y-axis remain unchanged and all translation is along the xz-axis (Fig. 2-21(b)). An example of simple shear is the

movement of a deck of cards. Note that if rotation or translation is added to pure shear, the result would be simple shear [30].

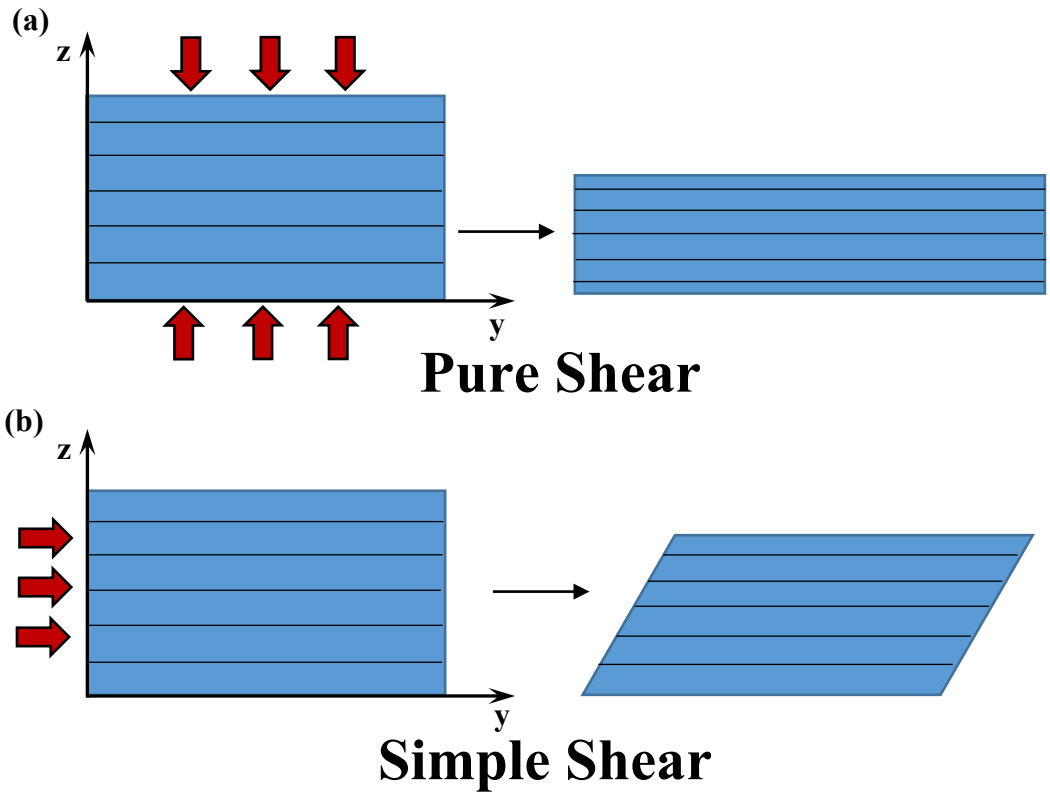

Figure 2-21: Schematic representation of (a) pure shear, and (b) simple shear [30].

Folds form different profiles during deformation, therefore, defining different regions and locations of a folded layer geometry would help in describing the interactions taking place during deformation. Figure 2-22 shows a schematic representation defining different parts of a folded layer [31]. The hinges are points of maximum curvature within a single folded layer. They could be represented by a point or zone. Limbs are the area of a layer between hinge points. Inflection points are the points on the layer where the curvature changes direction. It is typically, but not necessarily, half the distance between hinge points.

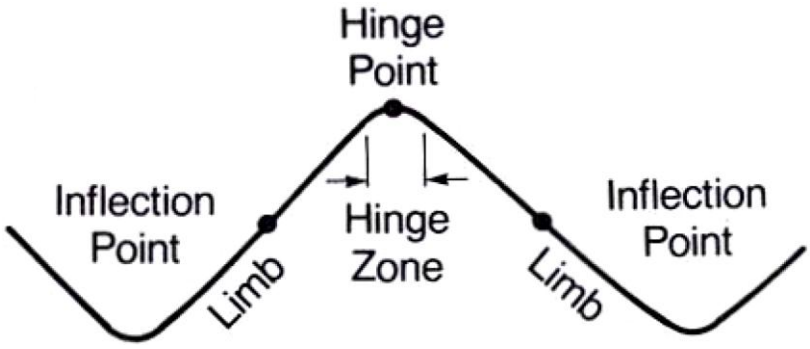

Figure 2-22: Schematic representation defining different parts of a folded layer [31].

The angle between the limbs of a fold (interlimb angle) is variable changing the fold profile. Figure 2-23 shows the classification of fold profiles based on the interlimb angle [31]. The fold is considered gentle when the interlimb angle is between 180-170º, open from 170-90º, tight from 90-10º and isoclinal when < 10º.

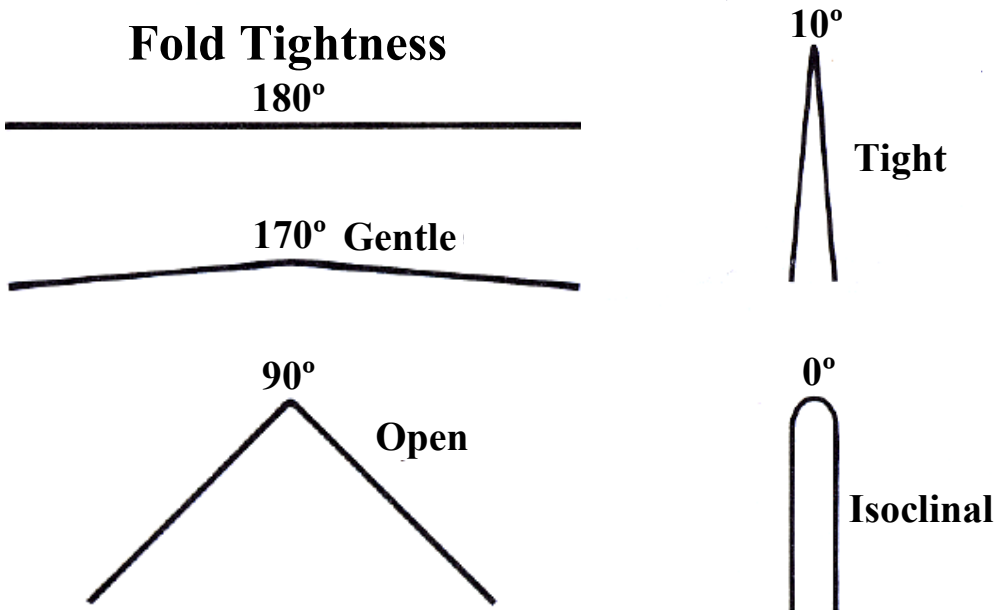

Figure 2-23: Fold profile classification based on angle between fold layers' limbs [31].

During deformation of multiple layers, the layers interact with each other forming different fold profiles and curvatures. John Ramsay classified fold profiles based upon

the curvature of the inner and outer lines of a fold, and the behavior of the dip isogons (Fig. 2-24). A dip isogon is a line that connects points of equal inclination (or dip) on the outer and inner bounding surfaces of a folded layer. Class 1 is where the inner arc is greater than the outer arc. However, class 1A is where thinning in the hinge and thickening in the limbs is observed. Class 1B is where parallel folds take place maintaining a constant layers thickness at the folds and the dip isogons are perpendicular to the layers, while class 1C shows modest thickening at the hinge zone and modest thinning in the limbs.

Class 2 demonstrates ideal similar folds maintaining constant layer thickness parallel to the axial plane while outer and inner arc curvatures are equal. Class 3 displays extreme thickening in the fold hinge zone while the dip isogons are far away from axial plane, signifying that the curvature of the outer arc is greater than the inner arc [32, 33].

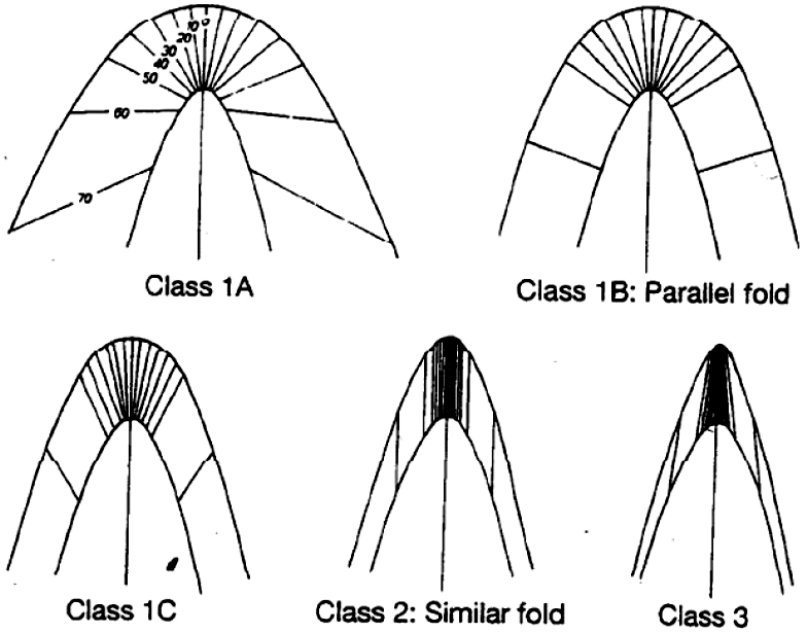

Figure 2-24: Ramsay's classification of folds based on curvature of the inner and outer lines of a fold, and the behavior of the dip isogons [33].

There are different fold types that occur in geological layers that also apply to crystalline layered solids. Flexural-slip folds are parallel concentric folds that form by buckling or bending. Slip in these folds is parallel to the layers and characterized by slickensides surfaces. They maintain constant layers thickness. It is considered brittle deformation and generally forms class 1B folds. Passive-slip folds on the other hand form by slip parallel to axial plane (i.e. simple shear across the layers). The deformation is ductile and class 2 (similar) folds are generally formed. Kink bands are formed by passive-slip folds [30, 34, 35].

2.4.1 Kink Bands in Geological Structures

Kink bands are observed in geological structures scaling in size to kilometers observed between earth plates resulting from tectonic plate interactions. Anderson studied several hundred kink bands in the Silurian slates of the southern part of the Ards Peninsula in northern Ireland [36]. Anderson describes “the confining planes, which were termed kink planes by Hills [37], as a pair of sharply angular folds”[36]. Flinn stated that kink bands are "the expression of a movement which can have a component parallel to the strike of the S-surface" [38]. This conclusion is supported by numerous experimental studies. Majority of the observations in which kink bands deformation takes place in northern Ireland occurred without any displacement along the two confining planes. In addition, kink bands were seen to terminate through the convergence of the kink planes defining a flat lens as shown in Fig. 2-25. The same features are observed at all scale levels.

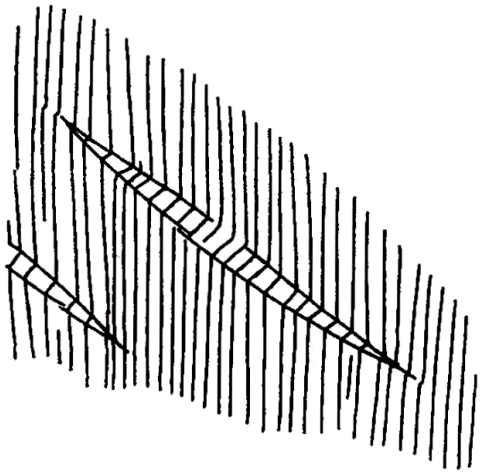

Figure 2-25: Lenticular lens shape of kink bands observed at all scale sizes [36].

Anderson proved that the cleavage planes (planes within the kink band) tend to expand [36]. “This expansion is commonly measurable in real examples. The cleavage planes tend to have opened within the kink bands and the resulting partings may be filled with small segregation veins of quartz or calcite which terminate at the kink planes in the Ards Peninsula where the rows of veins are parallel to the kink-bands of the shales”[36]. A majority of kink bands are features of many structurally complicated areas in the British Isles. Examination of kink bands in other areas, including examples in Dalradian schists in north Donegal, Devonian slates in south-west Ireland, Lower Palaeozoic slates in North Wales and Ordovician slates in the central Pyrenees, and examination of many diagrams and photographs in the geological literature on kink bands, afforded further examples of the parallel and lenticular lens kink bands.

There are theoretical studies performed that concentrate on the buckling behavior of layers embedded in materials of different properties to investigate the response of geological layered structures in different regions of the earth's crust [39]. Paterson and Weiss performed compression experiments on phyllite at different angles of its layers

embedded inside different jacket materials[40, 41]. Flexural slip, which results into kinking in crystals, is thought to be a characteristic feature during deformation of layered rocks like slates, phyllites and mica schists. Deformed fine-grained phyllite and mica schist demonstrated noticeable geometrical similarities with large-scale geological layered kinks. Several conjugate kink bands formed during extensive deformation of phyllite, however, the folds at the kink band intersections appear to be clearly different in style and orientation from the folds forming the kink bands. The thick brass and copper jackets used during deformation of phyllite resulted in kink bands formation, while the rubber jacket allowed inhomogeneous deformation and extensive simple shear to take place. The objective of such experiments is to simulate the situation of layered solids in nature. The surrounding material properties affect the layers deformation possible routes depending on the constraints imposed. The applied stresses causes deformation of the whole system, therefore, the layered solid must conform with the deformation of the neighboring parts.

2.4.2 Modeling Kink Bands

There are several attempts by research groups in the past decades to theoretically reproduce kink bands from different perspectives. Rosen [42] and Argon [43] were the first to develop mechanical models, followed by Budiansky [44] using continuum mechanics and Vogler [45] employing a numerical technique. There are numerous problems encountered when modeling kink bands. Two-dimensional modeling is commonly performed by researchers [46], however, kink band deformation is a three-dimensional phenomenon which adds substantial modeling complications.

Wadee *et al.* [47, 48] studied kink band instabilities and propagation in layered structures. To obtain an insight into the mechanism, layers of paper are compressed in the layers-parallel direction, while being constrained by transversely applied overburden pressure (Fig. 2-26). Measurement of the transverse compressibility adds a significantly new component into the formulation.

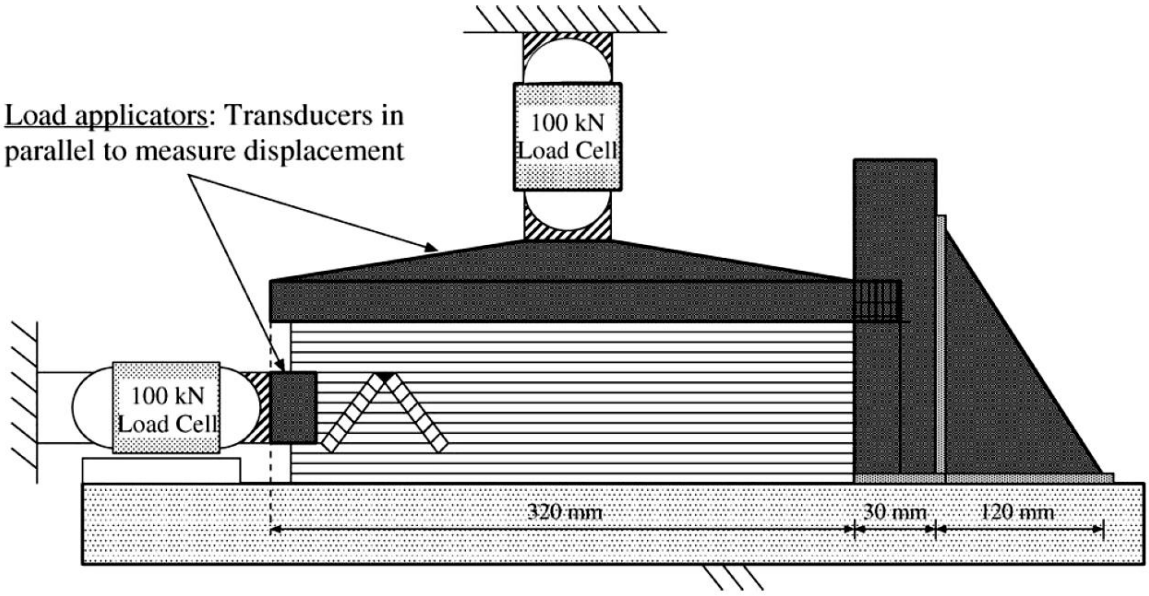

Figure 2-26: Schematic side elevation of the experimental rig. Displacement control via two screw jacks can be applied both axially and transversely. The rig can accommodate paper of size A4 (210 mm ×297 mm) and a sample height of 150 mm [48].

Measurements of the coefficient of frictions, overburden pressure and compressive loads are obtained during experimentation. The kink bands form across the paper layers as shown in Fig. 2-26. The transverse load measurement therefore infers the resistance from the stiffness of the supporting system to kink band formation. The bending energy required for layers deformation is difficult to measure. It is assumed that the bands form straight limbs and sharp corners, therefore, the corner curvature is selected to be a compromise between work done for bending and against the overburden pressure for kink band formation. An energy minimization formulation is solved and

parameters adjusted to obtain an agreement between the experimental and theoretical loading curves. Different paper dimensions and properties were experimented on to ensure validity of the theoretical parameters obtained from the model.

The non-linear behavior during loading originate from the energy required for kink band nucleation and growth, in addition to the work done against the frictional forces between the layers. There are two phases observed in the experimental response, layers instability and kink band propagation. The kink band rotation and width in addition to in-plane and transverse layers compressibility are the degrees of freedom included in the formulation. The formation of successive kink bands is tracked on the paper layers and loading curves to be applied on the mechanical model. The formulation managed to obtain the kink band angle with and error of only 2º employing the transverse strain measurements obtained from the transverse load cell (axial end shortening).

The earlier models assumed that kink bands form in a pressure bath and the overburden pressure keeps the layers together. The transverse forces required for deflection of the layers and kink band formation were not taken into account. The transverse forces from the bed of layers outside the loading regime play a major role in resisting growth of the kink band. This is due to the required retraction in the layers length for the kink bands to form. This effect is pronounced in multi-layered samples.

Dodwell *et al.*[5, 21] developed a model to predict the nucleation of voids in single and multi-layered structures during folding. Their model is applicable to kink boundaries since two of the three experiments they analyzed form kink bands and only one experiment demonstrates extensive folding due to the change in the surrounding foam support stiffness.

All research preformed until now are on kink bands and buckling while analyzing various parameters affecting their behavior. There are two kink bands configurations observed at different size scales that occur (Fig. 2-27). There is a governing mechanism that dictates the shape of the kink bands and kink boundaries that develop during deformation of layered solids. Chapter 3 exemplifies the governing shape the kink boundaries have to follow during deformation, and chapter 4 demonstrates an application of the governing 3D profile shape on the paper pile setup by Dodwell *et al.* [5, 20, 21] in Fig. 2-12 and the evolution of the kink boundaries shape and motion during loading.

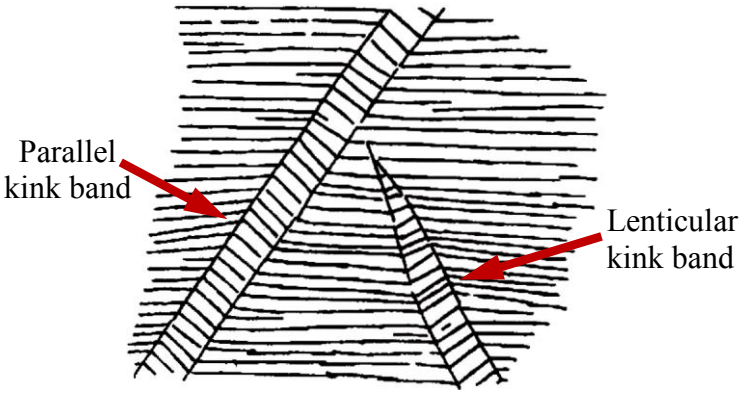

Figure 2-27: Schematic of two kink band configurations observed in layered solids at all size scales [36].

2.5 Summary and Conclusions

Layered solid can deform by buckling. The dislocation mechanisms occurring in layered grains is different than conventional slip and/or twinning. Layers buckle by forming DWs to accommodate strain. In addition, DWs could move to accommodate strain as well. DWs are observed in single crystals and polycrystalline layered materials. The surrounding support around the layered structure determines the buckle direction, DWs that would form and if kink bands are present. There are hexagonal materials where

buckling dislocation mechanism takes place by the formation of DWs, in addition to slip and twin activity, because their c/a ratio is ~ 1.4. Euler's elastic buckling condition governs layered structure buckling. However, the RSS on a buckled layer changes due to the change in the layers tilt angle. The RSSes acting on layers is studied in Ch. 3.

Kink bands and kink boundaries are observed in layered solids at all scale sizes ranging from earth plates interactions to the microscale in SEM and TEM images of MAX phases. Kink band formation is a specific type of folding that takes place in geological structures. Remarkable experiments were performed on layered minerals simulating the behavior of geological layers observing strikingly very similar geometrical features. Modeling kink bands is a challenging assignment due to its three-dimensional nature and various interactions taking place from the whole layered structured system. There were several attempts to model kink bands in the past decades from different perspectives. The latest mechanical model by Wadee *et al.* [47, 48] managed to predict the kink band angle with a negligible error after introducing the effect of the transverse load and obtaining in-plane and transverse strain measurements of the paper layers experimented on.

Upto my knowledge, the shape of the kink bands and kink boundaries nucleation and motion have not been investigated. One of the main contributions of this thesis is demonstrating the governing shapes of the kink bands and kink boundaries, and providing explanations for the development of the different shapes in deformed layered solids. Chapter 3 demonstrates the governing shape in which the kink boundaries must follow and chapter 4 shows an application of the developed shapes on the deformation of a paper pile.

Chapter 3: Normal and Shear Stresses on Layered Solids

During buckling of a layered structure a group of layers are displaced (Fig. 3-1(b)). It is crucial to study the forces generated from the load applied on the layered structure for buckling to take place and result in lateral displacement of the layers. This is done by understanding the shear and normal stresses applied to a layered structure during loading.

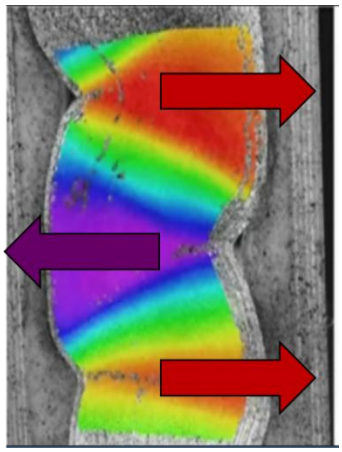

Figure 3-1: The final stage of buckled paper pile experiment by Dodwell *et al.*; arrows indicate lateral displacement of a group of layers, red arrows to the right and purple arrow to the left. [5, 20, 21, 24].

The forces and moments created during buckling of a column is studied as a preliminary stage to be applied on layered structures. Figure 3-2 shows the force P_C applied on an inclined column and the resulting moment, M, created along the column. The force P_C could be resolved into two component, P_P and P_N. The moment about point T would be:

$$\mathbf{P_P \,.\, (0) = 0}$$

$$\mathbf{P_C \,.\, x = P_N \,.\, y}$$

Hence,

$$\mathbf{P_N = \frac{P_C \,.\, x}{y}}$$

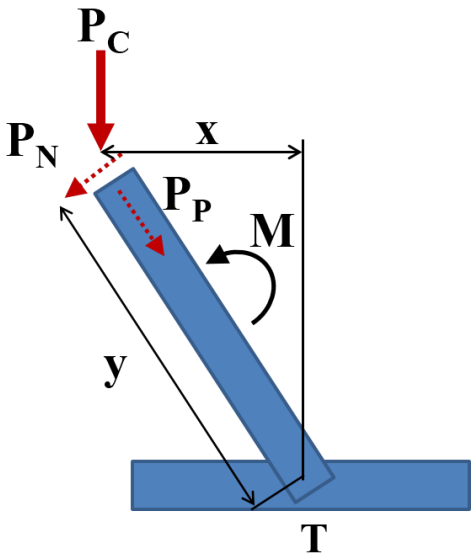

Figure 3-2: Forces and moment created during buckling of an inclined column.

The moment calculation about point T indicates that the resolved component P_P does not have any contribution on the moment created in the column. However, the resolved component P_N is the resolved component responsible for the moment, M, created in the column. To apply this on a layered structure, assume a matrix with layered structure while a compressive load is applied as shown in Fig. 3-3. Traction will be generated in all directions on the layered structure due to the compressive load applied. The layered structure will buckle inside the matrix due to the tractions generated. However, the traction components normal to the layers will contribute in buckling, while the traction components parallel to the layers will result in compressive or tensile stresses on the layers.

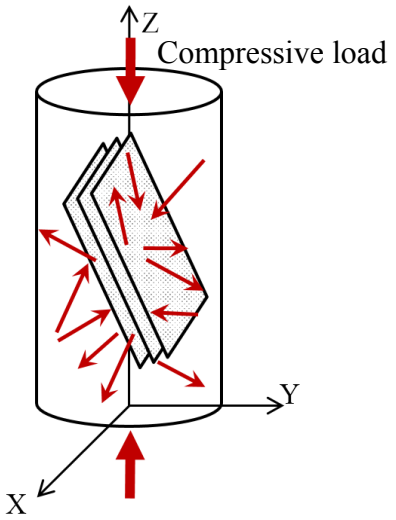

Figure 3-3: Traction applied in all directions on a layered structure in a matrix when a compressive load along z is applied.

In this section, the shear and normal stresses on individual layers resulting from a remote applied compressive load (Fig. 3-3) are defined and calculated. To begin, we start with a single tilted plane as shown in Fig. 3-4. This plane can represent a single layer in a layered solid. Because this is the plane in which slip occurs it will henceforth be referred to as the slip or basal plane. The angle between the loading direction and slip plane is represented by χ (Fig. 3-4). There are an infinite number of possible slip directions on the plane that have to be considered. Hence, the angle between the loading and slip directions, λ, (Fig. 3-4) changes and comprises an angle range indicated by the black dashed arrows. The angle ϕ represents the angle between the loading direction and the slip plane normal Z'.

The resolved shear stress, RSS, on a slip plane is given by:

$$\tau = \sigma \cos\phi \cos\lambda \tag{2}$$

where $\cos\phi \cos\lambda$ is known as Schmid's factor and σ is the axial applied stress.

First we consider two extreme cases where the plane is either perfectly vertical or horizontal. When the plane is perfectly vertical, ϕ is always equal to 90º, hence, cos(90)cosλ is always equal to zero as well. Conversely, when the plane is perfectly horizontal, λ is always equal to 90º, hence, cosϕcos(90) is again equal to zero.

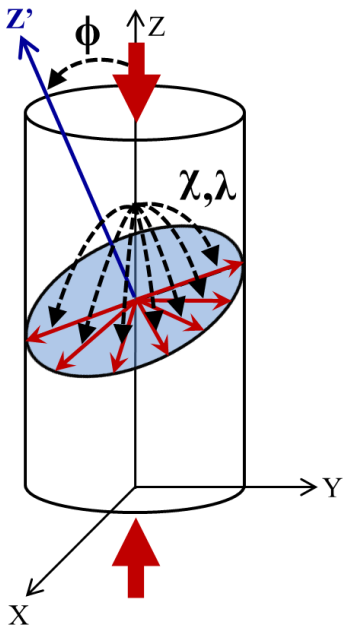

Figure 3-4: Schematic of possible slip directions in a material. Thick red arrows represent compressive load, light blue plane is the slip plane, thin red arrows are the possible slip directions on the slip plane; χ represents the angle between the loading direction and the slip plane, black dashed arrows represent the angle between the loading direction and slip direction λ on the slip plane, Z' is the vector normal to the slip plane. ϕ represents the angle between the loading direction and slip plane normal Z'. Note that angles ϕ and χ are complementary.

For the remainder of this chapter and thesis, the focus will be on planes that have a tilt 1º from the horizontal (Fig. 3-5(a)) or vertical (Fig. 3-5(b)). In the former case, we assume a solid or single crystal in which ϕ is fixed to be 1º. This sample will henceforth be referred to as the N-sample since the slip plane is "Normal" to the loading direction (Fig. 3-5(a)). In this case λ can only vary from 89-91º. A plot of Schmid's factor versus λ is shown in Fig. 3-6(a).

Next consider the situation shown in Fig. 3-5(b), where ϕ is fixed to be 89º. This sample will henceforth be referred to as the P-sample since the slip plane is "Parallel" to

the loading direction. In this case, λ can vary from 1-179º. Thus the slip directions are constrained within 1-179º. A plot of Schmid's factor versus λ for this case is shown in Fig. 3-6(b). Note that in either case no dislocations can be active if the slip plane is either perfectly horizontal or vertical.

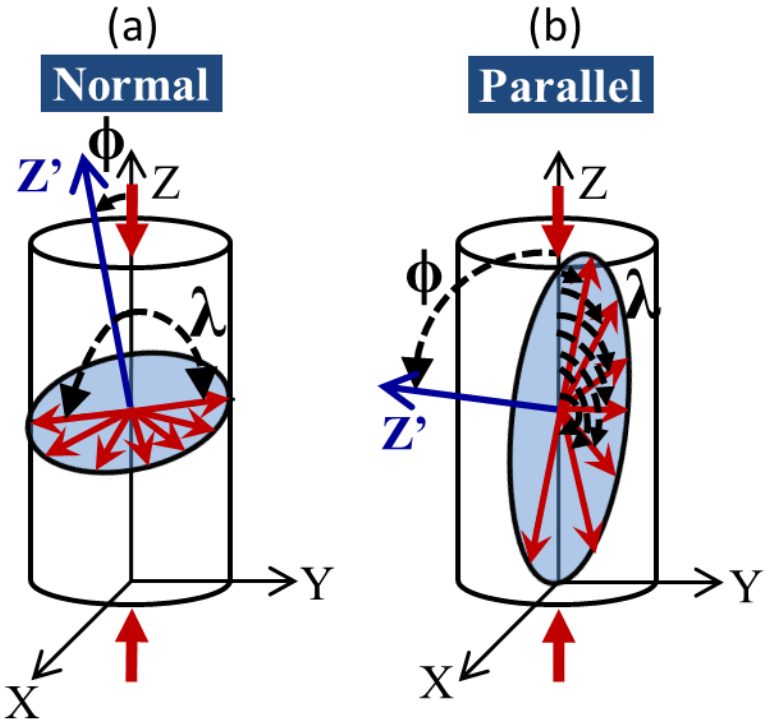

Figure 3-5: Schematic of possible slip directions (and/or shear stress vectors) in, a) N-sample and, b) P-sample, assuming tilts of 1º from horizontal or vertical, respectively.

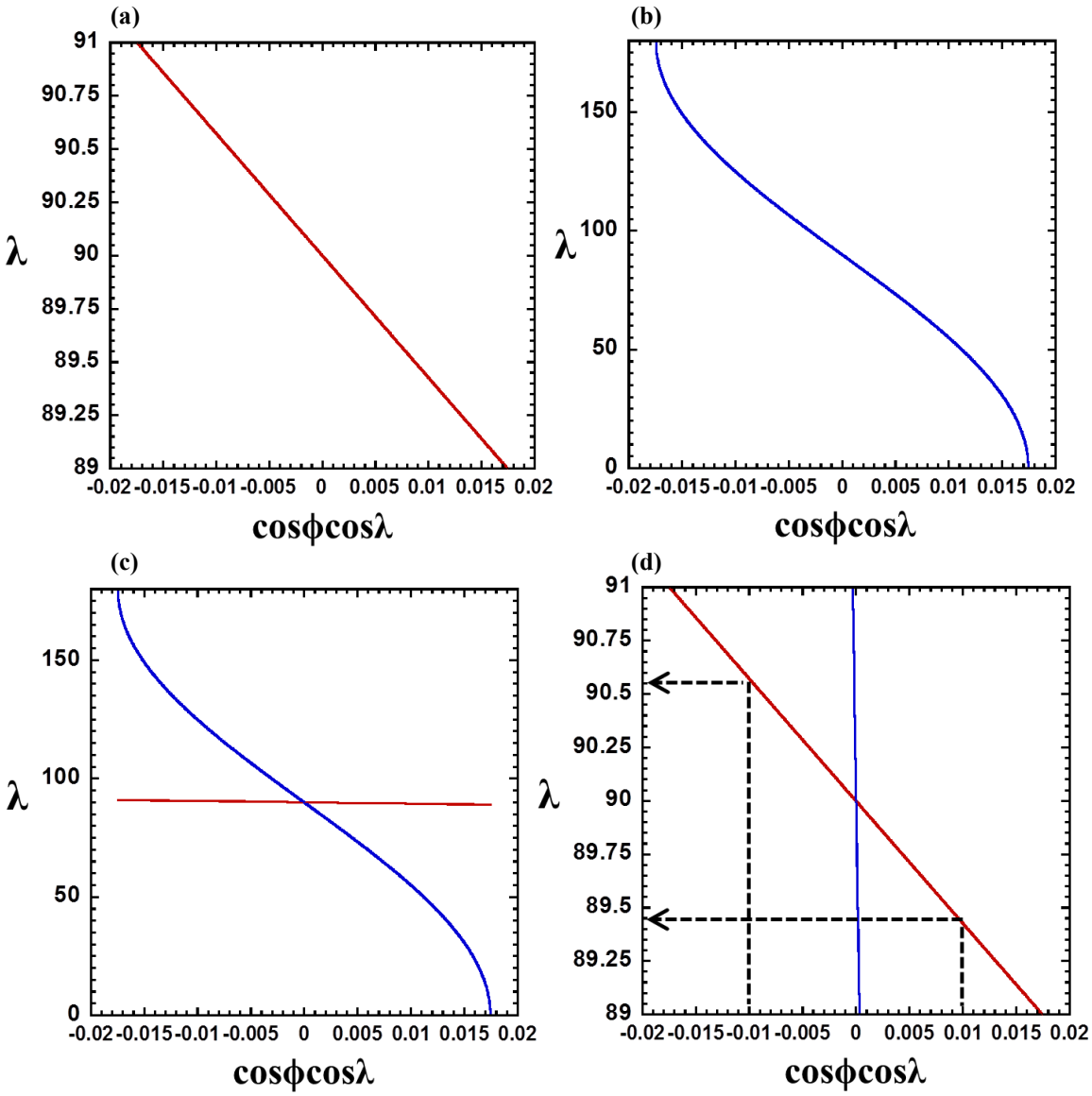

Figure 3-6: Possible variations of the Schmid factor for the, a) N-sample and, b) P-sample; and c) both samples together (red line N-sample, blue line P-sample), for λ range from 0-180º and, d) λ range from 91-89º. The dashed line corresponds to a RSS of ±0.01, above which slip is assumed to be activated. In other words, at values > 0.01, slip is possible. The corresponding ranges of λ from 89.45-89.00º & 90.55-91.00º in which the dislocations will be activated. Note that under those conditions, no dislocations can be activated in the P-sample.

Figure 3-6(c) compares the Schmid factors of both N- and P-samples as λ varies from 0-180º. Figure 3-6(d) is the same plot, but now λ only varies between 89-91º. Looking at Fig. 3-6(c), all possible slip for the N-sample (red line) lies within 2º (between 89-91º). This renders the probability of slip on the planes relatively high; i.e. minor changes in λ result in a substantial increases in the Schmid factor. For the P-sample (blue

line), on the other hand, the range of λ is significantly higher (1-179º), and thus compared to the N-sample, for a given stress, a significantly lower number of dislocations will experience a high enough Schmid factor to render them mobile.

Another way to look at the problem is to focus on Fig. 3-6(d). If we assume that a Schmid factor of > ±0.01 is needed for dislocation slip to be active, it is clear that, for a given stress, dislocations can **only** move in the N-sample. Conversely, **none** of the dislocations in the P-sample can move. As discussed below this result is crucial in understanding one of the most counterintuitive results obtained in this work.

3.1 Resolved Shear and Normal Stresses Extended in 3D

The aforementioned analysis was only concerned with the shear stresses on a plane titled 1° to the horizontal or vertical as a result of a vertically applied normal force (Fig. 3-5). In this section, the analysis is extended to 3D by summing all forces – shear and normal – that act on a set of imaginary planes (light blue planes in Fig. 3-7(b)) that intersect the 1° tilted plane (dark blue plane in Fig. 3-7(b)). Said otherwise, the shear stresses acting on each of the light blue planes depicted in Fig. 3-7(b), are resolved into their X, Y and Z components as shown in Fig. 3-7(a). Note that the X, Y, and Z axis are in the laboratory frame of reference and are thus almost identical to the 1° tilted planes. Said otherwise, the sum of these components represents the forces acting along and normal to the 1° titled or slip planes of interest to this work.

The rationale for such an analysis is simple. In layered structures, there is only one plane that is active during deformation. Hence, the contributions of the RSS components resulting from all **inactive** planes (that are infinite) can be resolved in a 3D

RSS map projected onto the active slip plane. Figure 3-8 plots the 3D map of the Schmid factors acting on a layer under loading.

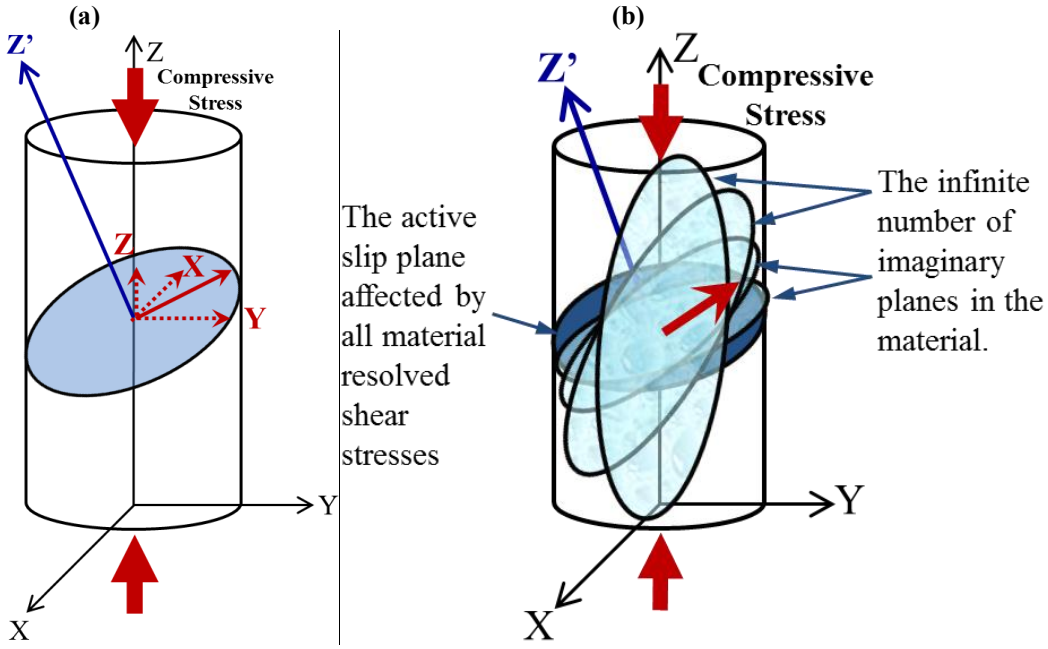

Figure 3-7: (a) Schematic of resolved components X, Y, and Z of shear vector given by solid red line. The thin solid red arrow is the shear stress vector and the thin dashed red arrows are the RSS components in 3D; (b) on the active slip plane, in addition to the infinite number of imaginary planes, (inactive slip planes shown as transparent light blue planes) whose RSS components can also contribute to that of the active slip plane.

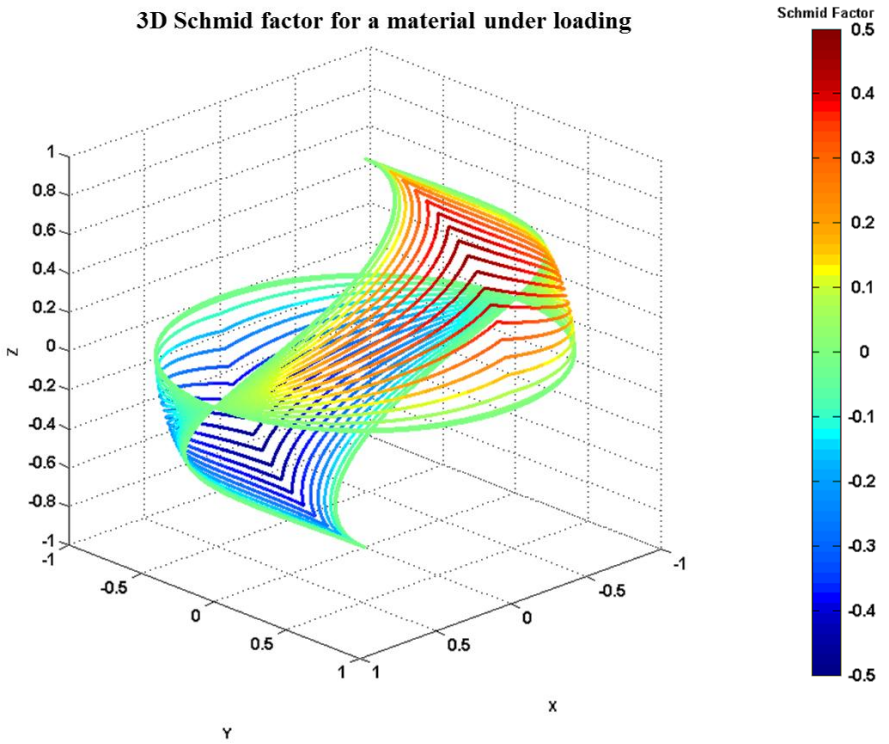

Figure 3-8: 3D Schmid factor of each layer under loading. The lines shown are from values obtained from inactive planes, rotated 5° each from the loading direction.

The effect of the 3D RSS map on layered solids is necessarily different than on materials in which slip and/or twin is possible when exceeding the CRSS or twin threshold stresses. Figure 3-9 is a schematic of a layered structure in a material under loading where the layers are normal to the applied compressive stress (N-sample). There are two main RSS components acting on the layered structure. One is normal to the layers (i.e. normal to the XY plane) represented by the Z-component, and the other is parallel to the layers (i.e. parallel to the XY plane) representing the XY-component. Note that the Z-component will tend to bend and/or buckle the layers, while the XY-component will move any dislocations that forms or are originally present in the layered structure once the CRSS is exceeded.

According to Fig. 3-10, the highest Schmid factor is equal to ±0.5 for both components resulting from the highest RSS at 45º. The Schmid factor X, Y, and Z components resulting from the 45º shear stress play a major role in the deformation mechanism since it is the location in which the highest shear stresses occur. Note that a plot of the absolute values of Fig. 3-10(b) is the XY plane projection of Fig. 3-10(a), giving equal absolute values of RSS of Figs. 3-10(a) & (b) at identical locations. Figure 3-11 displays the Z-component Schmid factor views from both the X-axis and Y-axes.

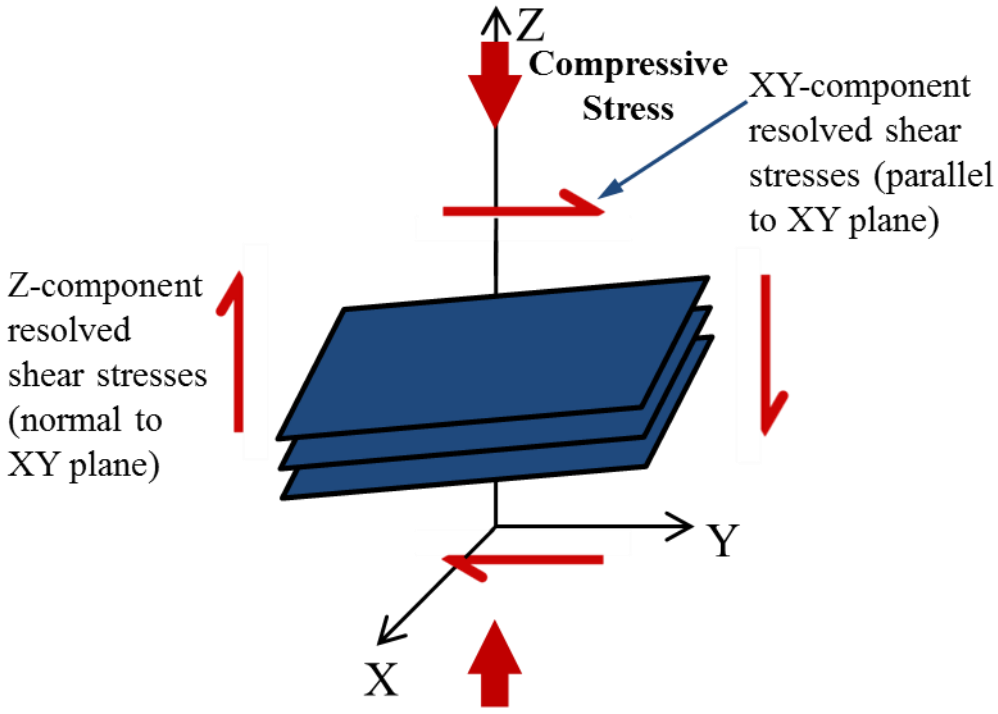

Figure 3-9: Schematic of layered structure of N-sample loaded in compression, and the resulting RSS components acting on the layers. The red half arrows designate the stresses normal to, and along the layers.

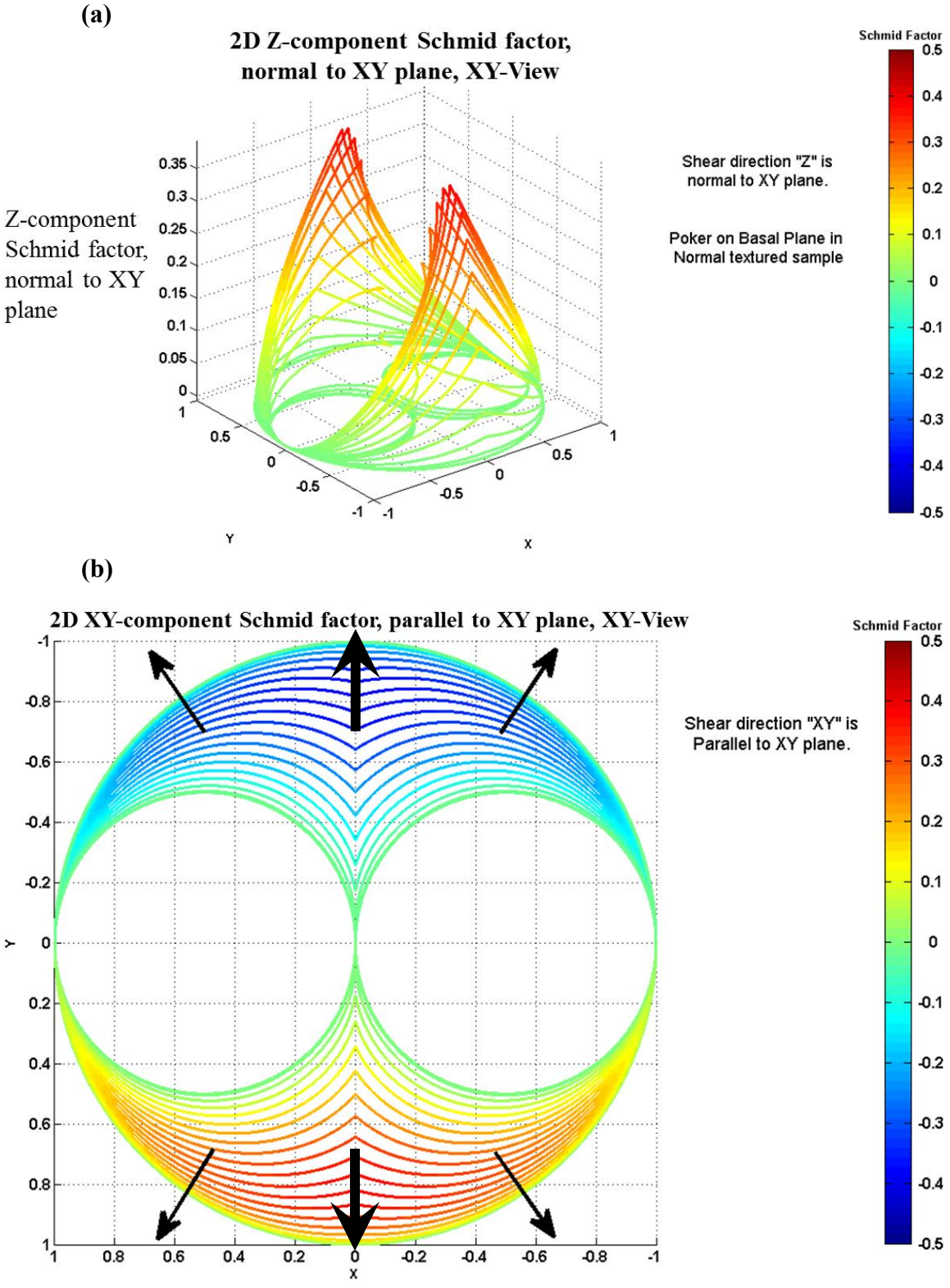

Figure 3-10: Plot of, (a) normal forces to the XY plane, and, (b) shear forces on the XY plane; both plots are for the N-sample configuration.

(a)

Z-component Schmid factor, normal to XY plane

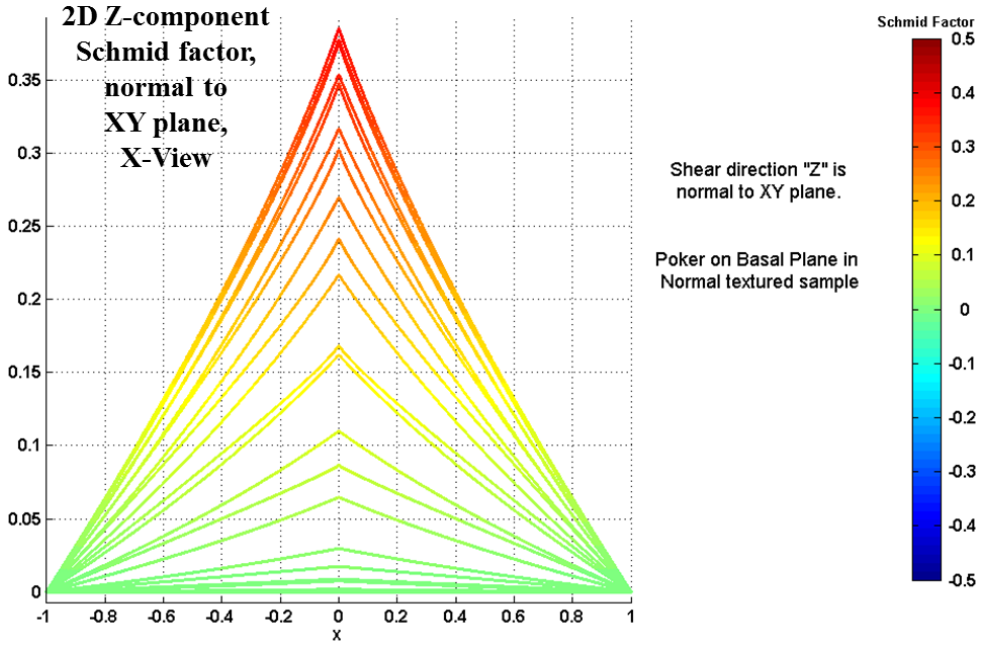

(b)

Z-component Schmid factor, normal to XY plane

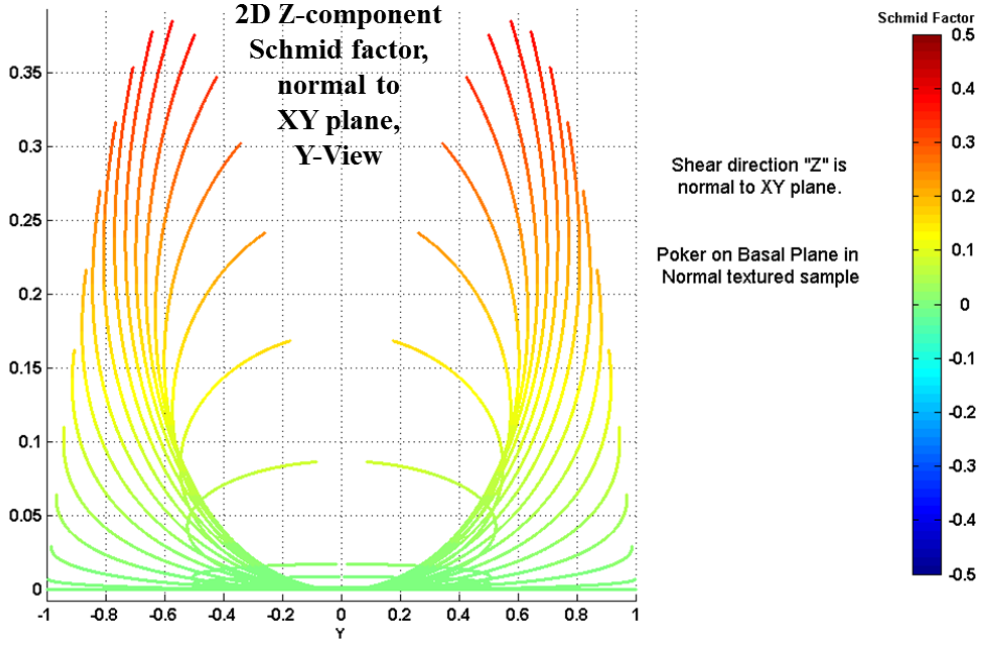

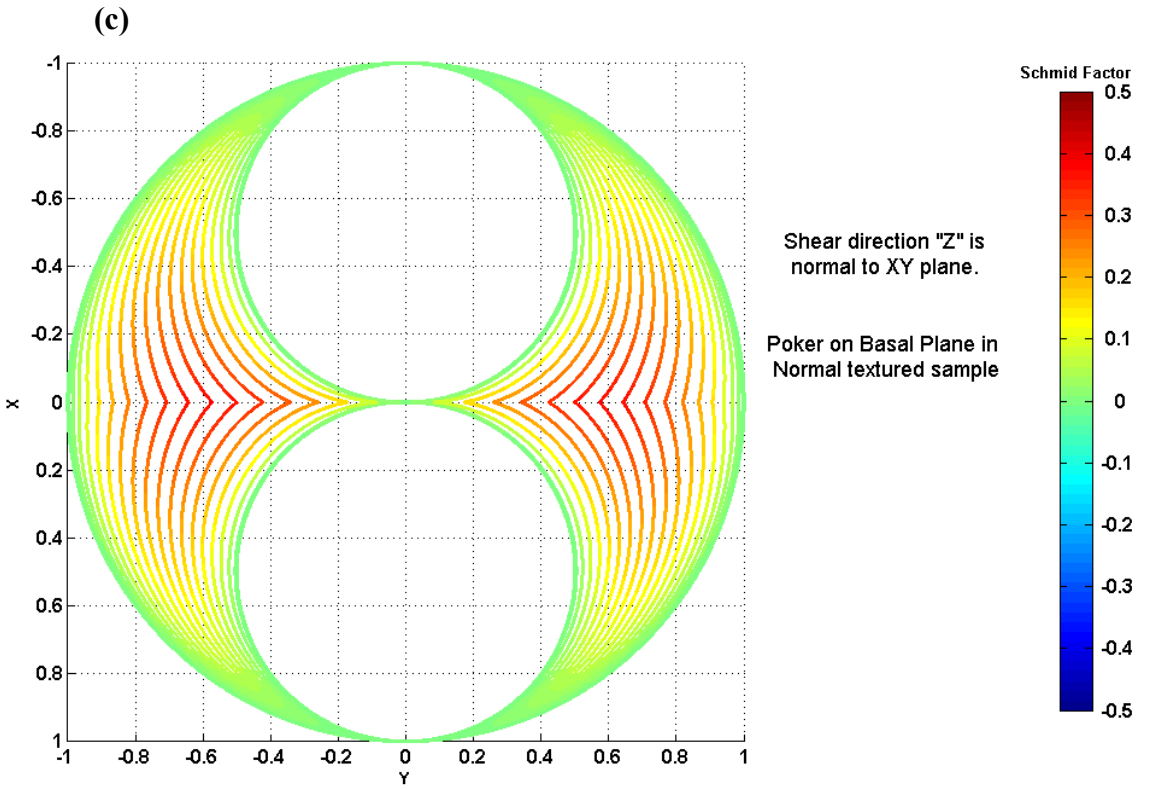

Figure 3-11: Plots of normal forces onto the XY plane, (a) X-View, (b) Y-View and, (c) XY-View (forces are acting normal to the page). All plots are for N-sample configuration.

Figures 3-10 & 3-11 show the resolved forces map from different views for loading of the N-sample. Figure 3-12 shows the resolved forces for the P-sample. In this case, the two main RSS components acting on the layered structure reverse their roles. The Z-RSS component is now parallel to the layers (i.e. parallel to the XZ plane) and would move any ridge/dislocation that forms or is originally present on the layered structure when the CRSS is exceeded. The X-RSS component plays the same role as the Z-RSS component. The Y-component (normal to the XZ plane), on the other hand, will tend to bend and buckle the layers. From the Schmid factor map shown in Fig. 3-8, the Schmid factor Y-component and XZ-components are generated as well and displayed in Fig. 3-13. The same features about the absolute values and plane projections observed in the N-sample apply here as well. Figure 3-14 displays the Z-component Schmid factor

views from the X-axis and Y-axis. In Figs. 3-10(b) & 3-13(b) note that at X = 0 there are two regions in which a maximum shear stress exists in opposite directions. The black arrows indicate that the shear stress attempts to move the dislocation/ridge in the slip plane. The thick black arrows, in the middle, denote the location and direction of the highest RSS on the slip plane. The latter decreases gradually from the center to the edges of the shear diagram. The importance of these RSS views will become clear later in Ch. 4 showing the applicability of these shear diagrams on a single crystal P-sample texture. Special thanks for Dr. Hamad Al-Harbi (King Saud University) for his guidance in plotting the RSS diagrams, in addition to fruitful discussions about them.

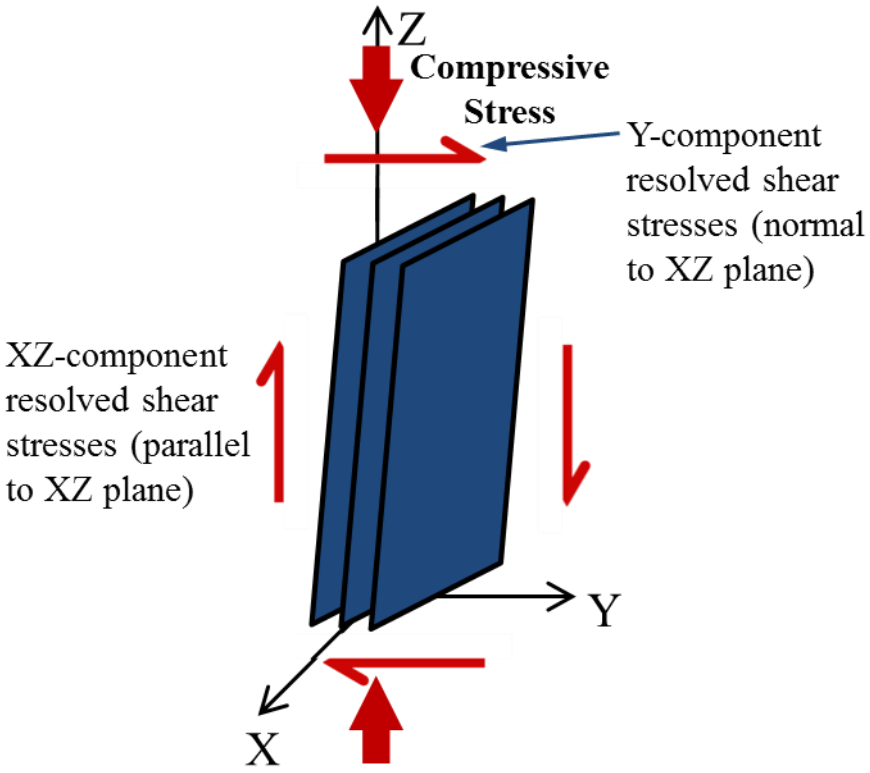

Figure 3-12: Schematic of layered structure under compressive loading, P-sample texture, and the resulting RSS components acting on the layered structure. The red half arrows designate the shear stresses applied.

(a)

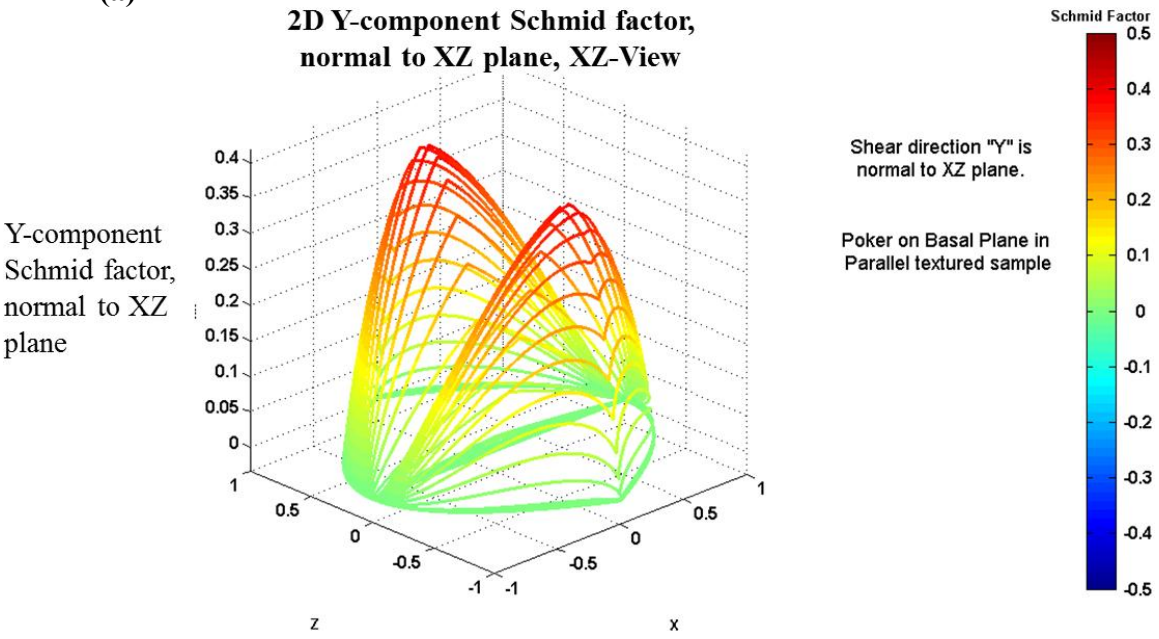

(b)

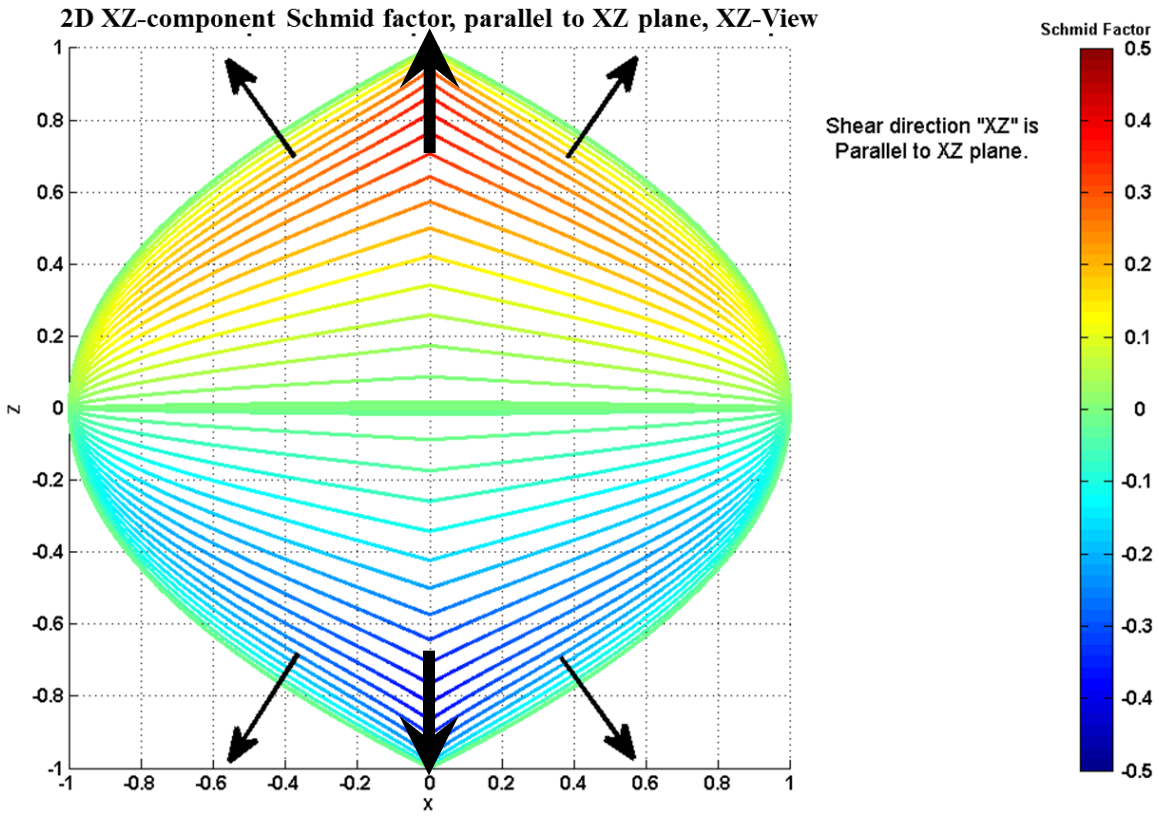

Figure 3-13: Plot of, a) normal force to the XZ plane, and (b) shear force on XZ plane. Both are for the P-sample configuration.

(a)

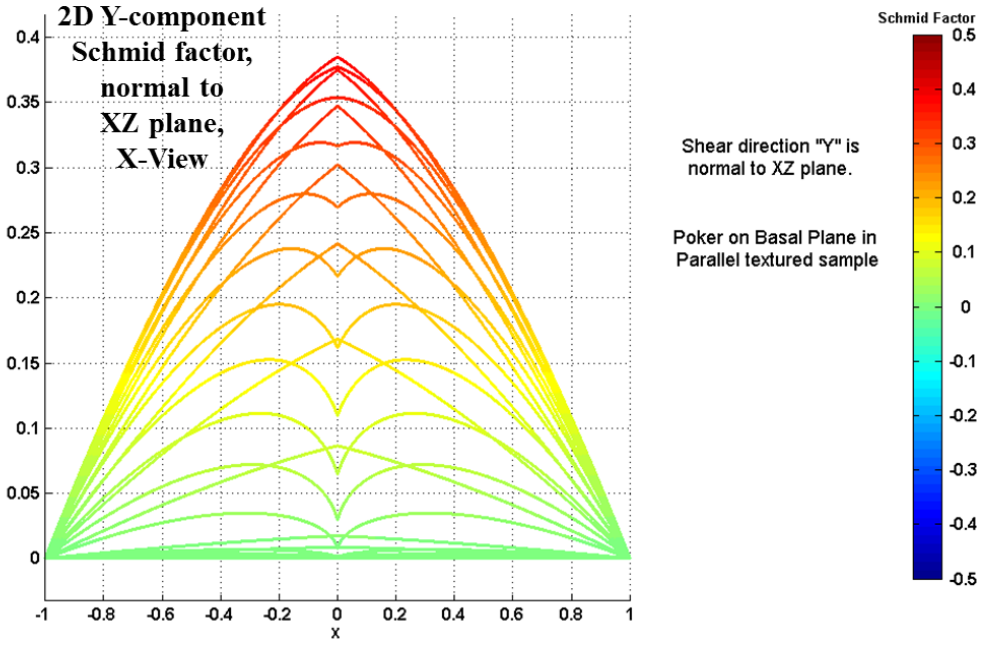
2D Y-component
Schmid factor,
normal to
XZ plane,
X-View
Y-component
Schmid factor,
normal to XZ
plane
Shear direction "Y" is
normal to XZ plane.
Poker on Basal Plane in
Parallel textured sample
Schmid Factor
0.5
0.4
0.3
0.2
0.1
0
-0.1
-0.2
-0.3
-0.4
-0.5
0.4
0.35
0.3
0.25
0.2
0.15
0.1
0.05
0
-1
-0.8
-0.6
-0.4
-0.2
0
0.2
0.4
0.6
0.8
1
X

(b)

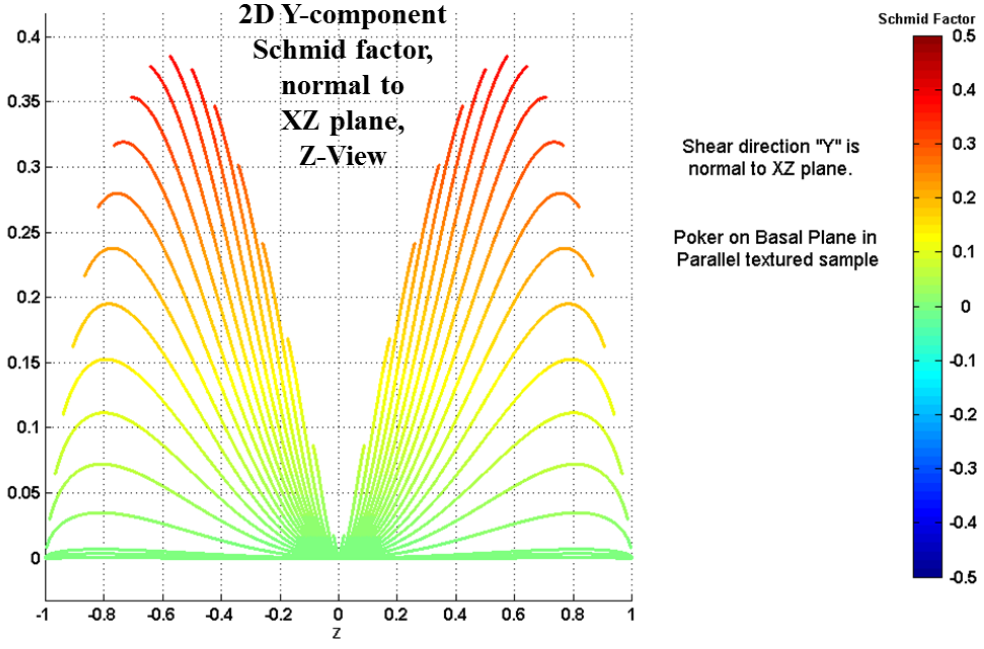
2D Y-component
Schmid factor,
normal to
XZ plane,
Z-View
Y-component
Schmid factor,
normal to XZ
plane
Shear direction "Y" is
normal to XZ plane.
Poker on Basal Plane in
Parallel textured sample
Schmid Factor
0.5
0.4
0.3
0.2
0.1
0
-0.1
-0.2
-0.3
-0.4
-0.5
0.4
0.35
0.3
0.25
0.2
0.15
0.1
0.05
0
-1
-0.8
-0.6
-0.4
-0.2
0
0.2
0.4
0.6
0.8
1
Z

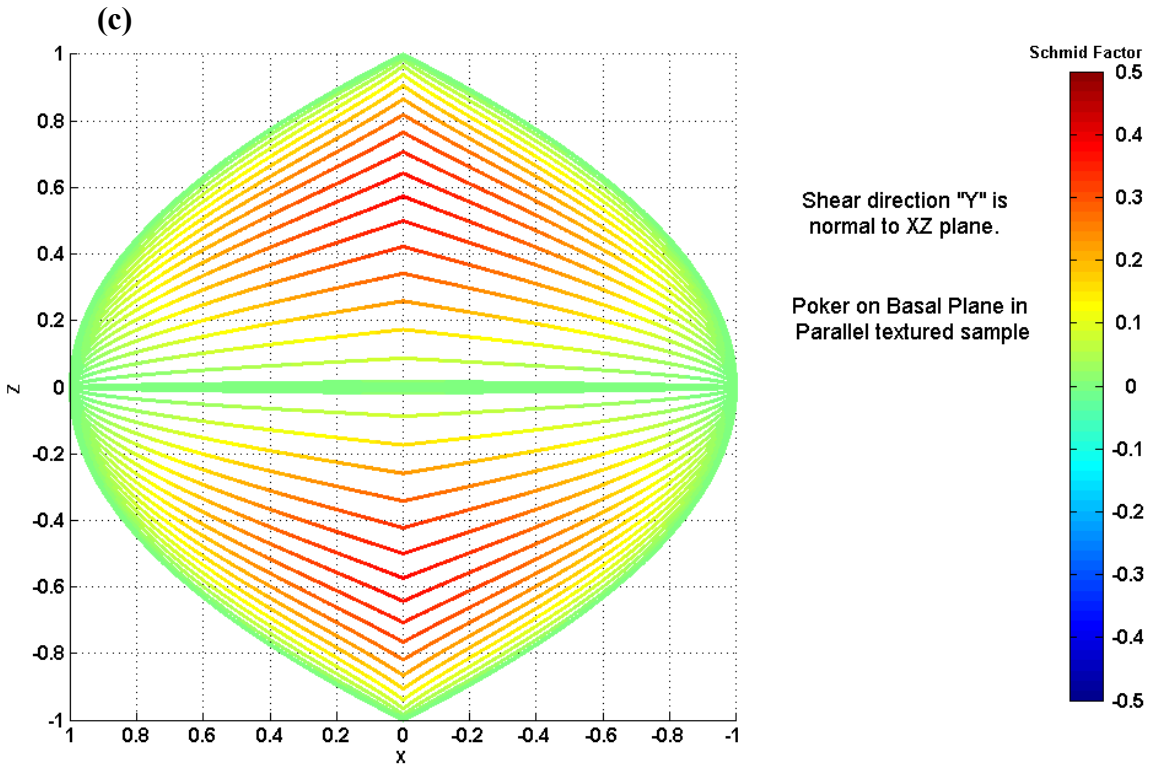

Figure 3-14: Plots of normal forces onto the XZ plane, (a) X-View (b) Z-View and, (c) XZ-View (forces are acting normal to the page). All plots are for a P-sample configuration.

3.2 Summary and Conclusions

In layered solids, forces acting normal to the layers surface are important since they are responsible for buckling during deformation. Only when a plane is tilted, is a force generated. Perfect horizontal or vertical planes do not experience such forces. The differences between the N- and P-sample slopes in Fig. 3-6 (λ versus $\cos\phi\cos\lambda$ plots) indicate the activation of dislocations in the N-sample at a lower stress level than the P-sample.

The normal and shear force maps acting on layered solids are analyzed for N- and P-sample configurations to be applied on layered structures. The P-sample force maps are applied on the paper pile experiment by Dodwell *et al.*[20] in Ch. 4.

Chapter 4: Single Crystal Buckling Dislocation Mechanism

The video showing the deformation of stack of a paper under compression using Digital Imaging Correlation (DIC) technology presented by Dodwell *et al.* [5, 20, 21] in Chapter 2 is revisited here to explore the dislocation mechanisms operative in KNE materials. The setup is composed of 1000 vertically aligned A4 half paper sheets, surrounded by sponge, with both inside ply wood. A closer view of this experiment indicates that the setup corresponds to investigating the mechanical behavior of a single crystal layered structure with a P-texture, such as the one shown in Fig. 3-5. Here the paper sheets represent the basal planes that in most cases are close-or near-close packed planes. The differences between different layered solids lie in the strength of the bonds within and between the close-packed planes. Therefore, the DIC paper experiment represents a layered material, albeit with very weak bonds between the planes. As shown previously, twinning is not possible in layered solids (due to the large c/a ratio); dislocation slip is thus the only possible mechanism for strain release. In this chapter, the dislocation mechanisms by which strain is released in layered structures are explained in detail.

4.1 Carpet-like edge dislocation configuration in layered structures

In this thesis, the dislocation configurations in layered structures will be denoted by the carpet-like convention, "⎍". When the layers are bent they respond by creating dislocations that, in turn, release the strain. "The way in which a dislocation moves in layered structures is similar to the way a carpet can be moved across the floor simply by moving rucks along the carpet (Fig. 4-1). This is a much easier process than pulling the

whole carpet across the floor at one go."[49] The carpet-like dislocation convention "⌒" is equivalent to the "⊥" (inverted "T") convention. Both conventions will be used in the figures in this thesis (for schematic representation) depending on which one better clarifies the concept of interest; however, keep in mind that in layered structures, the carpet-like dislocation is what is actually nucleated. The carpet-like dislocations are termed folds by geologists. They will be called dislocations henceforth due to their presence as kink boundaries in crystalline KNE materials studied in this thesis. It is hereby acknowledged that dislocations and folds are not necessarily equivalent. However, since this is a materials science thesis, and our ultimate aim is to understand the response of KNE solids in which dislocations are present, the folds will be referred to as "dislocations" or "dislocation like".

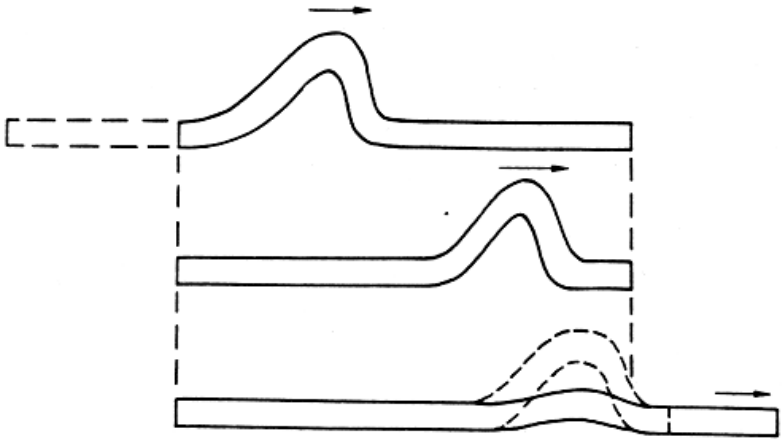

Figure 4-1: The 'carpet' analogy for the motion of an edge dislocation [49].

An important feature concerning the carpet-like dislocation configuration in layered structures needs to be considered. The magnitude of shear stresses applied on the layers in a layered structure will vary the resulting degree of bending of the layers. Figure 4-2 shows the development of A4 paper sheets buckling starting with a P-sample orientation (i.e. vertical) with foam used as the supporting medium. Single black paper

layers are inserted between every 25 layers of white paper to highlight the developments occurring during deformation. An increase in degree of bending of the layers at different locations is demonstrated from (a) – (e) in Fig. 4-2. Hence, three carpet-like dislocation configurations are used to designate the increase in a layer's bend angle's acuteness in ascending order from lowest "⌒", to intermediate "∩", to the highest "Λ" intensities.

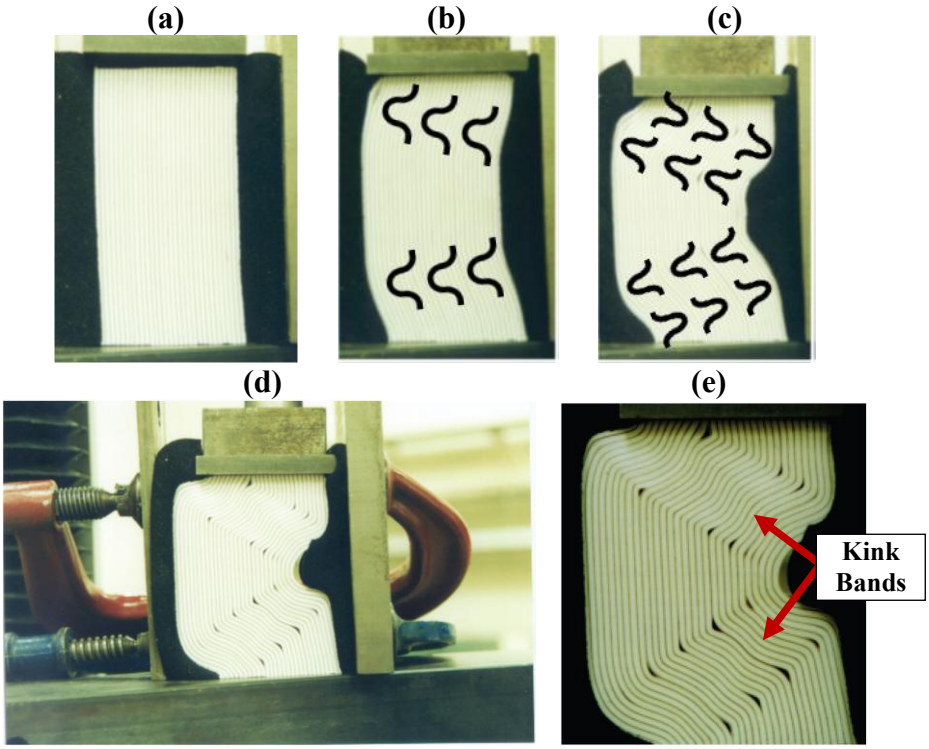

Figure 4-2: Experimental arrangement of 800 sheets of A4 paper loaded in a pseudo-single crystal P-sample texture. Foam is used as the supporting medium. (a) Initial state before deformation, (b) & (c) show progress in the paper sheets' buckling, demonstrating changes in the carpet-like dislocation intensity shown on the figures, (d) Final state after deformation by compression, with highest carpet-like dislocation intensity at the kink edges, (e) Zoomed in view of the buckled paper sheets in (d). The black lines are for illustrative purposes, and were produced by inserting a single black layer of paper between every 25 layers of white sheets [5].

Dodwell *et al.* [5, 20, 21] paper compression experiment is explained with insight of all phenomenological features shown in Ch. 2 and the resolved shear stress analysis in Ch. 3. Figure 4-3 shows a schematic of the PP setup made by Dodwell *et al.* [5, 20, 21], (a), a video snapshot of the DIC horizontal displacement measurement before any

deformation occurs, (b), and after completion of the 3rd harmonic buckle, (c). The whole DIC color spectrum "correspond to global horizontal displacement, red right to purple left" [5, 20, 21], with all color gradients in between, in which green represents the neutral state with zero horizontal displacement (Fig. 4-3 (b) & (c)). However, it must be noted that the PP buckles in a 3rd harmonic buckling mode (Figs. 2-14(ii) & 2-15(b)). Based on the observations made in the DIC video, the deformation starts at the right lower corner with a right buckle. As the deformation develops, a 2nd left buckle is established, and finally a 3rd right buckle in the remaining top section of the PP setup is observed. Note that, according to Fig. 4-3(c), kink bands exist between every two oppositely directed buckled regions.

Figure 4-4 shows video snapshots of the DIC horizontal displacement measurements before, and after, deformation with schematic representations reflecting the resulting carpet-like dislocations at different locations. Figure 4-4(a) displays the DIC snapshot before any deformation, and Fig. 4-4(b) demonstrates the paper layers with no dislocations, since no deformation took place. Figure 4-4(c) displays the DIC snapshot after completion of the 3rd harmonic buckling mode across the PP layers' lengths. The color code used by Dodwell *et al.* [5, 20, 21] during the DIC horizontal displacement measurements is red = right; purple = left. However, it is observed in Fig. 4-4(c) that localized displacement measurements of yellow and blue surround the red and purple buckled regions. Careful examination of the video frames shows that the localized yellow-colored regions corresponds to right buckled carpet-like dislocations, "⊃" while the localized, blue-colored regions correspond to left buckled carpet-like dislocations, "

ς " (note the relation in curvature between the buckle direction and carpet-like dislocation configuration shape). Translation of these configurations on the PP schematics for Fig. 4-4(c) is presented in Fig. 4-4(d). The detailed evolution of this pseudo-single crystal layered structured material dislocation mechanism during loading (which occurs in KNE materials) is illustrated in Table 4-1.

Table 4-1 shows the dislocation evolution during the loading deformation of the PP setup. [5, 20, 21]. The evolution is divided into 40 steps in order to identify all features in detail. The steps are grouped into four stages; each stage focuses on the displacement changes and dislocation evolution of a certain region during the deformation. The first stage describes the development of the 1st buckle; the second stage the development of the 2nd buckle and the formation of a kink band; the third stage describes the 3rd buckle and formation of a second kink band. During the final fourth stage, all buckled regions compress to their maximum extent and the dislocations dislocation walls, DWs, nucleated, reach their closest possible proximity to each other.

Figure 3-12 plots the normal and shear stresses acting on a given sheet of paper. In this orientation, the XZ plane is in the plane of the paper and the normal forces to it act along Y. The in-plane and normal component forces are shown in columns (i) & (ii), respectively, throughout Table 4-1 since they are applicable to all regions irrespective of any changes (Figs. 4-5 & 4-6).

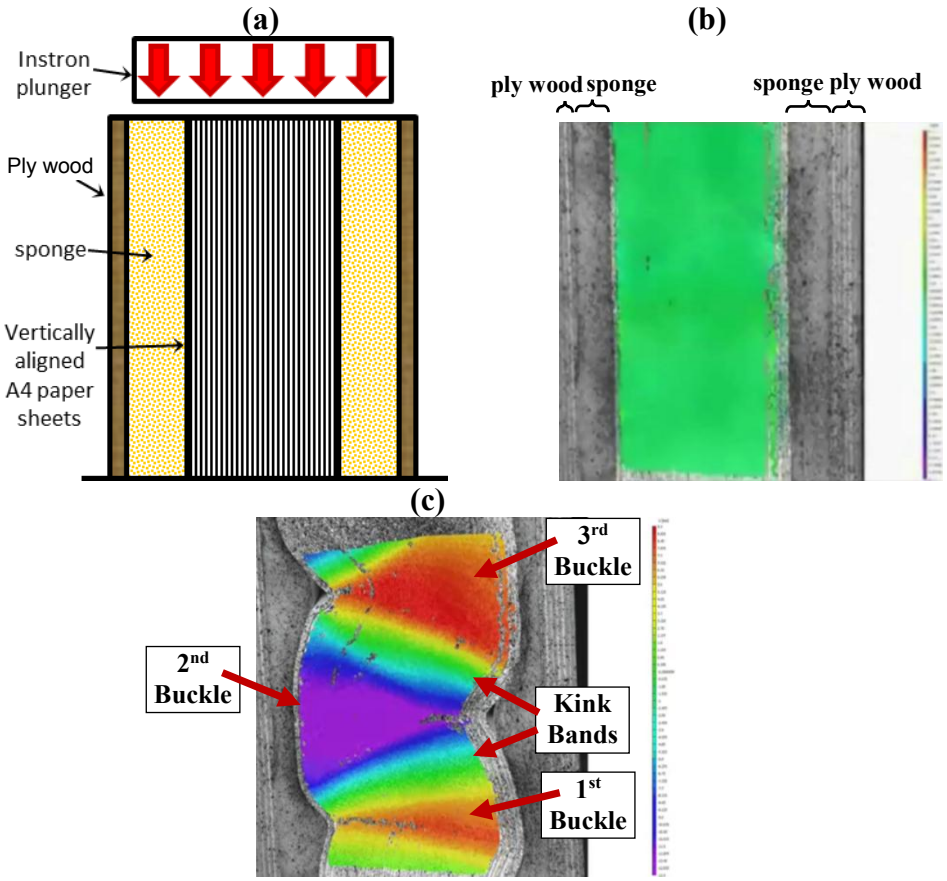

Figure 4-3: Pseudo-single crystal setup of a layered material (a). Initial configuration (b), (c) DIC snapshot after completion of the 3rd harmonic buckling mode across the PP layers length [5, 20, 21].

However, when the deformation occurs beyond the 1st buckling harmonic mode, the orientation of the forces applied changes (Figs. 3-13 & 3-14). This is shown in steps 6 & 26 in Table 4-1. The XZ-component forces parallel to the XZ-plane in column (i) is demonstrated in a slanted manner to demonstrate its 3D nature (i.e. it acts through the paper layers' thickness). Column (iii) shows DIC video snapshots taken from Dodwell *et al.* [5, 20, 21]. The snapshots are zoomed in and out at certain events to clarify the development of the various carpet-like dislocations stages in detail. Thanks to Ms. Melina Smith from Dragon Productions for editing the video by zooming in and out and changing the video speed at certain events to illuminate the dislocation deformation details.

The dislocation evolution using the carpet-like dislocation configuration depicted from the DIC displacement measurement video snapshots viewed from the PP edge side plane is shown in column (iv). The carpet-like edge dislocation configuration intensity gradient, shown in column (iv) (Lowest intensity "∩", Intermediate intensity "∩" and highest intensity "∩") are exaggerated for illustrative purposes. Finally column (v) shows the forces applied normal to the PP stack.

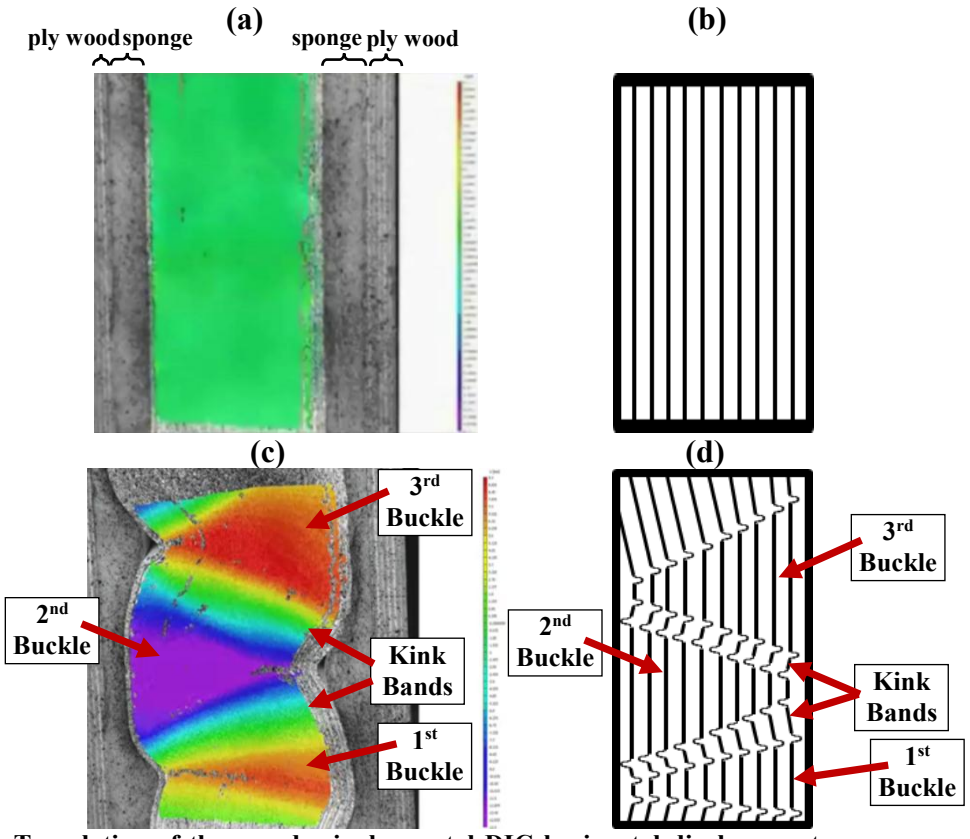

Figure 4-4: Translation of the pseudo-single crystal DIC horizontal displacement measurements to carpet-like configuration dislocations. (a) video snapshot of the DIC horizontal displacement measurement before any deformation, (b) schematic representation of the paper layers of (a); (c) DIC video snapshot after completion of the 3rd harmonic buckling mode [5, 20, 21]; (d) schematic representation of PP layers with resulting carpet-like dislocations reflecting localized displacements in (c).

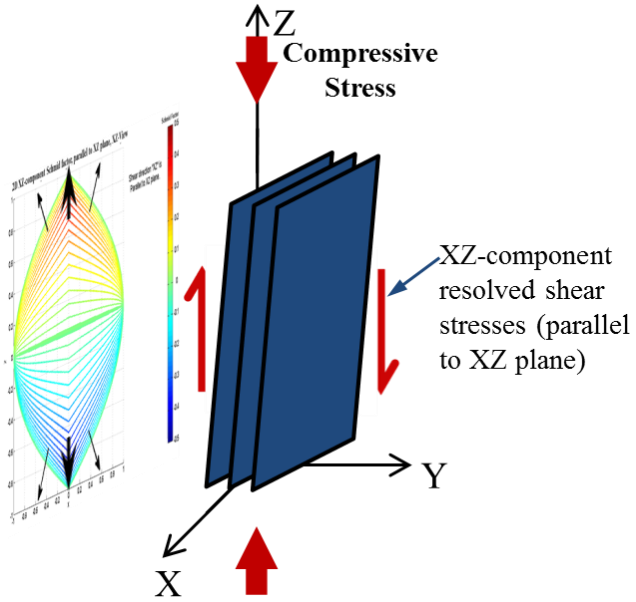

Figure 4-5: In plane shear forces acting on layers tilted 1° about the X-axis for P-sample texture (2D view of XZ-component forces acting parallel to XZ-plane is on the left).

4.2 Pseudo-Single Crystal Layered Structure Buckling Dislocation Mechanisms

Initially the PP is vertically aligned in the setup without any bends as shown in Figs. 4-3(a) & (b) and 4-4(a) & (b). The PP behaves as a whole system, hence, every paper in the 1000 will contribute in supporting the whole system and all will interact with each other during deformation. As noted above, the buckling can be divided into four stages. Each is discussed separately below.

Stage I:

As discussed in Ch. 3, most vertically aligned columns are not perfect. Therefore, definitely there is a general tilt in the PP setup under investigation. The tilt direction will be amplified when a compressive load is applied. As the compressive load increases, the Y-component forces, normal to the PP's flat side, will apply if the layers are tilted about

the X-axis, as shown in Fig. 4-6. The application of the 3D force diagram is displayed in Fig. 4-6(a). However, in the analysis performed here, the only information available is gleaned from the DIC 2D displacement video snapshots viewed from the PP edges' side. Said otherwise, the 3D displacements through the PP are not observed in this setup, in Fig. 4-6(b) only the 2D Y-component force diagrams (Z-axis view) are applicable.

With increasing compressive load, the normal forces increase until a threshold stress is reached where edge dislocations nucleate on multiple layers forming a U-shape (same shape as the Y-component forces in 2D) as shown in Table 4-1, step 1 (iii) & (iv). The U-edge dislocations are of the *same* sign, and thus repel each other. The first three paper layers on the far bottom right in schematic (iv) buckled due to the forces normal to them (ii). The location and size of the normal forces which led to the carpet-like, U-shaped edge dislocations are shown in (v).

The reason(s) for buckling could be any, or a combination of, the conditions illustrated in Fig. 2-14. However, since the system is composed of 1000 sheets of paper, it is most probably a combination of several reasons. Hence, in analyzing the deformation of this PP, we are studying the buckling deformation of a group of layers, that support and interact with each other, which is why the deformation of a single column or layer is different than a group behaving as one entity as investigated here. Looking at the PP as a whole system, the misalignment of the PP layers and/or localized stresses at the bottom right corner led to buckling there first. The right buckle observed corresponds to Figs. 2-14 (a)(ii), (b)(ii) & (c)(ii); therefore, the material in the buckled region has displaced to the right due to the normal forces. This force also nucleates carpet-like edge dislocations, "ↄ", that displace the sheets to the right. The edge dislocations lower the total energy of

the system and provide extra material on the right side (analogous to the conventional dislocation configuration oriented in this manner " ⊢ "). The end result is the 'movement' of the PP from the left to the right side. Note, the schematic representation in column (iv) only demonstrate the carpet-like edge dislocations. The forces that nucleate the carpet-like edge dislocations generate a moment that causes a deflection of the buckled layers and results in their 'movement'. This is observed in the DIC snapshot images in column (iii).

Another important feature that needs to be considered is the color gradients obtained in the DIC images. Recall that at maximum right displacement, the color is red and at the maximum left displacement, the color is purple. At the threshold stress for the formation of the U-edge dislocations in multiple PP layers, the red color covers the region between the U-edge dislocations. The intense yellow color occurs at the location of the dislocation walls. The green color, representing neutral displacement, is spread around the yellow color in a larger area.

The gradient, intensity and width of the colors play a major role in identifying the nature of the carpet-like dislocation configurations present. During step 1, the U-edge dislocation bends are of the lowest intensity, "ↄ", since the forces have just passed the threshold stress for the nucleation of these dislocations indicating that the load applied is still relatively low. This is confirmed by the DIC color gradients in step 1(iii), where the surrounding displacement field around the yellow color (representing the edge-dislocations) are green and thus neutral (i.e. not exerting much force on the U-edge dislocations formed).

Reviewing step 1(iii), notice that the dark blue strip forms an inclination to the left and reaches a mild trace of purple at the top left corner (step 1(iii)). Hence, this confirms the depicted general tilt of the PP to be of a right buckle (Fig. 2-15(b)) and the loading conditions are thus similar to those depicted in Figs. 2-14 (a)(ii), (b)(ii) & (c)(ii).

A prominent characteristic of the normal force is its 3D character (Fig. 4-6(a)). The horizontal green line (representing zero forces) of the XZ-component forces in Fig. 4-5 along the X-axis through the layered structure thickness coincides with the green line where Z = 0 in Fig. 4-6, separating the normal force crests T & T'. Recall that all of dislocation that nucleate and move (Table 4-1) are in 3D in the depth of the PP according to the 3D force diagrams that are active there and henceforth throughout the process in all of the steps and stages to be explained.

Step 2 is the same as step 1, representing the nucleation of the U-edge dislocations at a threshold stress. Here the image is zoomed in order to highlight some of the events taking place in the area of interest. As the compressive load increases and the green neutral region transforms into light blue in step 3, a slight increase in the size of the a-b U-edge dislocations is noticed as well from the DIC displacement snapshot (step 3(iii)) due to the increase in the magnitude of the normal forces (step 3(v)), resulting in an increase in the buckled layers on the bottom right corner in step 3(iv). Since a higher color intensity field (blue) is now present around the thin yellow color representing the U-edge dislocations, it follows that the intensity of the edge dislocation bends increased from the lowest, "⌒", to an intermediate level, "⌒". The same events occur in steps 4 & 5, with an increase in the extent of the a-b U-edge dislocations (steps 4 & 5 columns (iii) (iv) & (v)). Looking at the system as a whole, the increase in extent of the a-b U-

edge dislocations from right to left is due to the localized stresses and strains concentrated in the buckled region.

Clearly, the buckled region is the weakest volume in the PP. The rest of the PP remains stiff and continues to deform in, presumably, a linear elastic manner. The buckled region will continue to deform and accommodate strain as long as there is still room for dislocation nucleation and/or growth in that region. Note that as the number of buckled layers increases from steps 1-5, the size of the buckled region increases as well as displacing more material to the right. Hence, progressively, more material moves to the right as the deformation proceeds.

The a-b U-edge dislocations extend from the right to left of the PP layers in an autocatalytic process. Therefore, the compressive load from steps 1-5 remains constant and this stage accelerates until the a-b U-edge dislocations meets the left flat side of the PP. This is confirmed by the high time in which this stage takes place in Dodwell *et al*. video [5, 20, 21]. The time taken for the a-b U-edge dislocations since nucleation until they reach the left flat side is 0.36 s.

At this point, the a-b U-edge dislocation walls split into two separate dislocation walls, a-a’ and b-b’, as shown in step 6(iv). Note that as the two dislocation walls a-a' and b-b' form, the forces parallel to layers (step 6 (i) bottom) are acting - in addition to the normal forces in the buckled region - to further move the two walls away from each other.

Another form of strain accommodation is the change in angle of the dislocation walls a-a’ & b-b’. The width of the region between a & b is wider than a’ & b’. This is due to the local tilt of the buckled region to the right (Fig. 2-15(b)), increasing the angle

between a-a' & b-b' after the split of the U-edge dislocations to DWs. Furthermore, the intensity of the yellow band increases further implying that the dislocation bends increase from, "⌒", to the highest level, "⌒". The point at which the U-edge dislocations split into two DWs represents the end of the first stage.

(a)

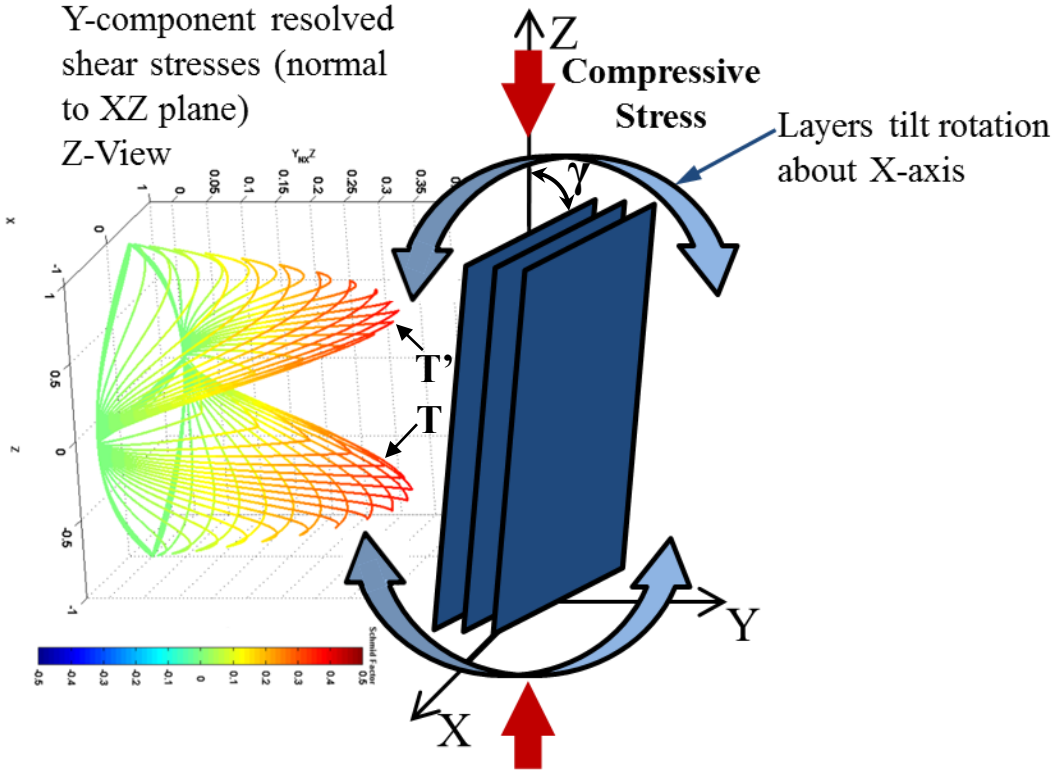

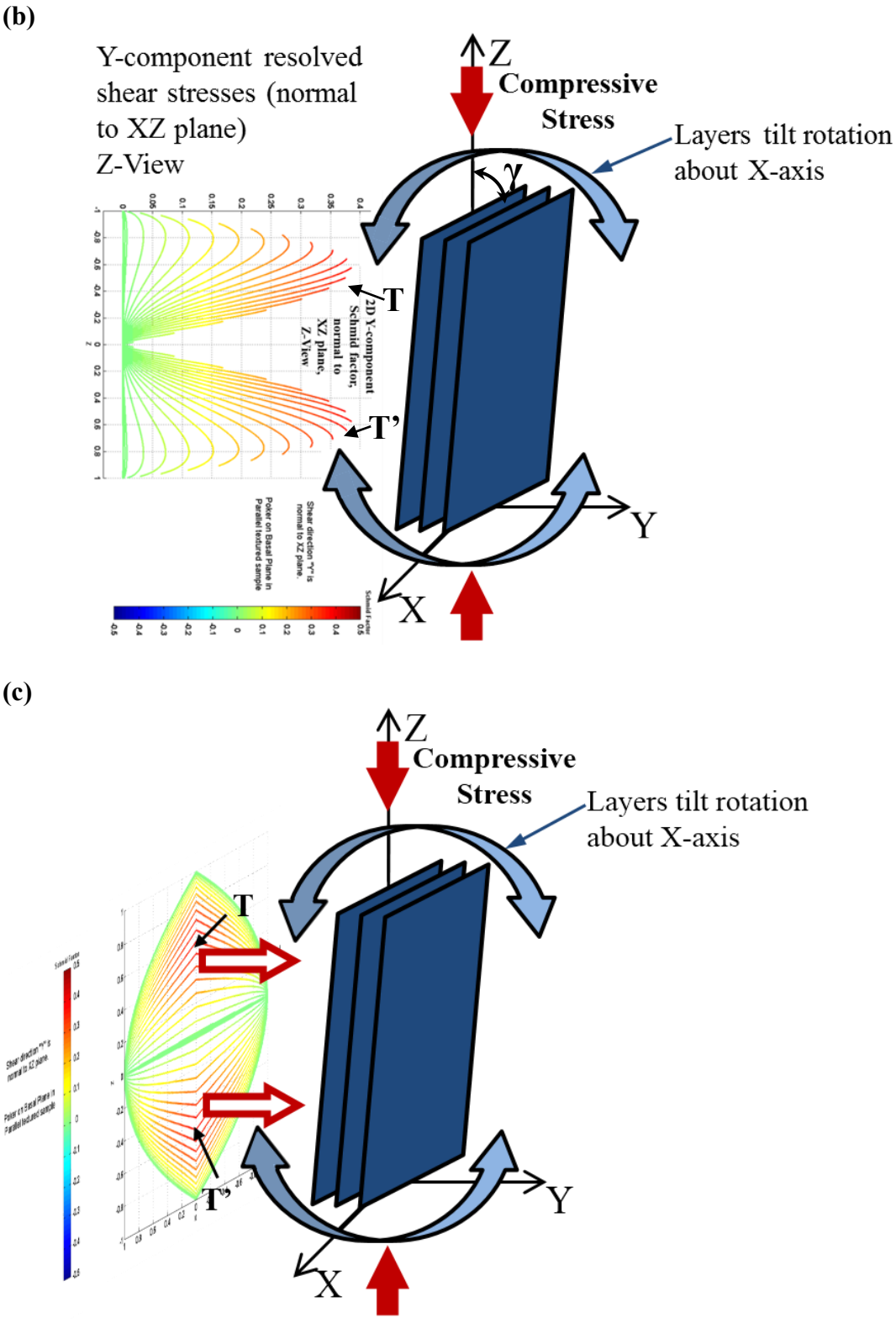

Figure 4-6: Forces acting normal to the layers tilted about the X-axis for a P-sample texture; (a) 3D view, (b) 2D Z-axis view and, (c) XZ-view of normal forces acting on to XZ-plane. The maximum forces T and T' correlate in (a), (b) and (c).

Recall that the surrounding support around a layered structure dictates the buckling condition and sign as shown in section 2.3.1 (Figs. 2-17, 2-18, 2-19 & 2-20). In this experiment, the sponge and ply wood support enforce that each adjacent buckle generated is of an opposite sign as shown in Fig. 4-3(c), creating kink bands (see below) between the buckled regions.

One of the most important observations to be made here before considering stage II is that despite the fact that the overall force on the first buckle came from the *left*, the dislocations nucleated on the *right*. Given that this behavior is comparable to an extrusion problem, it will be henceforth sometimes by referred to as an "extrusion" process. In summary, the first buckle was due an "extrusion" of paper through a weakness on the right hand side that resulted in a U shape deformation characterized by two parallel dislocation walls of the same sign.

Another very important observation is that in this stage there are two DWs, of the same sign that nucleated simultaneously and moved in tandem. The existence of these two walls must correspond to the presence of two forces that are not only acting in the same direction but must be of similar magnitudes. At this stage it is reasonable to assume that these two forces are the twin forces shown in Fig. 4-6.

Stage II

At the conclusion of stage I, the state of the PP is quite different from its initial state before deformation. Initially, there was a slight general tilt in the PP to the right (step 1(iii)). Now there are two DWs, characterized by the highest intensity level edge dislocation bends "⊃". In addition the increase in angle between a-a' & b-b', created a

localized tilt, in very close proximity above b-b', equivalent to the tilt shown in Fig. 2-14(c)(i) that should lead to a **left** buckle. Said otherwise, the paper layers' tilt just above b-b' is opposite in direction to the right buckled region that led to a-a' & b-b'.

Notice the trace of purple color just above b in the DIC snapshot of step 6(iii). This thin dark blue band represents the nucleation of edge-like dislocations. The latter nucleated at c (step 6(iv)) are of the lowest intensity, "∩", since the displacement above them (represented by the purple trace) is not large enough. Recall, that, thin dark blue regions represent edge dislocations bent to the left, viz. "ς".

The localized tilt just above b-b' enables the nucleation of edge dislocations at the weakest location c in the volume where the highest normal forces apply. The nucleation of these edge dislocations accommodates the strain required during deformation.

The second stage starts at step 6, by the nucleation of edge dislocations at location c just above b-b' (step 6(v). Note the change on orientation of the XZ-component forces applied above b-b' (see top in step 6(i)). Due to the change in orientation of the normal forces above b-b', step 6 (ii) top (Fig. 4-7), the corresponding orientation of the XZ-component would be as shown in step 6(i) top, Fig. 4-8. The vertical green (representing zero strain) line of the XZ-component forces in Fig. 4-8 along the Z-axis coincides with the green line where X = 0 in Fig. 4-7 separating the normal forces crests T & T'.

(a)

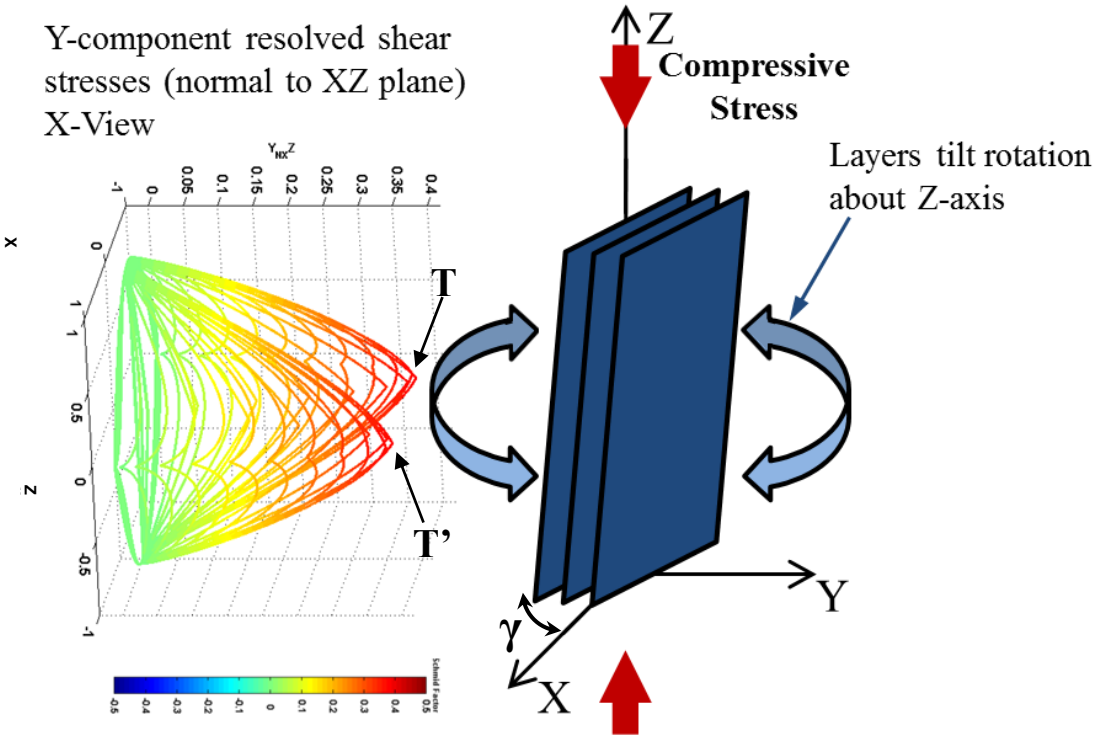
Y-component resolved shear stresses (normal to XZ plane)
X-View
Z
Compressive Stress
Layers tilt rotation about Z-axis
T
T'
Y
X
γ

(b)

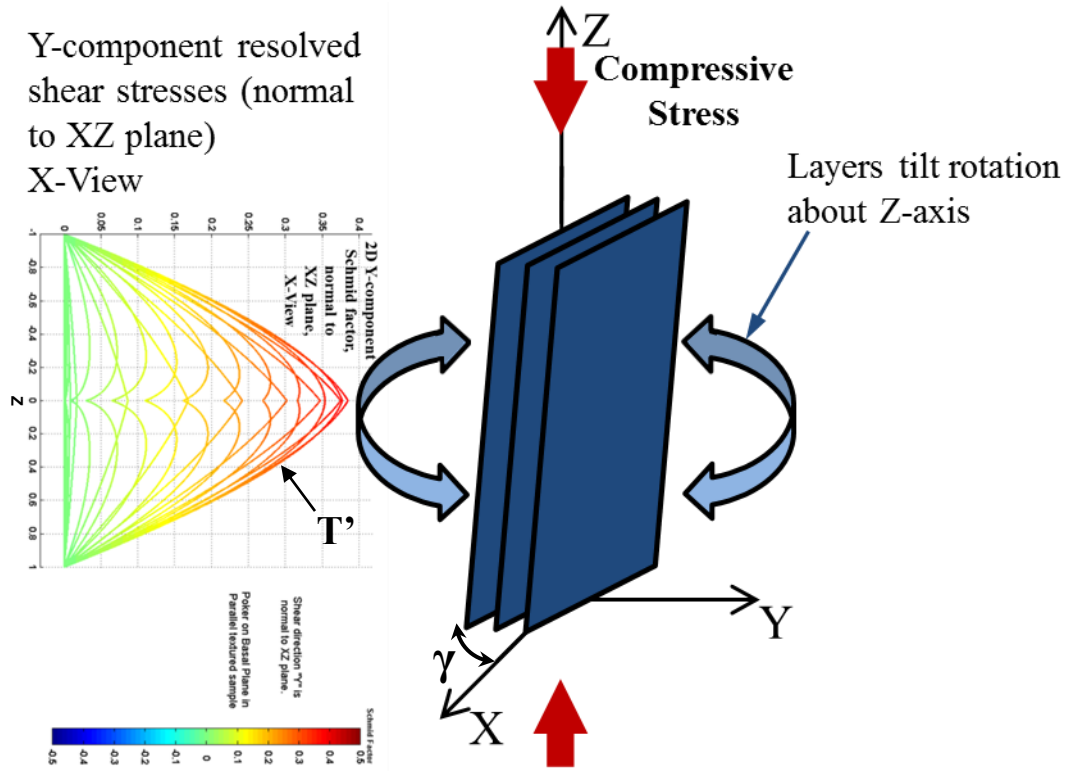
Y-component resolved shear stresses (normal to XZ plane)
X-View
Z
Compressive Stress
Layers tilt rotation about Z-axis
T'
Y
X
γ

(c)

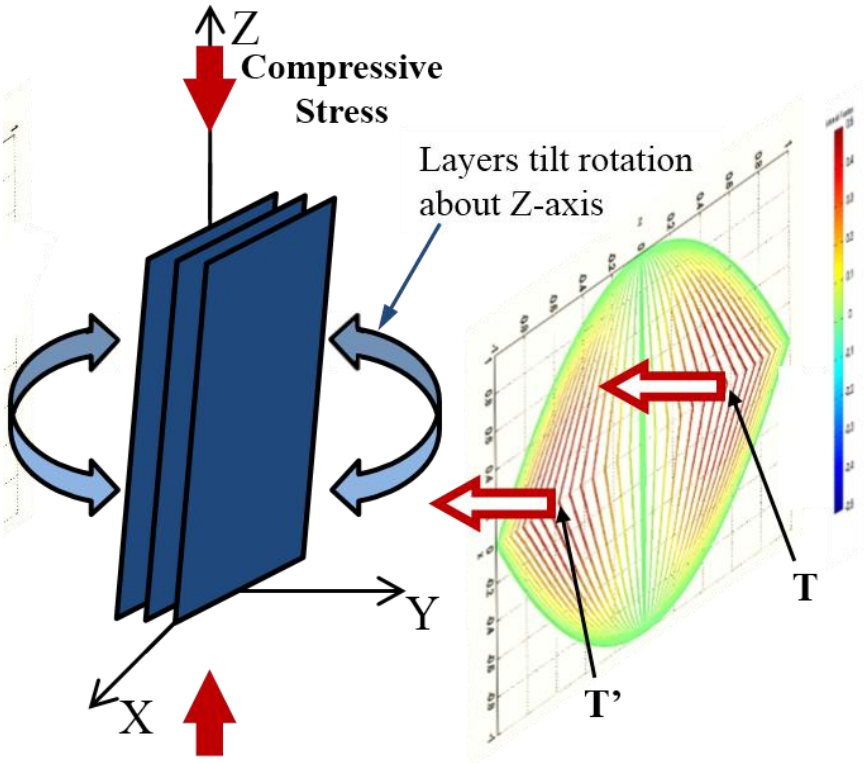

Figure 4-7: Forces acting normal to the layers tilted about the Z-axis for a P-sample texture; (a) 3D view, (b) 2D X-axis view and (c) XZ-view of normal forces acting on to XZ-plane. The maximum forces T and T' correlate in (a), (b) and (c).

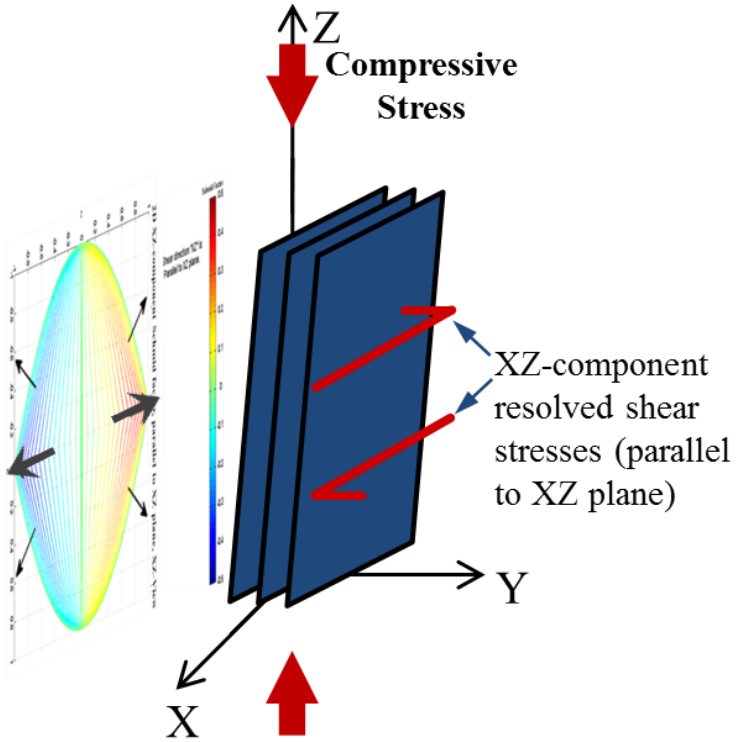

Figure 4-8: Forces acting parallel to sheets tilted about the Z-axis for a P-sample texture. 2D view of XZ-component forces acting parallel to XZ-plane is depicted on the left.

As the load increases, the normal forces at location c increase in magnitude across the PP width (step 7(v)) resulting in the extension of the edge-like dislocation wall across the PP layers until it reaches the left side at c'. Recall that the localized tilt just above b-b' enables the nucleation of edge dislocations at the weakest locations. At this stage the edge dislocations are of intermediate intensity, "⊂", from location c until mid-point across the PP, and of the lowest intensity, "⊂", thereafter. This feature corresponds to the thin dark blue color in step 7(iii) and the purple color gradient above c-c' from the right to the left side of the PP. The compressive load continues to increase in step 8, and the purple color above c-c' becomes more pronounced, increasing the intensity of the dislocations to, "⊂".

Note the concomitant widening of the gap between a-a' & b-b' representing the red region in step 8(iii) compared to steps 7(iii) & 6(iii). This is due to the role of the in-plane shear forces acting on the plane of the paper between a-a' & b-b' (lower figure in column (i) of step 6 and Fig. 4-5).

As the loading proceeds in step 9, the purple color extends across the entire region above c-c' (step 9(iii)) until a thin dark blue band representing dislocations "⊂" of the highest intensity (step 9(iv)). In addition, the gap between a-a'& b-b' expands further, and the angle between them increases even more. Note the interconnection between DWs b-b' & c-c'; both are moving upwards together as deformation proceeds (although they are comprised of oppositely signed edge dislocations). The region between DWs b-b' & c-c' is a kink band represented by a combination of green and light blue colored regions in steps 8(iii) & 9(iii) and thereafter. This kink band started to form in step 6

between locations c & b with paper layers inclined at a high angle from horizontal to the left, "↖" . With further loading, the angle becomes more acute as the c-c' dislocation intensities increase and as the DW extends from c to c'. The buckled region accommodates the strain through the DWs a-a' and b-b' which facilitate the relocation and shift of the layers between these DWs to the right.

As the compressive loading increases, the events described in step 9 are amplified. For example, the inclination of edge dislocations c-c' (Fig. 4-7) of the lower half from steps 9-12 columns (iii) (iv) & (v) increases.

A crucial feature that needs to be recognized, that may ultimately be responsible for KNE behavior, is the mobility of the DWs. The carpet-like dislocations configurations that are present in reality are non-crystallographic [10]. The edge dislocations nucleate at different stages, and they change in intensity (due to the carpet-like configuration), - to accommodate strain. Unlike twinning in which the strain is crystallographically fixed, the strain accommodated by these edge dislocations is variable.

From steps 6-12, the in-plane shear forces widen the gap between a-a' & b-b' (and c-c' eventually) and changes the angle between DWs as well. Revisiting the initial state of the PP setup (Fig. 2-12(b)) and steps 1-5, the effect of normal and in-plane force components, on the localized right buckled region, in addition to the localized tilt is now evident.

At step 6, the dislocations at b-b' reach their highest intensity and the slight kink band above it, assist in the nucleation of dislocations at c. Once nucleated, the DWs extends across the width of the PP with increasing loads (step 7).

At step 12, the deformed region below c-c’ has "work hardened" enough for its strength to be higher than the layers above and on either side of c-c’. After step 12, the only possible mechanism to accommodate strain is the nucleation of new “ ” dislocations at d (step 17(iv)) as evidenced by the formation of a thin blue band on the right of the PP above the purple color in step 17(iii).. The edge dislocation nucleated are of a left buckle “ ” since the band is blue (step 17(iii)) and will move to the left to accommodate more strain. A noteworthy feature occurring during steps 13-22(iii), is the decrease in lateral displacement above d with increasing compressive load from purple to light blue color. This is compensated for by nucleation of the d-d' DW, whose intensity gradually increases from, “ ”, to“ ”, to “ ”, from steps 17-22. At step 17, the lowest intensity edge dislocations form until midpoint across the PP setup. At step 18, the DW extends from left to right with an intermediate intensity, “ ”, to location d. At step 20, all the edge dislocations are of intermediate intensity and gradually increase to the highest intensity by step 22, “ ”. This gradual increase in dislocation intensity is most probably due to two factors: (1) the lateral displacement magnitude decreases above d-d’ gradually to a light blue region and, (2) displacement level increase between c-c’ & d-d’ as evidenced by the purple color in that region.

The complete formation of the highest intensity dislocations at d-d’, signifies the end of the second stage. At this stage there are two buckled regions: the first is a right buckle at the bottom between a-a’ & b-b’ (red color designating layer displacement to the

right) and the second left buckle in the middle (purple color designating layers displacement to the left).

One of the most important observations to be made here before considering stage 3 and in sharp contradistinction to stage I, is that in stage II, the normal forces, acting from the right, nucleate dislocations on the same side. In other words, this behavior is analogous to an indentation problem, and will be henceforth sometimes by referred to as an "indentation" process. Note that this process is not autocatalytic, and thus is significantly slower than the "extrusion" process. The time taken for d-d' DW since nucleation until it reaches the left flat side is 1.64 s, hence it is ~ 4.5 times slower than "extrusion".

The difference between the "extrusion" and "indentation" processes is fundamental. In the former, the outermost layers buckle first, and in turn, autocatalytically result in the buckling of all layers into the space created by this first movement to the right. The situation for the "indentation" problem is quite different in that the process is ***not*** autocatalytic, but only proceeds when the applied load is increased. Note that the normal forces acting on the basal planes are what is causing the "indentation" and creating the DWs c-c' and d-d'. In contrast to what is occurring in stage I, here the two dislocation walls nucleated are **not** nucleated simultaneously, but sequentially.

Stage III

Stage III is a repeat of stage II, except that in this case the normal forces are acting from the left side of the PP and ultimately result in DWs e-e' and f-f'. In addition,

DW f-f’ starts at an early step due to the stress concentration at the top left corner of the PP.

Stage IV

By step 34 all possible DWs that can nucleated have been nucleated and stage III ends. Looking at the PP setup as a whole, after stage III, all possible edge dislocations have been nucleated, and all potential edge dislocations rotations (due to the XZ-component forces and localized tilts), movements of the buckled regions (the right buckled regions in stages I & III moved to the right and the second left buckled region in the middle of the deformed PP setup moved to the left) are concluded and the kink bands (between b-b’ & c-c’ “◺” and between d-d’ & e-e' “◿”) have reached their maximum tilt angle based on the available space. At this state, the capability of the system to accommodate more strain becomes limited.

At this stage the compressive strengths of the three buckled regions, are comparable. However, the weakest locations in this state are the grooves (between a’ & b’, c & d, e’ & f’) that were formed at various stages during deformation (step 35(iii) & (iv)). The only means available for further deformation is thus the physical compression of the whole setup at the cost of the surrounding material (the sponge in this case). This leads to a deepening of the grooves and a concomitant increase in the curvature of the buckled regions between a & b, c’ & d’, e & f (step 35(iii) & (iv)).

The events in step 35 continue to aggravate until step 40 (step 40(iii)). One of the factors that accommodate strain is the change in the angle of the kink bands between b-b’ & c-c’ “◺” and d-d’ & e’-e “◿”. The DWs b-b’, c-c’, d-d’ & e-e' act as pivots for the

kink bands between them. The angle of the kink bands vary from one kink to another depending on the localized stresses applied around them (especially above and below the kink bands) and the available space in the transverse direction from the surrounding material (the sponge in this case).

DIC colors relation to dislocations and layers displacement:

The analysis of the colors in the DIC images and their relation to the predicted layered structure schematic representation in columns (iii) & (iv) of Table 4-1 is based on identification of the nature of the displacement (right or left) and whether the color is spread out or concentrated in a certain region. When a wide colored region is observed, the group of layers displacement is to the right, left or neutral depending on the color. However, if the color seen is localized in a narrow band, that signifies a DW or kink boundary. The sign of the edge-dislocation (positive or negative) depends on the displacement color reflecting its nature. The exact location of the edge-dislocation is within the small proximity range between the neutral (green color) and wide displacement regions, whether to the right (red color) or left (purple color). The green color represents kink bands where the layers are inclined with zero horizontal displacement.

Expected crack initiation locations in layered solids

In analyzing the different steps and stages of this experiment, we assumed that the setup represents a single crystal with a P-texture. In this configuration the paper layers represent the close-packed planes, where in a crystalline solid dislocations would

nucleate and move. The strengths of the layers represent the bond strength within the layers and the bonds between the paper sheets represent the bond strengths between layers. In crystalline solids, bonds between layers, ease of sliding between layers and layer stiffness render the analogy with the PP inexact. Nevertheless, the experiment carried out by Dodwell *et al.* [5, 20, 21] provides important information concerning the details of the deformation occurring in different stages and steps. Due to the high flexibility and ease of sliding of the PP relative to each other, stage IV in this setup could aggravate from steps 35-40. Though, in layered structured crystalline single crystals or polycrystalline materials, stage IV might not extend much (might stop at step 35 or between steps 34 & 35) due to limited flexibility and the elastic stiffness constants. Crack initiation (that might advance to failure) is expected to occur at locations of highest curvature regions and at groove locations (between a' & b', c & d, e' & f') as the compressive load continues to increase (i.e. not in the kink bands between b-b' & c-c' "⟍" and between d-d' & e'-e "⟋").

Surrounding support dictating buckling harmonic mode

The buckling harmonic mode (i.e. 1st, 2nd, 3rd or higher) that occurs in a layered structure depends on a variety of parameters including the layers' bond strengths, thickness & length, bond strength between layers, ease of sliding between layers, the surrounding matter's properties and its flexibility. The critical condition needed for each setup of layered structure in which the localized tilt changes resulting in increasing the buckling harmonic mode (i.e. 2nd or higher) by enforcing normal forces in the opposite direction needs further research. However, it is evident that it depends on bracing and the

surrounding support around the layered structure and polycrystalline materials grain boundaries are quite important. If a layered structure or column is loaded without support, it will buckle in 1st buckling harmonic mode in one direction. In other words, they would look like the buckled columns in Figs. 2-14 & 2-15.

Effect of layers end restriction

Figure 4-2 & Table 4-2 shows another experiment performed by Dodwell *et al.* [5, 21] with A4 paper, as well, which starts with a general left buckle tilt (Fig. 4-2(a)) and clarified during deformation (step 1 in Table 4-2). In Table 4-2, the edge dislocation intensity increased gradually with increasing load in steps 1-3. The effect of a right buckle at the top and bottom ends of the PP setup took place with excessive deformation in step 2 & 3 in Table 4-2. Only part (half) of the normal forces have an effect on the deformation evolution and buckling harmonic mode of the PP in steps 2 & 3(iv). An important factor that played a key role in the deformation events in steps 2 & 3 is the fixation of the A4 PP layers at the top and bottom ends of the setup. This factor has a major contribution providing the support that resulted in formation of a kink band at the top and bottom of the PP. This is the case in layered structured crystalline materials where the end edges of the layers at the grain boundaries are not free to slide and/or move against the grain boundaries during deformation. This is analogous to the fixed column shown in Fig. 4-9. Due to this restriction, a higher critical load (P_{cr}) is required for the column to deform under the 1st order buckling harmonic mode changing Eulers buckling formula accordingly to:

$$P_{cr} = \frac{4\pi^2 EI}{L^2} \qquad \text{Eq.(3)}$$

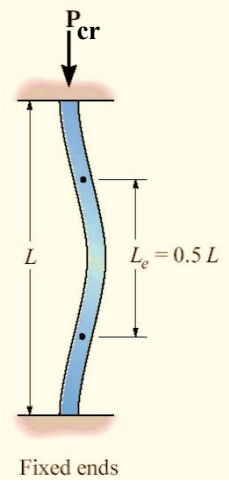

Figure 4-9: Built-in column setup under compressive loading after deforming under the 1st order buckling harmonic mode [50].

Reversibility of dislocation motion in layered structure

Recall the layered structure deformation analogy in Fig. 2-16 showing a buckled slinky in a 3rd harmonic mode. Depending on their location, different parts and regions in the slinky are under tension, compression, or a neutral stress state. The state of the slinky in Fig. 2-16 will remain in equilibrium and stable as long as the load on the slinky persists. However, if the compressive load is removed gradually, the slinky will gradually revert to its undeformed state. The restoring forces in the slinky originate from the elastic strains (whether tension or compression) in the different parts of the slinky that want to revert back to their original unloaded unstressed condition. The procedure of loading/unloading could be repeated infinitely without any changes in the details of the deformation performed by the slinky. The regions, parts and strips will repeatedly be subjected to the same stress and strain states, as long as the same load is applied.

Unfortunately Dodwell *et al.* [5, 20, 21] (Table 4-1) did not record events during unloading. The reversibility of the P setup experiment in Table 4-1 during unloading is expected to be analogous to the slinky reaction during unloading. Each object in the PP

setup performs a function resulting in a comparable behavior to layered structured crystalline materials. However, the reversibility of layered structured materials during unloading needs to be investigated.

4.3 Buckling dislocation stages analogy to extrusion and indentation

One of the major contributions of this work to understanding the deformation of layered solids is the identification of two elementary processes labeled extrusion and indentation. The latter can be used to explain the evolution of DWs taking place during buckling of most layered solids. Figure 4-10(a) show a schematic of the extrusion configuration comparable to the buckling of stage I (from steps 1-6) in the PP experiment by Dodwell *et al.* [5, 20, 21]. The configuration is composed of a rigid body containing a layered structure under loading, with an orifice near the bottom right corner. The rigid body represents the support by the sponge and ply wood, and the orifice represents the weakest location in which the layers are allowed to buckle and displace to the right. When a load is applied, there are high forces exerted by the layers at the orifice edges (red nodes) and the layers tend to displace out of the rigid body, though the orifice opening, Fig. 4-10(b). When a critical load is reached, multiple layers buckle simultaneously and U-shaped DWs are nucleated at the buckled layer's boundaries, (red dashed line in Fig. 4-10(c)). As soon as this process is initiated it proceeds in an autocatalytic fashion such that the buckle reaches the left side of the layered structure. This "extrusion" of layers is analogous to stage I (steps 1-6) that took place in the PP experiment by Dodwell *et al.* [5, 20, 21].

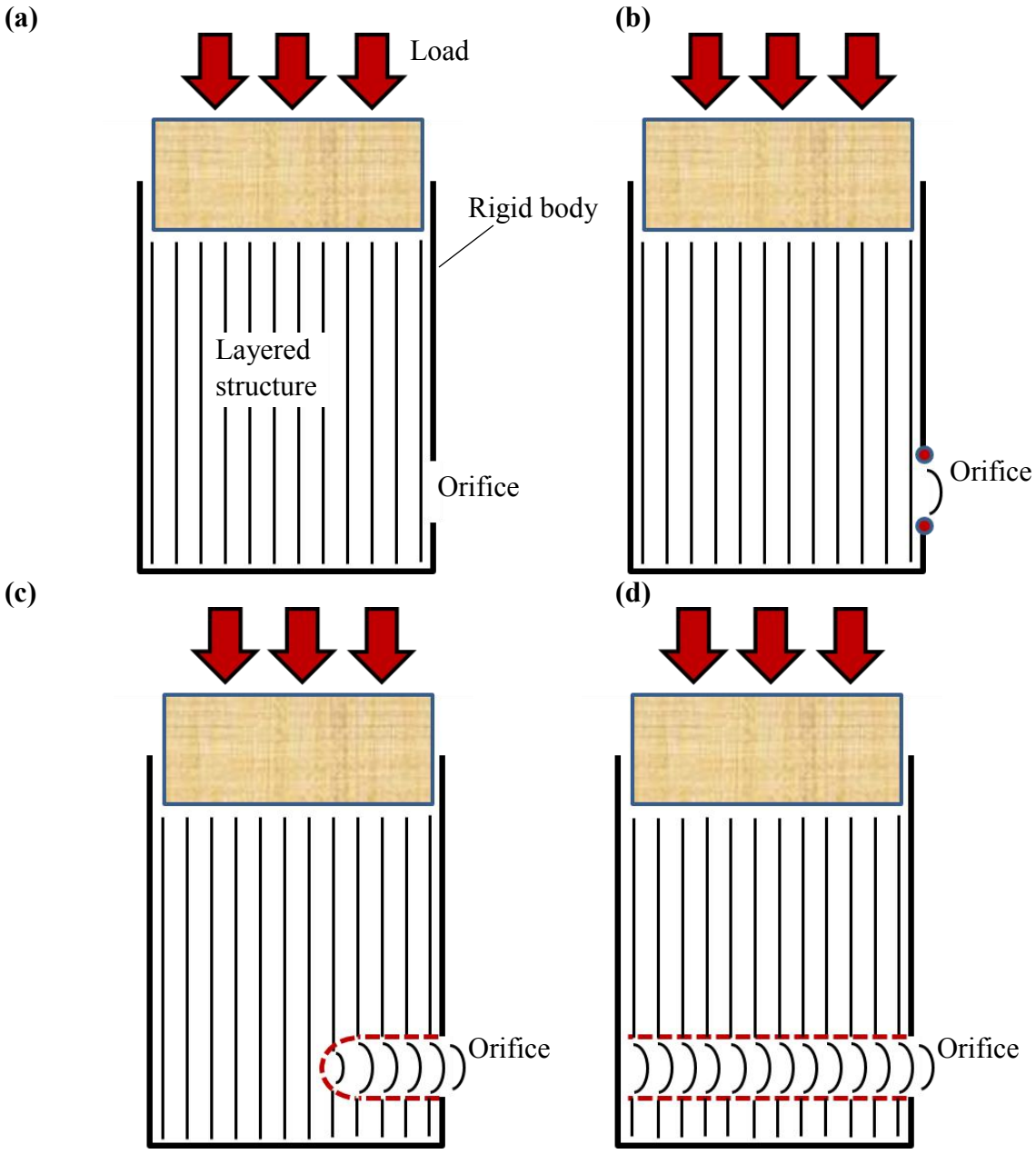

Figure 4-10: Extrusion configuration comparable to stage I buckling in the PP experiment by Dodwell *et al.* [5, 20, 21]; (a) Initial situation; (b) Edges of the orifice are highly stressed (red nodes) (c) Red dashed line represents the U-shapes DWs that nucleated at the boundaries of the layers that buckled locally, d) Configuration at end of stage 1 where the buckling has swept across the layers. Note that at this step, the U shape transforms into two near parallel DWs of the *same* sign.

The indentation configuration, that occur during stages II and III, is shown in Fig. 4-11. Two inclined DWs will nucleate, as shown, resulting in buckling of the layers in

between them to the left. Note here the two DWs do not occur simultaneouslty, but sequentially.

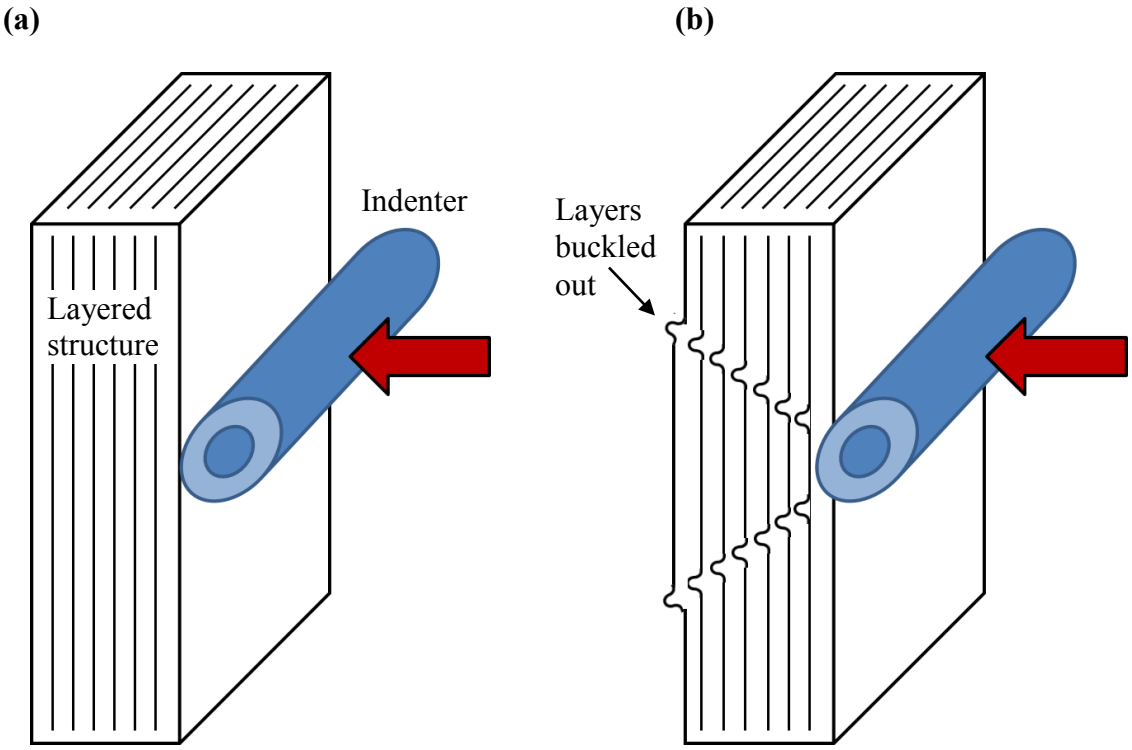

Figure 4-11: Indentation configuration comparable to stage II and III buckling in the PP experiment by Dodwell *et al.* [5, 20, 21]; (a). (b) After indentation two DWs nucleated at an inclined angle and the layers buckled out to the left. The two DWs are not nucleated simultaneouslty, but sequentially.

Depending on the orientation of the normal forces applied on the layers and the constraints placed on them by their surroundings, they will respond as if they "extruded" (Fig. 4-6) or "indented" (Fig. 4-7). For the sake of brevity and clarity, the following two symbols will be used to represent extrusion and indentation, respectively.

The symbols where designed to represent the process (▶ for extrusion and ● for indentation), indicate the DWs sign (the carpet-like dislocation at the end of the red line) and the approximate angle in which the DWs end up (red lines). For example, the extrusion and indentation symbols can be used as shown in Fig. 4-12.

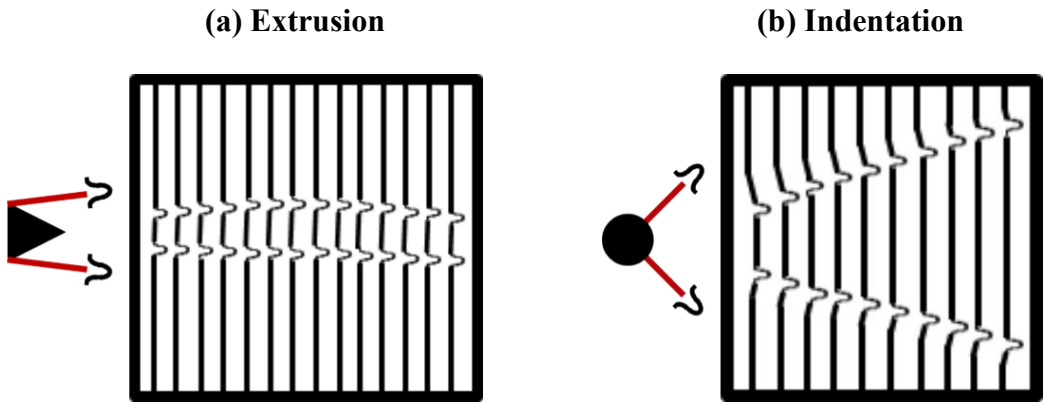

Figure 4-12: a) Extrusion and, (b), indentation, symbols with their corresponding resulting DWs applied to a stack of paper.

An important distinguishing characteristic of the extrusion and indentation processes is the location at which the DWs nucleate relative to the sign of the buckle. In Fig. 4-12, both figures are a right buckle. However, when extrusion takes place (Fig. 4-12(a)), the DWs nucleate simultaneously from the right side and move to the left in an autocatalytic process. Conversely, during indentation (Fig. 4-12(b)), the DWs nucleate on the left and extend to the right. They also occur slowly and sequentially. Contrariwise, a left buckle will result in DWs nucleation in the opposite directions indicated for extrusion and indentation respectively Note that the DWs that nucleate in indentation are identical to those one would expect in an indentation experiment, hence the label.

Figure 4-13 shows the application of those symbols on the PP experiment by Dodwell *et al.* [5, 20, 21]. The symbols could also be applied to fractured surfaces of layered structures.

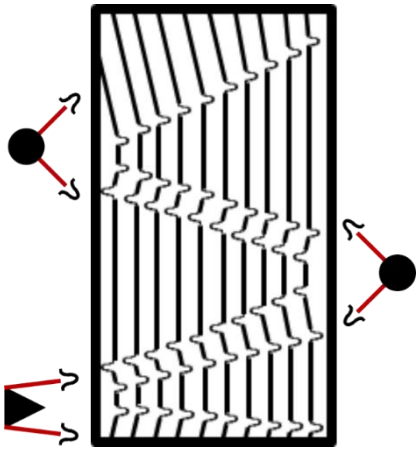

Figure 4-13: Application of the extrusion and indentation symbols to the buckled PP experiment by Dodwell *et al.* [5, 20, 21].

Using these symbols, all possibilities on buckled layered structures could be labeled. For example, Orowan [8] showed that when Zn single crystals were loaded parallel to the basal planes, quite complex deformation modes were possible (Fig. 4a). Here we focus on the one labeled by the red arrow. Figure 4-14(b) shows a schematic of the deformation.

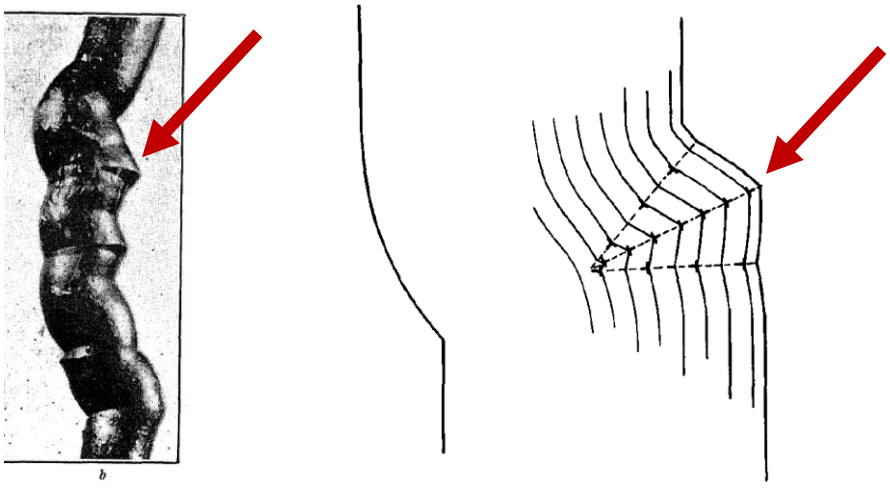

Figure 4-14: (a) Photograph of Zn single crystal after buckling deformation indicating nucleation of a single DW as indicated by ridge. Schematic representation of single DW after buckling. [8, 12]

Figure 4-15 shows a schematic for the development of a 2nd harmonic buckling mode for the deformation of a layered structure by Hess and Barrett [12]. Note this is the

classic stove-pipe configuration, also known as a kink band, comprised of two kink boundaries. Such a kink boundary can be produced by two extrusions of opposite signs. Here, for reasons that are not totally understood, the two DWs associated with the extrusion appear to merge into a single sharp DW or kink boundary. Under what conditions and for what materials, the two extrusion DWs merge into one, is unclear at this time and requires more work.

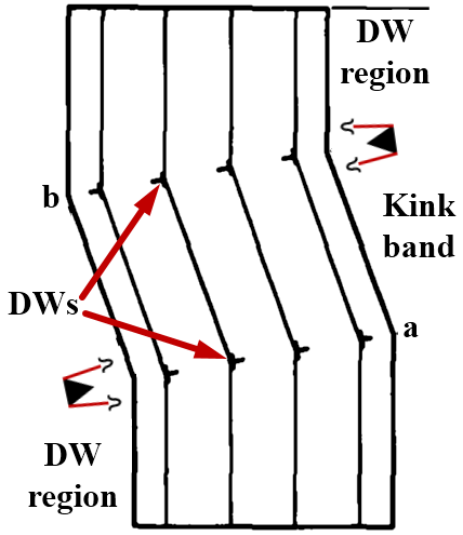

Figure 4-15: Development of a 2nd harmonic buckling mode – or classic kink boundary - for the deformation of the Zn [12]. Extrusion symbols added at corresponding locations where they may have taken place.

In Figure 4-16 the extrusion and indentation symbols are added to the TEM image to explain the multiple buckles of the same sign observed. Note that the symbols are added here for illustrative purposes only, since which process – extrusion or indentation – cannot be determined from the fracture surfaces alone. In order to determine which process actually causes the kinking can only be determined by observing the dynamic process.

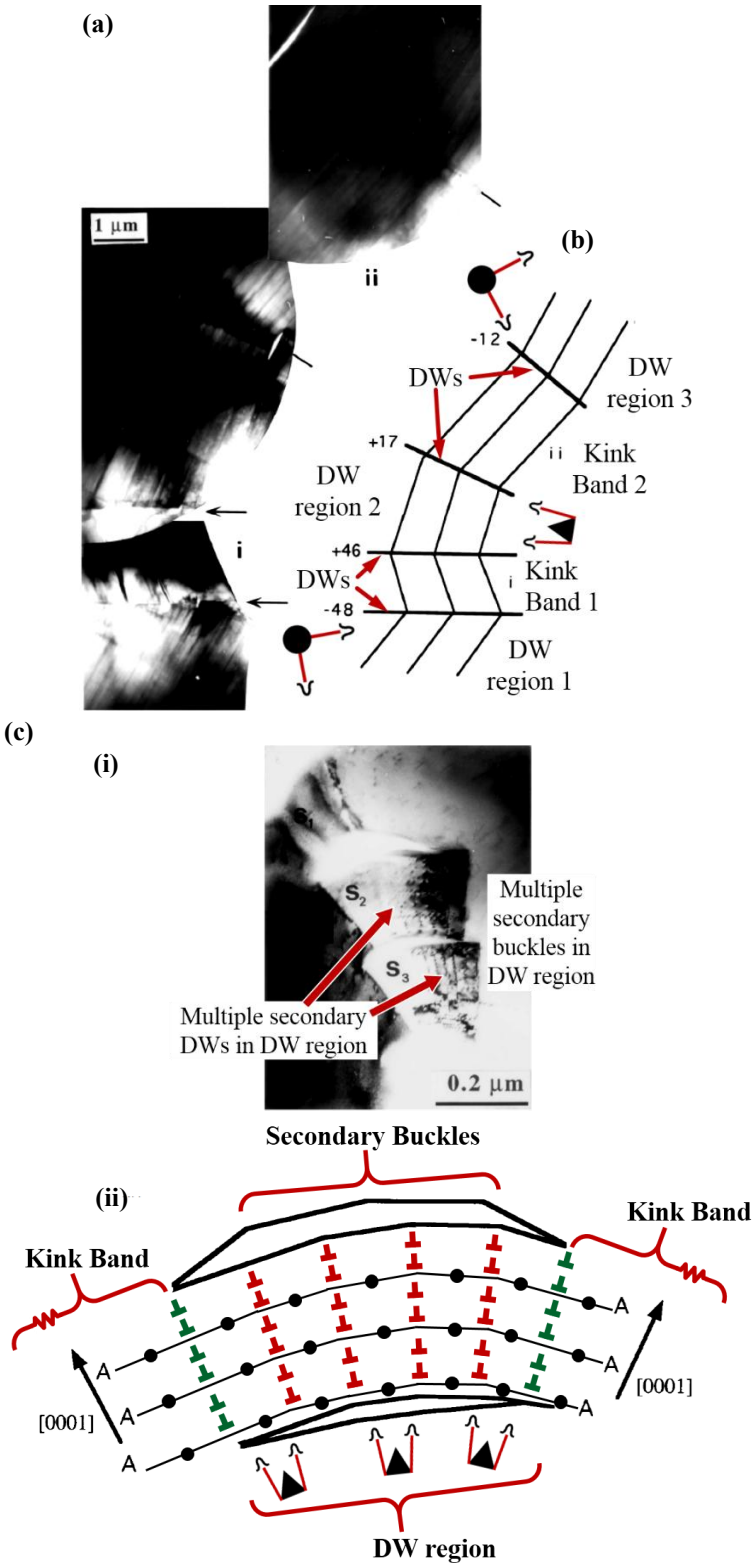

Figure 4-16: TEM bright-field images and corresponding schematics of fractured Ti_3SiC_2 by Barsoum *et al.* [13]. Extrusion and indentation symbols are marked in the possible locations on schematics (a) DWs in different directions with possible extrusion and indentation processes, (b) All DWs in one direction with no surface support on sample indicating extrusion process for all DWs nucleated.

4.4 Inverse Expansion Effect

Figure 4-17a, b and c show the initial and final deformed stage of A4 paper sheets loaded in a P-sample orientation (i.e. vertical) with foam used as the supporting medium. Figure 4-17(a) shows the initial stage of the paper pile setup before deformation; while Fig. 4-17(b) & (c) display the final stage. The lengths, L1, and widths, W1, of the paper pile are labelled in Fig. 4-17(a) in order to track the dimensions' development during deformation upon axial compression. After buckling and the nucleation of the DWs it is clear that ΔL decreased while the width increased by ΔW.

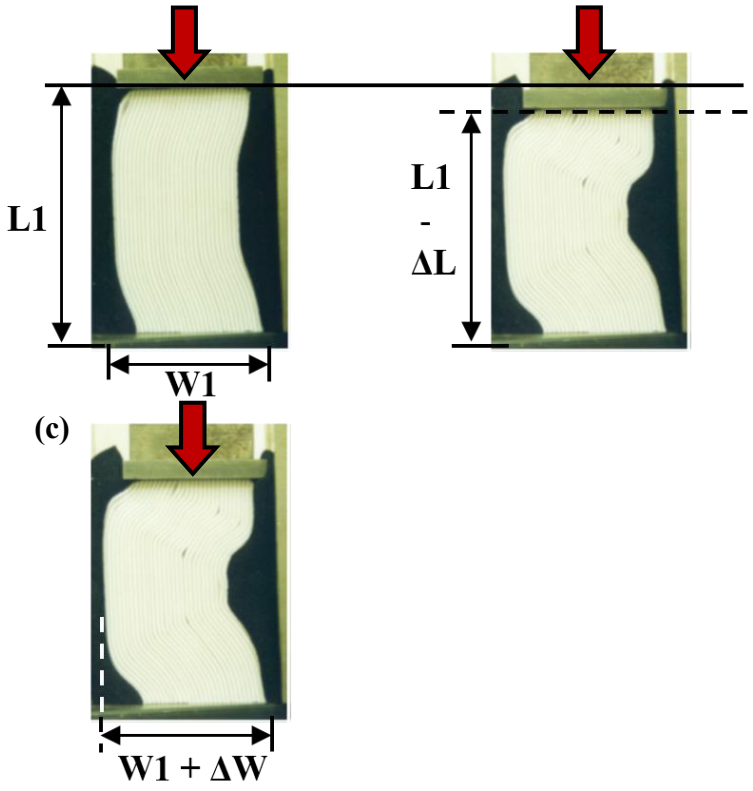

Figure 4-17: Buckling of A4 paper sheets loaded in a P-sample orientation (i.e. vertical) with foam used as the supporting medium (Table 4-2). (a) Initial stage before deformation, and (b) & (c) after deformation. (b) shows the changes in heights while, (c) shows the changes in widths of the paper stack after deformation.

Figure 4-18 displays the same configuration as Fig. 4-17 but for the N-sample configuration. In this case, the overall axial strain in positive, and the transverse strain is

negative. This is the opposite of what occurs during linear elastic deformation.. We label this effect as an inverse expansion effect.

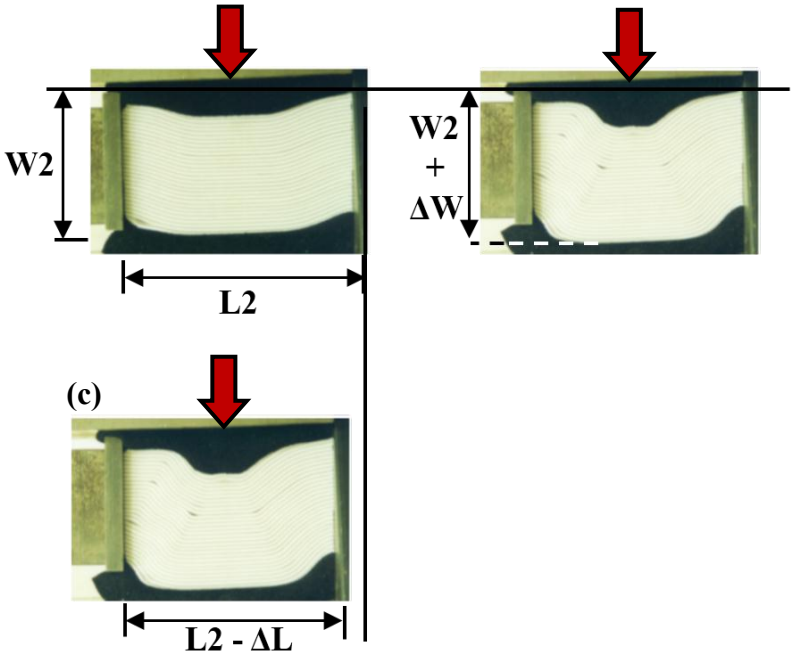

Figure 4-18: The initial and final stage of the development of A4 paper sheets buckling starting from a P-sample orientation but horizontally inclined with foam used as the supporting medium (Table 4-2). (a) Initial stage before any deformation, (b) & (c) are the final stage, (b) is for comparison of width while (c) for length.

An important phenomenon to note in buckling of layered structures is that during deformation, the layers fold against each other. This occurs in all layered structures in all orientations (i.e. irrespective of the layers inclination angle). In the P-sample orientation (Fig. 4-17), the layers fold which results in a decrease in the layers' length and increase in their width. When the same layers' fold in the N-sample orientation, they increase in width in a direction opposite of that of the applied load! Said otherwise, the layers buckle into a direction that is opposite to that of their strain energy consideration. Buckling of layers always expands in the transverse direction to the layers' flat surfaces and contract along the layers' lengths, regardless of the direction of loading It follows that in the N-configuration, buckling results in an inverse expansion effect.

Note that in the N-configuration if buckling and kinking is occurring without allowing for delaminations, (as in a polycrystal for example), then there are two counter effects taking place simultaneously: The inverse expansion effect due to buckling deformation and folding of the layers, in addition to the positive expansion taking place due to linear elasticity. In a N-configuration, both effects are taking place simultaneously.

4.5 Summary & Conclusion

The PP experiment by Dodwell *et al.* [5, 20, 21] was used to shed important light on the deformation of layered solids. The non-crystallographic nature of the carpet-like edge dislocation configuration enables variable strain accommodations during buckling deformation of the layers.

There are two possible normal force contours that can induce layers to buckle. The surrounding support around the layered structure dictates the buckle direction and the normal forces' contours. There are variations in crystalline materials that need to be considered like layers ends restrictions and ease of sliding between the layers for buckling to be possible. However, the PP experiment provides valuable insight about the buckling dislocation-like mechanisms.

The developed symbols of extrusion and indentation simplify the possible events that could take place during layers deformation and will be useful in further research on KNE materials and layered structures in general at all lengths scales. The inverse expansion effect is an important observation that can be tested experimentally in polycrystalline materials.

Table 4-1: Dislocation evolution of KNE layered structured materials employing a pseudo-single crystal PP setup with P-sample texture. (i) In-plane forces, (ii) Normal forces, (iii) DIC displacement snapshots of the A4 PP experiment made from Dodwell *et al.* [5, 20, 21] video, (iv) Schematic evolution of DWs as function of loading, (v) Representation of the resolved forces acting at different locations of the layered structure pseudo-single crystal resulting in the dislocations evolution observed in (iv).

Step	(i) In-plane shear forces	(ii) Normal forces	(iii) DIC Video snapshot	(iv) Dislocation Evolution	(v) Normal forces applied at various locations
1	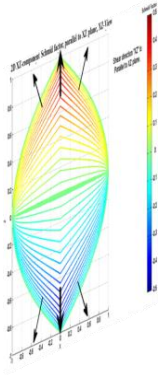	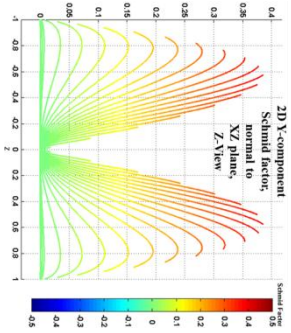	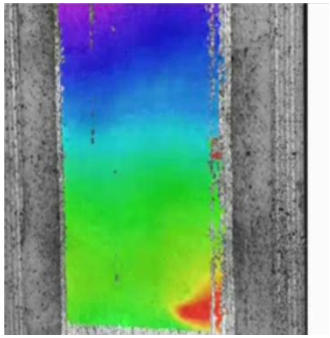	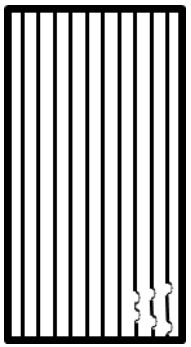	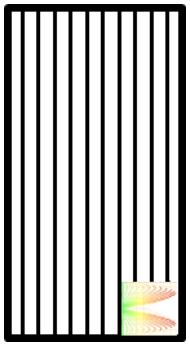
2	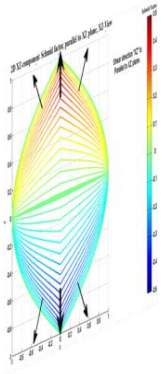	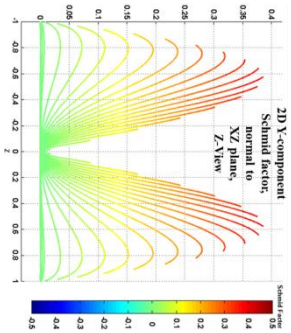	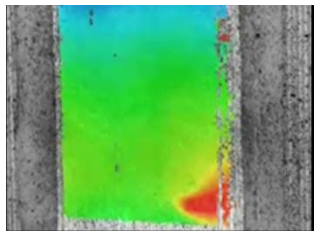	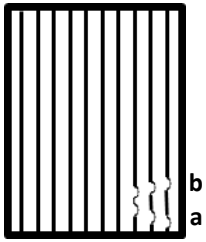	

3	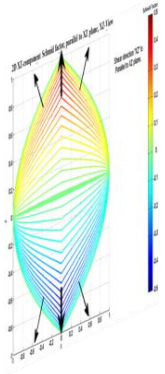	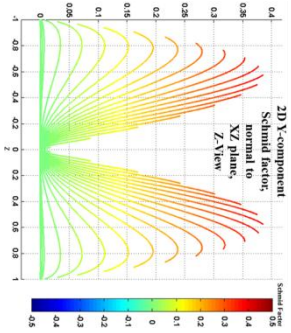 2D Y-component Schmid factor, normal to XZ plane, Z-View	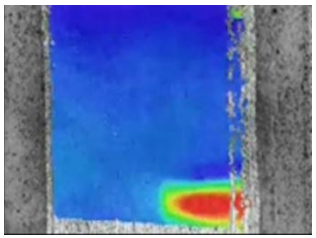	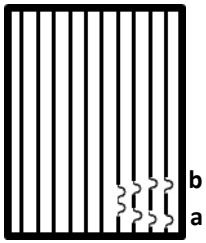 b a	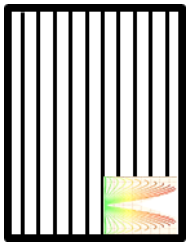
4	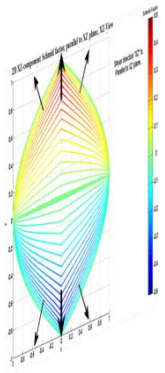	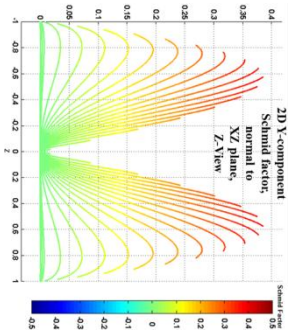 2D Y-component Schmid factor, normal to XZ plane, Z-View	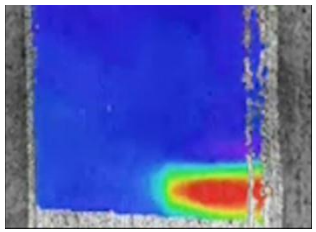	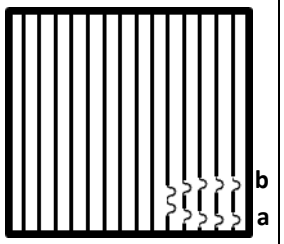 b a	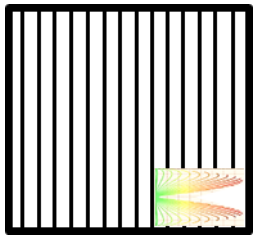
5	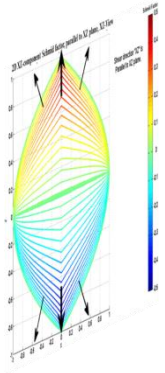	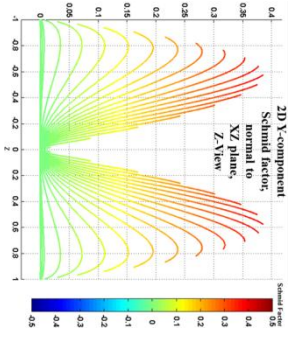 2D Y-component Schmid factor, normal to XZ plane, Z-View	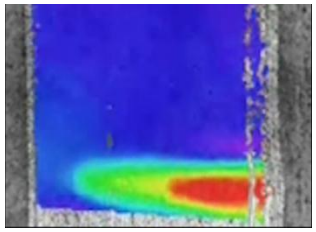	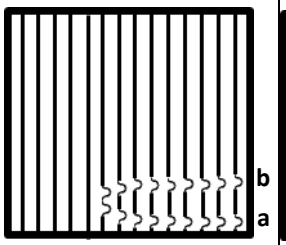 b a	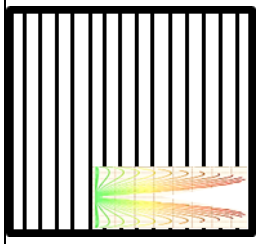

6	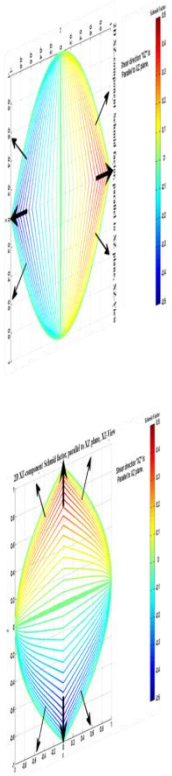	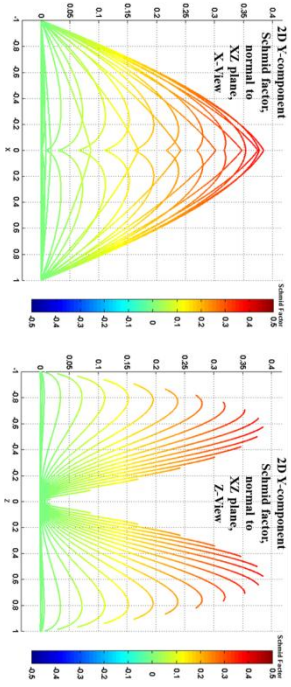	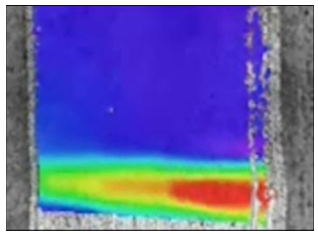	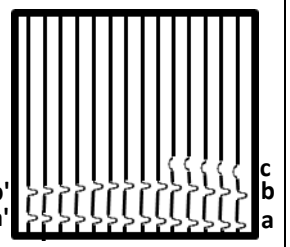	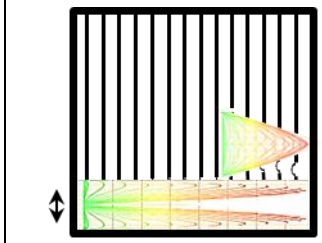
7	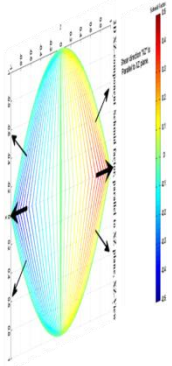	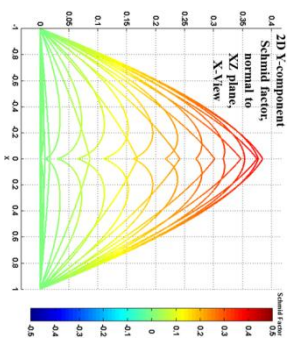	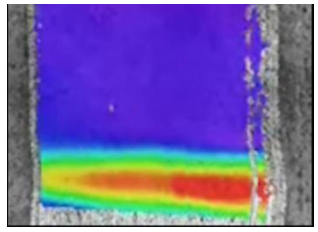	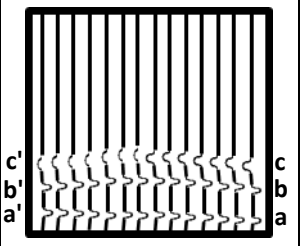	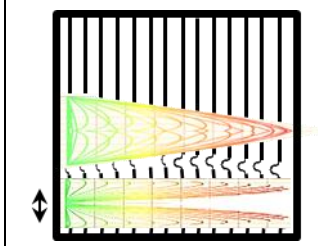

8	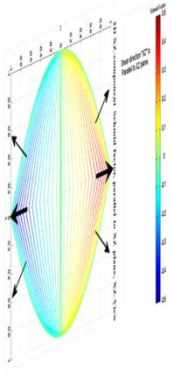	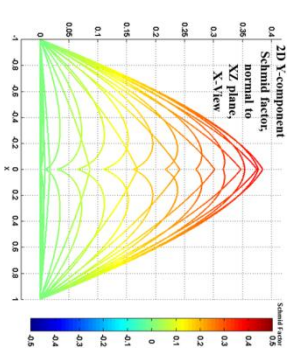 2D Y-component Schmid factor, normal to XZ plane, X-View	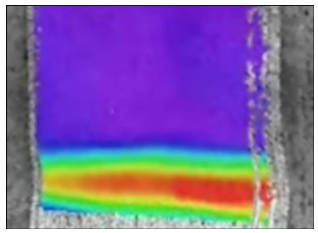	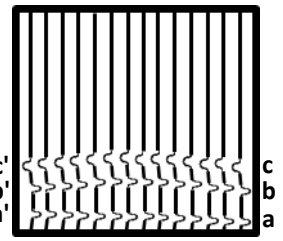 c' b' a' c b a	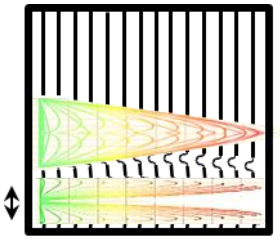
9	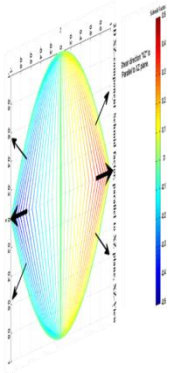	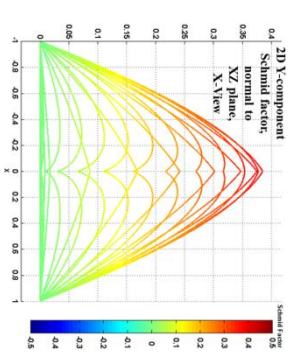 2D Y-component Schmid factor, normal to XZ plane, X-View	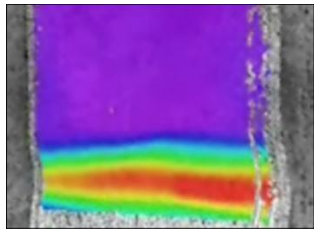	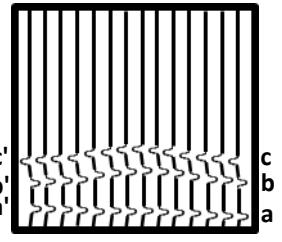 c' b' a' c b a	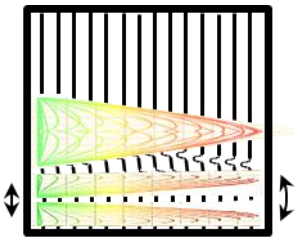
10	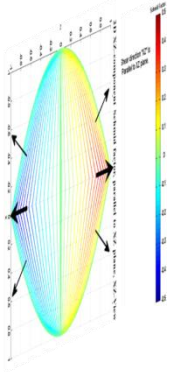	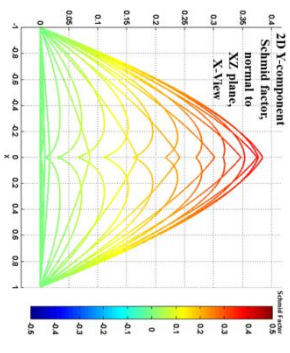 2D Y-component Schmid factor, normal to XZ plane, X-View	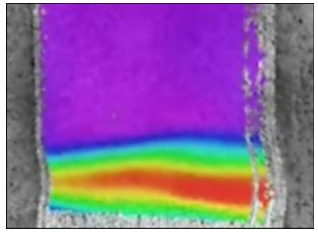	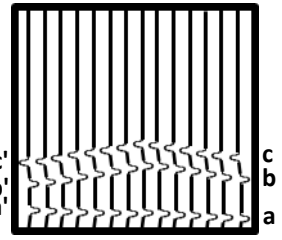 c' b' a' c b a	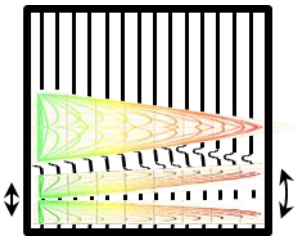

11	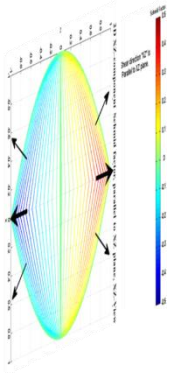	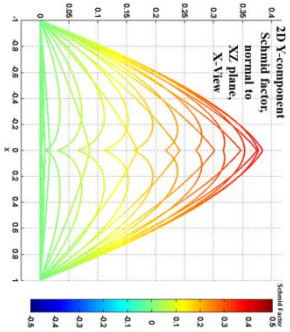 2D Y-component Schmid factor, normal to XZ plane, X-View	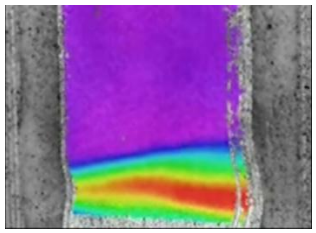	-	-
12	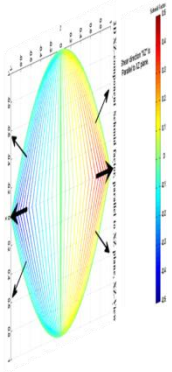	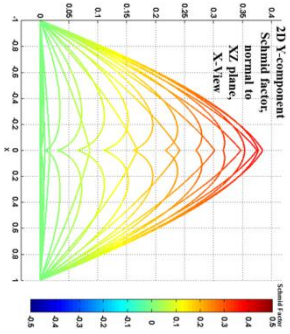 2D Y-component Schmid factor, normal to XZ plane, X-View	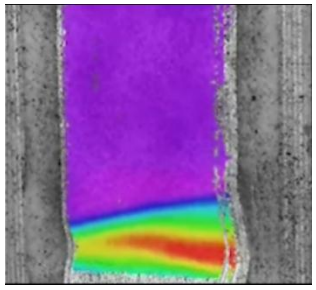	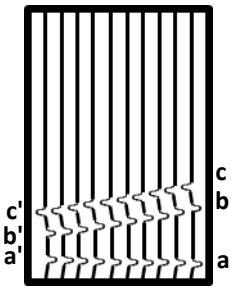 c b a c' b' a'	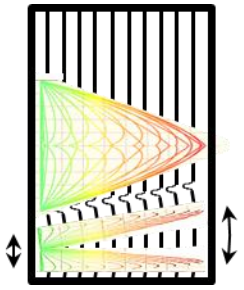

13	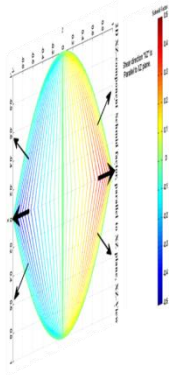	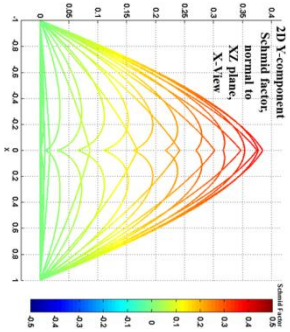 2D Y-component Schmid factor, normal to XZ plane, X-View	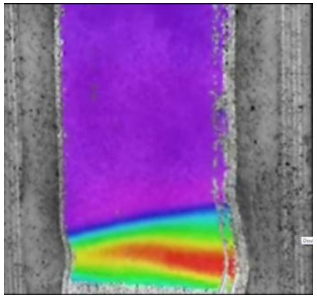	-	-
14	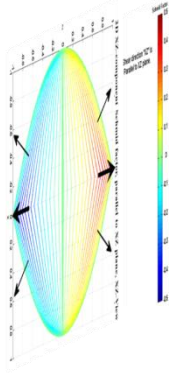	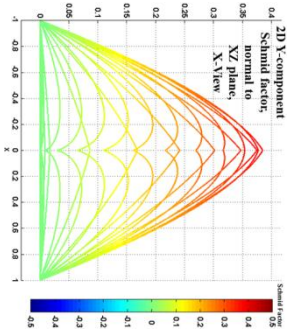 2D Y-component Schmid factor, normal to XZ plane, X-View	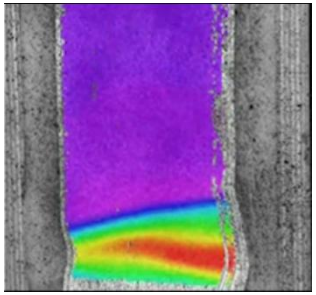	-	-

15	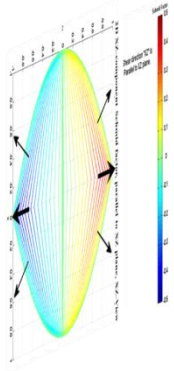	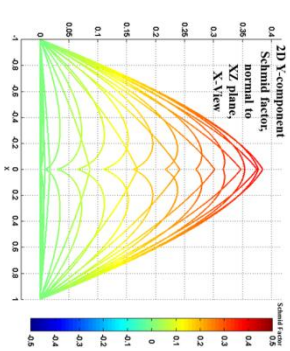	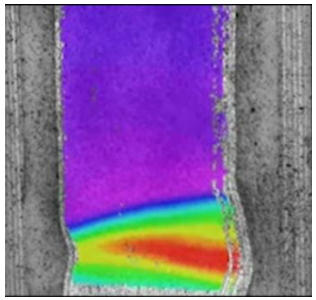	–	–
16	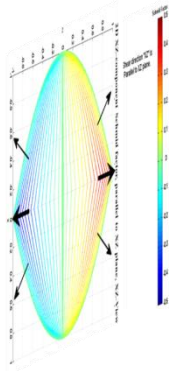	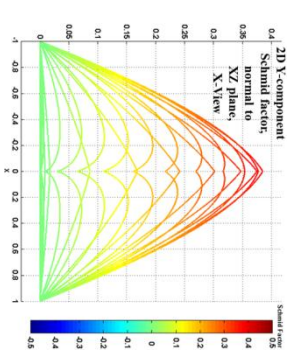	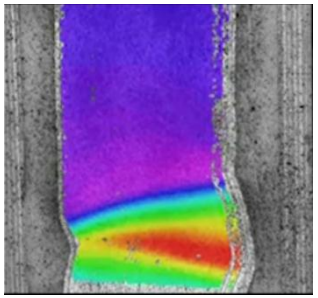	–	–
17	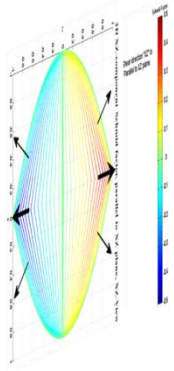	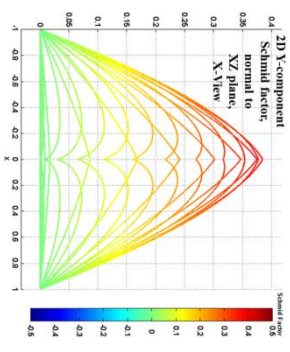	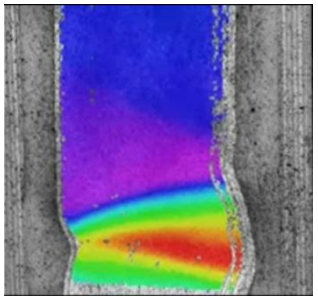	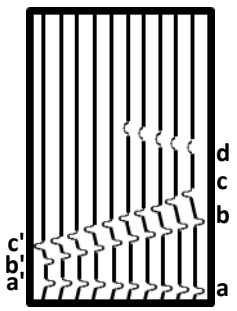	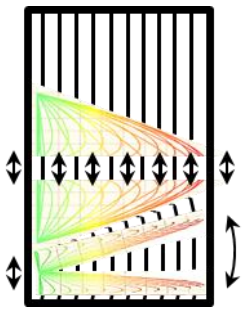

18	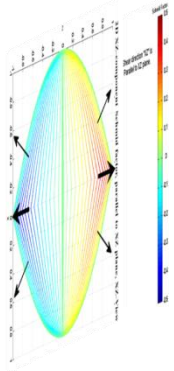	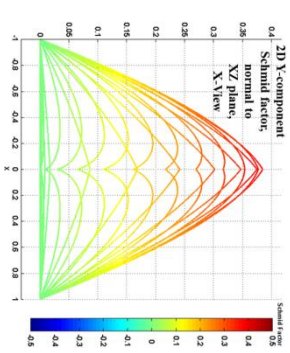 2D Y-component Schmid factor, normal to XZ plane, X-View	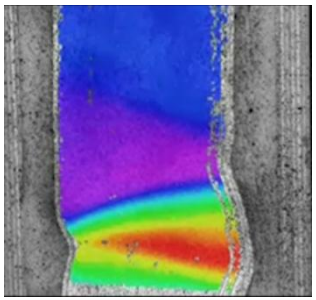	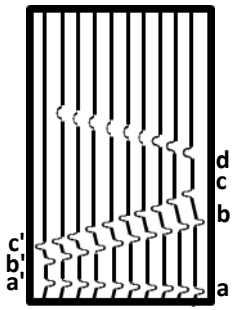 d c b a c' b' a'	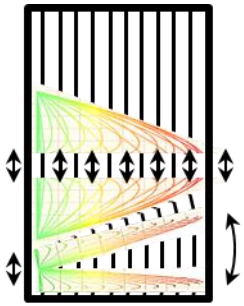
19	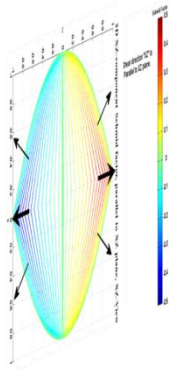	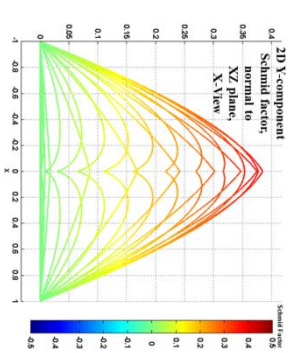 2D Y-component Schmid factor, normal to XZ plane, X-View	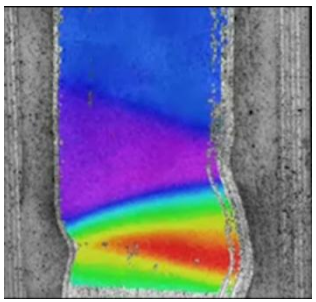	—	—
20	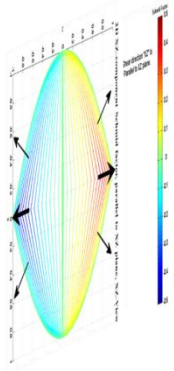	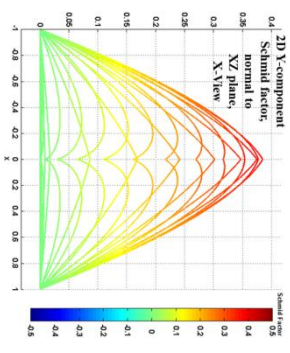 2D Y-component Schmid factor, normal to XZ plane, X-View	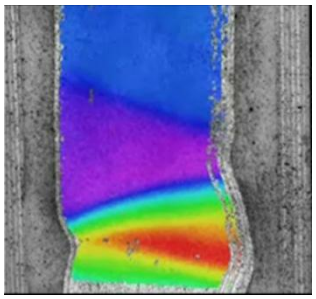	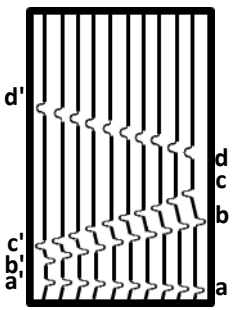 d' d c b c' b' a' a	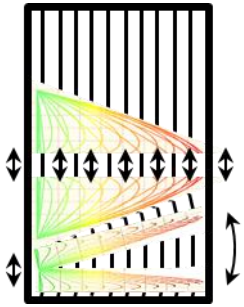

21	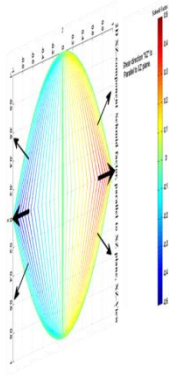	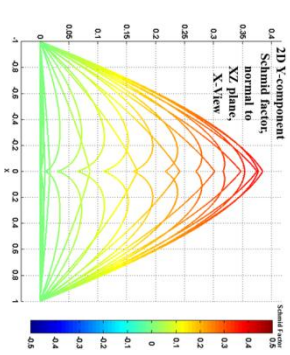 2D Y-component Schmid factor, normal to XZ plane, X-View	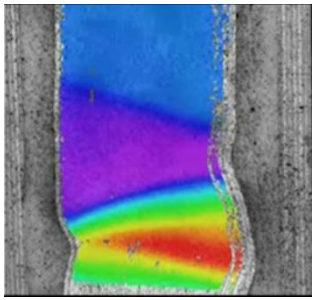	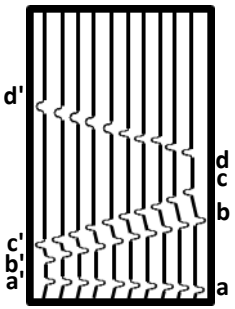 d' c' b' a' d c b a	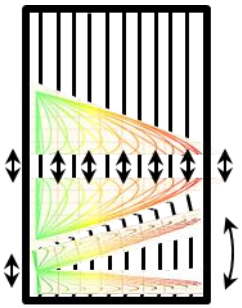
22	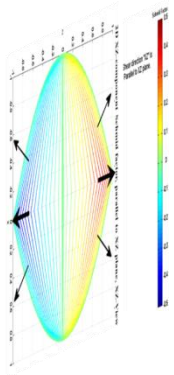	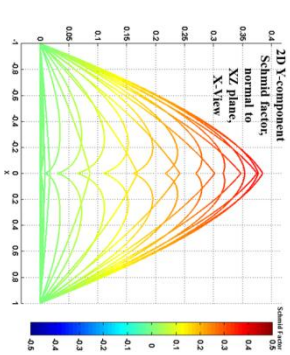 2D Y-component Schmid factor, normal to XZ plane, X-View	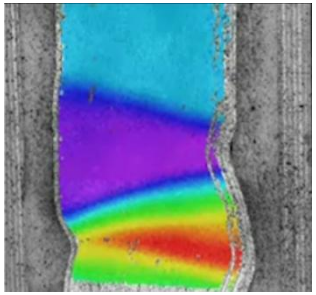	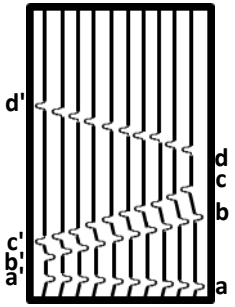 d' c' b' a' d c b a	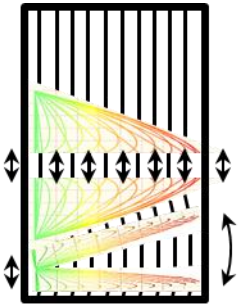

23	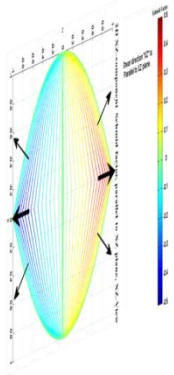	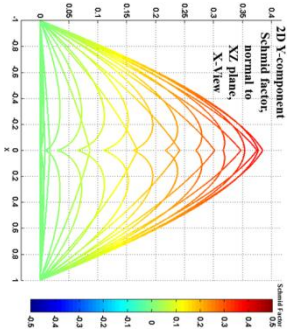 2D Y-component Schmid factor, normal to XZ plane, X-View	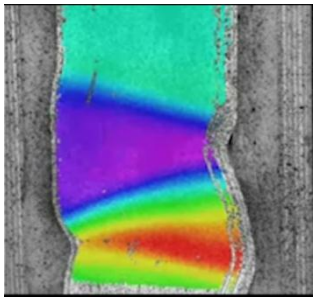	-	-
24	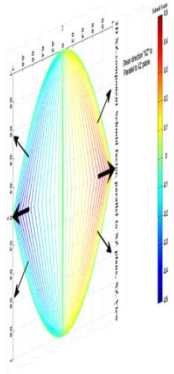	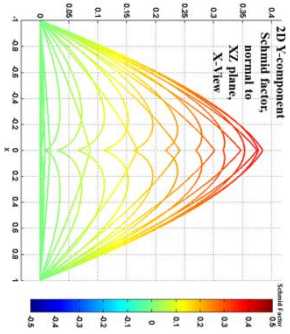 2D Y-component Schmid factor, normal to XZ plane, X-View	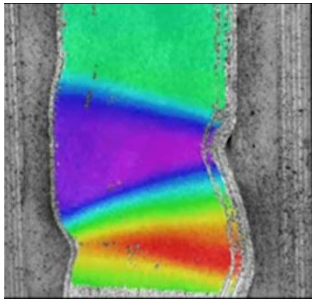	-	-

25	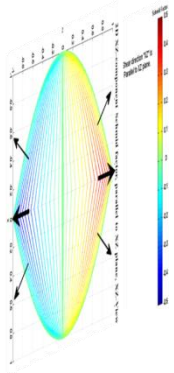	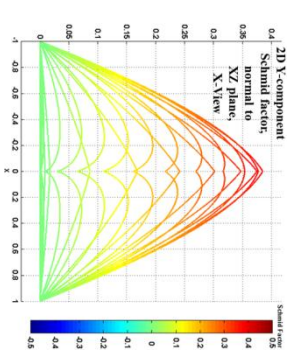 2D Y-component Schmid factor, normal to XZ plane, X-View	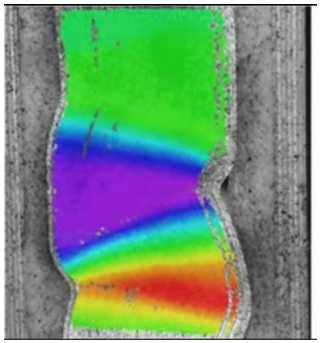	-	-
26	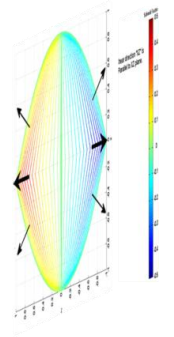 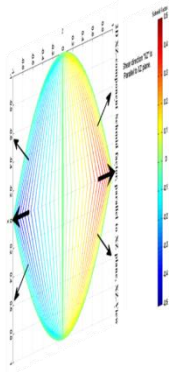	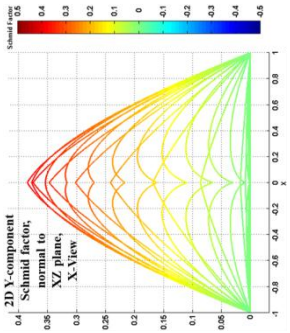 2D Y-component Schmid factor, normal to XZ plane, X-View 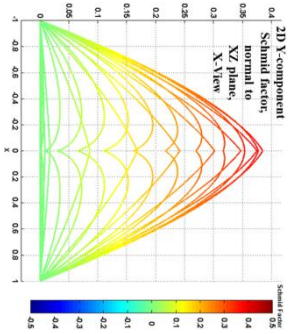 2D Y-component Schmid factor, normal to XZ plane, X-View	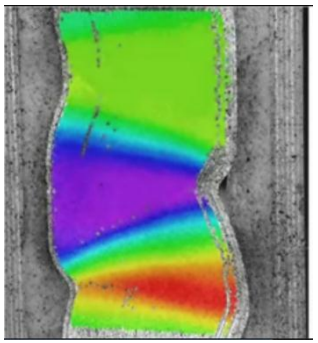	-	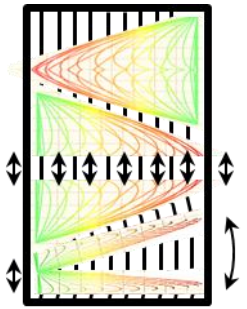 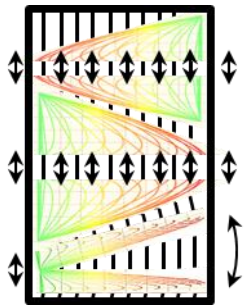

27	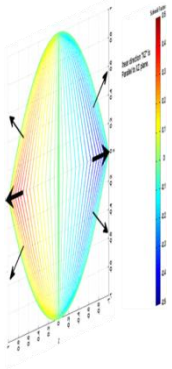	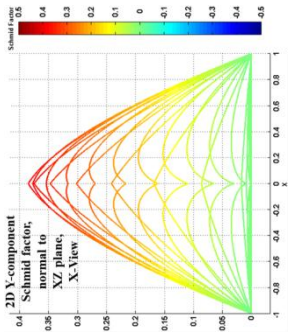 2D Y-component Schmid factor, normal to XZ plane, X-View	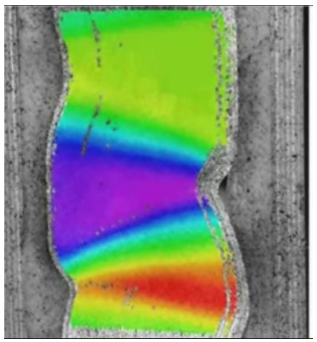	-	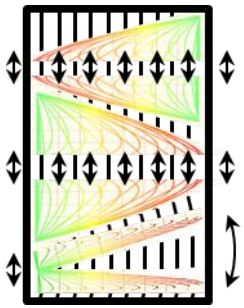
28	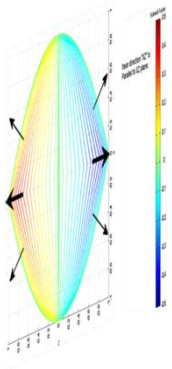	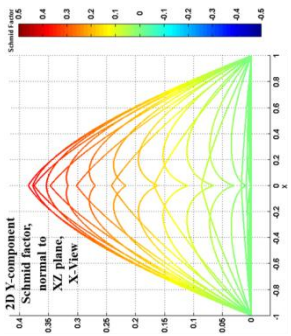 2D Y-component Schmid factor, normal to XZ plane, X-View	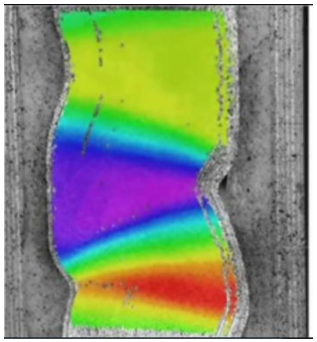	-	-

29	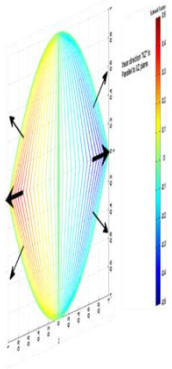	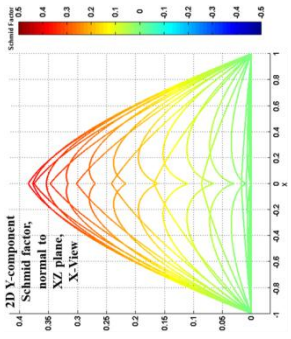 2D Y-component Schmid factor, normal to XZ plane, X-View	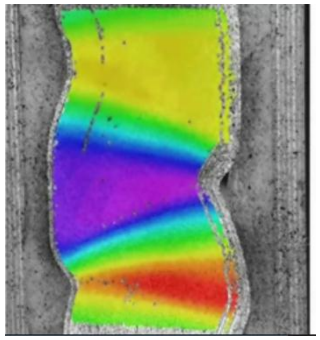	-	-
30	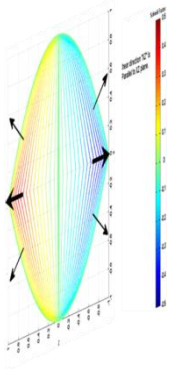	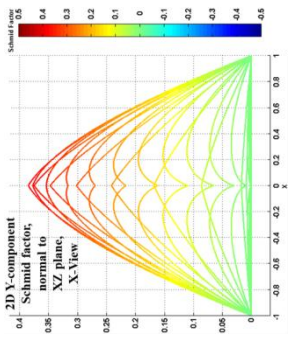 2D Y-component Schmid factor, normal to XZ plane, X-View	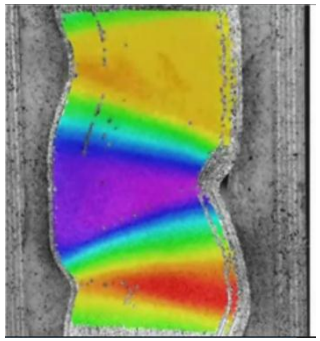	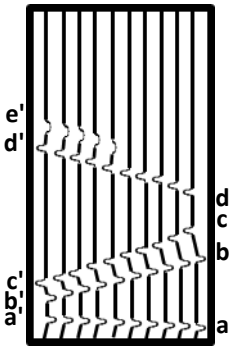 e' d' c' b' a' d c b a	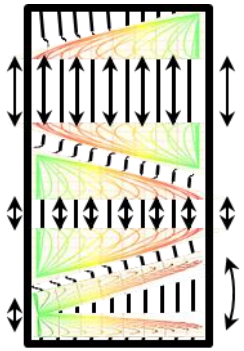
31	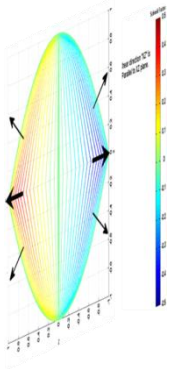	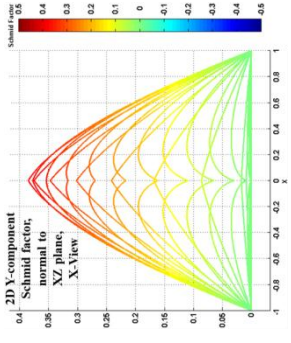 2D Y-component Schmid factor, normal to XZ plane, X-View	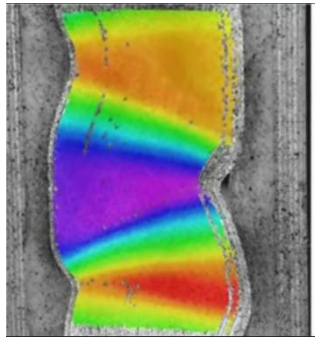	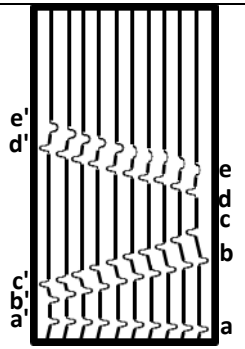 e' d' c' b' a' e d c b a	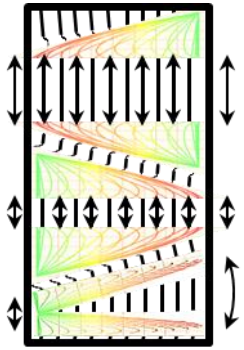

32	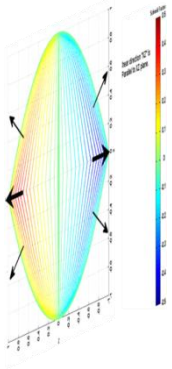	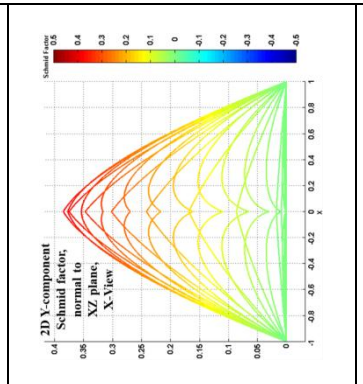 2D Y-component Schmid factor, normal to XZ plane, X-View	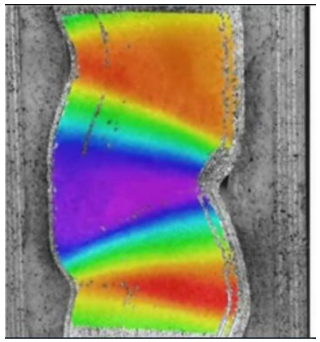	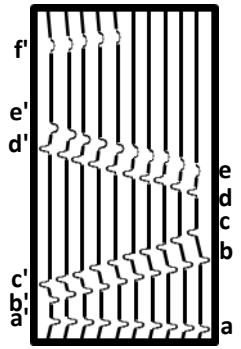 f' e' d' c' b' a' e d c b a	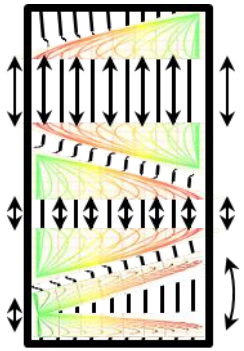
33	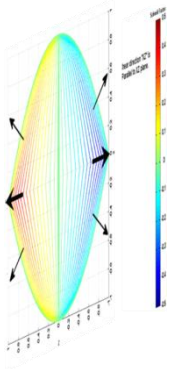	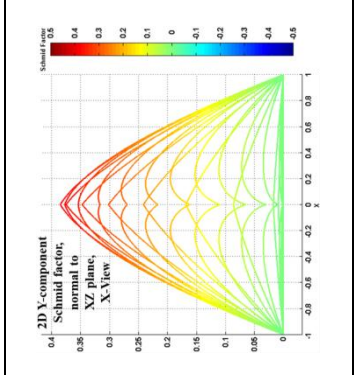 2D Y-component Schmid factor, normal to XZ plane, X-View	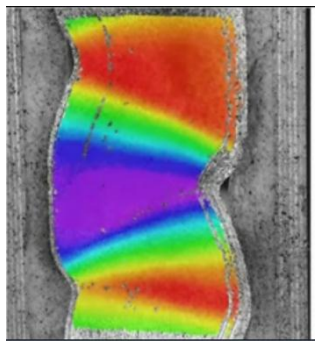	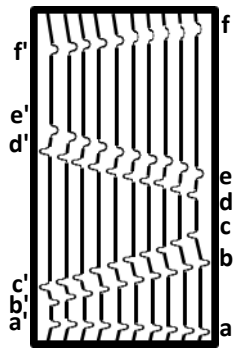 f' e' d' c' b' a' f e d c b a	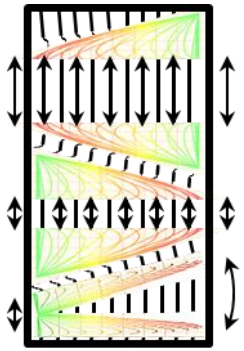
34	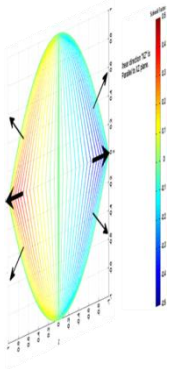	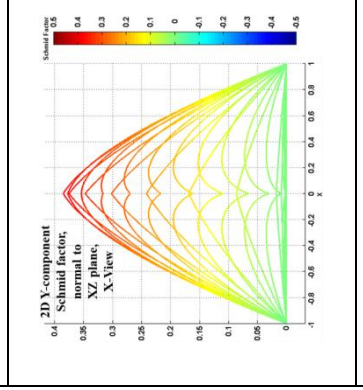 2D Y-component Schmid factor, normal to XZ plane, X-View	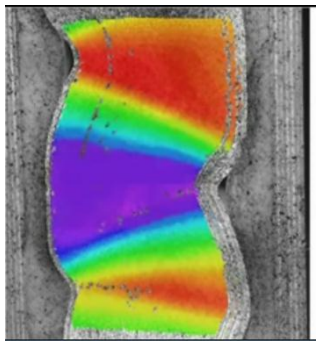	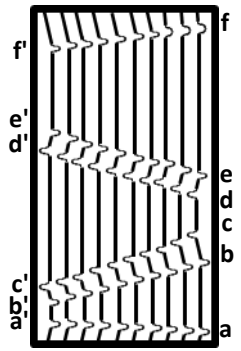 f' e' d' c' b' a' f e d c b a	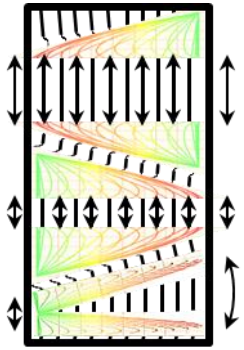

35	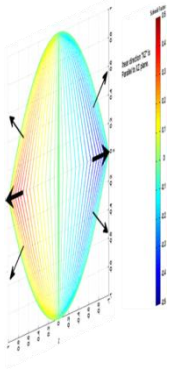	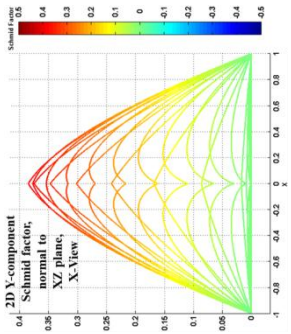 2D Y-component Schmid factor, normal to XZ plane, X-View	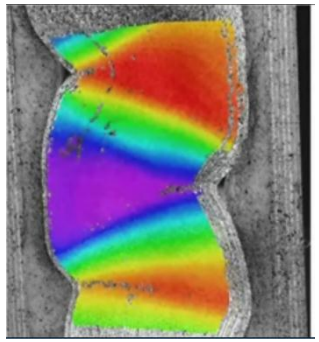	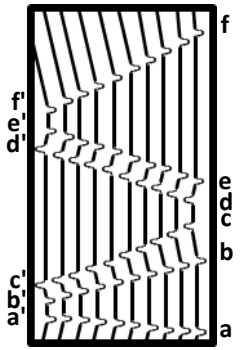 f f' e' d' e d c b c' b' a' a	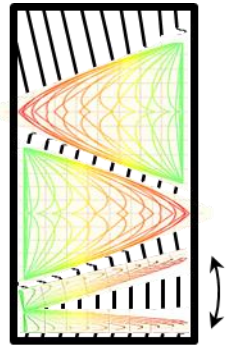
36	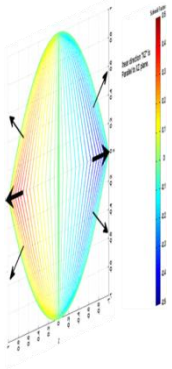	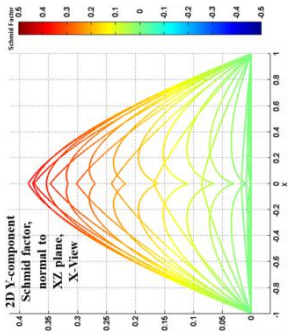 2D Y-component Schmid factor, normal to XZ plane, X-View	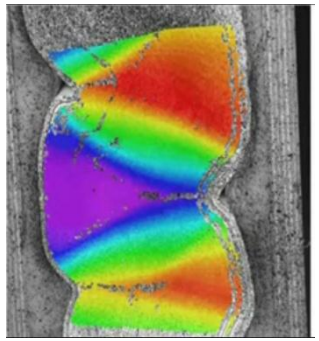	-	-

37	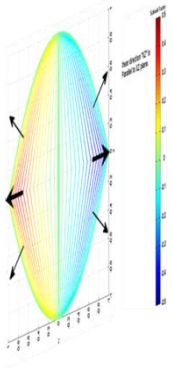	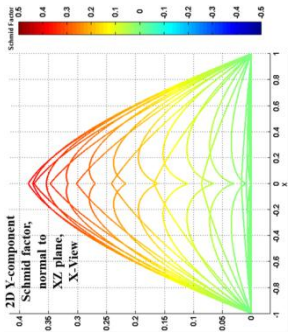 2D Y-component Schmid factor, normal to XZ plane, X-View	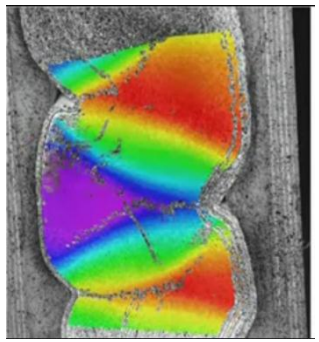	-	-
38	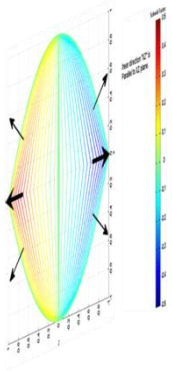	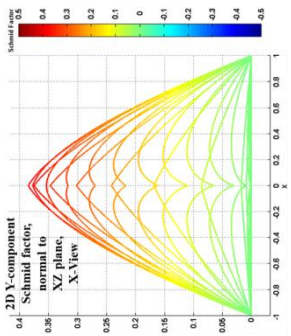 2D Y-component Schmid factor, normal to XZ plane, X-View	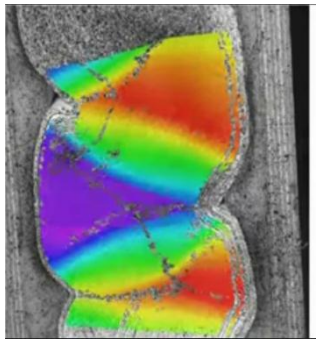	-	-

39	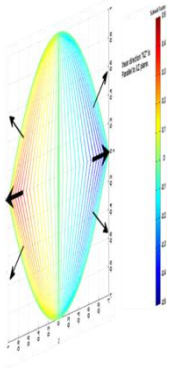	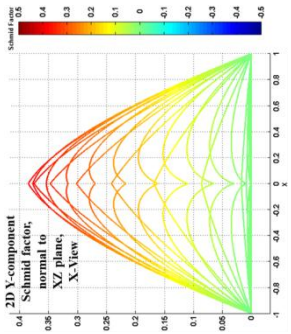 2D Y-component Schmid factor, normal to XZ plane, X-View	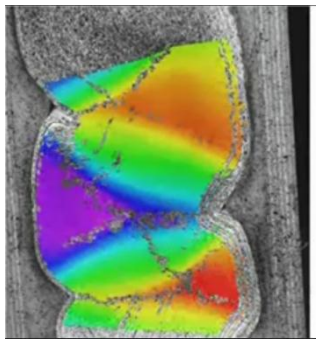	-	-
40	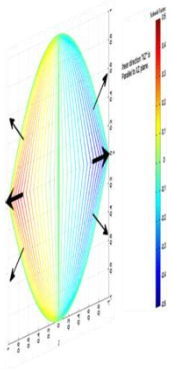	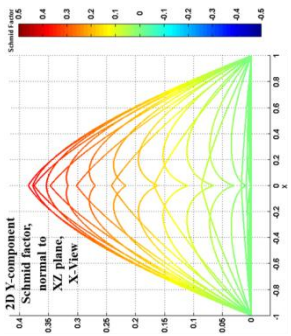 2D Y-component Schmid factor, normal to XZ plane, X-View	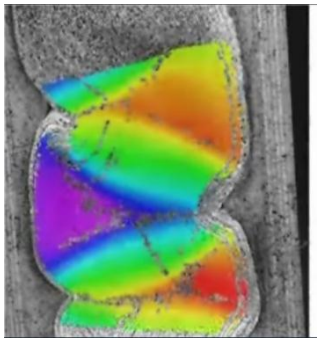	-	-

Table 4-2: Dislocation evolution of KNE layered structured materials employing a pseudo-single crystal PP setup with P-sample texture. (i) In-plane forces, (ii) Normal forces, (iii) Deformation evolution of the A4 paper sheets in Fig. 4-8, (iv) Representation of the resolved forces acting at different locations of the layered structure pseudo-single crystal resulting in the dislocations evolution observed in (iii)[5, 21].

Step	(i) In-plane shear forces	(ii) Normal forces	(iii) Deformation evolution	(iv) Normal forces applied at various locations
1	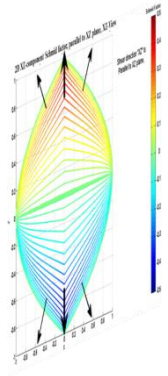	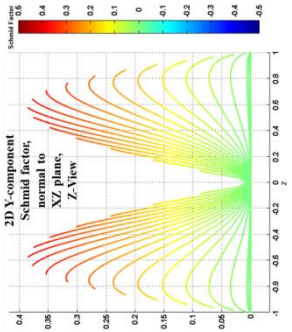		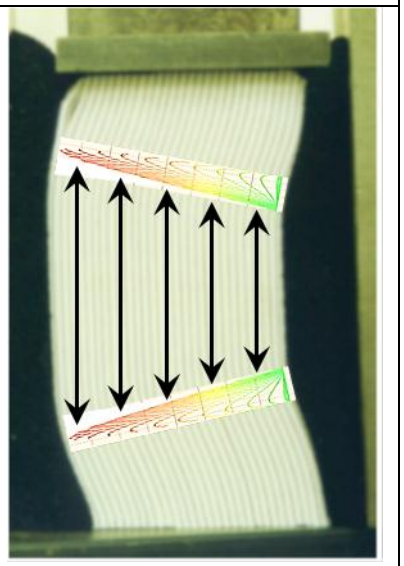

2	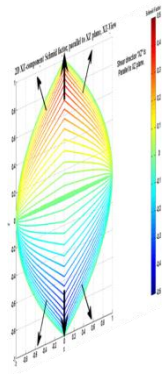	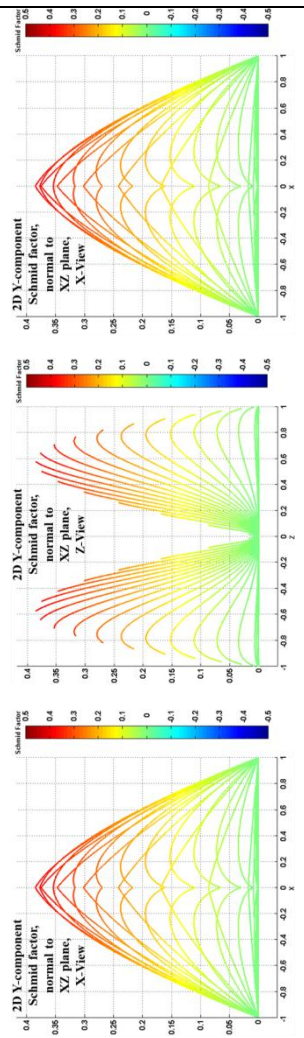 2D Y-component Schmid factor, normal to XZ plane, X-View 2D Y-component Schmid factor, normal to XZ plane, Z-View 2D Y-component Schmid factor, normal to XZ plane, X-View		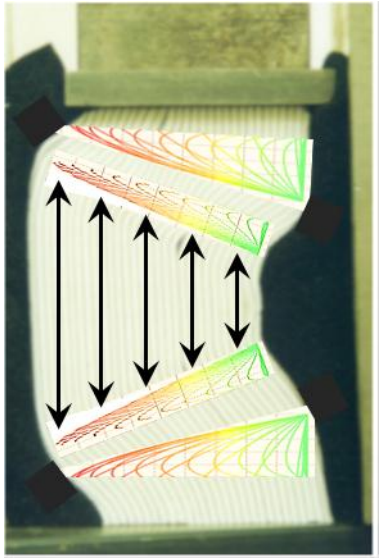

3	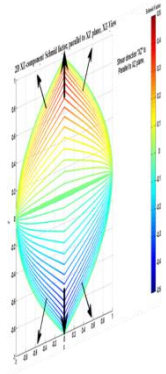	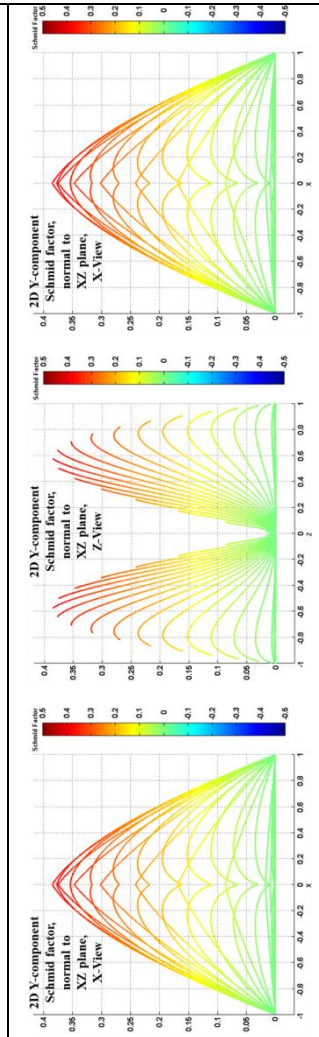 2D Y-component Schmid factor, normal to XZ plane, X-View 2D Y-component Schmid factor, normal to XZ plane, Z-View 2D Y-component Schmid factor, normal to XZ plane, X-View	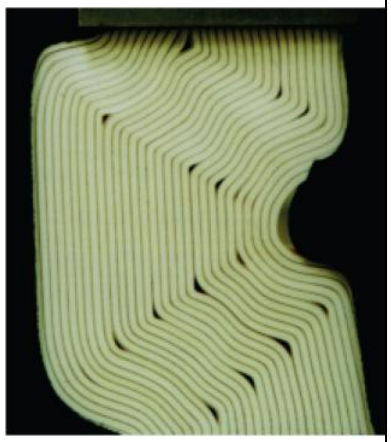	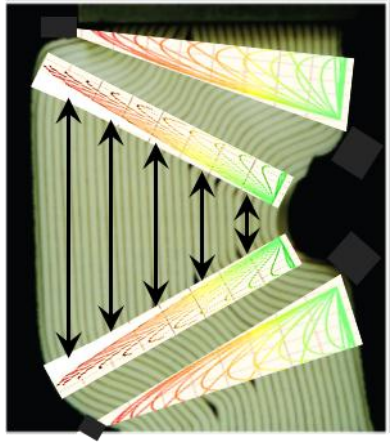

Chapter 5: MAX Phases Sample Fabrication & Characterization

In this study, most experiments were carried on MAX phases due to their unique KNE mechanical behavior. The three MAX phases studied here are Ti_2SC, Ti_3SiC_2 and Ti_2AlC. These phases encompass typical members of the 211 and 312 MAX phases. The reasons for choosing these phases are the following. Ti_2SC was deliberately chosen, since it is the only MAX phase known to date that is fully linear elastic when bulk samples are loaded in compression [51]. However, under a nanoindentor KNE mechanical response was observed [52]. The effect of grain size and porosity were studied on Ti_3SiC_2 polycrystalline samples. Highly textured, coarse-grained Ti_2AlC polycrystalline samples were used to study the effect of texture on KNE behavior.

All MAX phase samples were fabricated by hot pressing (HPing) starting with pre-reacted MAX phase powders (3-ONE-2, Voorhees, USA) wrapped with graphfoil inside a graphite die placed in a vacuum atmosphere hot press, HP, (Series 3600, Centorr Vacuum Industries, Somerville, MA). The heating and cooling rate was 10ºC/min and a uniaxial load corresponding to a stress of ≈ 45 MPa was maintained at the maximum processing temperature of 1500 °C. The holding times for the Ti_3SiC_2 and Ti_2AlC samples was 4 h; that for Ti_2SC was 5 h.

After the graphite die cooled to room temperature, the MAX phase billet was ejected and the graphfoil removed from the billet surface. The Ti_2AlC powder used is flake-like. To fabricate a textured sample, an amount of the flake-like powder is poured inside the graphite die and the whole die is mechanically tapped for ~ 10 minutes to align the flaky particles. This process is repeated consecutively until the graphite die is filled

with the powder to be HPed. However, since this technique is done manually, the texture obtained is not perfect; a small percentage of grains will not be oriented.

And finally the 5% porous Ti_3SiC_2 was fabricated by reactive Hot Isostatic Pressing (HIPing) a stoichiometric powder mixture of titanium (-325 mesh, 99.5%, Alfa Aesar, Ward Hill, MA), silicon carbide (-400 mesh, 99.5%, Atlantic Engineering Equipment, Bergenfield, NJ) and graphite (-300 mesh, 99%, Alfa Aesar, Ward Hill, MA) at 300MPa and 1600ºC for 8 h [53].

The grain sizes of the HPed samples were small. To grow the grains the MAX phase was annealed in high purity Ar atmospheres in a tube furnace. The Ti_2SC was annealed at 1600 ºC for 20 h resulting in a fully dense sample (4.59 g cm^{-3}) with random texture that contained < 6% volume % anatase and TiC and had an average grain size of approximately 8 μm as determined by the line intercept method.

The fine grained (FG) Ti_3SiC_2 sample used is from the billet sample produced directly from HPing with an average grain size of ≈ 15 ± 3.5μm. The coarse-grained (CG) Ti_3SiC_2 was produced by annealing the FG samples at 1600 ºC for 10 h. The final grain size was ≈ 100±17 μm and the sample contained < 7.9 vol. % TiC. As the annealing temperature or holding time increased, more TiC formed in the MAX phases[54]. Coarse grained textured Ti_2AlC samples were obtained by annealing in an Ar atmosphere at 1450 ºC for 12 h resulting in a fully dense (4.1 g/cm^3) sample, with a final average grain diameter of 60 ± 40 μm and a thickness of 25 ± 10 μm (Values after ± symbol indicate the standard deviation in each sample).

The density and composition of the HPed billet samples were verified using Archimedes' method and X-ray diffraction, XRD, (Model 500D, Siemens, Karlsruhe,

Germany, with Cu Kα radiation at 40kV and 30 mA), respectively. For Ti_2AlC, the XRD measurements were used for composition determination and texture confirmation. The intensity of the 000l planes is highest in one of the textured samples relative to the other and in the random texture Ti_3SiC_2 as well. In addition, optical microscope, OM, images were obtained after sectioning, mounting, and polishing down to 0.5 μm, and etching using a H_2O:HNO_3:HF etching solution with a 1:1:1 volume fraction for 10 s.

Figure 5-1 shows OM images of the Ti_2SC, Ti_3SiC_2 and textured Ti_2AlC bulk samples used in this study. The MAX phases billet samples were electro-discharge machined (EDMed) to bulk cylinders (30 mm high, 9 mm diameter) for further in situ mechanical tests. Two cylinders from the *same* HPed billet were EDMed for the textured Ti_2AlC. One sample, henceforth referred to as N-sample, was machined such that the basal planes were "Normal" to the loading axis. The other sample, referred to herein as the P-sample, was machined such that the basal planes were loaded edge-on ("Parallel").

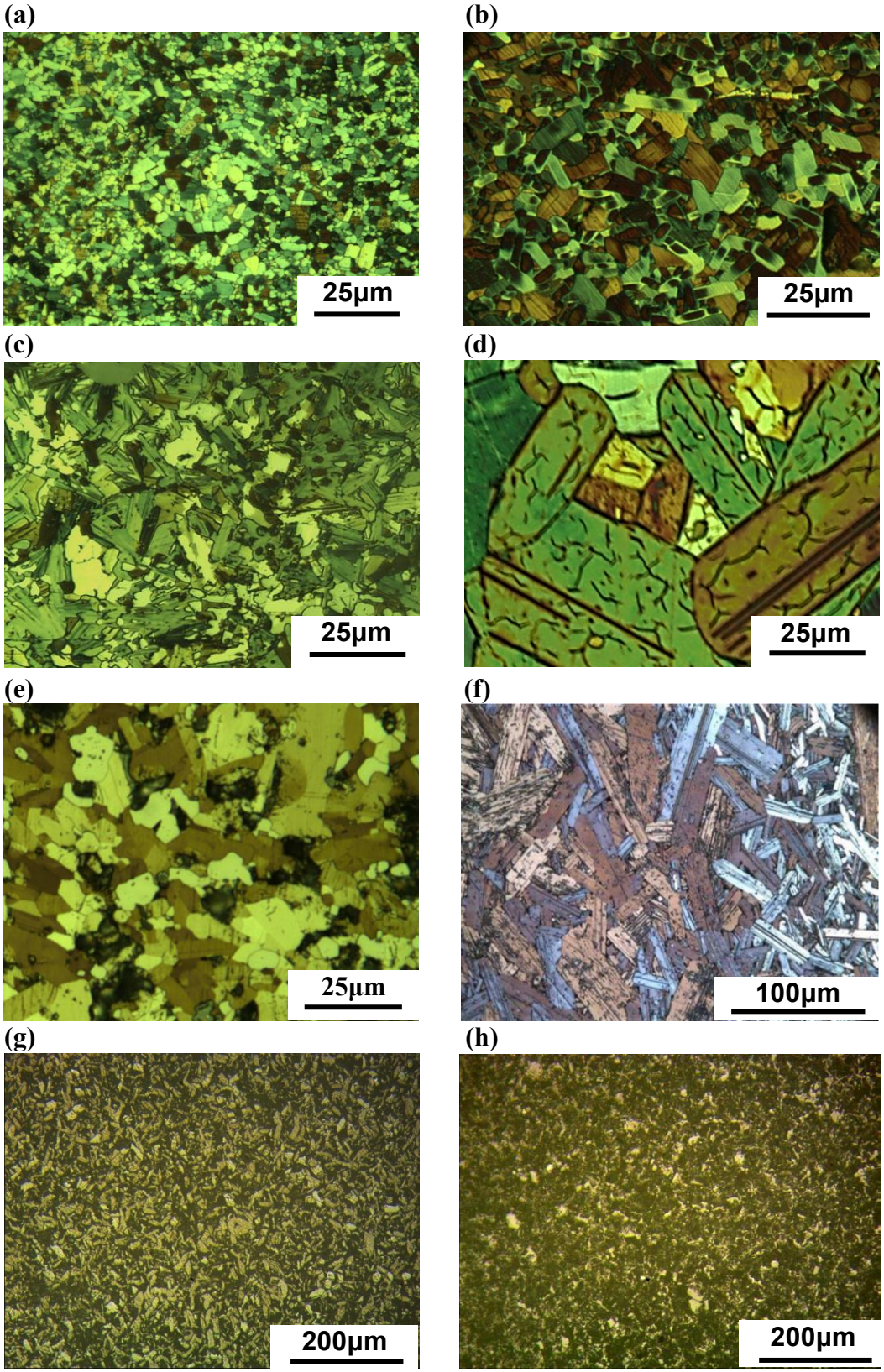

Figure 5-1: Microstructures of the MAX phases used in this study: (a) FG Ti_2SC, (b) CG Ti_2SC, (c) FG Ti_3SiC_2, (d) CG Ti_3SiC_2, (e) Porous Ti_3SiC_2, (f) CG Textured Ti_2AlC, (g) FG Alumina, (h) CG Alumina.

5.1 MAX phases mechanical behavior

The mechanical response of the MAX phases investigated are shown in Fig. 5-2 illustrating the variations in stress-strain response of, a) Ti_2SC (a), b) FG & CG Ti_3SiC_2 and (c) the textured Ti_2AlC samples. Figure 5-2(d) schematically shows the relationship of the basal planes (shown as thin black lines within each grain) in the various grains to the vertically applied compressive stress for the textured Ti_2AlC. Figure 5-2(d)(i) is a schematic of what will henceforth be referred to N-sample because the majority of the grains have their basal planes normal to the loading direction. Figure 5-2(d)(ii) will henceforth be referred to P-sample because the majority of the grains have their basal planes parallel to the load direction. The minority fraction of grains, that are oriented in all other directions are depicted in red and blue.

For investigating the textured Ti_2AlC samples it is vital to differentiate between “hard” and “soft” grains. The former are ones for which the resolved shear stresses, RSS, on the basal planes is low, and vice versa for the latter. Because their c/a ratios are high (3 to 5), neither non-basal dislocations nor twins have been implicated in the deformation of the MAX phases. Referring to (i) and (ii) in Fig. 5-2(d), it is clear that in both microstructures the majority of grains - represented by the black and red grains - are hard. However, from the macroscopic stress-strain relationships of the N- & P-samples in Fig. 5-2(c), it could be deduced that the P-sample is "stiffer" than the N-sample, since at the same stress level the P-sample accommodates a lower strain level and half the amount of energy dissipation (P-sample energy dissipation is $0.136MJ/m^3$, and $0.267MJ/m^3$ for the N-sample Fig. 5-2(c)). Therefore, it is concluded that the RSS on the basal planes that are parallel to the loading direction in the P-sample, (black grains in Fig. 5-2(d)(ii), which

represent the majority), is lower than on the majority basal planes in the black grains in the N-sample (Fig. 5-2(d)(i)), that are normal to the loading direction. Conversely, the opposite is true for the red grains in the N- & P-samples as well. The blue colored grains, on the other hand, are soft. It follows that these grains are the ones for which the RSS are the highest and therefore would demonstrate the highest deformation level of all grains.

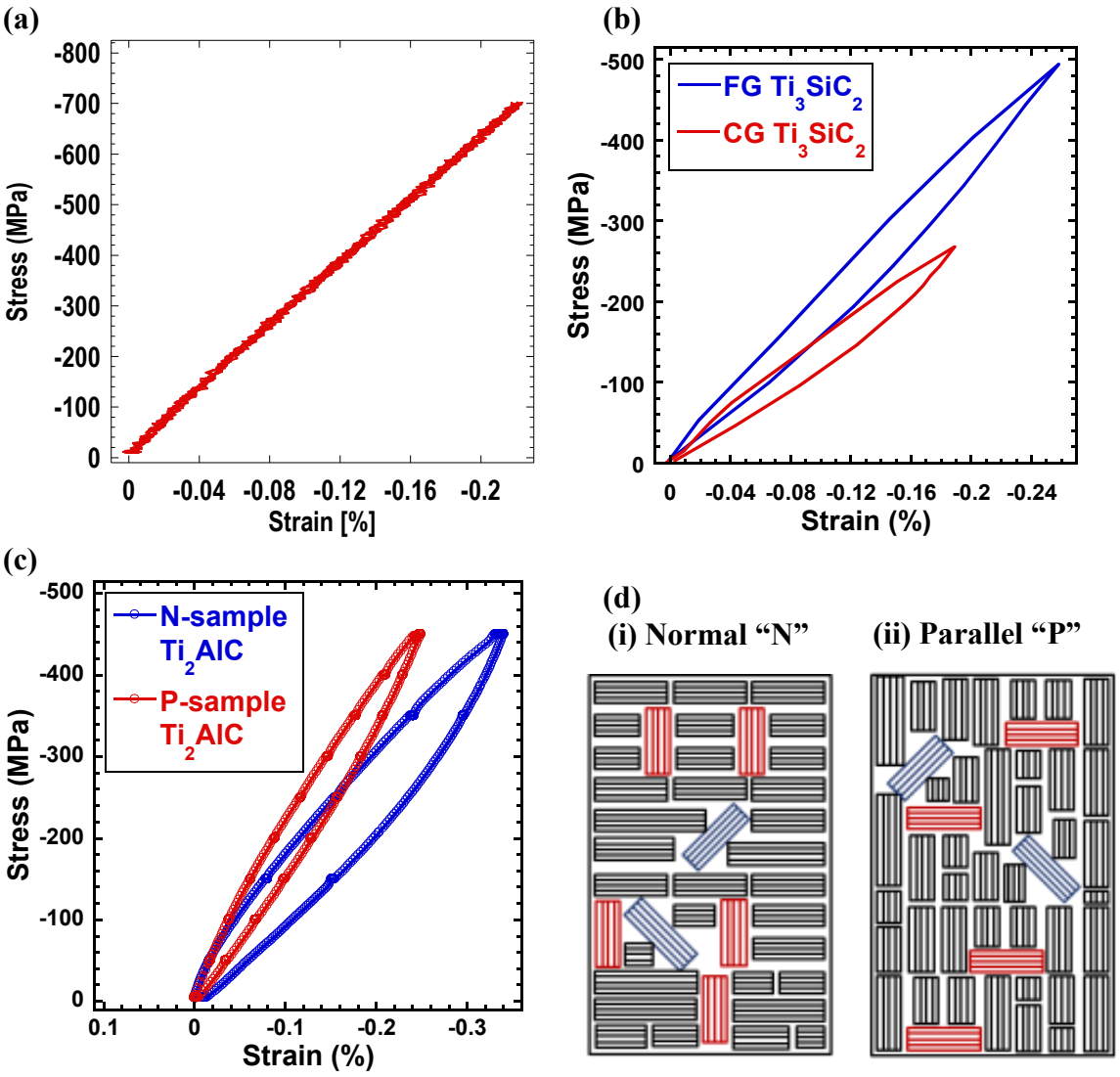

Figure 5-2: Stress-strain curves for: (a) CG Ti_2SC. (b) FG & CG Ti_3SiC_2. (c) Ti_2AlC N-texture (blue circles) and P-texture (red circles) samples. Both stress and strain axes are reversed to render the plots similar to conventional tensile stress-strain curves. (d) Schematic representation of a sample whose majority of grains have their basal planes i) normal "N" or ii) parallel "P" to the compressive loading direction.

5.2 Summary and Conclusions

The aim of this chapter is to report on the processing and characterization of the samples fabricated, in addition to the characteristics of the purchased samples. The MAX phase's fabrication conditions were selected to obtain high purity samples. The presence of multiple MAX phases, in addition to the percentage of impurities created due to the decomposition of MAX phases during annealing was traced using XRD.

The OM images are typical for the materials observed. Mechanical tapping performed during fabrication of the textured Ti_2AlC samples was done to induce a strong texture. The mechanical response of the MAX phases ensured their fabrication quality by illustrating pronounced differences between the mechanical behavior of FG and CG Ti_3SiC_2 and the textured Ti_2AlC samples.

Chapter 6: In situ Experimental Techniques Used

The dislocation mechanism associated with KNE mechanical response, where energy is dissipated with every loading cycle without causing any permanent plastic strain has to date not been embraced by most. The Incipient Kink Band (IKB) model developed by Barsoum *et al.* [19] is the latest proposed mechanism for this remarkable mechanical behavior. Various experimental techniques could be used to obtain information about the dislocation mechanisms active in KNE materials from different perspectives. However, a comprehensive understanding of the KNE mechanism can only be obtained by employing *in situ* techniques that probe the sample during mechanical loading/unloading and reversible dislocation activity. Compressive stress mode has been selected since the stress-strain loops are significantly larger

In situ Neutron Diffraction (ND) technique that has previously illustrated information about dislocations is to be employed here. In this section the theory behind the characterization technique is elucidated. The technique yields information about dislocations in the bulk of the samples. During *in situ* ND, the sample is irradiated by a neutron beam that is transmitted through the bulk. The information one obtains are the elastic strains of various crystallographic planes. Rather than just having a phenomenological description of the lattice planes, the Elasto-Plastic Self Consistent (EPSC) model is used (section 6.1.1), assuming selected twin or slip systems, to predict how the elastic strains of the various crystallographic planes vary with applied load.

6.1 In situ Neutron Diffraction (ND)

C. Shull and B. Brockhouse Nobel prize winners in 1994 stated: “Neutrons tell you where the atoms are and what the atoms do”[55]. Due to the large amount of information obtained using ND, today it serves communities as wide as Biology, Earth Sciences, Planetary Science, Engineering, Nanoscience, and Cultural Heritage.

In situ neutron diffraction (ND), wherein a sample is loaded while neutron diffraction measurements are performed, is a powerful technique that has been used successfully to probe the deformation of many crystalline solids. The main advantage of ND is the large penetration depth of the neutrons that, in turn, provides bulk information during deformation. Deformation on a macroscopic scale (more or less homogeneous in a sample), causes diffraction peak shifts. These shifts reflect the changes in interatomic distances in the material[56]. Profile-form analysis from the broadening of the peaks can also be used to depict information about crystal lattice distortion due to dislocations or concentration gradients[57]. Whole-pattern and single-peak based deconvolution can then be used for deconvolution of the diffraction patterns via Rietveld analysis.

The engineering time-of-flight (TOF) neutron diffractometer instrument, Spectrometer for Materials Research at Temperature and Stress (SMARTS), at the Lujan Neutron Scattering Center (LANSCE), Los Alamos National Laboratory (LANL)[58] was used to perform the *in situ* ND measurements under uniaxial compressive stress. The equipment records multiple lattice plane *hkl* reflections for a specific sample orientation. During the compression experiment, neutron diffractograms are obtained at predetermined load intervals. The elastic lattice strains were calculated from the changes in the spectra peak positions given by (Eq. 4):

$$\varepsilon^{hkl} = \frac{d^{hkl}}{d_0^{hkl}} \tag{4}$$

where ε is the elastic lattice strain due to sample deformation, d the *hkl*-dependent d-spacing of the deformed sample at a certain load level and d_0 the d-spacing of the un-deformed sample. The calculated elastic lattice strains represent the average of all grains that satisfy Bragg's law. Bragg diffraction is a specular diffraction effect that occurs when a wave is incident on the planes of a crystalline solid. The condition for Bragg diffraction is:

$$\lambda = 2d^{hkl}\sin\theta \tag{5}$$

where λ is the beam wavelength and θ is the angle of the diffracted wave.

In ND experiments, a spallation source is used were neutrons are produced with different energy levels. The neutrons bombard the sample at a fixed angle but with variable wavelengths. The neutron wavelengths are obtained from measurement of their flight times using the De Broglie relationship:

$$\frac{h}{\lambda_n} = m_n \mathrm{v} = \frac{m_n L}{t} \tag{6}$$

where h is Planck's constant (6.626 $X10^{-34}$ m^2kg/s), λ_n is neutron wavelength, m_n neutron mass (1.675$X10^{-27}$ kg), v is the neutron speed (m/s) , L is total path length, t is their time of flight, TOF. In each ND instrument there are detectors arranged in different fixed positions around the sample that collect the scattered intensities simultaneously. Hence, diffractograms of d-spacing versus intensity are obtained.

A schematic of the SMARTS setup is shown in Fig. 6-1. The longitudinal and transverse elastic lattice strains are measured simultaneously, using two detector banks at

± 90° from the incident beam while the sample is oriented at 45° to the incident beam. The orientation of the sample relative to the incident beam and the two detectors is the key to acquiring information about the crystallographic planes dynamics along the length and width of the sample. The incident neutron beam is directed on the 45° inclined sample. The longitudinal bank detectors receives the diffracted neutrons from the sample resulting from the scattering vector longitudinal to the sample (Q_L). The transverse bank detectors, on the other hand, receive the diffracted neutrons from the sample resulting from the scattering vector transverse to the sample (Q_T). The importance of this setup is that each detector bank reveals information about grain deformation in different orientations with respect to the length and width of the sample through the diffraction of the corresponding crystallographic planes. This feature is very crucial in analyzing the diffractograms especially textured samples. In this study, Rietveld analysis was performed on all diffractograms from the longitudinal and transverse banks to obtain the lattice parameters, in addition to single peak fits for all possible peaks to trace their shifts during loading/unloading.

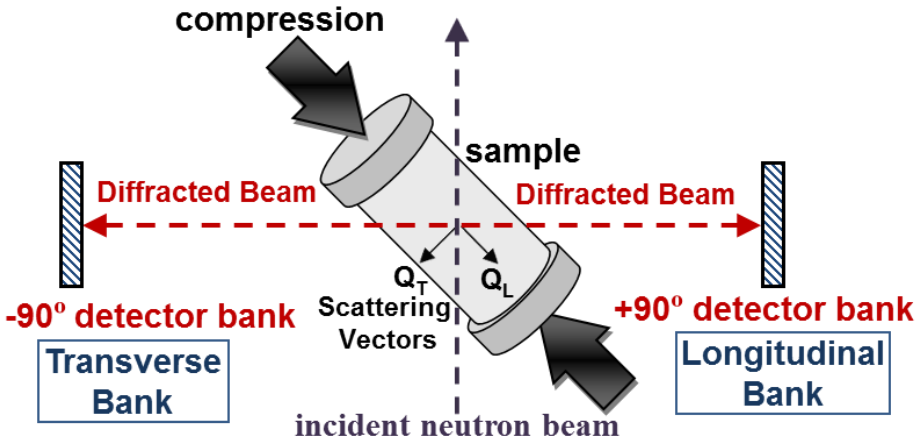

Figure 6-1: Schematic of sample configuration relative to incident neutron beam, detectors (Bank 1 - Transverse; Bank 2 - Longitudinal), and loading direction in SMARTS. Q_L is the longitudinal scattering vector resulting from the diffraction beam directed to the longitudinal bank, and Q_T is the transverse scattering vector resulting from the diffraction beam directed to the transverse bank.

The texture of the tested sample is obtained from the diffractogram results of the longitudinal and transverse banks of SMARTS. However, a more complete picture could be obtained if there are multiple detectors at all possible angles sensing the diffracted beams from all sample grains. This could be obtained using the HIgh Pressure Preferred Orientation (HIPPO) neutron diffractometer at LANSCE, LANL[59]. This instrument has circumferential detectors at 10º, 20º, 40º, 90º and 150º outlying from the sample. The texture file generated from the diffractogram of all angle banks is used to produce the pole figures of the sample grains' orientations.

In the past decades researchers investigated the details of dislocation nucleation and motion by slip and twinning during deformation. Any deformation that occurs in a material is governed by the shear stresses resulting from the applied load. If the shear stresses in a grain or crystal exceed a critical resolved shear stress (CRSS) and/or twin threshold (TT), dislocation slip and/or twinning will take place. The maximum amount of shear stress on a sample during tension or compression is at 45º. The resulting shear stresses, at different locations in the material, are transferred to the grains. The deformation of the grains depends on the direction of the shear stresses relative to the grains orientation. If a sample's texture is random, the probabilities of activating a specific slip system or twin activity depend solely on the RSS in the various grains. However, if the sample is textured, specific slip or twinning systems can be suppressed and/or promoted.

The amount of dislocation pile-ups and their motion, sources of dislocation multiplication or annihilation, size and shape of twins, amount of strain accommodated and amount of residual strain, all depend on the shear stresses applied on an individual

grain. In order to make sense of the ND results, the EPSC model – described in the next section - is not only used to predict the overall bulk response of a sample with a given texture, but, as importantly, the elastic strains on the various planes.

6.1.1 Elasto-Plastic Self-Consistent Model (EPSC)

The EPSC model [60] has been used to simulate the mechanical response of various materials yielding good agreement with *in situ* ND experimental data [61-63]. The EPSC treatment of grains agrees well with the experimental results obtained from the ND. The EPSC treats grains as elasto-plastic spherical inclusions in an infinite elasto-plastic homogenous matrix. The matrix modulus is equated to the average polycrystal moduli computed from the single crystal elastic constants of all grains in the model (the orientation of the grains is taken into account in this computation). Considering the large sampling volume of ND measurements, the diffraction data also averages over many grains. Unlike the upper bound Taylor and lower bound Sach models, [61] EPSC incorporates elastic and plastic anisotropy between matrices and inclusions. This is of particular importance when applying EPSC to the MAX phases due to their anisotropic plastic behavior. The constraint imposed during application of the EPSC method is that the average of the stress and strains of all modeled grains are equal to the total stress and strain of the sample [64]. The model performs iterations to fulfill this constraint.

6.1.2 Experimental Details

In MAX phases, the basal plane is the close-packed plane. Hence, all peaks on the diffractograms generated from neutron diffraction represent the basal planes orientations

in the samples. Therefore, each peak represents a group of grains in the sample with a specific orientation. In the highly textured samples, as the CG Ti_2AlC N- and P-samples, the intensity of the basal planes is high due to the high concentration of basal planes in a specific orientation. This is observed in Fig. 5-2(d) schematics of N- and P-samples. Thus, the 0004 peak from the longitudinal bank diffractogram for the CG N-sample can be used to calculate the d-spacing between the basal planes of all majority grains that are normal to the loading direction (longitudinal bank detects the scattering vector along the sample length). On the other hand, the 0004 peak in the transverse bank for the CG P-sample can be used to calculate the d-spacing between the basal planes of all majority grains that are parallel to the loading direction (transverse bank detects the scattering vector along the sample width). Accordingly, the same is true for all peaks studied; e.g. the $\{10\bar{1}5\}$ peak on the longitudinal bank represents the d-spacing between the $\{10\bar{1}5\}$ planes (which are the grains having their basal planes at ~ 45º from sample horizontal), while the transverse bank represents d-spacing behavior of those grains along the basal planes.

As noted above three MAX phases were tested using in situ ND and the EPSC model to investigate their different characteristics. Ti_2SC was deliberately chosen, which is the only MAX phase known to date that does not kink and whose response is thus fully linear elastic when a bulk sample is tested [51]. Since this was the first in situ diffraction study of any MAX phase, the first goal was to test whether the EPSC model— restricted to the elastic regime by excluding all slip and or twinning modes — can be used to model the response.

The FG and CG Ti_3SiC_2 samples have different KNE mechanical response (Fig. 5-2(b)). The CG Ti_3SiC_2 sample demonstrates nonlinear strain before the FG Ti_3SiC_2. It also demonstrates a maximum stress level that is much lower than FG Ti_3SiC_2 and exhibits a larger damping capacity when both are subjected to the same stress level. FG and CG Ti_3SiC_2 samples were tested to investigate the effect of these variations on the mechanical behavior of the material at the crystal level. Finally the N- and P-sample textured Ti_2AlC were tested to study the grains responsible for the different damping capacities observed in their mechanical response at the same stress level (Fig. 5-2(c)). Pole figures of the Ti_2AlC textured samples were generated and the texture files were used as inputs for the EPSC model.

EPSC, however, was never used to predict the mechanical behavior of KNE solids and this research is, to the best of our knowledge, the first applications of EPSC modeling to the MAX phases.

There are several variables and input files needed for the implementation of the model. The single crystal files include information about the material space group, lattice parameters, thermal expansion coefficients, single crystal elastic stiffness constant matrices and all possible slip and twin systems that can occur in the material during deformation. The texture file includes the axes of representative ellipsoid illustrating the morphology of the grain shape, number of assumed grains and the information about the orientation of the grains. The model is executed by activating the anticipated slip and/or twin system and inserting the critical resolved shear stress (CRSS) and/or twin threshold (TT) stress in addition to the hardening parameters (HR) resulting from the active dislocation mechanism(s).

The model result is a macroscopic stress-strain curve that can be compared to the experimental outcome from the instrument's load cell and extensometer. A curve fitting exercise is performed by comparing the two loading curves visually and adjusting the model parameters (CRSS, TT and HR) such that both curves overlap. There are a lot of possible parameters that can be used to obtain good fits. For example, dislocation slip is usually the first active mechanism after elastic deformation. The CRSS can be determined when the model prediction deviates from the experimental elastic region. However, there could be more than one active slip system. What is the CRSS for the second slip system? What is the hardening parameter for each slip system? The introduction of twin activity makes the matter even more difficult. The EPSC model has a feature of operating two hardening parameters (HR1 and HR2). There is a transition stress range to shift from the initial to final hardening parameter that is used to model curvatures in the plastic regime. This feature adds another complication for the macroscopic stress-strain curve fitting exercise and the resulting plane reflections.

Assumptions were made concerning the selection of the active dislocation mechanism(s) for fitting the macroscopic stress-strain curves of the different MAX phases modelled. The mechanical response of the textured Ti_2AlC and random Ti_3SiC_2 samples were modeled using the EPSC approach assuming basal slip and/or $[11\bar{2}1]$ tensile twin activation. The former was selected since the IKB microscale model has edge dislocation active on the basal plane [2, 19] (Figure. 6-2) and it is well established that basal slip and only basal slip is activated in the MAX phases at all temperatures. The $[11\bar{2}1]$ twin was chosen to represent an IKB since this twin is a special case of a kink boundary, where a basal plane dislocation is nucleated every c-lattice parameter [65].

As noted above, Ti_2SC was chosen since its response is fully linear elastic. It is the first MAX phase to be tested using SMARTS and the goal was to test whether the EPSC model approach — restricted to the linear elastic regime by excluding all slip/twin modes—can be used to model the response. Note that the EPSC model in its current form provides no description of IKBs and/or the observed reversibility. It is nevertheless a unique tool to investigate the mechanical behavior on a crystal plane level so that the effect of slip and twinning systems can be studied and compared to the measured mechanical response of the MAX phases.

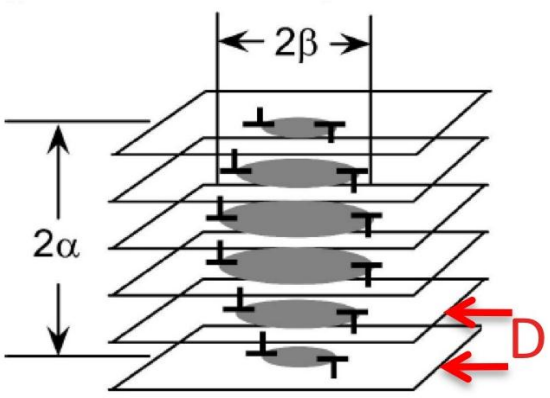

Figure 6-2: Schematic of a series of IKBs formed on basal planes[2].

To explore what possible mechanisms can account for the entire set of observations presented here, EPSC calculations were carried out by activating either DP, or $\{11\bar{2}1\}$ twin formation, or combinations thereof. Both the overall and elastic strains on the various planes are then compared to the experimentally observed ones. When comparing all EPSC calculations and the experimental results, three discrepancies are immediately apparent. The EPSC model does not model IKBs. The only argument that can thus be made on behalf of the IKB-based model is one of elimination. In other words by showing that the bulk and micro-stress-strain curves *cannot* be fit by the EPSC model

that takes $\{11\bar{2}1\}$ twins and/or dislocation pile-ups into account, the latter two cannot explain what is observed and can thus be safely eliminated as plausible mechanisms.

Each MAX phase has different crystal structure lattice parameters. Therefore, the angles between the different crystallographic planes and basal plane are different for each MAX phase. The bulk mechanical behavior of Ti_2SC is linear elastic, hence, the planes studied are: the basal plane, 0001 and a plane orthogonal to the basal plane, such as $10\bar{1}0$, and $10\bar{1}1$ representing a plane between the two extremes. However, for the highly textured Ti_2AlC and random textured Ti_3SiC_2 several planes where investigated. Table 6-1 shows the angles between the selected planes investigates in Ti_2AlC and Ti_3SiC_2 and basal plane.

Table 6-1: Angles between selected planes investigated in Ti_2AlC and Ti_3SiC_2 and basal plane.

	{0001}	$\{10\bar{1}0\}$	$\{10\bar{1}1\}$	$\{10\bar{1}2\}$	$\{10\bar{1}3\}$	$\{10\bar{1}5\}$	$\{10\bar{1}7\}$
Ti_2AlC	0	90	79	68.76	59.85	45.82	36.31
Ti_3SiC_2	0	90	81.45	73.27	65.73	53.08	43.54

Chapter 7: Linear Elastic & Textured MAX Phases In situ ND and EPSC Results

7.1 Linear Elastic Ti_2SC In situ Neutron Diffraction Results

The ternary compound Ti_2SC is a member of the layered crystal structure MAX phase family. It possesses the finest MAX phase grain size of 2-3 μm as received after HPing. In addition, it has the lowest anisotropic crystal structure aspect ratio in all MAX phases of 3.5. As noted above, the MAX phases deform by kinking, however, Ti_2SC is the only MAX phase that does not kink and whose response is fully linear elastic when a bulk samples is tested [51]. Figure 7-1 compares the mechanical behavior of bulk linear elastic Ti_2SC and the KNE response of FG Ti_3SiC_2. Nevertheless, at the grain level when examined using a nanoindenter, KNE mechanical response was observed in Ti_2SC [52].

Here *in situ* ND results of fine-grained (8 μm) polycrystalline titanium sulfocarbide sample loaded to 700 MPa is reported. The overall strains, and those on individual planes, are modeled via the ElastoPlastic Self-Consistent (EPSC) approach using elastic constants derived from *ab initio* calculations. Based on the results, it is concluded that the response at stresses below 1 GPa, is, for the most part linear elastic and that when the theoretical elastic constants are combined with the EPSC method, accurate predictions can be obtained of both the overall stress–strain curves and, more importantly, the 0001, $10\bar{1}1$ and $10\bar{1}0$ reflections.

The long-term goal was to prove the existence of reversible dislocations using ND. The goal of this experiment, as a first step, is to show the accurate EPSC model prediction of a linear elastic KNE solid. Since this is the first in situ diffraction study of any MAX phase, the first goal was to test whether the EPSC model approach—restricted to the elastic regime by excluding all slip modes—can be used to model the response. To

carry out the EPSC simulations, single-crystal elastic constants are required, and since there are no experimental values of the latter available, the values in literature derived from ab initio calculations listed in Table 7-1 were used. The variations between the results reflect the different approximations made. The local density approximation (LDA) results of Bouhemadou and Khenata [66] are higher than those using the generalized gradient approximation (GGA). The EPSC model was run — without activating any slip or twin systems — up to the measured strain levels, for both loading and unloading. No significant deviation from a fully random texture was observed.

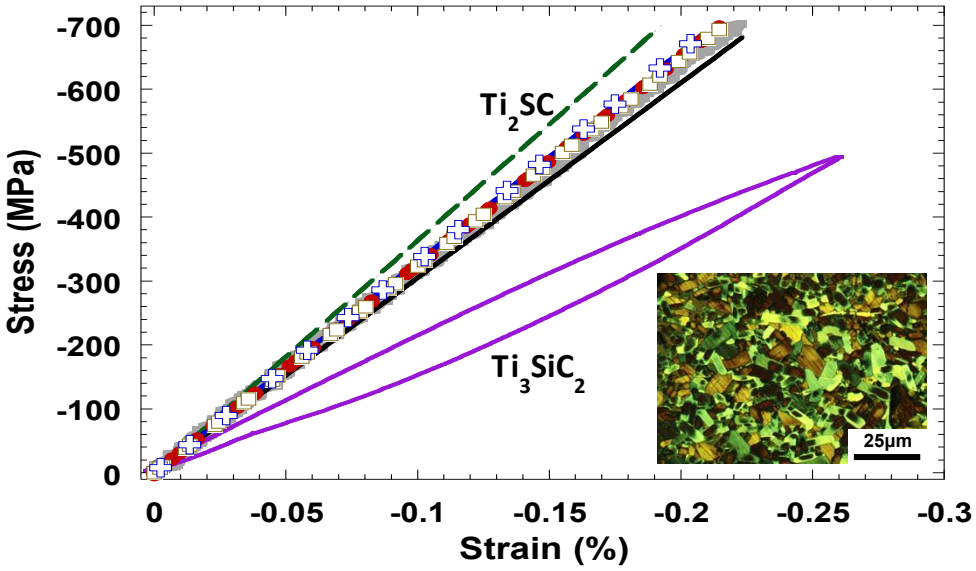

Figure 7-1: Stress–strain curves of Ti_3SiC_2 and Ti_2SC. The macroscopic stress–strain curve for the latter, on loading and unloading, is depicted as a thick gray line. The results of the EPSC model using the results of Bouhemadou and Khenata [66], Du et al.[67] , Cover et al. and Scabarozi et al.[68, 69] are plotted, respectively, as dashed line, open squares, filled diamonds and blue crosses. Inset shows an etched optical micrograph of the sample used.

Table 7-1: Elastic constants, C_{ij} (in GPa) for Ti_2SC used in the EPSC model.

C_{11}	C_{12}	C_{13}	C_{33}	C_{44}	C_{66}	Comments
368.0	108.0	123.0	395.0	189.0	130.0	Bouhemadou and Khenata.[66] (LDA)
331.0	98.0	97.0	384.0	157.0	117.0	Cover et al.[70] (GGA)
319.0	101.0	106.0	351.0	149.0	109.0	Cui et al. [71] (GGA)
336.0	106.0	99.0	348.0	163.0	115.0	Du et al. [67] (GGA)
339.0	90.0	100.0	354.0	162.0	125.0	Scabarozi et al. [68] (GGA)

Table 7-2 lists the bulk, shear and Young's moduli, as well as, the longitudinal and shear velocities computed from the elastic constants listed in Table 7-1 using the same equations and assumptions as Refs.[66-68, 70, 71]. The measured/calculated values in this work are in agreement with GGA approximations, especially with Scabarozi et al.[68, 69], while Bouhemadou and Khenata [66] illustrates a clear outlier for all parameters.

Table 7-2: Summary of sound velocities (m/s) and elastic moduli (GPa) in Ti_2SC and those predicted from the elastic constants listed in Table 7-1. Also shown are the values measured in this and previous work.

Long. velocity (m/s)	Shear velocity (m/s)	E (GPa)	G (GPa)	K (GPa)	Comments
8864	5713	363	150	162	Bouhemadou et al. [66] (LDA)
8216	5276	312	129	140	Cover et al. [72] (GGA)
8056	5155	300	123	136	Cui et al. [71] (GGA)
8194	5257	310	128	140	Du et al. [67] (GGA)
8197	5267	310	128	140	Scabarozi et al. [68] (GGA)
8200‡	5200‡	290	125	145	Scabarozi et al. [69], measured
8180±3‡	5248±7‡	295	129	137	This work; measured/calculated

‡ Measured

The macroscopic stress–strain curve for Ti_2SC obtained from the strain gauge is plotted along with stress–strain response of FG Ti_3SiC_2 (Fig. 7-1) as an example of typical KNE solid. The response of Ti_2SC appears to be—to a very good first approximation—linear elastic. Some nonlinear behavior may occur during very low loading, but these deviations are too small to be resolved. Neither permanent plastic strains nor loops are observed and the response is fully reversible. Figure 7-1 also plots the stress–strain curves calculated from the EPSC model using the c_{ij}s listed in Table 7-1. Comparing theory and experiment the following points are salient:

(a) For the most part the GGA results are in excellent agreement with each other, and with the experimental results.

(b) The LDA values (green dashed line in Fig. 7-1) result in stress–strain curves with slopes that are higher than experimental. Since this result [66] is the only outlier and does not fit the experimental results, it was not further considered.

(c) The resulting stress–strain curves obtained when the Young's modulus values calculated from the velocity of sound in this material (Table 7-2) are in excellent agreement with the stress–strain curves and the GGA results.

Figure 7-2(a) & (b) plot the 0001, $10\bar{1}1$ and $10\bar{1}0$ reflections on both loading and unloading (blue open circles) for the longitudinal and transverse directions and the EPSC model predictions using an average of the values listed in Table 7-1, excluding the results of Bouhemadou and Khenata[66]. Clearly, the agreement is quite good for the transverse and longitudinal strains.

At 316 and 327 GPa, the Young's moduli in the $[10\bar{1}0]$ and [0001] directions, respectively, calculated from the ND results, agree well with those predicted from ab

initio calculations, i.e. 324 and 337 GPa, respectively. Furthermore, at 0.215, the Poisson's ratio calculated from the in situ ND results is in excellent agreement with the value of 0.217 calculated from the EPSC model.

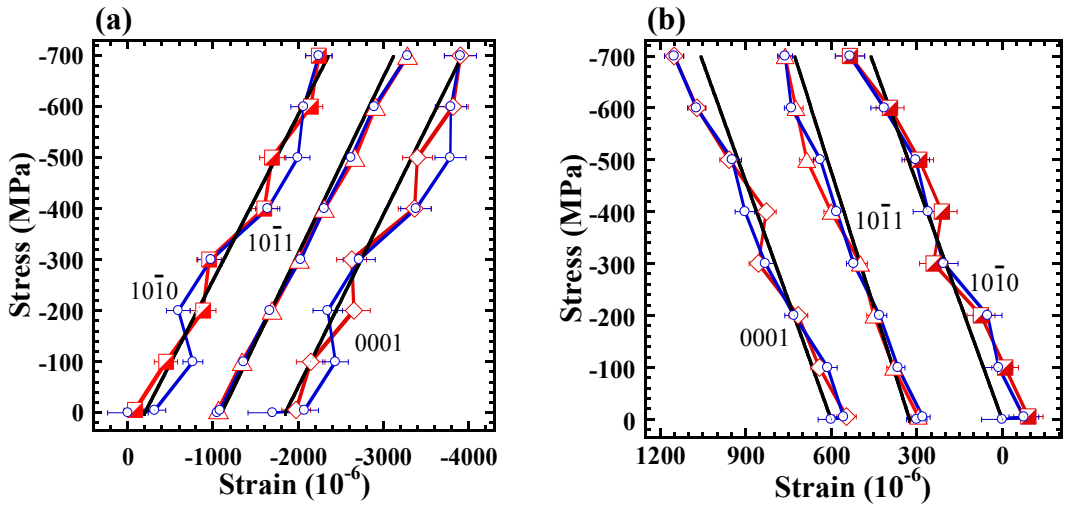

Figure 7-2: Stress-strain response along the (a) longitudinal and, (b) transverse directions to the compressive loading axis assuming linear elastic behavior given for the 0001, $10\bar{1}1$, and $10\bar{1}0$ reflections. The ND results are shown as data points; the EPSC model, as solid lines. The results are shifted for clarity. The results on loading are in blue while unloading in red.

The ND data were also used to extract the unit cell dimensions as a function of stress on loading and unloading. Within the studied load range, only a very marginal but fully reversible decrease in a and c can be observed, corresponding to a shrinkage of 0.4 vol.% per unit cell, which is in excellent agreement with the high elastic modulus of this ceramic. Figure 7-3 compares the normalized measured changes in a and c lattice parameters (data points) to those calculated from the ECPC model (solid lines) assuming the average of the elastic constants listed in Table 7-1, excluding Bouhemadou and Khenata's [66] results. Note again the excellent agreement between the two sets of results, confirming that the response is predominantly linear elastic and, as implied by that, fully reversible.

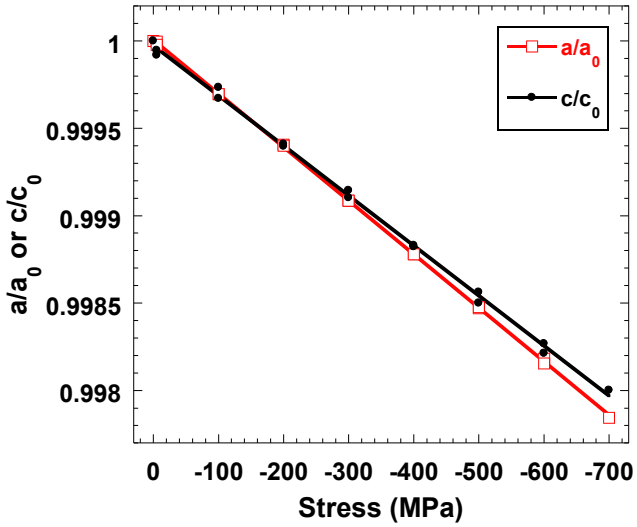

Figure 7-3: Variations in the lattice parameters, normalized by the values without load, as a function of compressive stresses on both loading and unloading.

Lastly, it is important to point out that at sufficiently high stress, even Ti_2SC will exhibit KNE behavior. This is best seen in Figure 7-4, where spherical nanoindentation stress–strain loops are obtained when polycrystalline Ti_2SC is repeatedly indented on the same location. The result of each indent is shifted for clarity. During the first cycle, at around 4 GPa, plastic deformation is observed. The nanoindenter is retracted from the surface and then indented into the same location five times at lower stress levels. All curves subsequent to the first indent (which effectively preconditions the sample) are fully reversible and, at higher maximum stresses (compared to 700 MPa in bulk Ti_2SC, Fig. 7-1), characterized by hysteresis loops (Fig. 7-4). This is strong evidence for KNE behavior and indicates a high threshold stress for reversible dislocations activation at the grain level. KNE closed loops are observed at high stresses; however, a reduction in loop width occurs as the stress applied decreases. Below about 1 GPa, no loops can be resolved and hence the behavior appears to be perfectly linear elastic. The latter is in full agreement with the macroscopic behavior of bulk Ti_2SC during static compression.

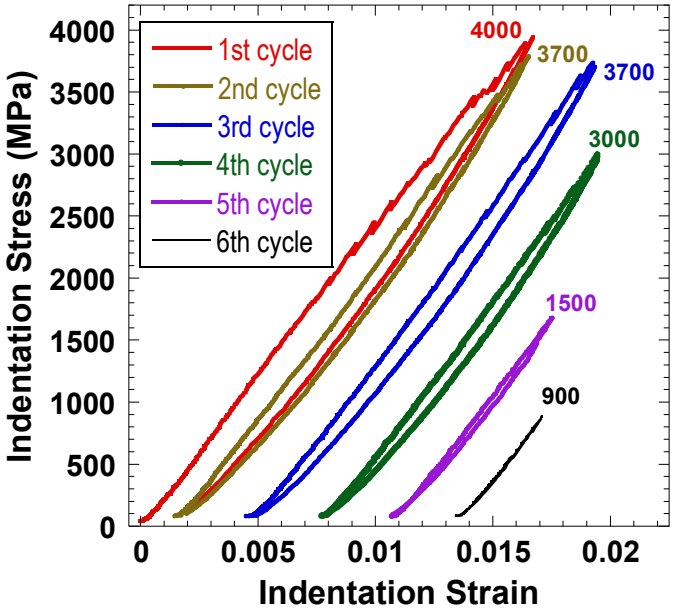

Figure 7-4: Spherical nanoindentation stress-strain of polycrystalline Ti_2SC of cyclic indents on the same location. The values given next to the stress-strain curves correspond to the maximum applied stress.

The main advantage of using nanoindentation to probe KNE behavior is its ability to apply large stresses on the sample surface. a. The difference between bulk mechanical compression and nanoindentation is in the vicinity of material affected during compression. Throughout compression of bulk materials, the whole sample is subjected to the stress applied, however, in nanoindentation the tip indents a minute region of the sample surface resulting in a localized effect on the grains in contact with the tip and some neighboring grains as well. The load applied creates a stress field in which its effect gradually decreases such that the grains at a distance from the tip are not affected. The volumetric size of the stress field created depends on many parameters including the material experimented, tip size, tip material & shape etc. The deformation mechanisms that are activated will influence the nanoindentation stress-strain response. The stresses applied during the nanoindentor exceed all elastic forces from the grains elastic stiffness constant matrix and surrounding grains as well. Such high stresses could not be reached

during conventional compression of bulk Ti_2SC. It is believed that during indentation of layered structured solids the response remains linear elastic until a grain layers' threshold is reached in which buckling is activated and kink boundaries nucleate. Figure 7-4 indicates the reversibility of the active dislocation mechanisms taking place. However, the layered grains on the sample surface in direct contact with the indenter are expected to develop permanent kink boundaries. They are responsible for the permanent plastic deformation observed in the first loading cycle. The fully reversible hysteretic stress-strain loops are believed to be due to buckling and de-buckling of the layered grains. The layered grains buckle during loading nucleating kink boundaries, and the energy stored generated enables de-buckling to take place during unloading.

7.1.1 Conclusions

In conclusion, for the first time, *in situ* ND results of a polycrystalline Ti_2SC sample loaded in compression to 700 MPa is reported. The response not only appears to be linear elastic, but is also well captured by the EPSC model calculations. The fact that the latter made use of elastic constants calculated from *ab initio* calculations is strong evidence for the validity of the latter.

The KNE mechanical response of Ti_2SC is only observed during nanoindentation experiments under high stresses. The polycrystalline layered grains behave in a linear elastic manner until a buckling threshold stress is reached and kink boundaries nucleate in the grains. It is believed that the reversible mechanical response is due to buckling and de-buckling of the layered grains during cyclic loading. However, further research is

needed to investigate the reversibility of the buckling dislocation mechanism occurring in layered structured solids

I would like to acknowledge the help of Justin Griggs for conducting nanoindentation tests and their analysis which was carried out at Drexel University's Centralized Research Facilities (CRF).

7.2 Textured Ti_2AlC In situ Neutron Diffraction Results

In this section careful analysis of *in situ* ND patterns obtained while cyclically loading highly textured polycrystalline Ti_2AlC samples, provides compelling experimental evidence for the existence of reversible dislocations in the form of fully reversible peak lattice elastic strain loops and peak widening and narrowing upon load cycling. It is further shown that dislocation pileups, DPs, are nucleated in grains that are well oriented for slip. Also, it is shown that because all dislocations, including those in the DPs, are confined to two dimensions, their motion is fully reversible. Given that KNE solids are ubiquitous in nature, the ramifications of this work on geology, metallurgy and other fields will prove quite important.

In 1934, Orowan, Polanyi and Taylor, roughly simultaneously, realized that plastic deformation could be explained in terms of the theory of dislocations. Since that time, dislocations, together with twinning, have been the two fundamental micromechanisms invoked to understand plastic deformation of most solids. In 2003 fully reversible and spontaneously stress-strain loops were observed when Ti_3SiC_2 cylinders were cyclically compressively loaded. At 1 GPa, the energy dissipated per cycle was roughly 25 % of the total energy.[73] This phenomenon named kinking nonlinear elasticity or KNE: Elastic because the process was fully and spontaneously reversible, nonlinear because the stress-strain curves were nonlinear (Figs. 7-5(a) & (b)) and kinking to emphasize that dislocations were involved.

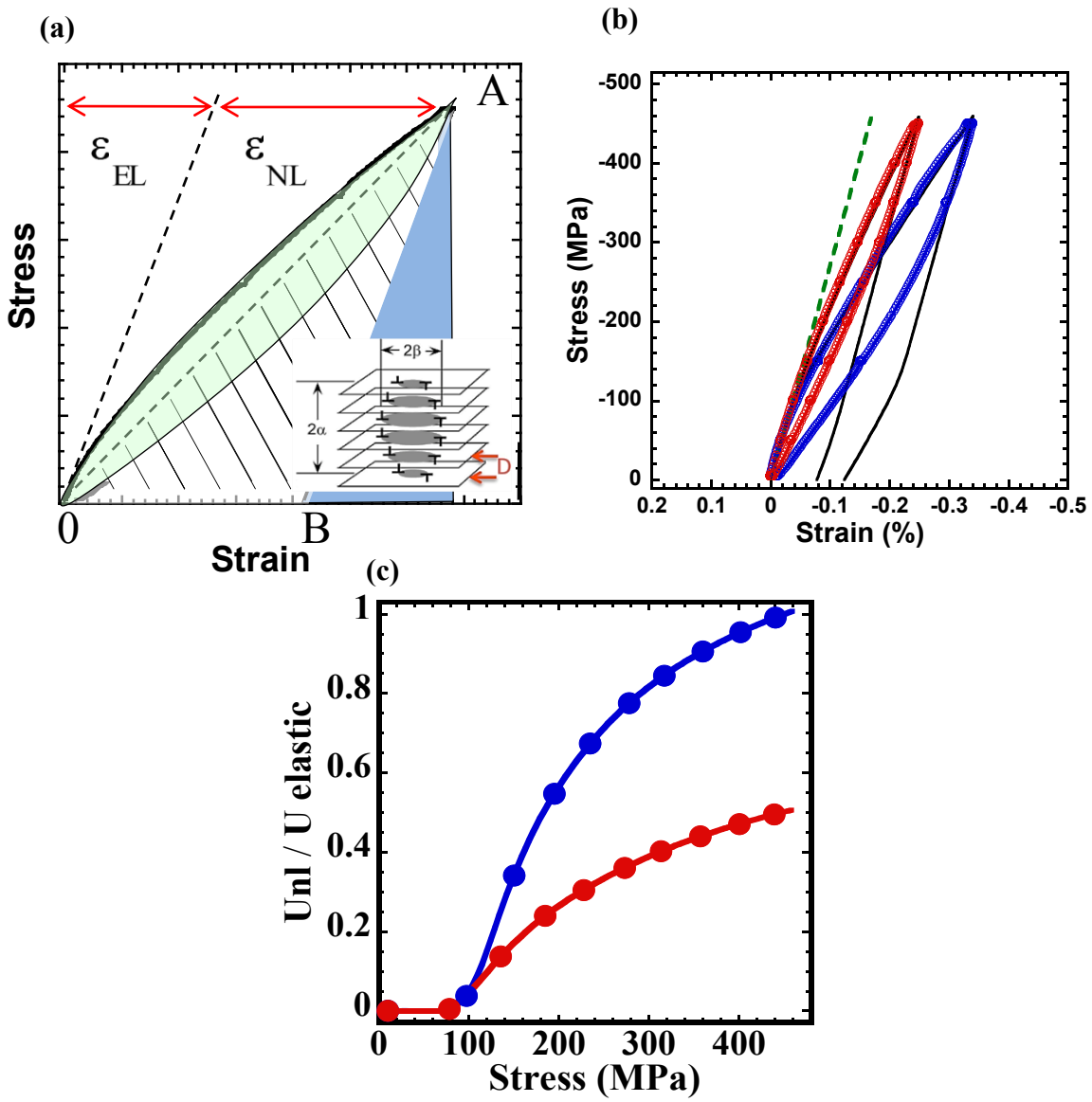

Figure 7-5: Stress-strain curves: (a) schematic showing the various parameters used in IKB model. The non-linear energy stored, U_{nl} at the maximum stress is given by hatched area; the linear elastic energy, U_{el} is given by blue triangle. Lower right corner inset shows schematic of prolate spheroid IKB formed on the parallel basal planes with D spacing between them assumed herein. (b) Stress-strain curves for "N" (blue circles) and "P" (red circles) samples and corresponding EPSC model prediction fits assuming either a purely linear elastic response (dashed line), or by activating basal slip, (solid black lines). Both stress and strain axes are reversed to render the plots similar to conventional tensile stress-strain curves. (c) Plot of U_{nl}/U_{el} for both loops shown in (b), using the same color code.

It was further conjectured that the micromechanism responsible for KNE behavior was the incipient kink bands or IKBs. The latter are multiple, co-axial parallel dislocation loops (lower bottom left inset in Fig. 7-5(a)) that only extend under stress; when the

stress is removed they disappear. It was also postulated that it is the to-and-fro motion of the dislocations comprising the IKBs that, in turn, gave rise to the energy dissipated per cycle per unit volume, W_d (green shaded area in Fig. 7-5(a)). Over the past decade it was shown that KNE solids are quite ubiquitous and exist in many types of solids: from graphite to mica, to hexagonal metals, to the MAX phases[74]. In 2005, a micromechanical model [75] was developed to explain KNE behavior in addition to several papers published thereafter presenting strong evidence for the existence of reversible dislocation motion[76-79].

However, to date, the evidence for the existence of IKBs has been unfounded and thus, not surprisingly, not embraced by the scientific community. The impossibility of IKBs observation using any characterization technique to date and its impermanent effect on the material after deformation (for any further post-deformation characterization), triggered uncertainty of the mechanism and micromechanical model developed. Nevertheless, Barsoum *et al.* [75] incorporated a significant feature in their model of the concomitant small shear angle, present on most cases, and shown here to be less than a degree. Therefore, an *in situ* approach is required. Herein *in situ* stress-strain neutron diffraction, ND, measurements, together with the Elasto-Plastic Self-Consistent (EPSC) modeling approach [60-63, 80] is used to shed light on the deformation of highly textured Ti_2AlC samples. The advantage of *in situ* ND measurements is the method's ability to probe the bulk's microscopic structural elastic response.

The ultimate purpose of this experiment was to prove, or disprove, the existence of IKBs and/or evidence for fully reversible dislocation motion. Herein two relatively coarse-grained, textured, Ti_2AlC polycrystalline cylinders are compressively loaded,

while *in situ* measuring their microscopic crystallographic response using ND. Figure 5-2(d) schematically show the relationship of the basal planes (shown as thin black lines within each grain) in the various grains to the vertically applied compressive stress. The black and red colored grains are hard, while the blue colored grains are soft. For example, in Ti_2AlC, the angle between the basal planes and the $\{10\bar{1}5\}$ normal is ~ 45°. It follows that these grains are the ones for which the RSS are the highest and therefore the ones that, as shown herein, demonstrate the highest reversible deformation level of all grains. Recall, the relationship between the neutron beam, detectors (Bank 1 - Transverse; Bank 2 - Longitudinal), and loading direction in SMARTS, at LANL, is shown in Fig. 6-1.

The pole figures of N- and P-samples measured on HIPPO also at LANL are shown in Fig. 7-6. Analysis of the ND data for texture determination, collected on HIPPO, revealed significant texture consistent with the predicted basal planes' orientations (compare Figs. 7-6(a)(i) and 7-6(b)(i)). The N-sample showed a maximal value of ≈ 6.1 random; the P, ≈ 4.6 times. In other words, the N-sample has more grains oriented normal to the loading direction compared to the grains oriented parallel to the loading direction in the P-sample. As expected from the experimentally observed texture, a minor, yet significant amount of differently oriented grains is also observed in both samples, as is exemplified by the pole plots for the $\{10\bar{1}5\}$ planes (Figs. 7-6(a)(ii) and 7-6(b)(ii)).

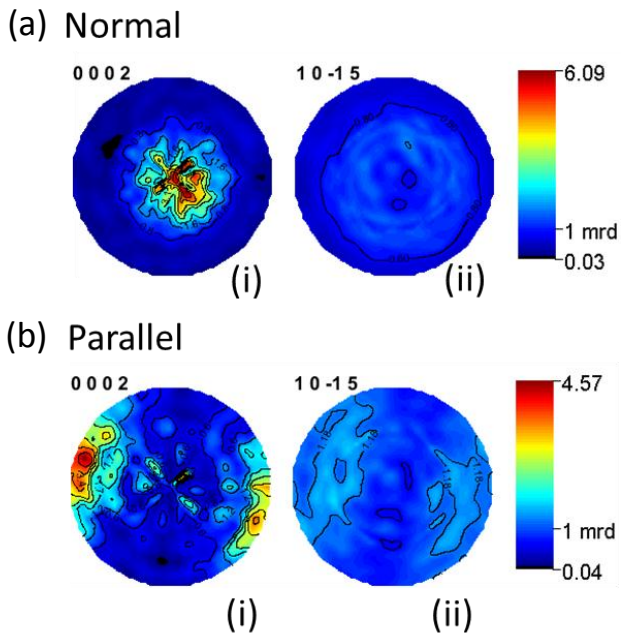

Figure 7-6: (a) Pole figures for (i) {0002}, and ii) $\{10\bar{1}5\}$ planes for N-sample. (b) same as (a) for P-sample.

Figure 7-5(b) plots the bulk stress strain curves for the N- and P-samples, represented by the blue and red loops, respectively. Also plotted on the figure are the EPSC model predictions. The EPSC model results - assuming linear elastic behavior only - are depicted by dashed lines (Fig. 7-5(b)). The elastic constants assumed were the average of six *ab initio* studies (see Table 7-3)[70, 81-85]. The black solid lines are the fits of the EPSC model assuming basal slip only. The critical resolved shear stress, CRSS, was assumed to be 35 MPa for both orientations. The hardening rates, however, were different (see Table 7-4). It is important to note here and elsewhere that because the EPSC model does *not* incorporate IKBs, it cannot capture the fully reversible deformation. Instead, the EPSC model predicts large residual elastic strains that is not observed experimentally.

Table 7-3: Ti_2AlC elastic constants from *ab initio* calculations (Refs. [70, 81-85]).

	C_{11}	C_{12}	C_{13}	C_{33}	C_{44}	C_{66}	Reference
	305	60	60	275	110	122.5	(Rosen et al., 2010)
	302	59	55	278	113	121.5	(Du et al., 2009)
	308	55	60	270	111	126.5	(Wang el al., 2004)
	321	76	100	318	144	122.5	(Sun et al., 2004)
	307	58	63	284	118	124.5	(Bouhemadou et al., 2007)
	302	62	61	269	109	120	(Cover et al., 2009)
Average Values Used	**307.5**	**61.7**	**66.5**	**282.3**	**117.5**	**122.9**	
Standard Deviation	**7.1**	**7.4**	**16.6**	**18.3**	**13.4**	**2.3**	

Table 7-4: Parameters used in the EPSC calculations. TwinVF is the Twin Volume Fraction; # of Twins is the value at the maximum strain; Max # Twins/Grain is the value at the maximum strain; Gradual is the range (in MPa) after the corresponding TTS, or CRSS where the HR changes linearily from HR1 to HR2. As an example, for Basal slip in Parallel, the HR changes from 23 MPa to 9.5 MPa in the RSS range of 35 MPa – 50 MPa.

		Initial # of grains	TwinVF	# of Twins	Max # Twins/Grain	TTS (MPa)	CRSS (MPa)	Gradual (MPa)	HR1 (MPa)	HR2 (MPa)
Basal Slip	Normal	15552	-	-	-	-	35	-	5.5	5.5
	Parallel	15552	-	-	-	-	35	15	23	9.5
$\{11\bar{2}1\}$	Normal	15552	0.03506	40398	4	35	-	-	0.1	0.1
	Parallel	15552	0.01116	19612	3	35	-	15	37	19
Slip+ $\{11\bar{2}1\}$	Normal	15552	0.00649	17460	3	35	35	-	8.5	8.5
	Parallel	15552	0.00772	11018	3	35	35	15	55	23

In both the N- and P-samples, three MAX phases were observed in both HIPPO and SMARTS. Rietveld analysis of the data sets is consistent with the existence of 71(5) wt.% of the Ti_2AlC phase, and 16(3) wt.% and 13(4) wt.% for the Ti_3AlC_2,[86] and $Ti_5Al_2C_3$ phases,[87] respectively (Fig. 7-7). In both samples all three phases had similar majority/minority orientation textures. Excellent Rietveld fits ($\chi^2 < 2.5$, and $R_{wp} \leq 4.5\%$ for all SMARTS data), full identification of all observed diffraction lines, as well as the existence of substantial amount of isolated Ti_2AlC peaks in the diffraction pattern, led to the results presented with almost negligible systematic errors, impurity phases notwithstanding. The structure and texture similarities of the three observed phases, as well as the negligible experimental systematic error in the ND analysis, enable us to safely consider the Ti_2AlC phase solely when comparing to the single phase, EPSC calculation. This is especially true here since the impurity phases are also MAX phases with very similar elastic and plastic properties as the majority phase.

Stress-strain curves, determined from single peak fits of the {000l}, $\{10\bar{1}0\}$, and $\{10\bar{1}5\}$ reflections in the ND data along the longitudinal and transverse directions to the compressive loading axis, for the N- and P-samples are shown in Figs. 7-8, 7-9 & 7-10. The experimental results on loading are depicted by red circles; those during unloading by blue squares. The EPSC model results - assuming linear elastic behavior only - are depicted by dashed lines (Figs. 7-8, 7-9 & 7-10). Values of least square fits to the {000l} and $\{10\bar{1}0\}$ results, viz. the experimental elastic moduli (c_{33} and c_{11}), are compared to values predicted by ESPC model assuming only elastic behavior in Table 7-5. The HIPPO texture files were used to account for sample textures in all EPSC predictions.

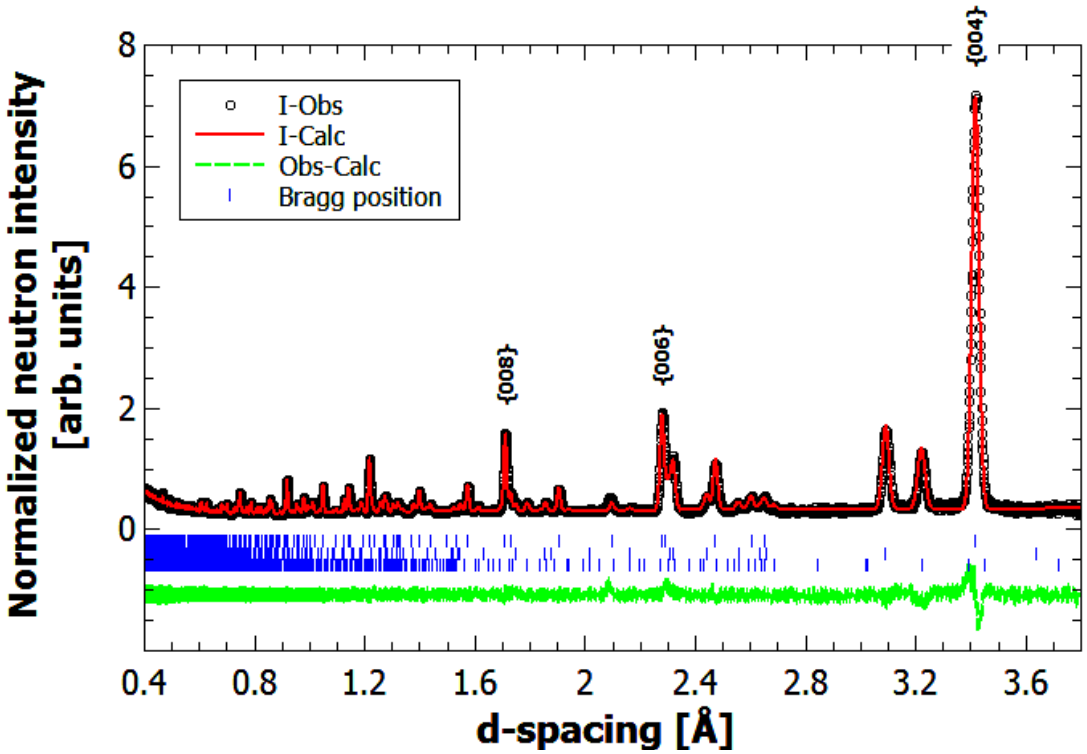

Figure 7-7: Rietveld analysis of powder ND data of the CG-N Ti_2AlC sample as measured on the SMARTS diffractometer, under a minimal compressive stress of 5.0 MPa load. The data presented here was collected using bank 2, configured to measure the longitudinal stress direction (Fig. 7-5(c)). Open circles, solid line, and dashed line in the bottom, represent the measured data, refined model, and the difference between the two, respectively. The three rows of vertical tags represent the calculated Bragg reflections' positions of the major Ti_2AlC (1st row), and the minor Ti_3AlC_2 (2nd), and $Ti_5Al_2C_3$ (3rd) phases. The strong preferred orientation of the {000l} reflections is marked for the major Ti_2AlC phase. In this fit χ^2=2.489.

Inspection of the results, shown in Figs. 7-8, 7-9 & 7-10 and summarized in Table 7-5, shows excellent agreement between the EPSC calculated *linear* elastic predictions for the hard majority grains (black grains) and the ND results. The agreement for the hard minority grains (red grains) is less good since the EPSC calculations (ND signals) have higher systematic (statistical) uncertainty when modeling a smaller grain population. Nevertheless, the worst agreement (first line in Table 7-5) is of the order of 15 %. Gratifyingly, and consistent with the EPSC results, for both majority and minority grains, the ND results indicate that $c_{11} > c_{33}$ beyond one standard deviation.

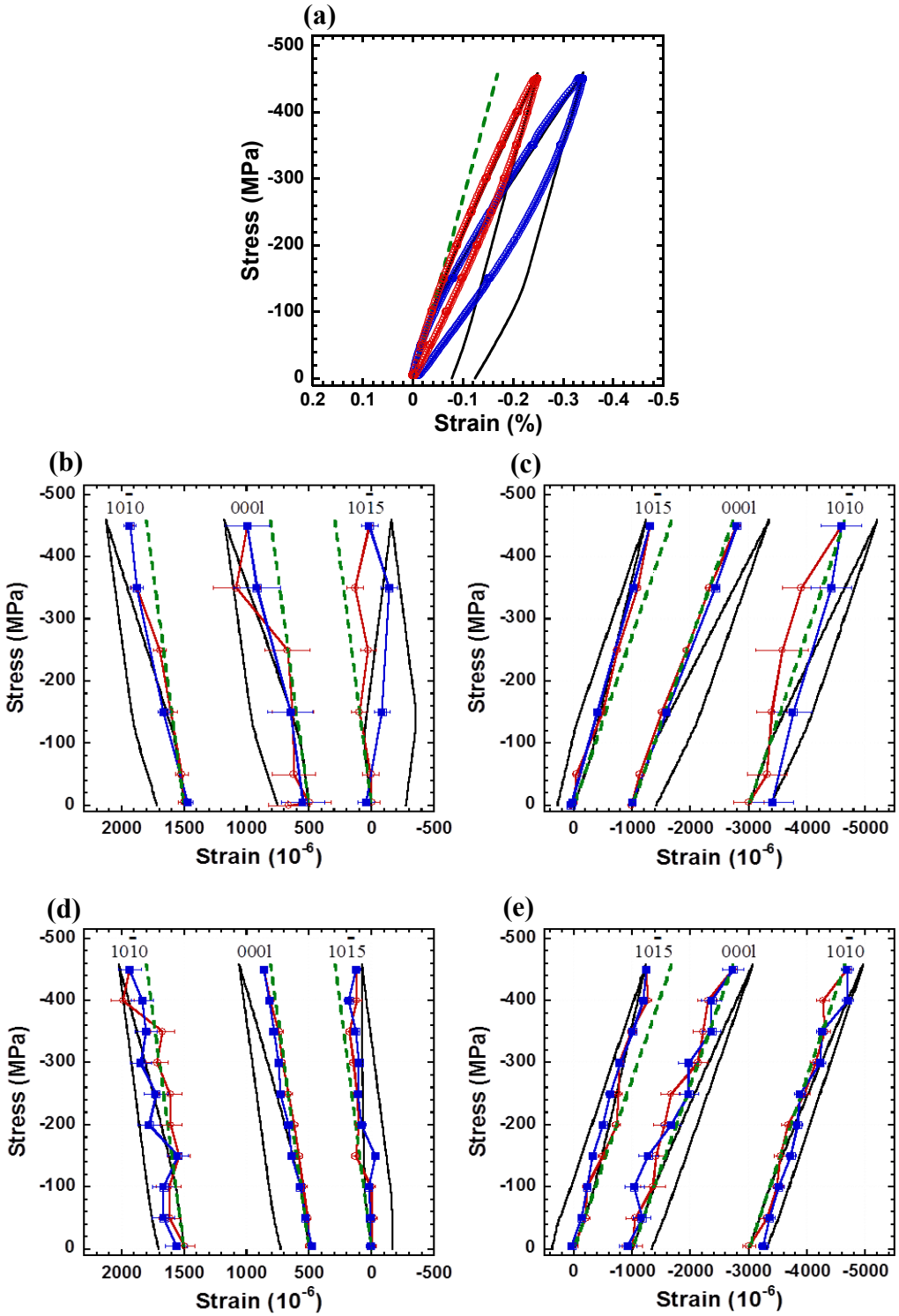

Figure 7-8: Ti_2AlC stress–strain curves: (a) bulk N- (blue), P- (red) samples and solid black lines are EPSC fits assuming DPs activity; (b) transverse and, (c) longitudinal directions for the N-sample; (d) transverse and (e) longitudinal directions for the P-sample. The experimental results, derived from ND data, taken on SMARTS, on loading (unloading) are represented by red circles (blue squares). The EPSC model results, assuming linear elastic behavior (green dash lines), and DP (black solid lines) are shown. Both axes are reversed to render the plots similar to conventional tensile stress-strain curves.

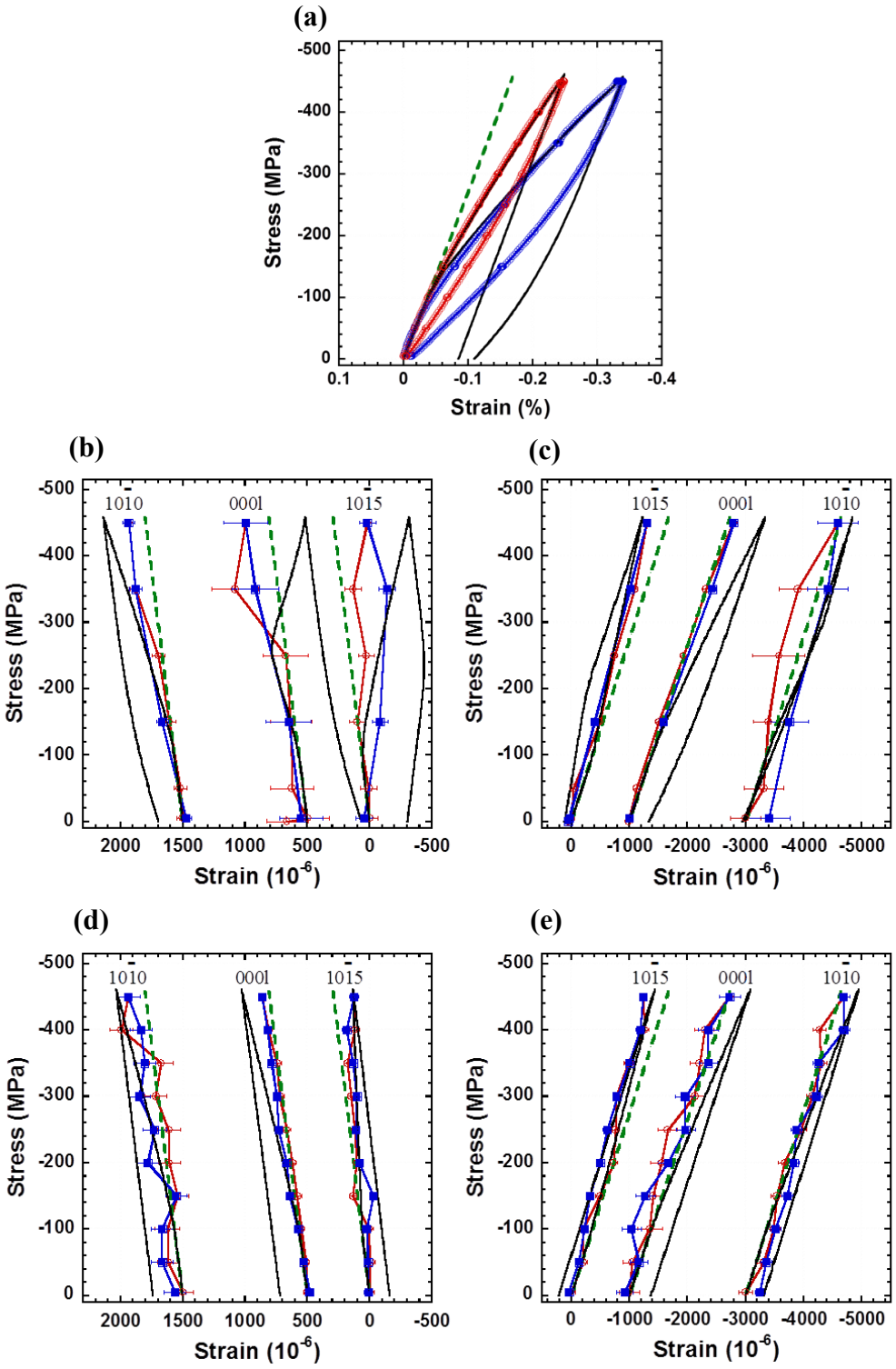

Figure 7-9: Ti_2AlC stress–strain curves: (a) bulk N- (blue) and P- (red) samples and solid black lines are EPSC fits assuming $\{11\bar{2}1\}$ twin activity; (b) transverse and, (c) longitudinal directions for the N-sample; (d) transverse and (e) longitudinal directions for the P-sample. The experimental results, derived from ND data, taken on SMARTS, on loading (unloading) are represented by red circles (blue squares). The EPSC model results, assuming linear elastic behavior (dash lines), and $\{11\bar{2}1\}$ twin (solid lines) are shown. Both axes are reversed to render the plots similar to conventional tensile stress-strain curves.

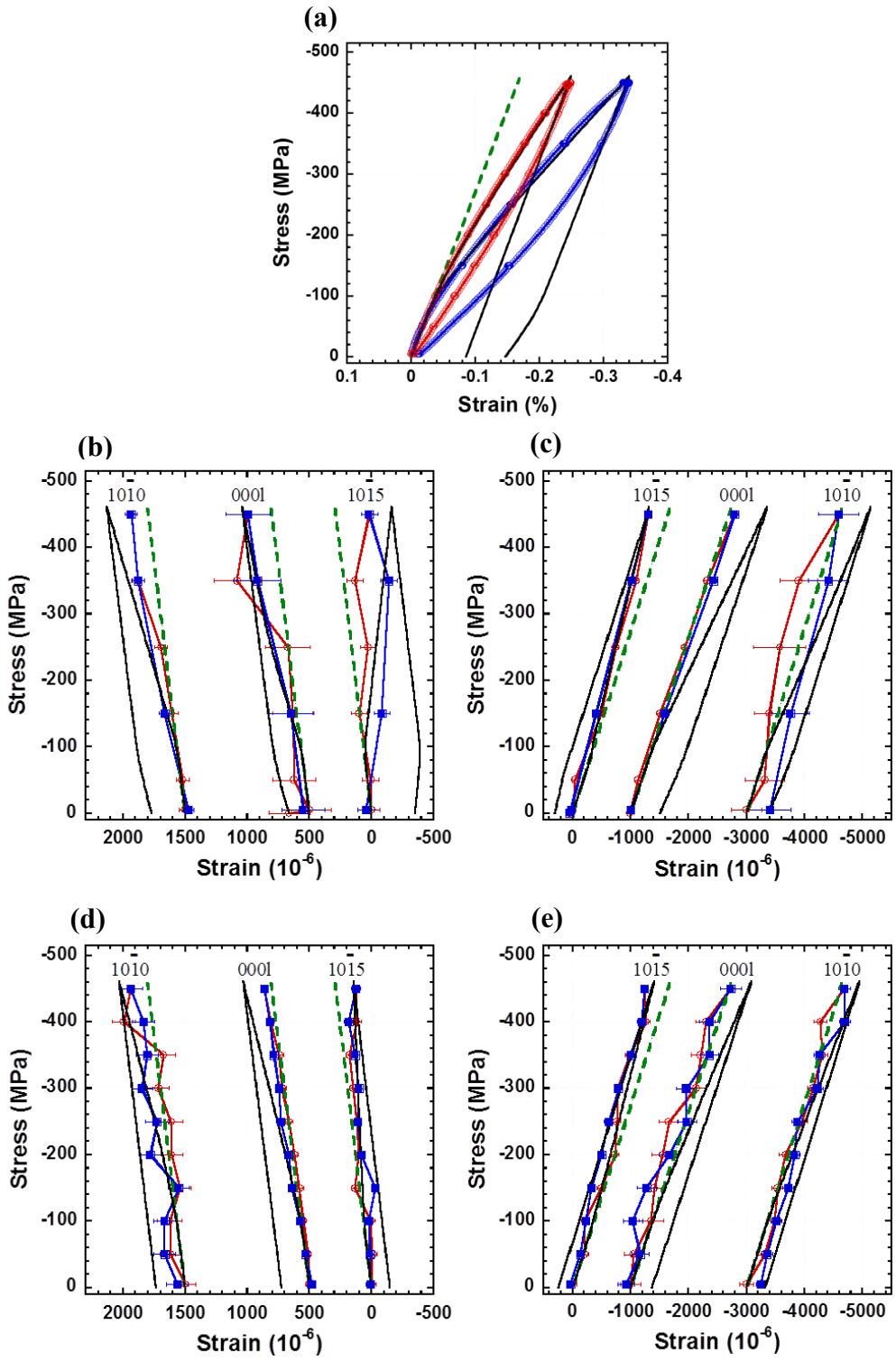

Figure 7-10: Ti_2AlC stress–strain curves: (a) bulk N- (blue) and P- (red) samples and solid black lines are EPSC fits assuming DPs + $\{11\bar{2}1\}$ twin activity ; (b) transverse and, (c) longitudinal directions for the N-sample; (d) transverse and (e) longitudinal directions for the P-sample. The experimental results, derived from ND data, taken on SMARTS, on loading (unloading) are represented by red circles (blue squares). The EPSC model results, assuming linear elastic behavior (dash lines), and DPs + $\{11\bar{2}1\}$ twin (solid lines) are shown. Both axes are reversed to render the plots similar to conventional tensile stress-strain curves.

Table 7-5: Comparison of measured ND elastic moduli (in GPa) versus those calculated from the ESPC model using *ab initio* calculated elastic constants, viz. c_{11} = 307.5; c_{12} = 61.7; c_{13} = 66.5; c_{33} = 282.3; c_{44} = 117.5 (see Table 7-4). ND results are obtained from single peak-fit to data measured on SMARTS longitudinal bank upon loading of either the N- or P-samples. The EPSC calculations account for samples' texture. Standard deviations are given in brackets.

Elastic constant		ND	EPSC	*Ab initio calculations*
c_{11}	Minority $\{10\bar{1}0\}$ in N	320(28)	277	307.5
	Majority $\{10\bar{1}0\}$ in P	274(8)	282	
c_{33}	Majority {000l} in N	260(6)	264	282.3
	Minority {000l} in P	289(12)	269	

In sharp contradistinction to the hard grains, the response of the soft grains observed by ND shows large deviations from that predicted by the EPSC linear elastic model. This effect is at its highest magnitude when the stress-strain curves of the $\{10\bar{1}5\}$ planes are considered (grains subjected to the highest shear stresses on the basal planes); Figs. 7-8, 7-9 and 7-10. Upon loading, and up to ~ -150 MPa, the response is initially linear elastic, in good agreement with the linear elastic EPSC predictions. However, at higher stresses, a concave curvature is observed in the ND strains that lead to elastic strains that are significantly less than those predicted for the $\{10\bar{1}5\}$ planes by the model assuming linear elasticity (i.e. dashed green lines in Fig. 7-8(a) & 7-11(a)). Figures 7-11, and 7-12 show the stress-strain curves of several $\{10\bar{1}l\}$ planes as measured by single peak fit of neutron diffraction data for the N, and P-samples, respectively. Of special note is the fully and spontaneously reversible stress-strain *hysteresis loop* of the $\{10\bar{1}5\}$

transverse plane reflections in Figs. 7-8(a) & 7-11(a). To the best of our knowledge, such an observation has never been seen in a polycrystalline material to date.

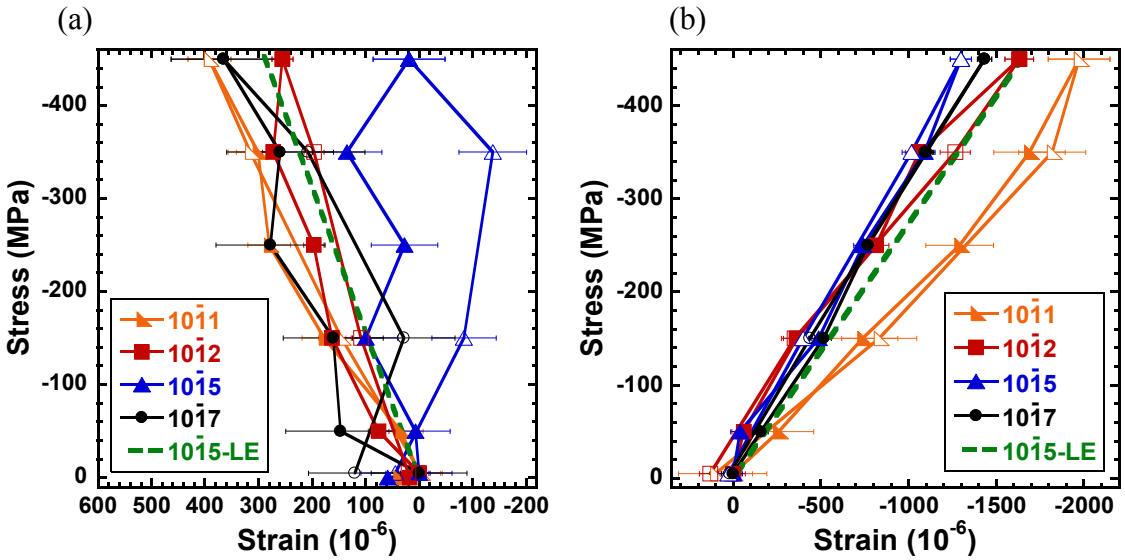

Figure 7-11: Stress–strain response of selected $\{10\bar{1}l\}$ planes along transverse (a) and, longitudinal (b) directions for the N-sample. The experimental results, derived from single peak fit to the ND data, taken on SMARTS. The EPSC model results, assuming linear elastic behavior are also presented (solid lines)

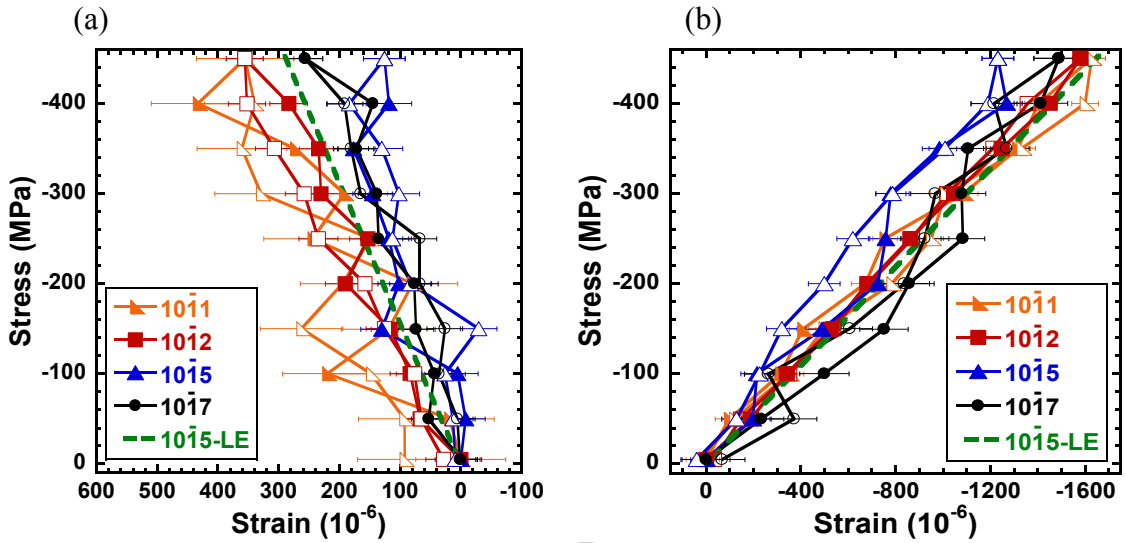

Figure 7-12: Stress–strain response of selected $\{10\bar{1}l\}$ planes along transverse (a) and, longitudinal (b) directions for the P-sample. The experimental results, derived from single peak fit to the ND data, taken on SMARTS. The EPSC model results, assuming linear elastic behavior are also presented (solid lines).

Since as noted above, $\{10\bar{1}5\}$ plane reflections are from grains whose basal planes make an angle of ≈ 45º with that of the applied loads, they are by definition soft grains, it is reasonable to conclude that the latter will experience the highest amount of deformation and activity of the acting dislocation mechanism (see below for more evidence). Note that as the angle between the loading direction and the basal planes deviate from ≈ 45º, the response moves toward that of the hard grains, i.e. it becomes for the most part more linear elastic (see Figs. 7-11 and 7-12).

To explore what possible mechanisms can account for the entire set of observations presented here, EPSC calculations were carried out by activating either DP (Figs. 7-5(b) and 7-8), or $\{11\bar{2}1\}$ twin formation (Fig. 7-9), or combinations thereof (Fig. 7-10). When comparing all EPSC calculations (shown as black solid lines in Figs. 7-5(b), 7-8, 7-9, and 7-10) and the experimental results (symbols in Figs. 7-5(b), 7-8, 7-9, and 7-10), three discrepancies are immediately apparent. First, and unsurprisingly, the unloading trajectories of the bulk curves are totally off, because they lead to plastic deformation that is *not* experimentally observed (Fig. 7-5(b)). Second, even when the loading trajectory is successfully modeled, the microscopic individual plane reflections predict non-zero final residual strains upon complete unloading, which again was not experimentally observed (Figs. 7-8, 7-9, and 7-10). Third, the best EPSC calculations cannot describe the response of the individual reflections from both hard and soft grains simultaneously with a single model (Figs. 7-8, 7-9, and 7-10). Said otherwise, whereas the linear elastic model describes well the hard grains' behavior, represented by the $\{10\bar{1}0\}$, and {000l} reflections, it does so poorly for the soft grains, represented by the $\{10\bar{1}5\}$ reflection (dashed line in Fig. 7-8). Conversely, when the basal slip model

describes the loading part of the soft grains well, it models the response of the hard grains quite poorly indeed (solid lines in Fig. 7-8). The same conclusions are reached when the $\{11\bar{2}1\}$ twins are activated (Fig. 7-9) and even when combinations of DPs and $\{11\bar{2}1\}$ twins are activated (Fig. 7-10). It follows that, at least within the limitations of the EPSC model, DPs and/or $\{11\bar{2}1\}$ twins *alone* cannot account for the deformation observed, neither at the macroscopic nor microscopic levels.

The stress-strain results for the $\{10\bar{1}1\}$ reflection, depicted in Fig. 7-13(a) by triangles, are also consistent with the activation of basal slip. The stress - no longer carried by the soft grains, because they deformed - is redistributed into the $\{10\bar{1}l\}$ reflections. Following the same logic, one would expect that the (0004) reflections – that belong to some of the hardest grains - to respond in the same manner. And indeed the EPSC results - depicted in Fig. 7-13(b) by the dotted line - not only predict a large deviation from elastic behavior starting at around -120 MPa, but also predict the largest (400 μstrain) elastic strain at maximum load. This is expected from the hardest grain which shoulder the largest applied stress due to the above mentioned stress redistribution. Experimentally, however, the single peak fits of the (0004) reflections – shown in Fig. 7-13(b) by solid red lines that trace a fully reversible clockwise loop (N-sample longitudinal bank) – respond in an *almost* linear elastic fashion depicted by the inclined green dotted line. These basal planes are thus carrying a significantly *lower* portion of the stress than they would have carried had they deformed by DPs. Said otherwise, instead of carrying a stress that would cause them to deform to an elastic strain of $2300\text{x}10^{-6}$ (point X in Fig. 7-13(b)), in reality they only deformed to a stress corresponding to an elastic strain of $1750\text{x}10^{-6}$ (point Y in Fig. 7-13(b)). On the other hand, it must be noted that

although $\{10\bar{1}5\}$ (soft grains) and (0004) planes accommodate lower strain than predicted by EPSC, however, they exhibit large clear reversible loops compared to the other minority grains at other inclination angles (Figs. 7-8, 7-9, 7-10 and 7-11(a)). This feature indicates intense dislocation activity on those planes. These observations are of *crucial and fundamental importance* because, they submit that, they are the *signature of basal plane dislocations that are not in the form of DPs*. Had the latter existed the response would have followed the dotted line, as they do for the other $\{10\bar{1}l\}$ planes. As discussed previously, these conclusions are valid for all reflections in the longitudinal and transverse banks in both N- and P- samples. They are also valid regardless of whether DPs or $11\bar{2}1$ twins or combinations thereof are activated in the EPSC model (see Fig. 7-14).

The hardest grains' behavior is *almost* linear elastic (Fig. 7-13(b)). A closer look at the highest, and thus the most statistically favored, reflection, i.e. 0004 (Figs. 7-7 & 7-13(b)), reveals a significant difference between linear elasticity and the observed results. Moreover, the microstrains of the majority grains, measured using this reflection, *trace fully closed hysteresis loops in both transverse and longitudinal banks for the P-sample, and N-sample*, respectively (Fig. 7-13(b)). In Fig. 7-13(b) the error bars are *smaller* than the symbols used. The combined observation of this clear loop along with its stark deviation from the deformation predicted by the EPSC for basal DP behavior, suggests energy dissipation within the basal planes, *not whose origin is not "classic" dislocation pileups*. Furthermore, the mechanism causing this dissipation should result in nearly linear elastic deformation within these planes. To the best of our knowledge, fully reversible micro strain hysteresis loops observed here by ND, and depicted in Figs. 7-

13(b), and 7-14(b) are the first of their kind to be reported.

The buckling dislocation mechanism is proposed to be the micromechanism taking place in all layered solids and in the textured Ti_2AlC samples experimented. The lower microstrain measurements observed in $\{10\bar{1}5\}$ and (0004) planes compared to their theoretically predicted values by EPSC in the N-sample is consistent with the inverse expansion effect explained in section 4.4. During buckling of layered structures, the layers fold against each other. Consequently, their length decreases while their thickness increases (Fig. 4-17 and 4-18). However, depending on the inclination angle of the layered structure relative to the loading direction, an inverse expansion effect could take place (Fig. 4-18). The inverse expansion effect is believed to be the reason for the expansion of the (0004) planes along the compressive axis. Since the (0004) plane grains are a majority in the N-sample, their effect is pronounced and observed in the ND results. In situ ND results observe the elastic strains in the material under deformation. During buckling of the grains in the Ti_2AlC samples the in situ ND results are a combination of the linear elastic strains in the grain and the non-linear elastic strain of the grain portion that buckled. The non-linear elastic strain is less than the predicted value due to the buckling dislocation mechanism where the layers length decrease. The inverse expansion effect was observed in other MAX phases [88] and Mg [89] , and is believed to be due to the buckling nature where the layers fold against each other as shown in Fig. 4-18.

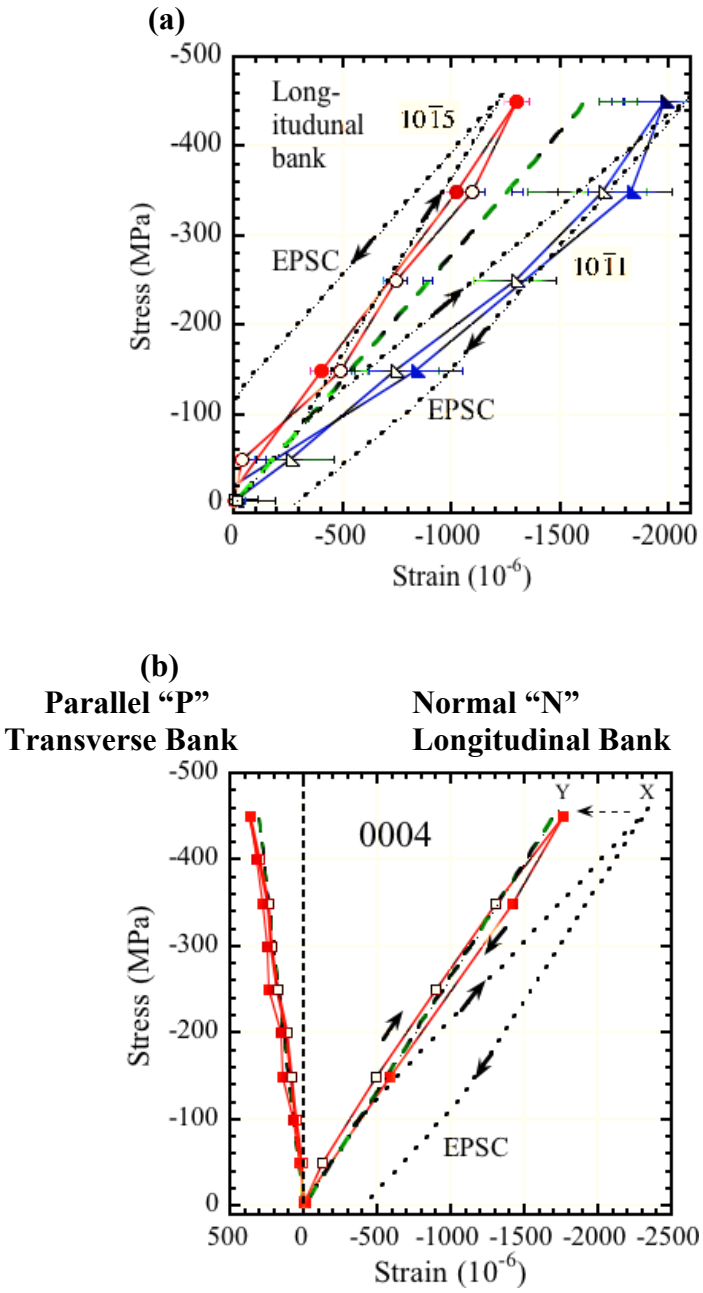

Figure 7-13: Stress–strain response of individual reflections obtained from single peak fits of the ND results of the N-sample. (a) Longitudinal $10\bar{1}1$ and $10\bar{1}5$; (b) N-sample 0004 in longitudinal (right hand side curve) and P-sample on transverse bank (left hand side). The EPSC results, where basal slip is activated are depicted by dotted black lines. The linear elastic EPSC results are depicted by green dashed lines. The elastic strains on loading are represented by open symbols; those on unloading by solid symbols with the same shape. Both axes are reversed to render the plots similar to conventional tensile stress-strain curves.

However, it is noticed that the $\{10\bar{1}5\}$ (soft grains) in the P-sample (7-14(d)) do not demonstrate a fully reversible closed loop as in the N-sample (Fig. 7-14(b)). This is explained by the Schmid factor magnitudes of the majority and minority grains of each texture. In the N- and P- samples, the basal plane in the majority grains are oriented either normal or parallel to the sample loading direction, Fig. 5-2(d). The majority grains in each sample will accommodate the majority of the load applied (the opposite is true as well), Fig. 5-2(d). The difference in Schmid factor between N- and P-samples shown in Fig. 3-6 clearly demonstrates that the N-sample will experience more deformation than the P-sample. The N-sample majority grains at 0004 are therefore soft relative to those in the P-sample. In the N-sample, the majority grains at 0004 deform demonstrating a closed hysteretic loop (Fig. 7-13(b)) due to the high Schmid factor they experience (Fig. 3-6). Hence, the load is redistributed on all minority grains in the N-sample which therefore experience a high stress level. Consequently the grains at $\{10\bar{1}5\}$ in the N-sample show a closed hysteretic loop due to the high deformation level they experience (Fig. 7-14(b)).

Unlike the majority grains at 0004 in the P-sample which experience a lower Schmid factor than the N-sample majority grains when the same stress level is applied (Fig. 3-6). Therefore the majority grains at 0004 in P-sample are hard relative to the majority grains in the N-sample. In addition, the P-sample majority grains would accommodate the majority of the load applied without undergoing considerable deformation as the N-sample majority grains. Hence, a low stress is applied on the P-sample minority grains relative to the N-sample minority grains at the same macroscopic stress level. Therefore, the grains at $\{10\bar{1}5\}$ in the P-sample would not demonstrate a

closed reversible loop as shown experimentally in Fig. 7-14(d) due to the low deformation level they experience.

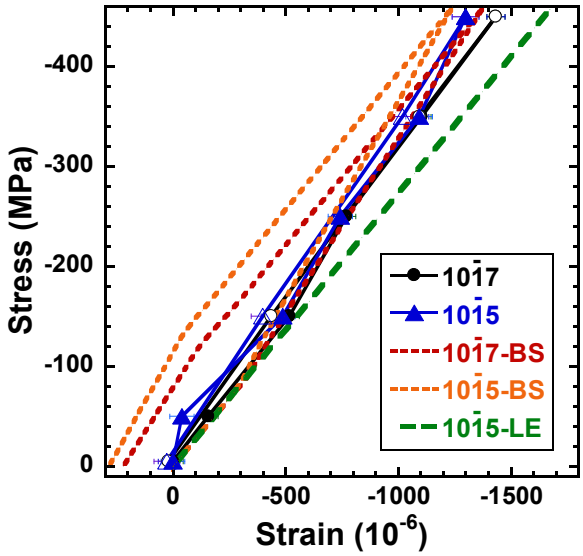

(a) Longitudinal experimental results of N-sample, derived from ND data, taken on SMARTS, on loading (unloading) are represented by filled (empty) symbol. The EPSC model results, assuming linear elastic behavior (LE, solid lines), and basal slip (BS, dash lines) are shown. The ND results obtained from the two soft grains, represented by the $\{10\bar{1}7\}$ and $\{10\bar{1}5\}$ reflections, whose basal planes form an angle of ~36, and ~45o with the loading direction, respectively. Both axes are reversed to render the plots similar to conventional tensile stress-strain curves.

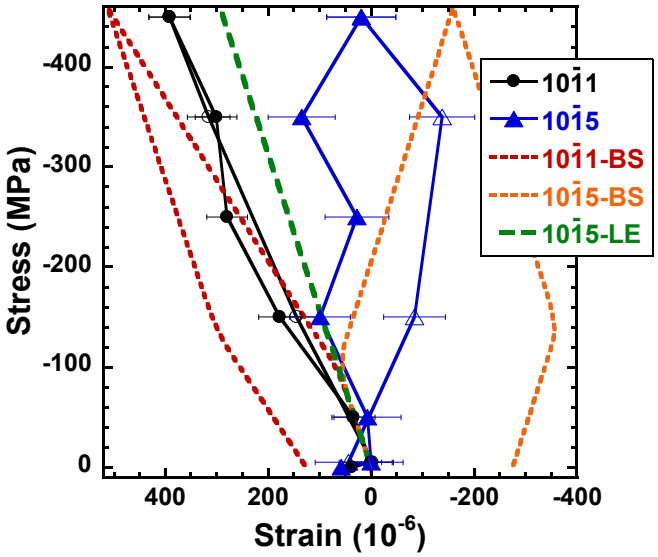

(b) Transverse experimental results of N-sample, derived from ND data, taken on SMARTS, on loading (unloading) are represented by filled (empty) symbol. The EPSC model results, assuming linear elastic behavior (LE, solid lines), and basal slip (BS, dash lines) are shown. The ND results obtained from the two soft grains, represented by the $\{10\bar{1}1\}$ and $\{10\bar{1}5\}$ reflections, whose basal planes form an angle of ~11, and ~45º with the loading direction, respectively. Both axes are reversed to render the plots similar to conventional tensile stress-strain curves.

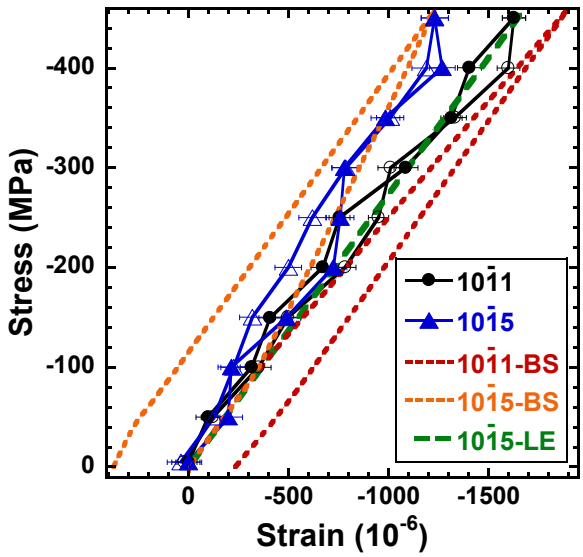

(c) Longitudinal experimental results of P-sample, derived from ND data, taken on SMARTS, on loading (unloading) are represented by filled (empty) symbol. The EPSC model results, assuming linear elastic behavior (LE, solid lines), and basal slip (BS, dash lines) are shown. The ND results obtained from the two soft grains, represented by the $\{10\bar{1}1\}$ and $\{10\bar{1}5\}$ reflections, whose basal planes form an angle of ~79, and ~45º with the loading direction, respectively. Both axes are reversed to render the plots similar to conventional tensile stress-strain curves.

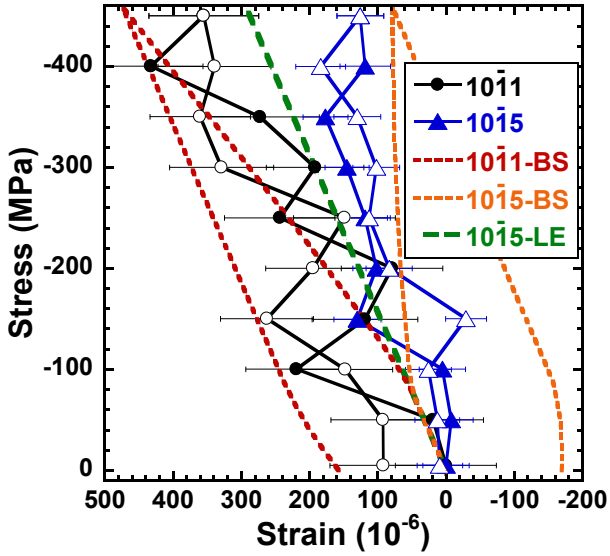

(d) Transverse experimental results of P-sample, derived from ND data, taken on SMARTS, on loading (unloading) are represented by filled (empty) symbol. The EPSC model results, assuming linear elastic behavior (LE, solid lines), and basal slip (BS, dash lines) are shown. The ND results obtained from the two soft grains, represented by the $\{10\bar{1}1\}$ and $\{10\bar{1}5\}$ reflections, whose basal planes form an angle of ~11, and ~45º with the loading direction, respectively. Both axes are reversed to render the plots similar to conventional tensile stress-strain curves.

Figure 7-14: Stress–strain response along longitudinal and transverse direction for the N- and P-sample.

As noted several times above the EPSC model does not model IKBs. The only argument that can be made on behalf of the IKB-based model is one of elimination. In other words by showing that the bulk and micro-stress-strain curves *cannot* be fit by the EPSC model that takes $\{11\bar{2}1\}$ twins and/or dislocation pile-ups into account, the latter two cannot explain what is observed and can thus be safely eliminated as plausible mechanisms. Needless to add, this is not the *only* argument, but one of several. For example, since there is no rationale/theory/driving force that renders dislocation pile-ups fully and *spontaneously* reversible they, *by themselves*, cannot explain what is observed.

Based on Barsoum et al.[75] an IKB is a fraction of a grain that tilts by an angle γ_c from the original grain orientation. Such a small tilt (~ 0.7º) will result in a small increase of the {000l} reflections widths, similar to observed mosaicity in single crystals.[90],[91] Indeed, plotting the {0004} reflection width as a function of stress for the N-sample reveals a small, yet statistically significant, broadening of this peak (Fig. 7-15). Most remarkably, and in line with Barsoum et al.[75] microscale model, this peak broadening is fully and spontaneously reversible. An increase in mosaicity is also expected upon loading for the $\{10\bar{1}0\}$ reflections in the P-sample. However, the lower intensity of this reflection compared to that of the {0004} reflections in the N-sample, along with the fact that this effect is roughly twice as small as the effect in the latter (Fig. 7-5(c)), renders the widths variations of these peaks quite noisy and inconclusive (see inset in Fig. 7-15).

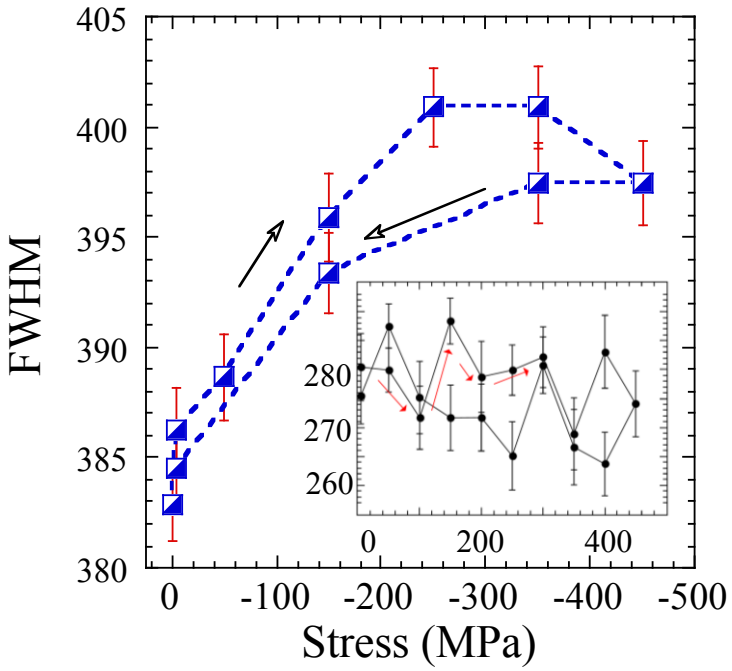

Figure 7-15: Full width at half maximum (FWHM) of the N-sample {0004} ND reflection on the longitudinal bank as a function of stress. Note hysteresis. Inset shows FWHM for the $\{10\bar{1}0\}$ reflections in the P-sample.

At this stage it is important to eliminate some common sources of mechanical hysteresis that could explain the results such as the Bauschinger effect, microcracking, reversible twinning, etc. Quite recently, stress-strain hysteresis loops of austenitic stainless steel samples were observed in SMARTS and attributed to the Bauschinger effect[80]. Along the same lines, twinning can be reversed in some situations.[92] In both cases, however, *full* reversibility is achieved *only by reversing* the loading direction. Herein the reversibility is *full and spontaneous*, a most crucial distinction indeed.

Microcracking can also result in hysteretic bulk stress-strain curves, especially in ceramics[93]. For example, in a recent SMARTS study on porous alumina - with porosities as high as 47 vol.% - small loops were only observed at the highest porosities.[94] Given that alumina is significantly more brittle than Ti_2AlC, it is unlikely that the hysteresis loops observed herein are due to porosity and/or microcracking,

especially since the samples used herein were fully dense. In another SMARTS study on rock samples[95] bulk hysteresis loops were observed and related to microcracks. However, opposite of what is observed here, the stress-strain curves traced counter-clockwise loops. As important, at the microscopic, i.e. ND level, the response was fully *linear elastic* in all directions,[95] again, in stark contrast to the results shown in Figs. 7-13(b) & 7-14(b). It is thus concluded that the behavior observed herein cannot be primarily a result of microcracking.

The EPSC model showed that dislocation-pileups (DPs) through basal slip alone cannot predict the KNE mechanical behavior of textured Ti_2AlC. The dislocation density generated from DPs is estimated to be compared with the experimental value that could be calculated from broadening of various diffraction peaks. Before estimating the dislocation densities, it is important to define some terms. The total strain, ε_{tot}, of a solid loaded to a uniaxial stress, σ, is given by:

$$\varepsilon_{tot} = \varepsilon_{EL} + \varepsilon_{NL} = \frac{\sigma}{E} + [\varepsilon_{KB} + \varepsilon_{DP}] \tag{7}$$

where E is Young's modulus, ε_{EL} is the elastic strain and ε_{NL} is the total nonlinear strain shown schematically in Fig. 7-5(a). The strains ε_{KB} and ε_{DP} - both fully reversible - are associated with the kink bands and DPs, respectively.

The dislocation density, ρ_{exp}, can be calculated from the broadening, $\Delta d/d_0$ of the various diffraction peaks. The two are related by:[96]

$$\rho_{\exp} \approx \frac{3E}{Gb^2(1+2\nu^2)} \left(\frac{\Delta d}{d}\right)^2 \tag{8}$$

At maximum stress the measured $\Delta d/d_0$ was $\approx 3.4 \times 10^{-4}$ (Fig. 7-15). Assuming b = 0.306 nm, E = 277 GPa, G = 118 GPa, $\nu = 0.19$,[76] ρ_{exp} is calculated to be $8(2) \times 10^{12}$ m^{-}

[2]. The estimated uncertainty is mainly due to the uncertainty in measured $\Delta d/d_0$. The next step is to compare this value to that of DPs micromechanism that can cause such a reversible increase in dislocation densities. The corresponding dislocation densities are given by (Appendix B):

$$\rho_{DP} \approx \frac{2.1(1+\nu)\varepsilon_{DP}}{Mb\lambda} \tag{9}$$

where M is the Taylor factor and λ is the grain diameter. For the microstructures used in this work, if one assumes that the total nonlinear strain for the N-microstructure (0.0017) are due entirely to either DPs, the respective dislocation densities is 6.7×10^{10} m^{-2}. The uncertainty estimated on these values is ~ 50 % arising from the large deviations in λ, and α. From these calculations it is clear that the dislocation density of the DPs is not enough to explain our findings, since it is two-order of magnitude *less* than the density needed to explain the observed {0004} peak widening (Fig. 7-15).

7.2.1 Summary and Conclusions

By summing up all ND results, and the attempts to model them using EPSC, it is clear that neither DPs nor twins can explain the experimental results. Another mechanism is needed. The latter must: a) explain the fully reversible, but energy dissipative stress-strain loops, both the macroscopic (Fig. 7-5(b)), and microscopic (Fig. 7-13(b) & 7-14(b)); b) account for the unusually large energy stored at maximum stress (Fig. 7-5(c)) that in turn creates the driving force necessary to spontaneously reverse the non-linear deformation; c) should allow for the formation of DPs (i.e. dislocations), and; d) transform into kink bands at higher temperatures or stresses.

In conclusion, careful analysis of *in situ* ND results of polycrystalline textured Ti_2AlC samples, loaded in compression to 450 MPa, is consistent with kinking. The lattice strains are reversible, showing a pronounced hysteresis loop of selected grains' directions. It is crucial to note here that in the N-sample, at least some of the hard grains deform *against* their strain energy considerations. This comes about because when the latter kink, they do so with a strain component *opposite to the loading* direction. Said otherwise, the grains *expand* along the compression axis! Such contrarian deformations at the individual grain level have been observed in the MAX phases,[88] and in polycrystalline Mg[89]. In passing, it was noted that in a recent quite careful ND study on polycrystalline Mg some aspects of the deformation were speculated to be due to the formation of reversible dislocations[92].

Thanks for E. Caspi who took the lead in performing Rietveld analysis with high accuracy and analyzing the ND diffraction results; B. Clausen, D. Brown and S. Vogel are the instrument scientists at LANL who collected the ND results on SMARTS and HIPPO; S. Amini fabricated the samples, S. Vogel and O. Yehezkel were involved in analyzing the ND results at various stages of the project and M. W. Barsoum who conceived and directed the project.

7.3 Effect of Grain Size

The basic governing principle for the buckling dislocation mechanism is Euler's formula (Eq. 1). In this section the effect of grains size on Euler's formula which reflects directly on the buckling dislocation mechanism is investigated. Figure 7-16 illustrated the effect of increasing the number of HCP crystal structure unit cells (which is the essence of grain coarsening) representing layered structures in the mechanism. Figure 7-16(a) displays five HCP unit cells clustered together and Fig. 7-16(b) shows the top view of the five unit cells were the atoms are at the corners of the hexagonal shape. The height (H) and width (W) dimensions of the layer are marked as a reference for comparison. It is assumed that one fine grain (the rectangular cuboid) in a polycrystalline layered structured material will contain those five unit cells as shown in Fig. 7-16(c) while compressive load is applied. Recall that the close-packed plane in HCP materials is the basal plane; hence, H & W dimensions denote multiples of the lattice parameter "a" while T (representing the thickness of the grain) indicate the number of basal plane layers stacking dictating multiples of "c" parameter in Figs. 7-16(b) & (c). The five unit cells in the fine grain in Fig. 7-16(b) are oriented in the P-sample direction for illustration of buckling condition.

Grain coarsening is achieved by heating the sample at a selected temperature for certain time duration. During grain coarsening the atoms in the grains rearrange themselves and move to the most stable and less energetic grain. The atoms at the grain boundaries of the grains are highly energetic in the sample and they are the ones that migrate to the most stable neighbor grain. Therefore, the most stable grains coarsen at the cost of the less stable highly energetic grains. This happens gradually during grain

coarsening at the soaking temperature and time such that the stable grains coarsen while the less stable grains become finer in size. This is the reason for the dual grained microstructures observed in Ti_3SiC_2[54], MAX phases and crystalline materials in general. This process continues to take place until all less stable fine grains vanish and are consumed by the highly stable coarse grains.

The grain sizes of the samples used in the in situ ND experiments on SMARTS for Ti_3SiC_2 are 15μm for fine grain and 100μm for the coarse grain. During grain coarsening more atoms join the most stable grains increasing the number of until cells in the grains. This will increase the multiples of "a" lattice parameter by increasing H & W dimensions of the close-packed basal plane (Fig. 7-16(d)) and the number of multiple basal plane layers stacked in the coarse grain (T dimension representing the thickness of the grain in Fig. 7-16(e)). The distance between the close-packed basal plane layers ("c" lattice parameter) is fixed however the number of layers stacking increases with grain coarsening. Notice the direction relation between grain coarsening and increase in the number of unit cells (i.e. the increase in the dimensions of the basal plane whether in height and/or width and the number of basal plane stacking). One of the very important features in grain coarsening that needs to be considered in layered solids is the probability of atomic migration to the different locations in the crystal structure. The close-packed planes are the least energetic and most stable plane in crystalline materials. Therefore, during grain coarsening of layered structured HCP materials the atoms at the grain boundaries will most probably migrate to enlarge the basal planes instead of formation of a new basal plane. This requires a lower energy magnitude to accomplish and will place the polycrystalline system in a more stable condition. Therefore, the ratio of enlargement

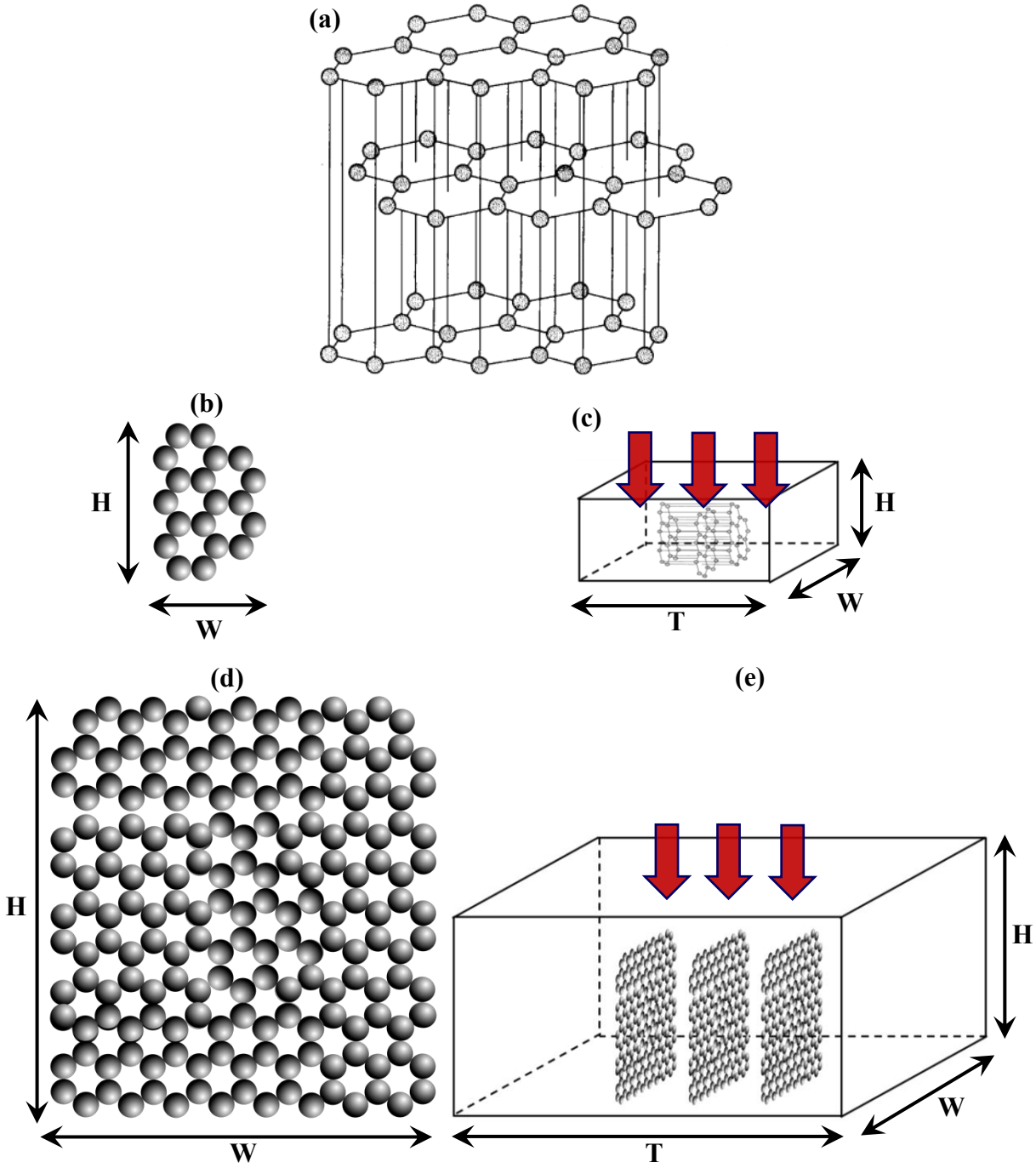

Figure 7-16: Difference between FG & CG layered structured materials in terms of buckling (a) Five of HCP crystals stacked together; (b) Top view of the five stacked crystals in (a); (c) The five HCP crystals constituting one fine grain (d) Top view of multiple (75) HCP crystals stacked together (e) The multiple HCP crystals in (d) constituting one coarse grain [97, 98].

of H & W is much larger than that of T during grain coarsening to reach the lowest energy level for the whole system.

As discussed in chapter 4, the grains deform according to the buckling dislocation mechanism in which a group of layers interact with each other and their response are interconnected while subjected to compressive load. Layered solids coarse grains have an enlarged layers dimensions and increase in the number of layers within the grains. This changes several variables in Euler's formula (Eq. 1) that directly affects the parameters controlling the activation and operation details of the buckling dislocation mechanism. In Euler's formula, the numerator variables are the order of buckling harmonic mode, "n"; the elastic modulus, "E"; and moment of inertia the structure, "I" (second moment of area for the structure's cross-sectional area; hence it is function of the structure shape). The variable "I" is a reflection of the structure resistance to bending about a certain axis; in terms if dislocation nucleation it is reflects the flexibility of the layered structure (a low value of "I" indicates a high level of flexibility for dislocation nucleation and motion). At the grain level, "I" is calculated from the grain shape with respect to the axis of bending relative to the load applied and stress distribution around the grain, in addition to the material crystal structure details including space group and elastic stiffness constant matrix. The constant "π" equal to 3.14159 is fixed; however, "E" is constant as well since it is a material property that does not change with the structure shape. The variables which change when the grains coarsen are "n" and "I", in addition to the only denominator in the formula, "L". Layered structured grain coarsening changes these three variables; "n" and "L" increase, but the change in "I" depends on the changes that occurred in the "n", "L" and "W" (width of the structure, Fig. 7-16). However, during

grain coarsening, the atomic preference to migrate to the close-packed basal planes (due to higher stability and lower energy requirement) causes the enlargement of the basal plane and minimal formation of new basal plane layers. This has the effect changing the shape and texture of the grains in a polycrystalline layered solid sample (Fig. 7-17).

Figure 7-17 illustrates the effect of favorable grain growth of the basal plane layers rather than formation of new basal planes during layered solids grain coarsening on the grain shape and texture. The nomenclatures used and their position with respect to the crystal structure orientation in Fig. 7-17 are the same as those in Fig. 7-16. It is assumed that the fine grains in a polycrystalline layered solid has dimensions of H = W = 2T in Fig. 7-17(a). Due to the favorable atomic migration during grain coarsening to the basal planes, and the equal probability of growth in H and W dimension, it is assume that both dimensions increase twice as much (Fig. 7-17(b)). However, the thickness T representing the number of basal plane layers formed would increase by only 30%. These ratios of growth in the different dimensions are not based on any calculations, they are assumed for illustrative purposes based on favorable atomic migration and lowest energy level to be reached by the system. By that, the number of unit cells is multiplied and are stacked such that they increase multiples of the lattice parameter “a” more than “c”. This phenomenon has been observed experimentally in the coarse grain microstructures of Ti_3SiC_2 and Ti_2AlC in Fig. 5-1(d) & (f). Figure 7-18 shows the microstructural development of Ti_3SiC_2 annealed at 1450ºC for 8, 16 & 24 hrs[54]. The growth observed exhibits a major anisotropic grain texture. A P-sample oriented coarse grain in a polycrystalline Ti_3SiC_2 sample that deformed by buckling is shown in Fig. 7-19. The buckled grain denoted by the black arrow clearly shows the basal plane layers, DWs &

kinked regions. The deformation and delamination that occurred during strain release is permanent and non-recoverable since the grain is at the surface of the sample and the grain is not surrounded by grains from its entire surface for full recovery.

The change in texture directly reflects on moment of inertia, "I", about the Y-axis in Fig. 7-17, and hence increasing flexibility of the grain layers promoting buckling occurrence. Consequently this permits higher orders of buckling harmonic modes, "n". Any structure liable to buckle responds in order to reduce the buckling harmonic mode to the lowest possible integer. This behavior enables reaching the lowest possible energy level of the structure and whole system. Recall that the first buckling mode (were n =1) requires the lowest critical force, P_{cr1}. The critical loads needed for higher buckling harmonics increase progressively as "n" increases; i.e. $P_{cr1} < P_{cr2} < P_{cr3}$. However, modes higher than n=1 do not occur unless bracing is placed around the structure to provide the support required. In layered grains, the extensive growth of the basal planes increases the buckling possibility; however, the surrounding support influences and dictates the buckling harmonic mode that would occur during deformation. Nevertheless, the increase in the structure length, "L" ("H" in Fig. 7-18), is the major factor that affects Euler's formula in decreasing the buckling threshold force significantly. This is the main reason for the drop in the threshold stress for activation of the buckling dislocation mechanism in the CG compared to the FG Ti_3SiC_2 as shown in the macroscopic stress-strain curves in Fig. 7-20. In addition the energy dissipation by the CG is larger than that in FG, reflected in larger stress-strain closed loop in CG. This occurs since a higher density of DWs is possible in the layered CG polycrystalline material due to the coarse grain size and lower critical force (P_{cr}) magnitudes are required for their nucleation and movement.

The reduced critical force magnitudes required in the layered CG polycrystalline material is the source of drop in the slope of the macroscopic stress-strain closed loop (Fig. 7-20). The ratio of grain size length to width (which is a reflection of the basal plane length to the number of basal planes stacked behind each other) is the important parameter in all layered structured polycrystalline materials that affects the buckling threshold load, P_{cr} , for activation of the buckling dislocation mechanism. In fine grained solids, the grain boundaries confine the variable "L" in Euler's equation (Eq. 1) to much lower magnitudes, increasing the P_{cr} required for deformation activation and inhibiting DWs nucleation and movement.

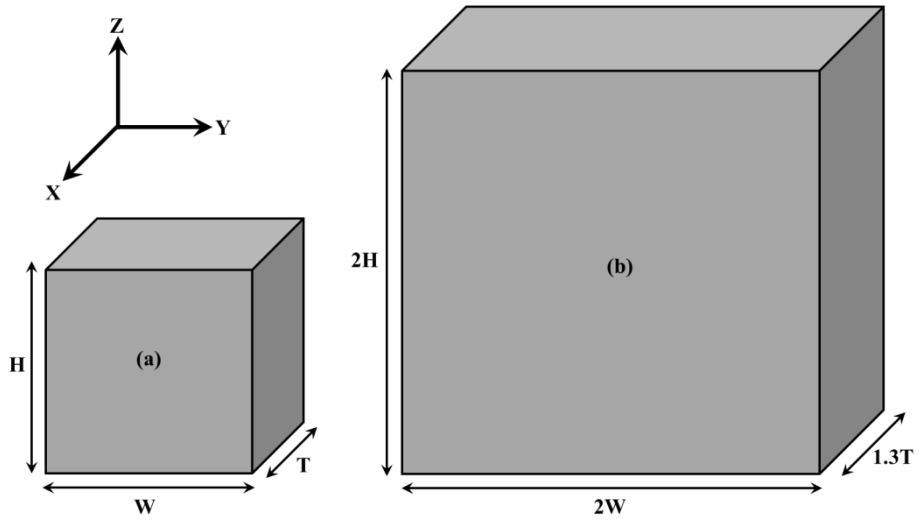

Figure 7-17: Effect of favorable growth on basal plane layers rather than formation of new basal planes during grain coarsening on grain texture; (a) Fine grain; (b) Coarse grain.

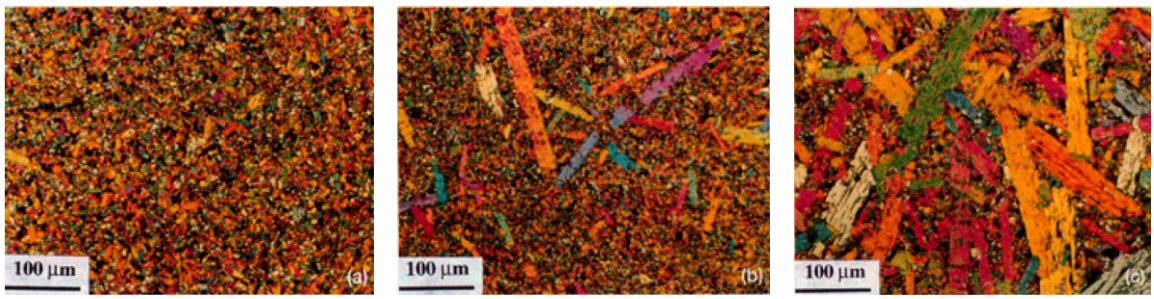

Figure 7-18: Optical micrographs of Ti_3SiC_2 samples HIPed at 1450°C for (a) 8 , (b) 16 , (c) 24h.

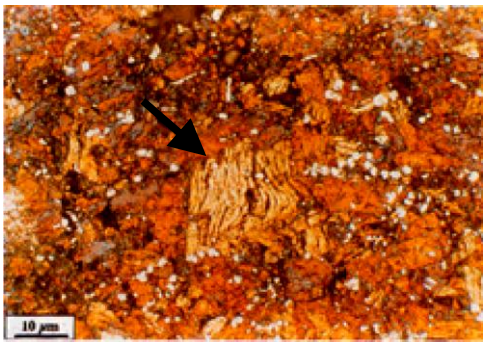

Fig. 7-19: Microstructure of CG Ti_3SiC_2 polycrystalline sample deformed at 1300ºC in compression. Compression direction is vertical. Grain denoted by black arrow buckled and delaminated into voids that formed to its right due to its presence at the sample surface[99].

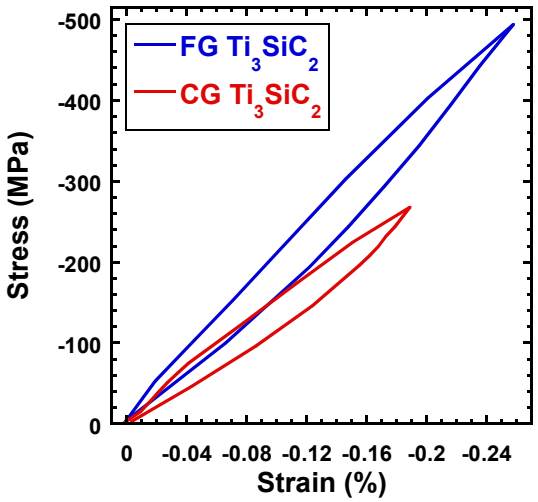

Figure 7-20: (a) Macroscopic stress-strain curve of FG & CG Ti_3SiC_2 for comparison. The coarse sample was annealed from the sample bulk (microstructures are in Fig. 5-1).

7.3.1 Random Textured Polycrystalline FG Ti_3SiC_2

Figure 7-21 show the macroscopic stress-strain KNE mechanical behavior of FG Ti_3SiC_2 (a), in addition to the longitudinal (b) and transverse (c) plane reflection results from in situ ND. The macroscopic stress-strain curve shows completely reversible closed stress-strain loop. The single peak fit plane reflection results for transverse and longitudinal banks are for selected $\{10\bar{1}l\}$ and 0006 & 0008 basal planes. Each plane is shifted from the others for clarity. The inclination angles of the selected planes in Ti_3SiC_2

crystal structure relative to the basal plane are: $10\bar{1}5$ (53.08º), $10\bar{1}3$ (65.73º), $10\bar{1}2$ (73.27º) & $10\bar{1}1$ (81.45º). Notice the increase in inclination angles of the planes selected. The basal planes 0006 & 0008 are the closest to linear elastic response of all planes. Although both planes represent the basal planes however each one represents a different level within the crystal structure. The plane $10\bar{1}5$ is the closest to the highest resolved shear stress at 45º. The grains that are inclined such that their basal plane are at $10\bar{1}5$ (53.08º) are thus the first from selected planes to buckle and will nucleate the highest density of DWs of all other grains selected. This is the reason for the uneven strain response in both transverse and longitudinal banks (Fig 7-21 (b) & (c)). The scatter in the results of $10\bar{1}5$ is due to the mosaicity of the basal planes within those grains, similar to those observed in single crystals [90],[91]. The changes in the inclination of the basal planes within layered grains during deformation is due to the DWs that nucleate as observed in Table 4-1. Although the tilt of the basal planes within the grains does not exceed a fraction of an angle, however their effect reflects clearly on the observed ND results. This becomes pronounced in random textured samples were the peak intensity is not enhanced to improve this drawback (unlike highly textured samples).

Despite the scatter in the $10\bar{1}5$ plane results on both banks, the existence of a fully reversible closed loop in the transverse bank cannot be denied (Fig. 7-25(b)). Microstrain and error bar intersections exist on the longitudinal bank. The intersections occur due to grain rotations during deformation and basal planes mosaicity[90],[91] as well. The grains with basal planes of *l* values lower than five in the selected plane reflections (i.e. $10\bar{1}3$, $10\bar{1}2$ & $10\bar{1}1$) gradually tend towards the vertical axis. The transverse bank illustrates close to linear elastic behavior according to the measurement accuracy and instrument

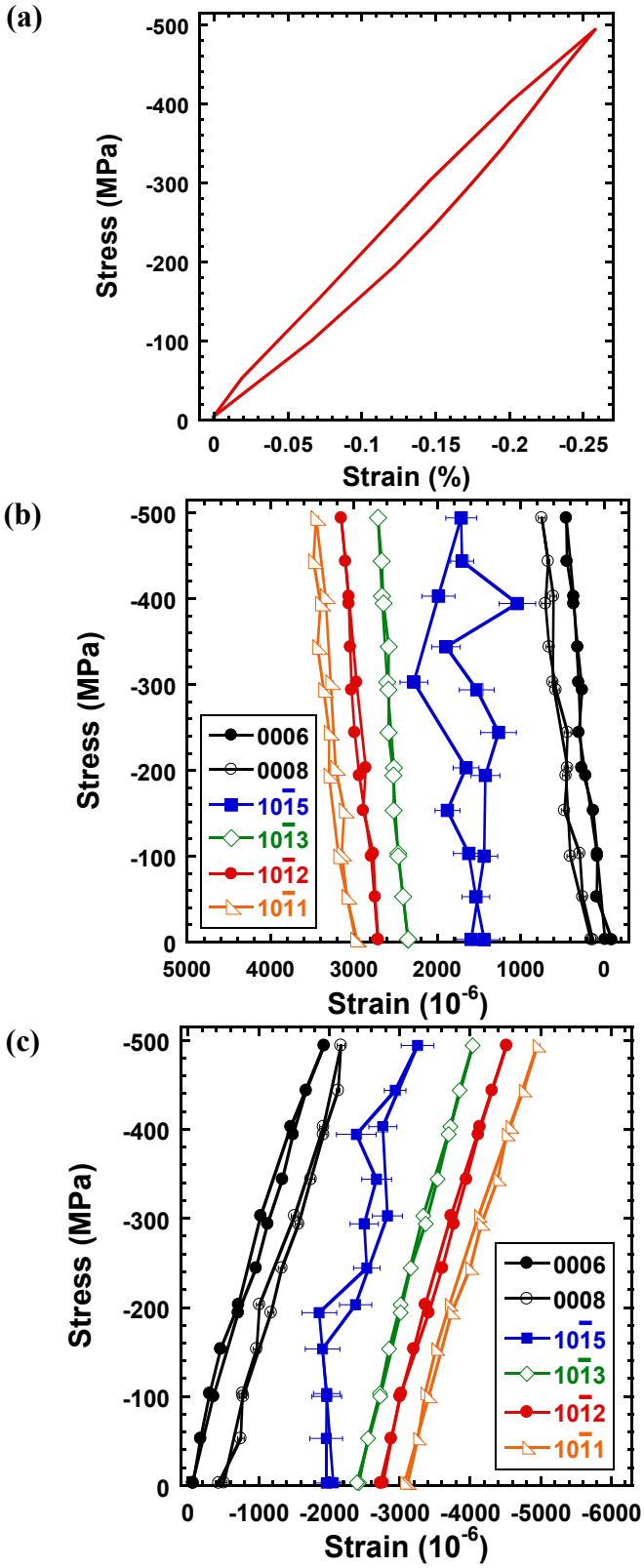

Figure 7-21: (a) Macroscopic stress-strain curve of FG Ti_3SiC_2. Complementary stress–strain response of selected $\{10\bar{1}l\}$ and basal planes along transverse (b) and, longitudinal (c) directions. The experimental results, derived from single peak fit to the ND data, taken on SMARTS.

resolution. However, the longitudinal bank displays a very important feature displaying the dual regime. A zoomed plot of the experimental measurements of $10\bar{1}3$, $10\bar{1}2$ & $10\bar{1}1$ plane reflections in addition to their linear elastic calculations obtained from EPSC execution are shown in Fig. 7-22. The experimental curves clearly show a fully reversible behavior. However, there is a deviation that occurs between the experimental results and linear elastic calculations. The stress level at which the deviation starts and the degree of deviation is different for each plane. This supports the variation in activity and development of the buckling dislocation mechanism based on the layered grain inclination angle relative to the applied load direction (a similar comparison was shown between grains at N- and P- orientations of layered grains in Fig. 3-6 and section 7.2). The experimental results show the dual behavior composed of linear and non-linear regimes.

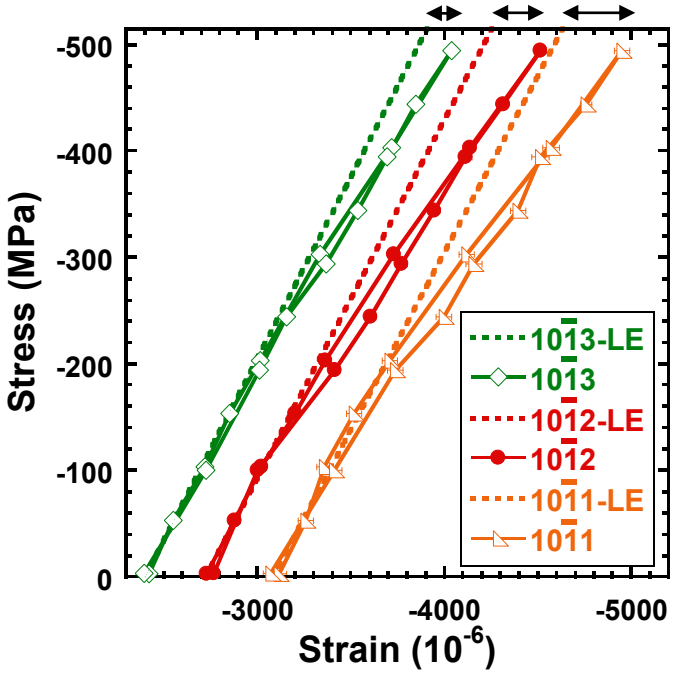

Figure 7-22: Zoom of figure 7-21(c) showing the complementary FG Ti_3SiC_2 stress–strain response of selected $\{10\bar{1}l\}$ along longitudinal direction. The dashed lines are the corresponding linear elastic response prediction obtained from EPSC calculations.

According to Schmid factor variations the percentage of deformation of the layered grain varies with the basal plane inclination angle of the grain. In addition, the percentage of grains that start to deform by buckling after reaching the critical load required for the nucleation of the initial U-shaped DWs will continue to deform according to the buckling dislocation mechanism. Strain accommodation and deformation is concentrated and restricted in those grains until the critical load is reached for additional layered grains to buckle. The layered grains that joined deformation by buckling will accommodate strain affecting the macroscopic stress-strain behavior of the system. Therefore, no additional grains will start to buckle until the critical buckling load required is reached. Hence, all unbuckled layered grained will respond to the applied load in a linear manner since there are other grains which accommodate the strain by buckling and nucleating U-shaped DWs as the load applied on them exceed the critical load for buckling. Within the grain, part of the grain behaves in a linear manner while the rest is non-linear due to the DWs nucleation and annihilation during loading and unloading.

The features of microstrain plane reflections response in Figs. 7-21 & 7-22 are a reflection of the predicted grain deformation at different basal plane inclination angles (which originate from the Schmid factor, Fig. 3-6 & 3-8). Furthermore, the relation of the hardness (or softness) of the grains due to their basal plane inclination angle with respect to the load is confirmed by the experimental plane reflection results in Figs. 7-21 & 7-22. The ratio of linear to non-linear regime varies according to the grain basal plane inclination angle relative to the loading direction. Notice that the non-linear deformation is largest on the $10\bar{1}5$ plane; in addition, it is the first to start the buckling dislocation mechanism of the selected planes. At the maximum stress applied on the sample, the

layered grains at $10\bar{1}5$ plane reach the maximum possible non-linear deformation with the maximum amount of DWs due to buckling. Those grains accommodate the maximum amount of non-linear strain of all grains since they are subjected to the highest resolved shear stress according to Schmid factor (highest shear stress is at ~ 45º, Figs. 3-6 & 3-8). All layered grains at other inclinations accommodate non-linear strain through buckling as well, however the amount of DWs nucleated is less since the percentage of the layered grain that buckle is less (i.e. there is a higher percentage of the layered grain that deforms linearly). The variation in the linear and non-linear regimes of the layered grains at different inclination angles (Figs. 7-21 & 7-22) of the crystals reflect on the sample mechanical behavior. The sum of the linear and non-linear regimes of all layered grains in the sample dictates the macroscopic mechanical response in terms of loading and unloading curves and energy dissipation.

An interesting trend is observed in Fig. 7-22 when comparing the selected plane reflections with their calculated linear elastic response. As the inclinations angle of the layered grains get closer to 45º the non-linear regime gets closer to the calculated linear elastic behavior. This feature indicates that the layered grains at angles closer to 45º will reach higher buckling harmonic modes, contain more DWs and accommodate a higher percentage of non-linear strain. The marked arrows indicating the distance between the plane reflection response and calculated linear elastic behavior demonstrate this phenomenon.

The buckling deformation that occurs in layered grained materials by applying the buckling dislocation mechanism is governed by Euler's equation (Eq.1). The surrounding forces around the grains dictate the bracing held at different locations of the layered

grains. The surrounding forces are non-uniform and uneven on the different gains. Hence, there are locations in the grain that are stronger than others. At the weakest location in the grain, the first U-shaped DWs will nucleate then develop progressively with load. The grains in layered polycrystalline materials strive not to start buckling deformation. Depending on the orientation the grain basal plane with respect to the load direction; the shear force components parallel to the basal plane layers exerts tension on the layers and inhibits deformation, while the normal force component normal to the layers promotes deformation initiation and development. Moreover, the grain layers bracing depends on the elastic modulus of the surrounding grains (which changes based on the grain orientation relative to the neighboring grain) which varies from one location to another. This is the reason why each sample fabricated is unique. Each sample has a different system of elastic modulus and force components normal and parallel to the grain layers. This spectrum of grain orientations and interconnection between them play a combined role in the response of the grains during loading and unloading. They dictate how and where will they deform, how many DWs and kinks will develop, what stage will be reached in the buckling dislocation mechanism, and the amount of initial irreversible plastic strain in the first loading cycle if the sample has not experienced the load level previously. All those factors contribute altogether in the resulting macroscopic stress-strain behavior and defining all details of loading/unloading curvature dictating the energy dissipated by each loading cycle.

The experimental results of plane reflections in Figs. 7-21 & 7-22 (in terms of initiation of microstrain deviation and amount of deviation from linear elastic response) indicate that the grains adapt to the conditions they experience and their response is

interconnected with the grains in the whole system. From this analysis, it is concluded that during unloading, the reverse occurs in the deformed layered grains in the reverse order since the largest elastic modulus applied on the grain is the last to allow deformation to occur and the first to restore it. In addition, the first U-shaped DWs allowed to form were at the lowest load applied with the weakest supporting elastic modulus. All these features describe the global mechanical behavior of polycrystalline materials containing layered structured grains and are universal to all layered structured materials.

The primary and secondary DWs in the buckling dislocation mechanism are not permanent. They rotate, move, enlarge or shrink and affect the final mechanical response. The DWs adjust their state depending on the loading conditions to accommodate the strain and force components applied (e.g. Table 4-1 & Fig. 2-10). Unlike dislocation slip and/or twin which result in permanent crystallographic deformation inside the grain crystal. After plastic deformation of non-layered crystal structured materials, there are grains that have plastically deformed while others deformed elastically. The elastic strains generated by all grains result in residual strain in the material. However, in layered solids which deform by the buckling dislocation mechanism the whole polycrystalline system contributes in restoring the deformed grains at any level to its original state during unloading. This remarkable feature is due to the non-crystallographic nature originating from the carpet-like edge dislocation configuration facility. The DWs mobility enables the edge dislocations to follow the force components on the close-packed basal slip plane (e.g. Table 4-1 & Fig. 2-10). The non-crystallographic nature plays a major role in the facilitating the whole layered structured system (whether polycrystalline or single crystal)

to have a fully reversible recoverable nature with no residual strain in the material after complete unloading.

7.3.2 Random Textured Polycrystalline CG and Porous Ti_3SiC_2

Figure 7-23 displays the macroscopic stress-strain KNE mechanical behavior of CG Ti_3SiC_2 (a), in addition to the longitudinal (b) and transverse (c) plane reflection results from in situ ND. The stress-strain curve for FG Ti_3SiC_2 is plotted in Fig. 7-23(a)(i) for comparative purposes. Notice that all of the features observed and perceived in the FG Ti_3SiC_2 (Fig. 7-21) results applies here as well. The only difference is in the maximum possible applied stress in CG being at 270MPa, rather than 500MPa in FG Ti_3SiC_2. Hence the single peak fit plane reflections for the transverse and longitudinal banks selected in Fig. 7-23 are the same as in Fig. 7-21 for FG Ti_3SiC_2 and are presented in the same manner. The corresponding zoomed plot of experimental measurements $10\bar{1}3$, $10\bar{1}2$ & $10\bar{1}1$ plane reflections for CG Ti_3SiC_2 in addition to their linear elastic calculations obtained from EPSC execution are shown in Fig. 7-24. The same characteristics observed here as in Fig. 7-22 for the FG Ti_3SiC_2. The same applies for the porous Ti_3SiC_2 ND results in Figs. 7-25 and 7-26 but at a macroscopic compressive load of 600MPa.

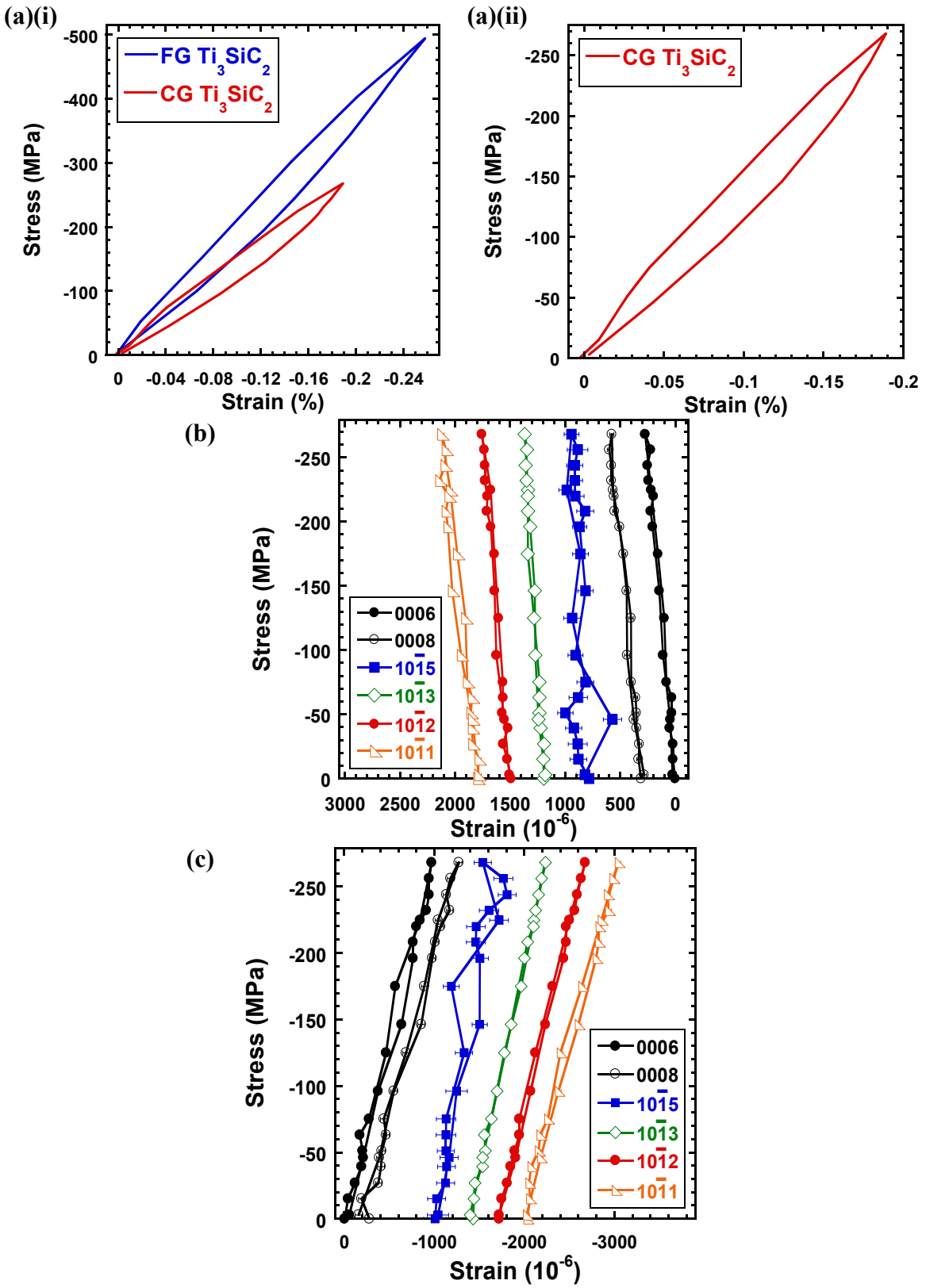

Figure 7-23: (a) Macroscopic stress-strain curve of FG & CG Ti_3SiC_2 for comparison. Complementary stress–strain response for CG Ti_3SiC_2 of selected $\{10\bar{1}l\}$ and basal planes along transverse (b) and, longitudinal (c) directions. The experimental results, derived from single peak fit to the ND data, taken on SMARTS.

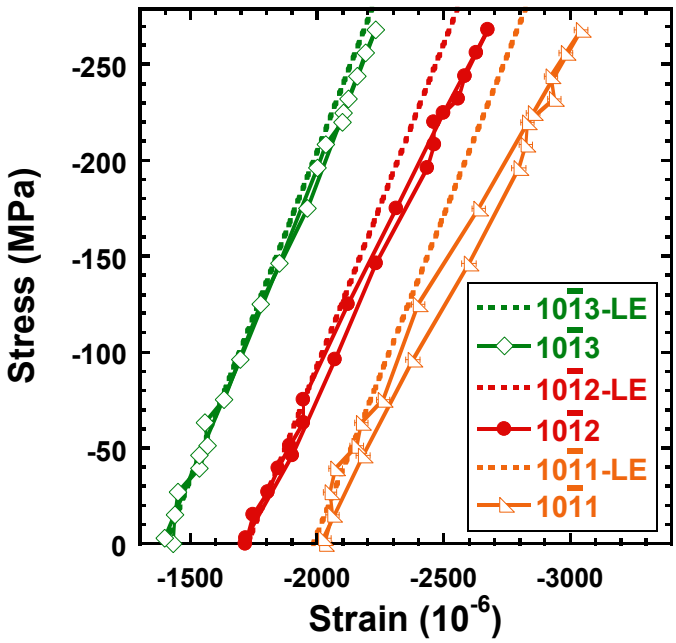

Figure 7-24: Zoom of figure 7-23 (c) showing the complementary CG Ti_3SiC_2 stress–strain response of selected $\{10\bar{1}l\}$ along longitudinal direction. The dashed lines are the corresponding linear elastic response prediction obtained from EPSC calculations.

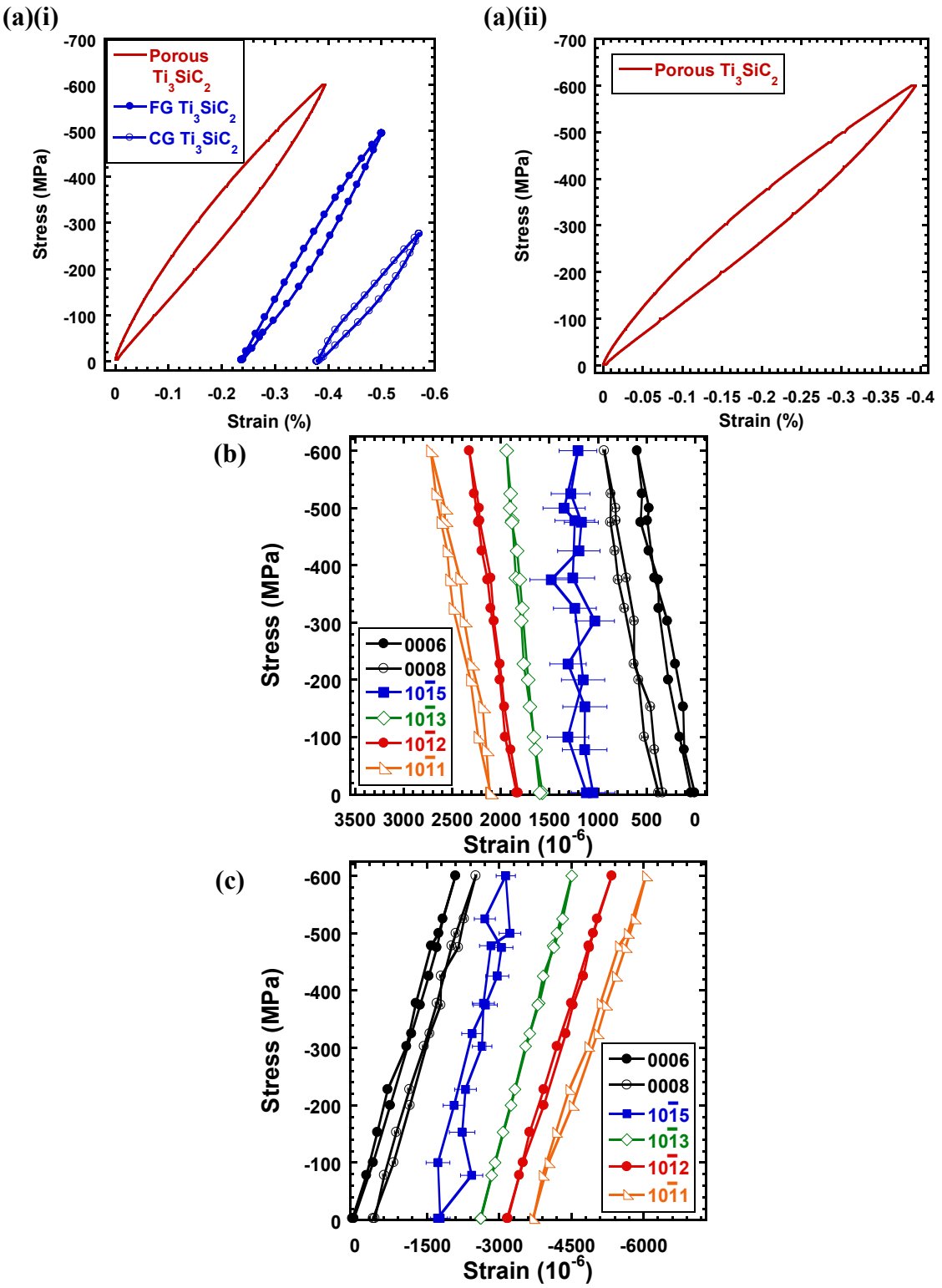

Figure 7-25: (a) Macroscopic stress-strain curve of Porous, FG & CG Ti_3SiC_2 for comparison. Complementary stress–strain response of Porous Ti_3SiC_2 for selected $\{10\bar{1}l\}$ and basal planes along transverse (b) and, longitudinal (c) directions. The experimental results are derived from single peak fits of the in situ ND diffractograms.

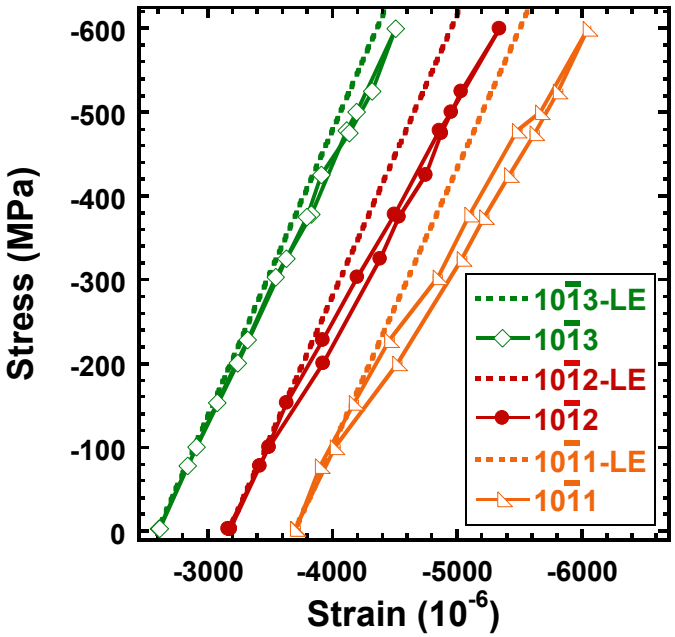

Figure 7-26: Zoom of figure 7-25(c) showing the complementary Porous Ti_3SiC_2 stress–strain response of selected $\{10\bar{1}l\}$ along longitudinal direction. The dashed lines are the corresponding linear elastic response prediction obtained from EPSC calculations.

7.3.1 Summary & Conclusions

The purpose of this chapter is to shed more light on kinking nonlinear elasticity and their crystal plane reflections response under mechanical deformation employing in situ ND technique. This was done by the study of random textured linear elastic Ti_2SC, fine, coarse and porous grained Ti_3SiC_2, in addition to highly textured Ti_2AlC. The results are discussed with an insight of the buckling dislocation mechanism demonstrated in previous chapters. The relation between grain size, Euler's equation (Eq. 1) and the buckling dislocation mechanism are discussed providing an understanding of the effect of grain size on the macroscopic stress-strain curves.

Chapter 8: Conclusions and Proposed Future Work

Features of buckling are observed in layered and layered-like (HCP materials with c/a ratio ~ 1.4) solid materials. The characteristics of the dislocation mechanism nucleation and motion observed in DWs, mosaic walls, primary and secondary DWs in different layered solid were shown in chapters 1 and 2. The relation between column buckling and layered solid buckling in polycrystalline materials has been described. Kink bands are observed in geological layers as well. The main types of layered solid folds observed in nature were clarified in addition to the available kink band models developed by different research groups.

In this work, the main features of the buckling dislocation mechanisms taking place in layered structures has been identified. In addition, the Schmid factor maps presented in Ch. 3 outline the shape of the traction that would be acting on layered structures in the N- and P-sample directions under loading. The Schmid factor maps where applied on the PP experiment by Dodwell *et al.* [5, 20, 21] in the P-sample direction. Analogies between extrusion and indentation where with different stages of the buckling dislocation mechanism for simplification of mechanism illustration.

The inverse expansion effect that occurs during buckling deformation of layered solids when inclined horizontally is believed to be the reason for the lower experimentally measured microstrain of the (0004) plane grains and expansion along compressive axis of the Ti_2AlC N-sample. This inverse expansion effect was observed by other layered solids as well. Common sources of mechanical hysteresis like Bauschinger effect, microcracking and reversible twinning were eliminated as possible mechanisms responsible for the macroscopic and microscopic mechanical response observed in the

textured Ti_2AlC samples. Dislocation pile-ups was eliminated as well through dislocation density calculations indicating two orders of magnitude less than that experimentally measured through the FWHM of the (0004) peak broadening.

The PP experiment performed by Dodwell *et al.* [5, 20, 21] is a valuable experiment that displayed vital information. It would have not been possible to validate the 3D Schmid factor maps acting on layered solids in the N- and P-sample directions without their experiment. Similar experiments need to be performed on different orientations since each angle would have a corresponding set of normal and shear force maps. The setup required for these experiments needs to be investigated. A lot of variable parameters in the PP experiment need to be changed to obtain the possible variations in the response of the structure during loading. These parameters include sponge strength, changing paper to cardboard or aluminum sheets of different thicknesses, the ply wood distance from the layered structure which would alter the support provided, changing the coefficient of friction between the layers (by adding grease between aluminum sheets or sticky glue to increase friction). All of these are parameters that need to be investigated to understand the nature of layered structures buckling at different conditions. This would help in understanding the response of crystalline layered structured materials in literature.

However, similar experiments performed via in situ SEM and TEM of crystalline layered structures is very important. The observation of extrusion and/or indentation buckling could be identified through these experiments. The surrounding support could be designed to enforce specific buckling harmonic modes resulting into secondary DWs and kink bands.

Extensive studies are available by geologists and mathematical groups on the formulae that govern the fold that occur during buckling or layered structures. The relation between the available work and the Schmid factor maps need to be established. This would set the ground for obtaining the mechanics required for modeling buckling of layered structured materials.

Slip, twinning and buckling are possible active dislocation mechanism in HCP materials at the borderline of c/a ~ 1.4, like Mg and Zn. The traction on the grains and their orientation would dictate which mechanism(s) would be activated. The availability of a model capable of activating buckling dislocation mechanism would assist in differentiating between the different mechanisms.

MAX phases have a KNE mechanical response where buckling is the dislocation mechanism taking place. Variations in grain size and texture result in large difference in their mechanical behavior. The relations between layers inclination, sample texture, layers dimensions and material needs to be investigated since each change in those parameters would alter the mechanical response of the sample. Further research on those parameters would optimally result in designing materials performing in the required mechanical response needed for practical applications.

Appendix

This appendix is divided into three sections. Section A presents the EPSC fittings done on FG, CG & Porous Ti_3SiC_2 assuming basal slip or $11\bar{2}1$ twin activated. Section B demonstrates the derivation of the dislocation pile-ups density equation used in chapter 7.2. The MAX phases experimented were tested using ultrasonic bias stress (UBS), another in situ characterization technique. For comparative purposes sapphire and alumina were selected to be tested on UBS as well; classified as linear elastic ceramic materials. FG and CG alumina were tested as well to observe the effect of grain size. The UBS theory is presented in section C, in addition to the selected linear ceramic materials characterization, experimental details and UBS results for the linear elastic ceramic materials and MAX phases.

A: EPSC fitting of stress- strain curve on CG, FG and porous Ti_3SiC_2

(a)

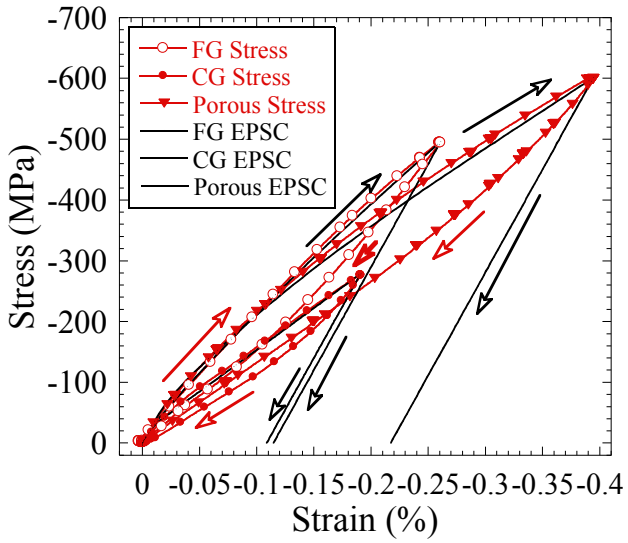

(b)

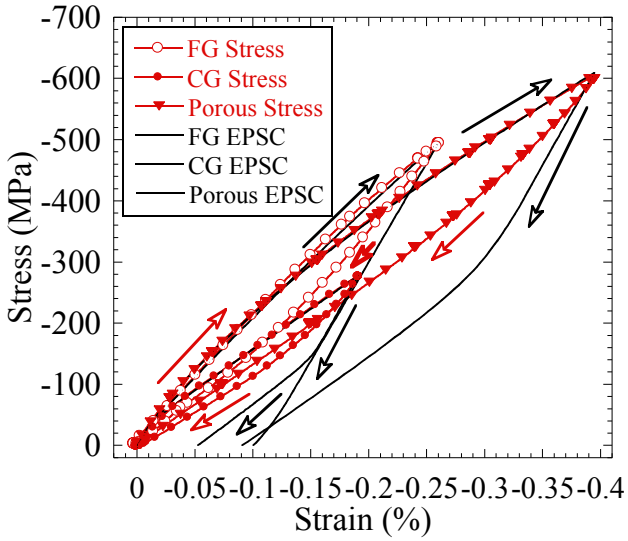

Figure A-1: Fine Grained (FG), Coarse Grained (CG) and porous Ti_3SiC_2 stress-strain curve and EPSC fits activating (a) $(11\bar{2}1)$ twin, (b) Basal slip systems. Note that EPSC yields residual mechanical deformation due to dislocation pile-ups and twinning whereas KNE solids show closed-loop hysteresis.

(a)

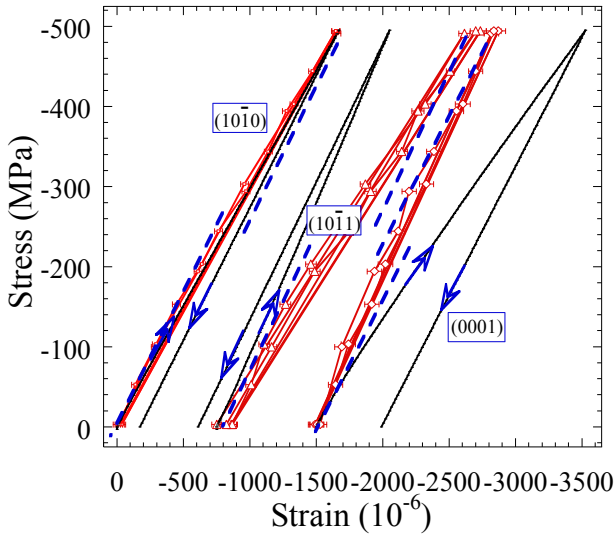
-500
-400
-300
-200
-100
0
Stress (MPa)
(10$\bar{1}$0)
(10$\bar{1}$1)
(0001)
0 -500 -1000 -1500 -2000 -2500 -3000 -3500
Strain (10^{-6})

(b)

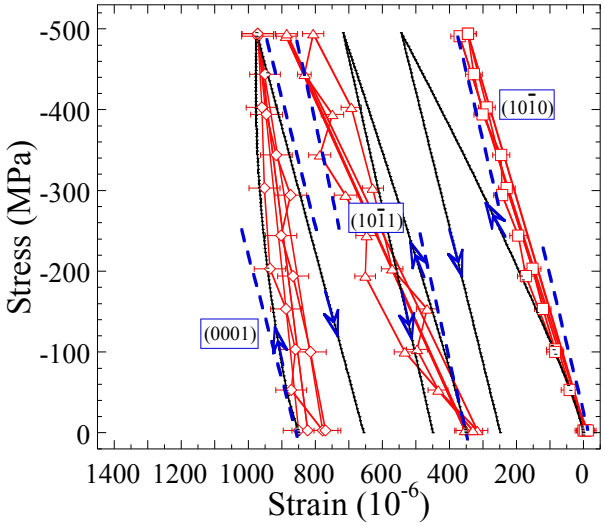
-500
-400
-300
-200
-100
0
Stress (MPa)
(10$\bar{1}$0)
(10$\bar{1}$1)
(0001)
1400 1200 1000 800 600 400 200 0
Strain (10^{-6})

(c)

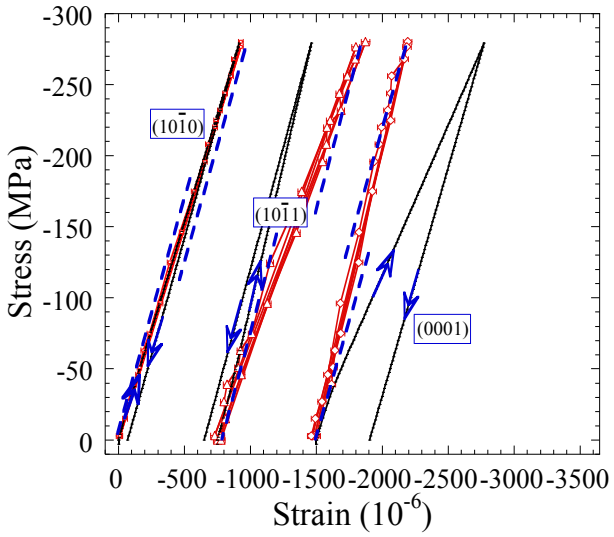
-300
-250
-200
-150
-100
-50
0
Stress (MPa)
(10$\bar{1}$0)
(10$\bar{1}$1)
(0001)
0
-500
-1000
-1500
-2000
-2500
-3000
-3500
Strain (10^{-6})

(d)

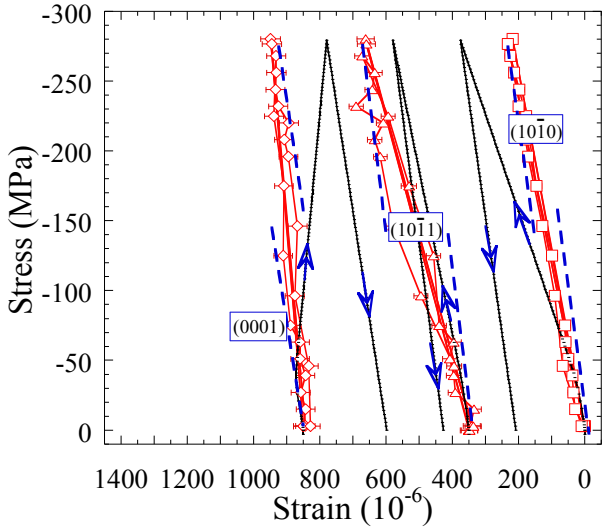
-300
-250
-200
-150
-100
-50
0
Stress (MPa)
(10$\bar{1}$0)
(10$\bar{1}$1)
(0001)
1400
1200
1000
800
600
400
200
0
Strain (10^{-6})

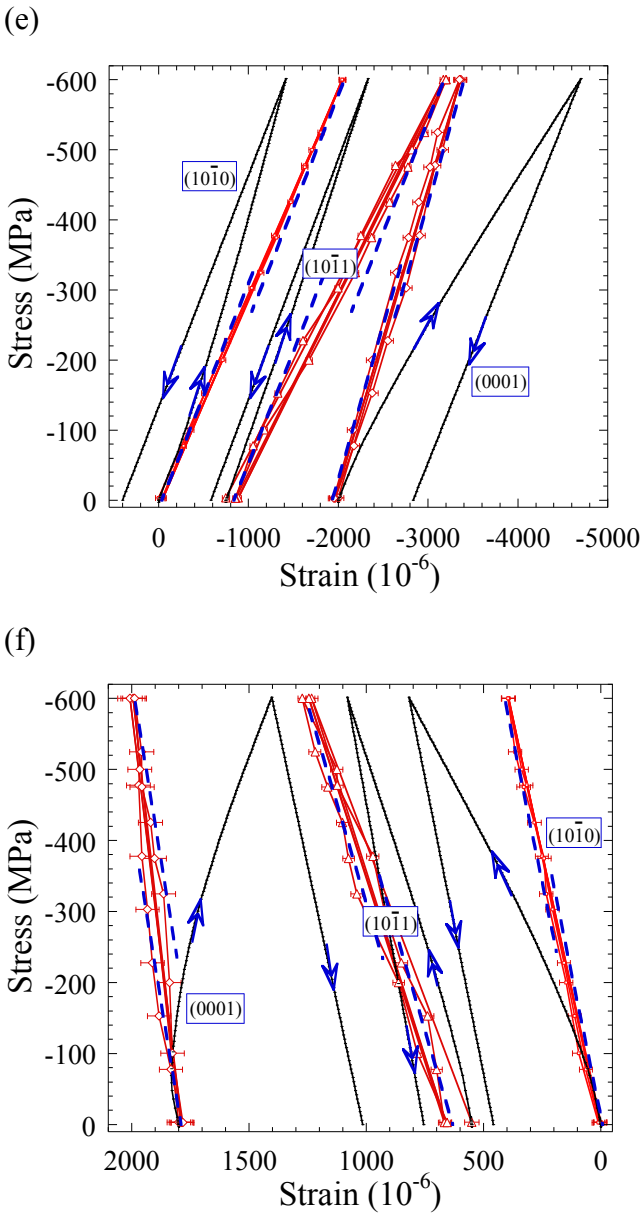

Figure A-2: Microstrain response for (10$\bar{1}$0), (10$\bar{1}$1), (0001) planes activating (11$\bar{2}$1) twin; (a) & (b) are for FG, longitudinal & transverse, respectively; (c) & (d) CG, longitudinal & transverse, respectively. (e) & (f) Porous Ti_3SiC_2 , longitudinal & transverse, respectively. The curves are shifted along the x-axis for better visibility. (Rietveld: Red lines, EPSC: Black lines)

(a)

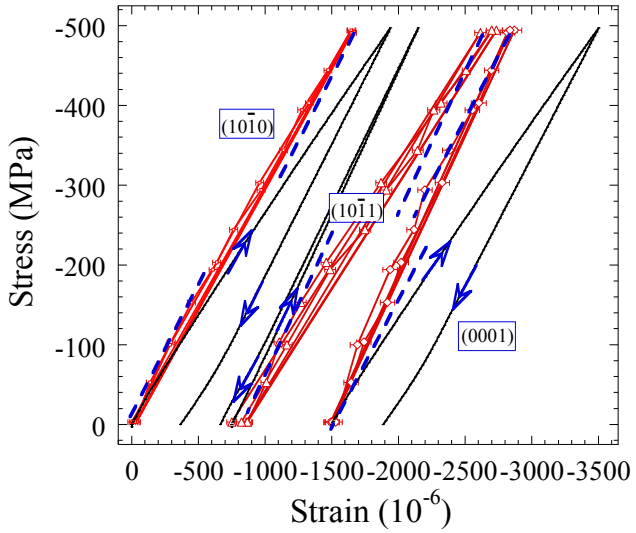
-500
-400
-300
-200
-100
0
Stress (MPa)
(10$\bar{1}$0)
(10$\bar{1}$1)
(0001)
0
-500
-1000
-1500
-2000
-2500
-3000
-3500
Strain (10^{-6})

(b)

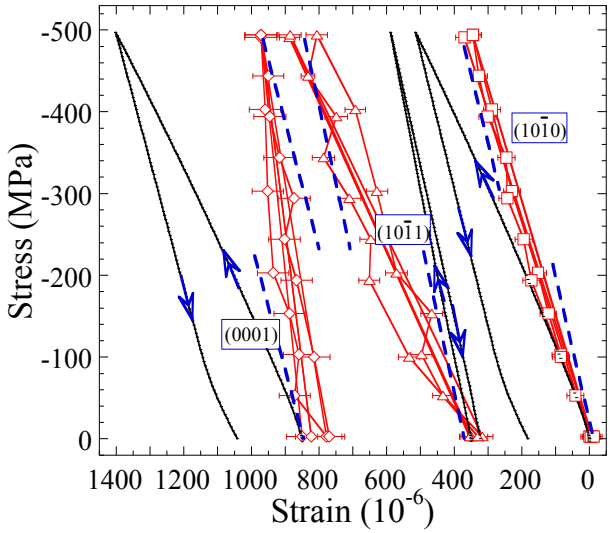
-500
-400
-300
-200
-100
0
Stress (MPa)
(10$\bar{1}$0)
(10$\bar{1}$1)
(0001)
1400
1200
1000
800
600
400
200
0
Strain (10^{-6})

(c)

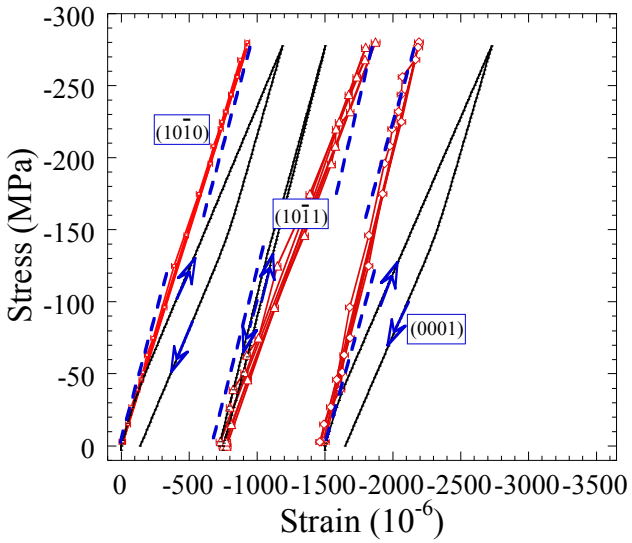
-300
-250
-200
-150
-100
-50
0
Stress (MPa)
(10$\bar{1}$0)
(10$\bar{1}$1)
(0001)
0
-500
-1000
-1500
-2000
-2500
-3000
-3500
Strain (10^{-6})

(d)

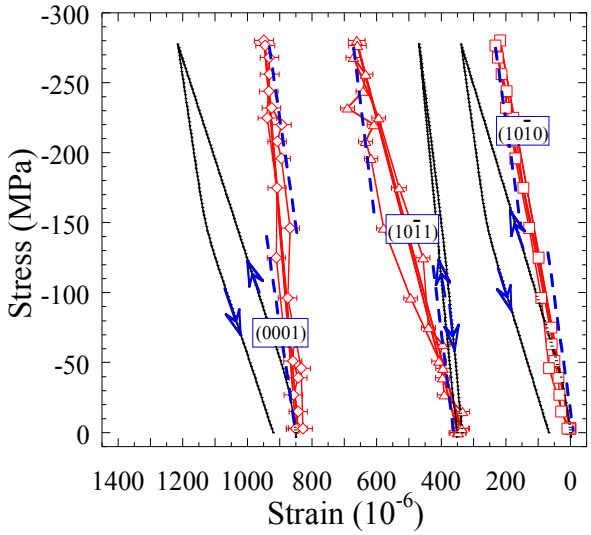
-300
-250
-200
-150
-100
-50
0
Stress (MPa)
(0001)
(10$\bar{1}$1)
(10$\bar{1}$0)
1400
1200
1000
800
600
400
200
0
Strain (10^{-6})

(e)

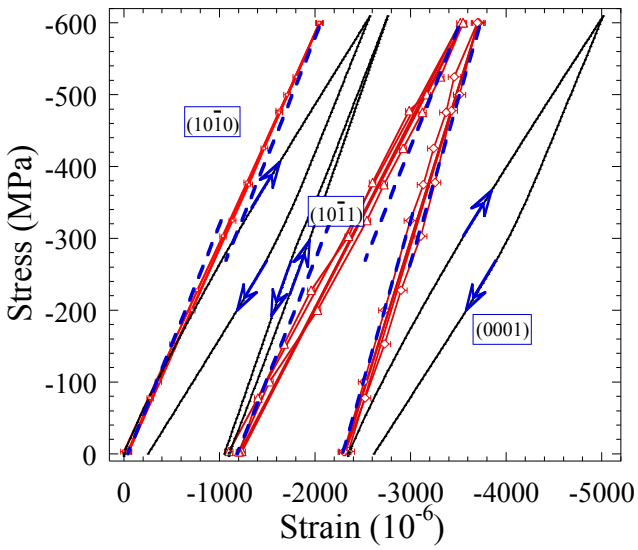

(f)

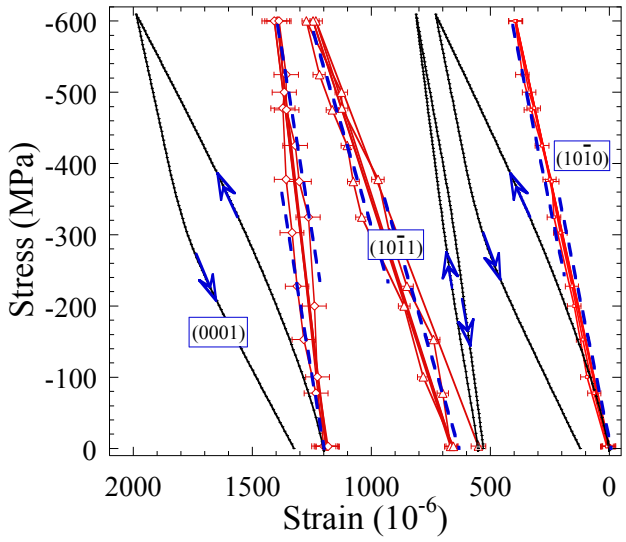

Figure A-3: Microstrain response for (10$\bar{1}$0), (10$\bar{1}$1), (0001) planes activating basal slip; (a) & (b) are for FG, longitudinal & transverse, respectively; (c) & (d) CG, longitudinal & transverse, respectively. (e) & (f) Porous Ti_3SiC_2 , longitudinal & transverse, respectively. The curves are shifted along the x-axis for better visibility. (Rietveld: Red lines, EPSC: Black lines)

Table A-1: Elastic constants, C_{ij} (in GPa) for Ti_3SiC_2. The average values were used in EPSC fittings.

C_{11}	C_{12}	C_{13}	C_{33}	C_{44}	C_{66}	Comments
365	125	120	375	122	120	LDA [100]
360	84	101	350	158	138	GGA [101]

B: Nonlinear Strains and Dislocation Densities

Dislocation Pileups

The energy stored - per unit length measured along their lines - in one pileup with n dislocations is given by: [102]

$$U_L = \frac{Gb^2}{4\pi(1-\nu)} n^2 \ln[4\sqrt{e}] \qquad \text{B1}$$

where G, b and ν are the shear modulus, Burgers vector and Poisson's ratio. Further assuming,[102]

$$n = \frac{\pi\lambda(1-\nu)}{Gb}\tau \qquad \text{B2}$$

where τ is the applied shear stress and λ the grain diameter. Converting to an energy per unit volume then:

$$U_{DP} = \frac{Gb^2}{4\pi(1-\nu)} 2\pi\lambda_{av} N_{DP} \frac{\pi^2\lambda^2(1-\nu)^2}{G^2b^2}\tau^2 \ln(4\sqrt{e})$$

$$U_{DP} = \frac{\pi^2\lambda^2\lambda_{av}(1-\nu)}{2G} N_{DP}\tau^2 \ln\left(4\sqrt{e}\right) \qquad \text{B3}$$

Where N_{DP} is the number of DP per unit volume and λ_{av} is the average length of a dislocation in a pileup. But since $U_{DP} = ½\,\gamma_{DP}\tau$, where τ is applied shear stress and γ_{DP} is the shear strain then:

$$\gamma_{DP} = \frac{\pi^2\lambda^2\lambda_{av}(1-\nu)}{G} N_{DP} \ln\left(4\sqrt{e}\right)\tau \qquad \text{B4}$$

Assuming $\lambda_{av} = \lambda/3$, then:

$$\gamma_{DP} = \frac{1.89\pi^2\lambda^3(1-\nu)}{3G} N_{DP}\ \tau \qquad \text{B5}$$

Further assuming, $\tau = \sigma/M$ and $\gamma_{DP} = 2\varepsilon_{DP}(1+\nu)/M$, then B5 can be recast to read:

$$\varepsilon_{DP} = \frac{1.89\pi^2\lambda^3(1-\nu)}{6G(1+\nu)} N_{DP}\sigma \qquad \text{B6}$$

The corresponding dislocation density associated with this strain is:

$$\rho_{DP} = 2\pi \frac{\lambda}{3} n N_{DP} \tag{B7}$$

Combining Eqs. B2, B6 and B7, it can shown that:

$$\rho_{DP} \approx \frac{2.1(1+\nu)\varepsilon_{DP}}{Mb\lambda} \tag{B8}$$

C: Ultrasonic Bias Stress (UBS) in situ characterization technique

C1: UBS in situ characterization technique theory

In this section the theory behind UBS characterization technique is elucidated. In general, quite different information about dislocations is obtained from the UBS and in situ ND techniques. What the two techniques share in common, however, is that they both yield information about dislocations in the bulks of the samples. The ultrasonic waves are transmitted through the entire volume of the material tested.

A brief background about anelastic mechanical behavior is needed before explaining the UBS characterization technique. Section C1.1 presents the theory of anelastic mechanical behavior and internal friction in materials.

C1.1 Anelastic Mechanical Behavior and Internal Friction

The mechanical behavior of any material starts by an elastic regime followed by plastic deformation. However, it is often observed in materials that well below the plastic yield stress, strain deviations from elastic behavior are encountered. This deformation is usually referred to as “anelastic deformation”, where energy is dissipated and the strain response is non-instantaneous but recoverable (unlike plastic deformation which is non-recoverable). Hence, in the elastic regime, strain is divided into elastic strain and anelastic strain. Figure C-1 illustrates the strain response observed in materials when a constant stress is applied on a solid material in the elastic regime for finite time duration. Figure C-1(a) shows the constant stress versus time, $\sigma(t)$, graph applied on the material. Figures C-1(b)-(d) show the corresponding strain versus time, $\varepsilon(t)$, of different materials mechanical behavior. If the material is stiff and does not deviate from Hooke’s law (i.e.

perfect elastic) a constant strain will be measured during the loading time and an instantaneous complete recovery to zero strain will occur at unloading (Fig. C-1(b)). This response is typically represented by a spring. At the other end, the material might behave in a perfectly plastic manner where the material does not recover to its initial strain upon unloading (Fig. C-1(d)). However, the material might illustrate a viscous Newtonian response, where a gradual increase in strain takes place and remains constant upon unloading (Fig. C-1(c)). The dashpot rheological model designates this mechanical behavior. Anelastic materials illustrate a viscous response; however there is a restoring force that retracts the strain back to zero. The rheological setup and strain response that represents anelastic deformation is shown in Fig. C-2.

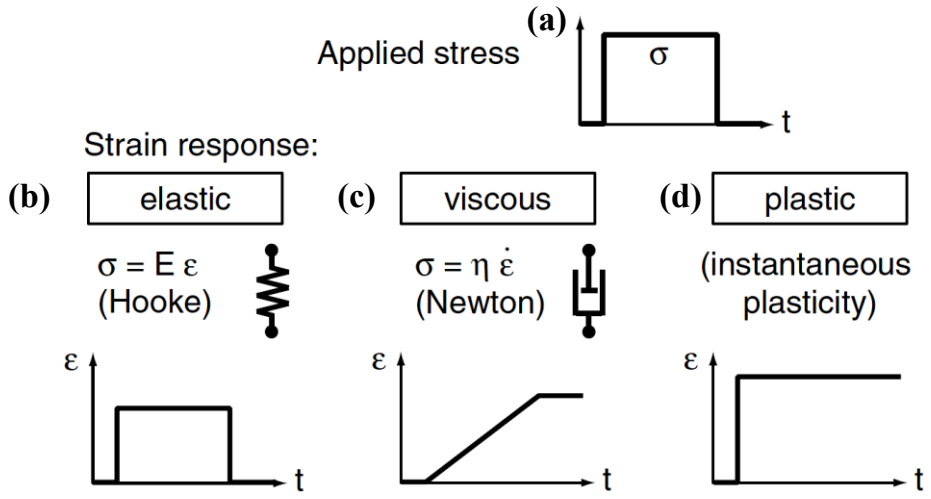

Figure C-1: Fundamental types of mechanical behavior: response of strain ε(*t*) to a constant stress of finite duration with abrupt loading and unloading[103].

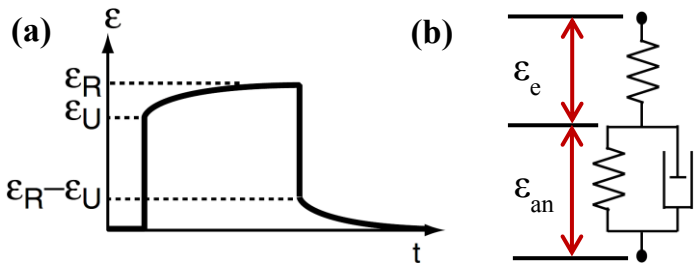

Figure C-2: Anelastic mechanical model with the same applied stress as in Fig. C-1: (a) ε(t) plot showing completely recoverable strain ("standard anelastic solid"), ε_R relaxed strain, ε_U unrelaxed strain; (b) Rheological setup of anelastic response, where ε_e is elastic strain and ε_{an} is anelastic strain.

There is an initial elastic strain, ε_e (Fig. C-2(b)) responsible for the unrelaxed strain, ε_U (Fig. C-2(a)), when the material is loaded. Due to the anelastic material visco-elastic behavior, strain continues to increase until the material reaches a relaxed state, ε_R (Fig. C-2(a)) at the constant load. As soon as the material is unloaded, the spring representing the material elastic strain shows an instantaneous strain recovery reaching a strain of $\varepsilon_R - \varepsilon_U$ (Fig. C-2(a)). As time proceeds, a complete strain recovery occurs due to the contribution of the elastic spring parallel to the viscous dashpot responsible for the material's anelastic behavior, ε_{an} (Fig. C-2(b)). This phenomenon of material self-adjusting with time to a new equilibrium state is called "relaxation".

It is perceived that dislocations have a major role in relaxation of anelastic materials[103]. Knowledge about dislocation motion mechanism during deformation is an important scientific topic studied theoretically and experimentally in order to predict materials mechanical behavior[8, 104-108]. One of the methods for studying dislocation motion is through measurement of Internal Friction (IF). "Internal friction is generally defined as the dissipation of mechanical energy inside a gaseous, liquid or solid medium. In solid materials – 'internal friction' usually means energy dissipation connected with

deviations from Hooke's law, as displayed by some stress–strain hysteresis in the case of cyclic loading of anelastic materials".[103]

In most crystalline solids, dislocations are pinned by defects in general. In the elastic regime, the dislocations are capable of bowing-out but not moving themselves, or the defects, from their positions (Fig. C-3). This bowing effect is believed to be responsible for the anelasticity observed in some solids. Different materials' internal friction, resulting from dislocation bowing, have been and studied at various temperatures and loading conditions by many researchers[103, 109-119].

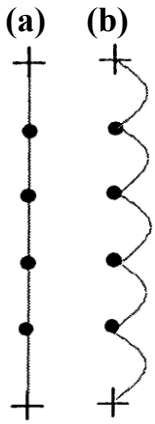

Figure C-3: Model of the interaction of dislocations and point or other defects during cyclic loading. Solid circles are mobile defects, crosses are strong pinning points. (a) Equilibrium state without any load, (b) Loading within the elastic regime.[120]

There are a variety of relaxation effects that can play a role, in addition to dislocation bowing. Figure C-4 gives an overview of various dislocation-damping contributions in a wide range of frequencies of the applied vibrations. The relaxation, internal friction, and peaks in Fig. C-4 are divided into:

(1) Those caused by movement of dislocations themselves due to the nucleation and propagation of thermal or geometrical kinks (Bordoni, Niblett–Wilks peaks)[103].

(2) Those caused by interaction of dislocations with lattice point defects (vacancies, self-interstitials: “Hasiguti Peaks”) [103].

(3) Those caused jointly by dissolved foreign interstitial atoms and dislocations (Snoek–Köster relaxation, dislocation-enhanced Snoek effect) at more elevated temperatures, “The Snoek–Köster Relaxation” and “Dislocation-Enhanced Snoek Effect” [103].

(4) Those caused, at still higher temperatures, by dislocation climbing, or other diffusion-controlled processes, “Dislocation Relaxation Peaks at Medium Temperatures”[103].

In MAX phases, it is expected to detect the effect of Hasiguti peaks where dislocation walls interact with material lattice point defects during their nucleation, growth and movement. An innovative characterization technique described in section C1.2 is needed to understand the nature of this interaction.

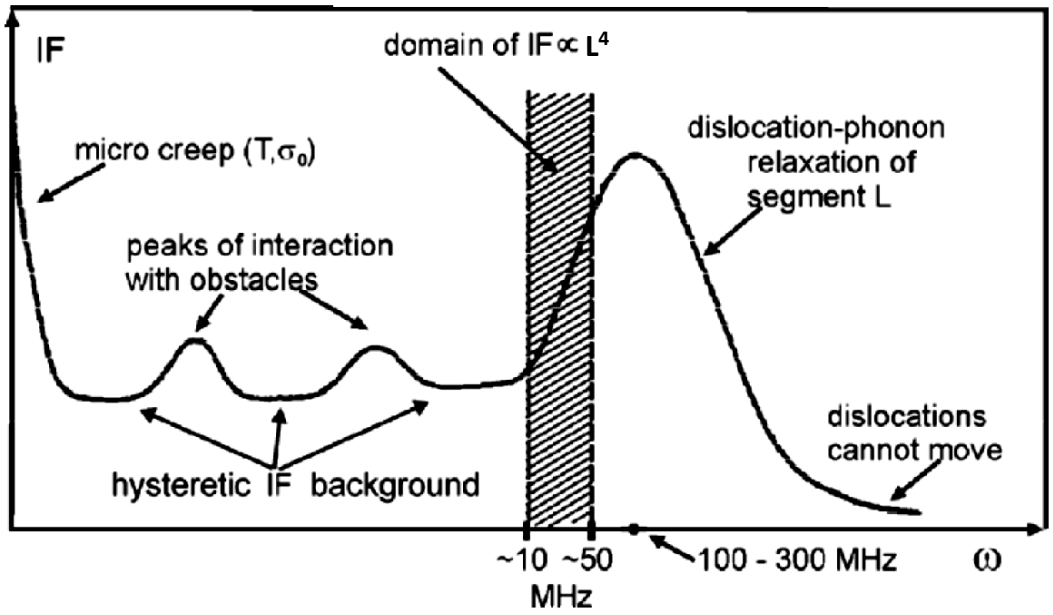

Figure C-4: Schematic damping spectrum (internal friction IF) due to dislocations on the frequency scale[103].

C1.2 Acoustic Coupling Technique (ACT) and Ultrasonic Bias Stress (UBS)

Internal friction measurements display peaks demonstrating resonance of dislocations interacting with a material's crystal periodicity and/or different point and other defects in the material[103, 117, 121-124]. A lot of research has been devoted to distinguish the different peaks due to the difficulty in deducing the interaction mechanism associated with a specific internal friction peak.[103, 114, 125] Acoustic Coupling technique, ACT, is a method devised by Gremaud [126] that can be used to distinguish between the different dislocation motion mechanisms attributed to specific peaks.[127]

Figure C-5(a) shows a schematic of an ACT setup. Here the sample is subjected to low-frequency cyclic stress of high amplitude in the form of compressive stress applied by a mechanical testing instrument. Simultaneously, a high-frequency stress of low amplitude carried as ultrasonic waves transverses through the sample. The ultrasonic wave is generated by a quartz transducer adhered normal to the compressive mechanical stress axis. Figure C-5(b) show schematic of ACT setup illustrating the stress mode applied on the sample. In this work, we used a variation of the ACT technique known as ultrasonic-bias stress (UBS) technique. In the latter, a saw-tooth loading-profile is applied, as opposed to the former where a sinusoidal profile is applied (Fig. 6-7(b)).

In the UBS technique a burst generated by the quartz transducer travels through the material and rebounds back to be read by the transducer again. During its flight, the burst losses some of its energy due to the interaction with the material bonds, defects, grain boundaries etc… resulting in a decrease in amplitude observed in the first echo. The echo makes repetitive flights through the material as its amplitude diminishes, forming a train of echoes (Fig. C-5(c) & (d)). The loss in signal amplitude with increasing

propagation distance is called attenuation “α”. In addition, a phase shift occurs when the burst/echoes rebounds at the material surface due to the difference in transmission media at the material boundary (Fig. C-5(d)).

The simultaneous application of ultrasonic waves and mechanical load during UBS experimentation exert different ranges of frequency (over a narrow range) and amplitude stress waves in the material, resulting in different strain effects on a material's dislocations. The high-amplitude, low-frequency mechanical load changes the position and size of the dislocation loops, whereas the low-amplitude high-frequency ultrasonic wave causes the dislocations to vibrate within its position. In other words, the ultrasonic wave probes the dislocation as they change shape and size.

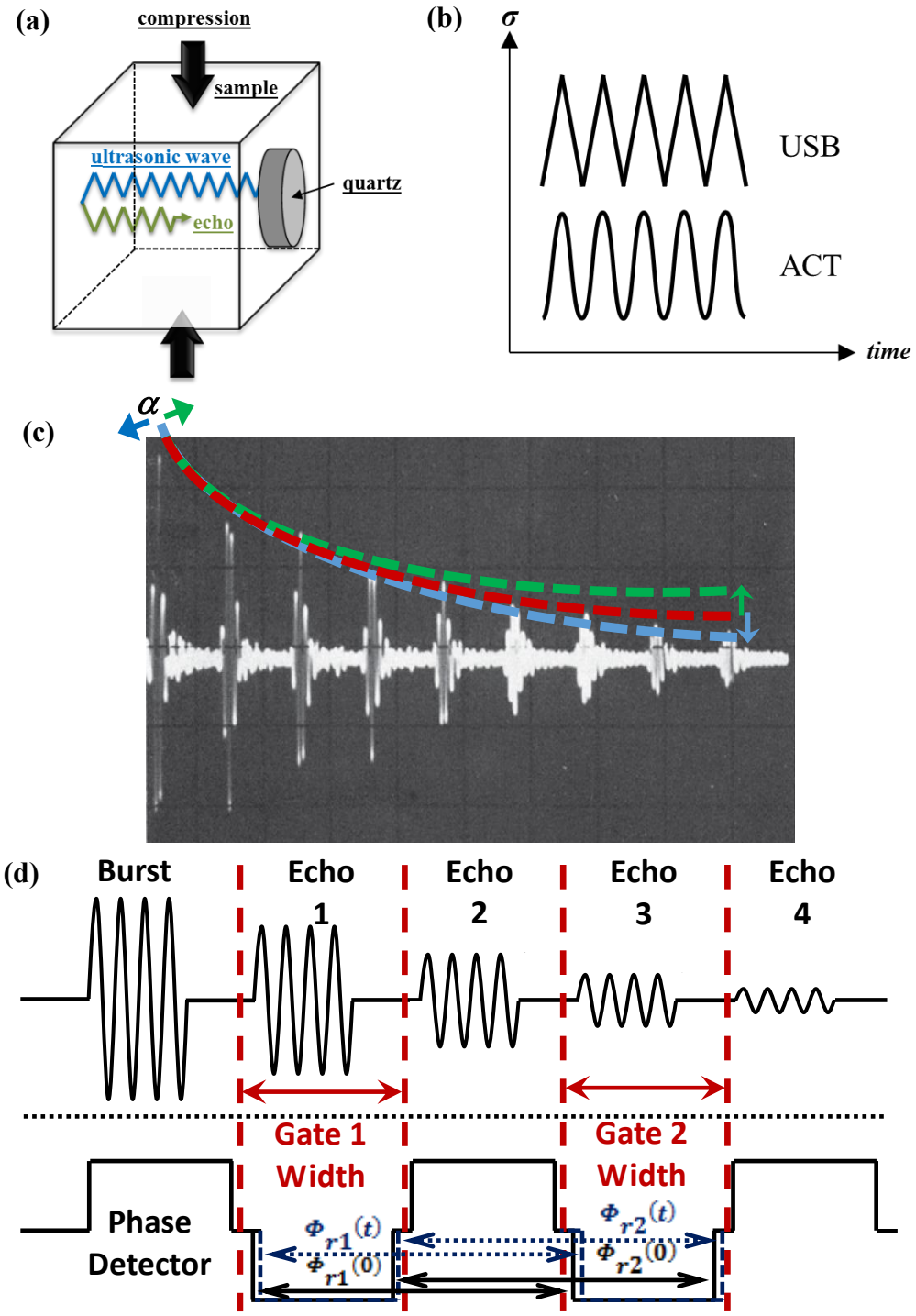

Figure C-5: (a) Schematic of sample and transducer configuration for UBS measurements. (b) Difference between Ultrasound-Bias Stress and Acoustic Coupling Technique, (c) Train of echoes resulting from pulse-echo technique. Red dashed line is on the peaks of the echo amplitudes showing the initial attenuation of the material, green dashed line indicates an increase in attenuation relative to the initial attenuation and, light blue dashed line indicates a decrease in attenuation relative to the initial attenuation[128], (d) Schematic of oscilloscope view of burst and resulting echoes. The phase detector channel is shown below where the red dashed lines indicate the width of the gates adjusted with respect to the echoes and phase detector; dotted blue double arrows and solid black double arrows indicate the phase shifts of echo 1 with respect to echo 3.

Figure C-6 (a)-(c) show the effect of the mechanical load on a dislocation. The ultrasonic stress wave stress, σ_{US}, is much lower than the low-frequency mechanical stress, σ_{LF}. At state (a), the mechanical applied load is minimal, σ_{min} and the dislocation line is slightly bowed. However as loading increases with time, $\sigma_{LF}(t)$, dislocation bows out to deform while pinned at its edges (Fig. C-6(b)). At maximum, σ_{max}, the dislocation bow more extensively. (Fig. C-6(c)).

Now, let's assume the mechanical load is held at a constant value $\sigma_{LF}(t)$ (Fig. C-6(b)), and track what occurs to the dislocation as the ultrasonic wave interacts with it (Fig. C-6 (d)-(f)). Initially, the ultrasonic wave does not interact with the dislocation (Fig. C-6 (d)), and the ultrasonic stress on the dislocation is zero, $\sigma_{US} = 0$. As the ultrasonic wave goes through the dislocation (Fig. C-6(e)), the dislocation vibrates is response to the ultrasound wave. The dislocation interference with the ultrasonic wave's journey through the material and affects its characteristics (e.g. amplitude, speed and frequency). The dislocation returns to its original state when the ultrasonic wave passes through the dislocation vicinity (Fig. C-6(f)) the dislocation reverts to its unperturbed state. Information about the dislocation motion at different mechanical stresses and strain rates is thus reflected in changes in the wave characteristics that occur during its propagation through the material. In this study, measurement of the *changes in amplitude and speed* of the ultrasonic wave in the material (by measuring changes in wave attenuation and transit time) is the means used to study dislocation behavior during mechanical loading.

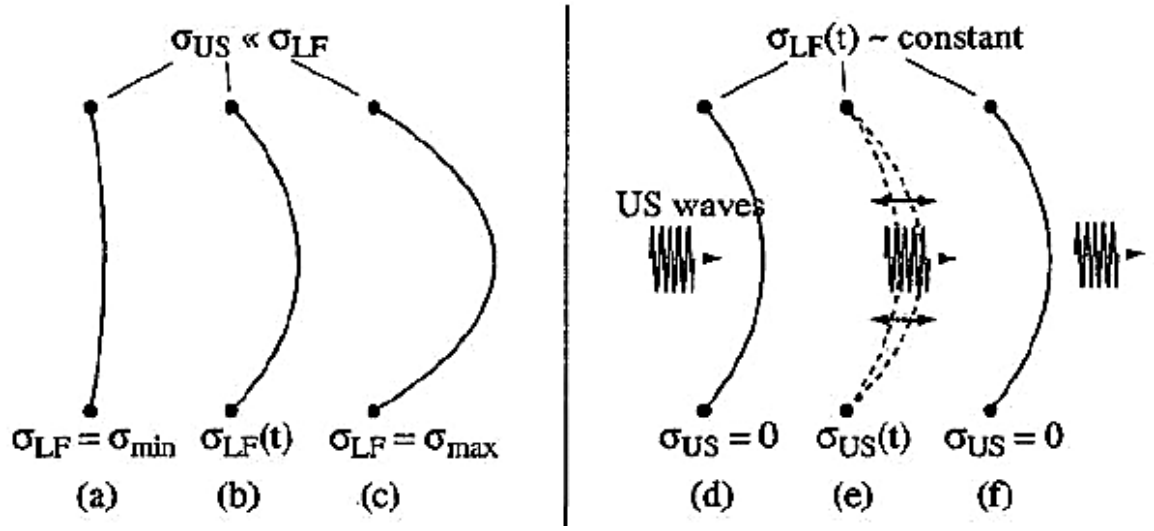

Figure C-6: Effect of dislocation bowing on a superimposed ultrasonic stress wave in UBS. The low frequency high amplitude mechanical stress applied (σ_{LF}) induces an increase in dislocation bowing size from σ_{min} (a), to σ_{max} (c). (d) - (f) show schematics demonstrating the interaction of a bowed dislocation at a constant stress (Fig. (b) where $\sigma_{LF}(t)$, is constant during time *t*) with a superimposed ultrasonic stress wave, σ_{US}, during it flight.

While material is subjected to mechanical load/unload, attenuation "α" can increase and/or decrease (Fig. C-5(c)). As noted above, the principle of the UBS measurement is to record the *changes* in ultrasonic wave attenuation, Δα, and transit time, Δτ, between known successive echoes, with respect to an applied strain, ε. Graphs of both Δα(ε) and Δτ(ε) can then be used to shed light on the various dislocation motion mechanisms occurring. Note that this technique only measures the changes in α and τ, relative to their values before a stress is applied. It follows that for the most part it is not an absolute measurement. The latter can be carried out, however, if needed. This comment notwithstanding, the measurement of absolute attenuation needs very accurate sample and experimental preparations. The evaluation of the reflected energy from each surface, diffraction effects, deviations from surface parallelism, and the acoustic bond character (i.e. the medium used to couple the sample to the transducer) are typical problems that have to be overcome in order to make accurate attenuation

measurements.[129]. However, in a differential technique all of these issues remain constant throughout experimentation and/or are cancelled out in the calculations.

The $\Delta\alpha$, and, $\Delta\tau$, are measured by electronically gating two different echoes (here echoes one and three were selected) and synchronizing the data acquisition of the echo magnitudes and shifts to be recorded (Fig. C-5(d)). Note that the electronic gates are set to be slightly larger than the phase shifts signal of each echo. This is to incorporate the entire echo signal for calculation of τ and α.

To calculate the transit time, T_M, a frequency scan is performed at a short interval (± 0.25 MHz of the nominal transducer frequency) and the slope of the phase shift of the signal, $\Delta\Phi_r$, versus frequency scan interval, ΔF, curve is inserted into the following equation:

$$T_M = \frac{\Delta\Phi_r}{2\pi\Delta F} \tag{C1}$$

The group velocity, v_g, can then be calculated using the transit time obtained. It is assumed here that v_g is equal to the phase velocity in most experimental conditions. Hence, a straight-line curve should result from the phase shift as a function of frequency scan interval selected. This assumption is valid except if strong multiple scattering occurs from material features near in size to the measurement wavelength. In that case, strong attenuation will take place as well. However, the transit time calculated incorporates all the time delays and phase shift mechanisms from the generation of the continuous wave used to produce the pulse to the phase sensitive detection process as shown in Eq.(C2)

$$T_M = T_{AC} + T_{Diff} + T_{Elec} + T_{PhBond}(F) + T_{PhTrans}(F) \tag{C2}$$

where T_{AC} is the acoustic time-of-flight, T_{Diff} accounts for diffraction effects, T_{Elec} accounts for all electronic transit times from the equipment, $T_{PhBond}(F)$ includes the phase shifts resulting from the acoustic bond and $T_{PhTrans}(F)$ accounts for the phase shift between the transducer/sample interface. All these effects cancel-out when two echoes are used for the measurements. Transit Time is then calculated from:

$$\text{Transit Time} = \frac{\left(\frac{\Delta\Phi_{r2}}{\Delta F} - \frac{\Delta\Phi_{r1}}{\Delta F}\right)}{4(N_2 - N_1)} \tag{C3}$$

where $\Delta\Phi_{r2}/\Delta F$ is the slope of the phase-frequency curve of the later echo and $\Delta\Phi_{r1}/\Delta F$ for the first echo, and N_2 is the echo number of the later echo and N_1 is the echo number of the earlier one. Measurements using two echoes eliminate all undesirable effects since both echoes are subject to the same shifts. Hence, $\Delta\tau$ is calculated from the difference between ΔT_2 for the later echo and ΔT_1 for the first:

$$\Delta\tau = \frac{\Delta T_2 - \Delta T_1}{2(N_2 - N_1)} = \frac{(\Phi_{r2}(t) - \Phi_{r1}(t)) - (\Phi_{r2}(0) - \Phi_{r1}(0))}{4\pi F(N_2 - N_1)} \tag{C4}$$

$\Phi_{ri}(t)$ is the phase of the ith signal at time *t*, and $\Phi_{ri}(0)$ is the phase at time zero (Fig. C-5(c)). $\Delta\tau$ is the change in the time - relative to time zero, when no load was applied - for the acoustic pulse to travel from one side of the sample to the other (i.e. it is not a full round trip).

To obtain the change in attenuation, $\Delta\alpha$, the logarithmic ratio of echo the amplitudes of the present signal relative to time zero amplitudes is calculated – when no load is applied - decibels (dB) per transit.

$$\Delta\text{Attenuation } (\alpha) = \frac{10}{(N_2 - N_1)} \log\left(\frac{A_1(0)\,A_2(t)}{A_2(0)\,A_1(t)}\right) \text{ dB per transit} \tag{C5}$$

where $A_1(0)$ & $A_2(0)$ are the amplitudes of the earlier and later echoes, respectively, at time zero, while $A_1(t)$ & $A_2(t)$ are the corresponding echo amplitudes at time *t*.

Each dislocation motion mechanism demonstrates a characteristic Δα(ε) and Δτ(ε) signature shape.. The bow-signature is an established signature demonstrating a reversible hysteresis loop in both Δα(ε) and Δτ(ε) signatures. The bow-signature is explained by the bowing of dislocations from immobile point defects with load (Fig. C-7(b)), and de-pinning of the dislocations from a row with increased stress, then re-pinning back to its original position upon unloading (Fig. C-7(c)). This signature was observed in high purity aluminum, Al, at cryogenic temperatures[111, 114, 119, 127]. Figure C-8 shows the Δα(σ) and Δτ/τ(σ) signatures of 5N aluminum after annealing for six months at room temperature and tested at different temperatures [111].

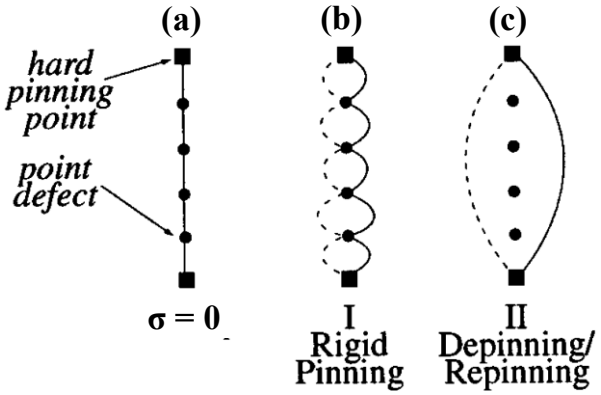

Figure C-7: Interaction mechanisms between an oscillating dislocation and a row of immobile point defects. "I" corresponds to the pinned state; in "II", the depinning-repinning mechanism is activated[119].

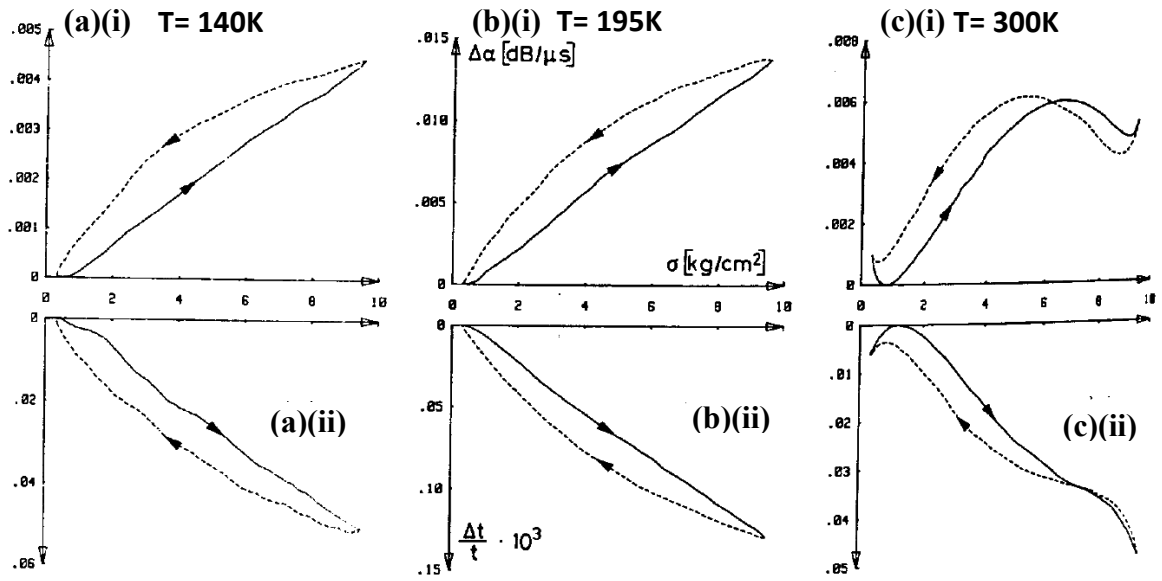

Figure C-8: Effect of temperature and stress on Δα ((i) figures) and Δτ ((ii) figures) of 5N aluminum after annealing for six months at 300 K. Temperatures of experimentation are: (a) 140 K, (b) 195 K and (c) 300 K. Solid line and dashed lines represent loading and unloading respectively [111].

Since the mobility of point defects varies with temperature, the resulting signature change accordingly. Figure C-8(c) demonstrates a different signature of the same material for $\Delta\alpha(\sigma)$ and $\Delta\tau(\sigma)$ at 300K than those at 195 and 140K.

Another example is shown in Figure C-9 shows the $\Delta\alpha(\sigma)$ signature differences for 5N aluminum after cold working to 0.4% at 4 K and tested at 150 , 250 and 300 K. At 150 K the point defects mobility is limited resulting into a bow signature (Fig. C-9(a)). Here the dislocations are, presumed to breakaway from a row of immobile point defects. As the temperature increases to 250 K the dislocations are assumed to pin-depin from point defects due to increase in their mobility. This results into slow migration of the point defects into two cloud regions. The symmetric signature is presumed to be due to the relocation of point defects to two cloud (Fig. C-9(b)). This signature is called a moustache signature due to the shape it develops. Finally at 300 K the dislocations drag the point defects easily due to their high mobility. Therefore, result is an eight signature

(Fig. C-9(c)) is observed as an adaptation of the moustache signature (Fig. C-9(b)). The bow signature is expected in ceramic materials due to the low mobility of dislocations and point defects at room temperature.

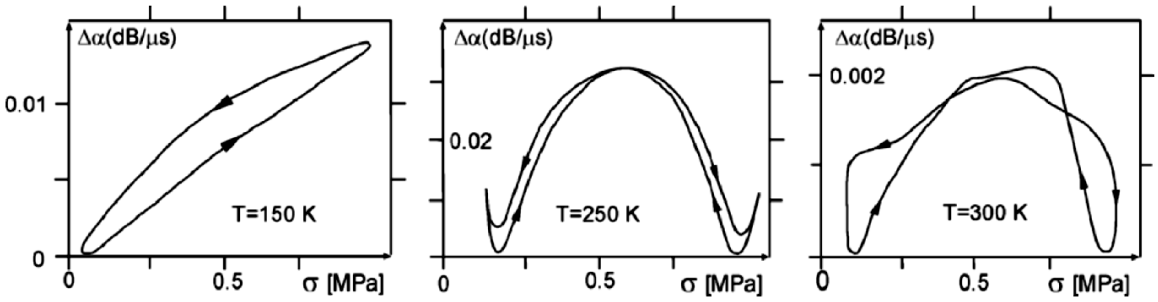

Figure C-9: Signatures of damping mechanisms measured by ACT for various dislocation-point defect interactions at different temperatures. Ultrasonic frequency used was 10 MHz.[127]

C1.3 Selected ceramic materials characteristics

Sapphire (Rayotek Scientific Inc., San Diego, CA), alumina (Kyocera Industrial Ceramic Corp., Atlanta, GA) and borosilicate glass (Specialty Glass Products, Willow Grove, PA) were also tested in order to compare them with the MAX phase results. The sapphire single crystal was ordered such that the basal plane is normal to the loading axis, i.e. comparable to a textured N-sample. The samples were ordered in the same dimensions as the EDMed MAX phase cylinders. Figures 5-1(g) & (h) shows the FG & CG microstructures of the alumina sample used after thermal etching at 300 ºC for 3h. The CG alumina sample was obtained by annealing a FG alumina sample in air at 1500 ºC for 6 h. XRD was performed on the purchased samples as well to confirm their composition and orientation of the sapphire sample.

C1.3 Experimental Details

In the current study, UBS experiments were performed with a minor modification of holding for 10 s after each load/unload interval (Fig. C-5(b)). The strain rates investigated are $1.65x10^{-4}s^{-1}$, $3.3x10^{-4}s^{-1}$, $6.6x10^{-4}s^{-1}$, and $13.2x10^{-4}s^{-1}$, and the strain was measured using an extensometer (2620-603C, Instron, Norwood, MA) directly attached to the sample. Stress and strain are recorded using Instron 5800R BlueHill software.

This echo phase shift could be detected using a RAM-5000 instrument and the user interface from Ritec (Warwick, USA) operating with 10 ppm time-of-flight resolution (Fig. C-5(d)). $\Delta\tau$ is calculated from the translation of the phase shift signal between the echoes with a resolution of 0.1º. Using a logarithmic differential amplifier, the user interface calculates the logarithmic ratio of the transient echo amplitudes to time zero amplitude for attenuation changes in decibels[126]. Measurements of $\Delta\alpha$, and $\Delta\tau$ are made every 0.5 s. To obtain the change in attenuation, $\Delta\alpha$, the software calculates the logarithmic ratio of echo the amplitudes of the present signal relative to time zero amplitudes – when no load is applied - decibels (dB) per transit.

Ultrasonic wave couplant, (SWC, Olympus NDT Inc., Waltham, USA) was used as a bonding agent between the ultrasonic transducers and the sample. Two longitudinal frequency transducers of 5 MHz and 10 MHz, in addition to two different directions of 5 MHz shear transducers (Valpey Fisher Corp. Hopkinton, USA) were used to experiment some of the more important vibration modes during uniaxial compressive loading.

Figure C-10(a) illustrates a schematic of the different ultrasonic wave modes applied on all samples experimented in this thesis. The longitudinal and shear waves stimulate dislocation vibration of different modes. The two shear wave's polarization

used provide additional information about the dislocations activity during mechanical loading. The selected linear elastic ceramic materials tested were borosilicate glass, alumina, and sapphire. These materials were selected to be compared with layered structured KNE MAX phases ceramic material investigated in this thesis.

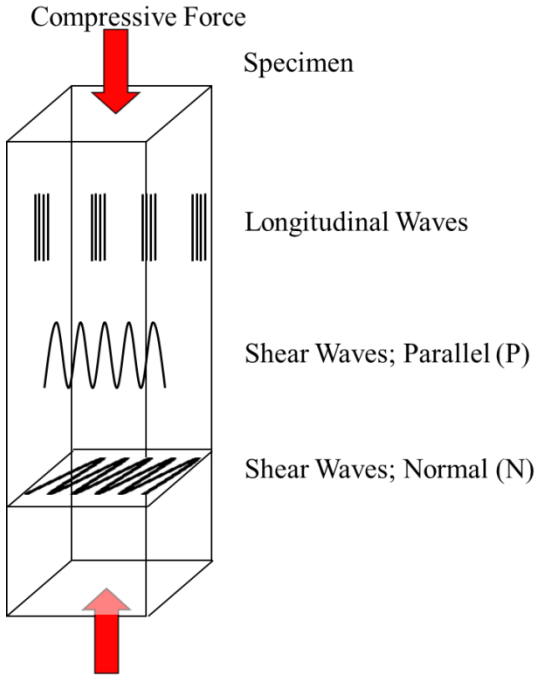

Figure C-10: (a) Schematic of ultrasonic wave modes applied during UBS. Longitudinal waves and two shear wave polarizations Parallel (P) and Normal (N) to the loading direction.

C1.4 Summary and Conclusions

To investigate the dislocation mechanism in KNE materials in situ experiments is essential since they are only active during mechanical loading/unloading. In situ ND and UBS characterization techniques yield information about dislocations in the bulk of the samples. In situ ND obtains information about dislocation behavior in gains at different orientations. On the other hand, UBS acquires information about the overall behavior of the dislocations within the ultrasonic wave volume irrespective of grain orientation. The

UBS experiments performed were all at room temperature. Linear elastic ceramic materials were experimented to be compared with the KNE layered structured MAX phases. Three ultrasonic wave modes were used, longitudinal and two directions of shear waves, to stimulate different dislocation vibrations and obtain information about their interaction with the lattice.

C2: UBS Results of Selected Linear Elastic Ceramics

As shown in Fig. C-10, three different types of waves were used. Color codes are used in the results presented to differentiate between the different wave types. For the longitudinal waves, two frequencies were used: 5 MHz (black) and 10 MHz (green). For the shear waves only 5MHz was used: shear wave parallel (red) and normal (blue). In the following sections, the UBS results for the various non-MAX phases are presented and discussed.

C2.1 Borosilicate Glass UBS results

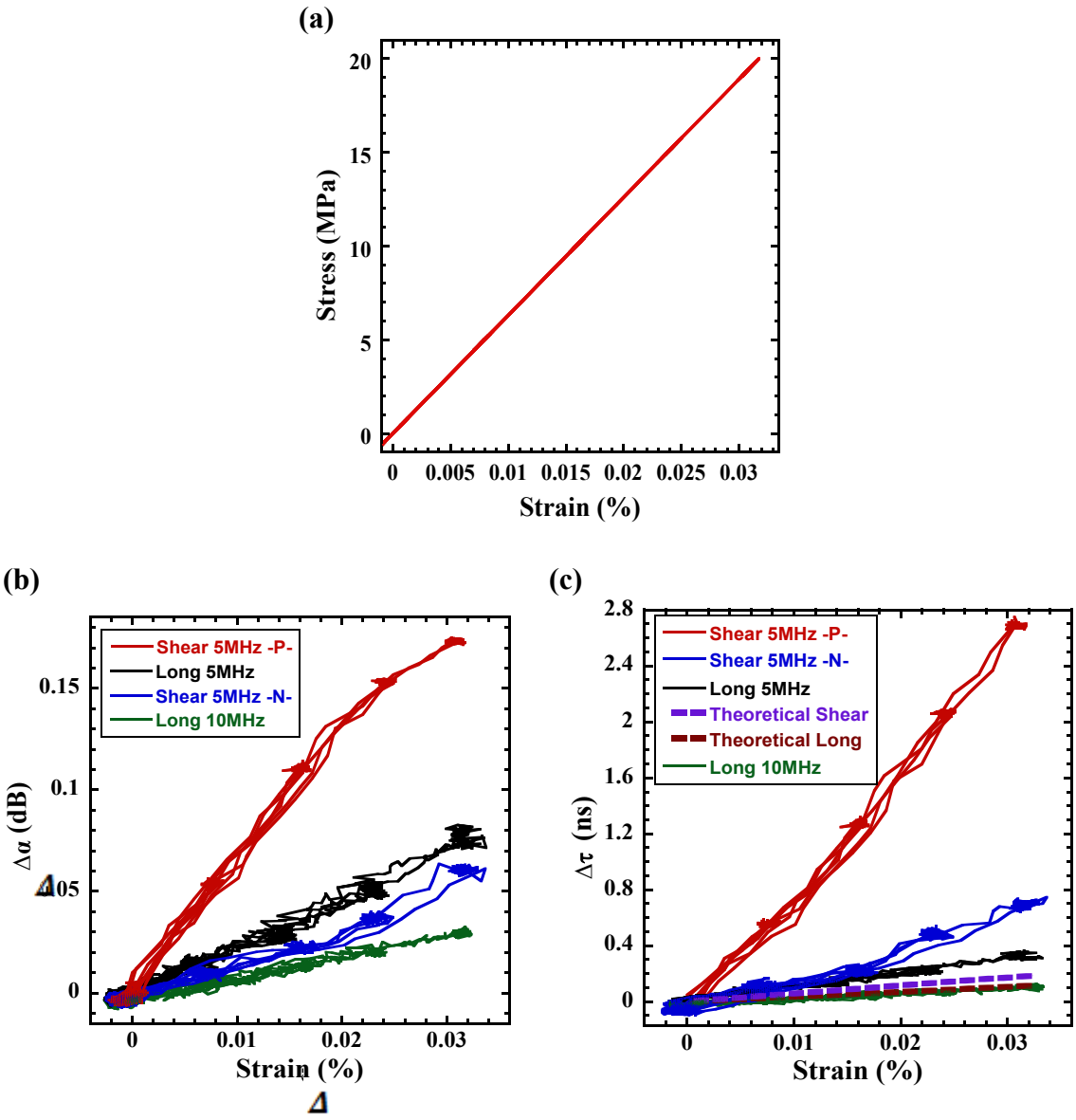

Figure C-11: (a) Macroscopic stress-strain response of borosilicate glass during UBS experimentation. (b) and (c) show the Δα(ε) and Δτ(ε) ultrasonic response of borosilicate glass from longitudinal: 10MHz (green), 5MHz (black); and shear 5MHz: P-(red) and N-(blue) ultrasonic wave modes, respectively. The purple and brown dashed lines represent the theoretical shear and longitudinal response assuming an ideal material without any defects interfering the ultrasonic wave.

C2.2 Sapphire UBS results

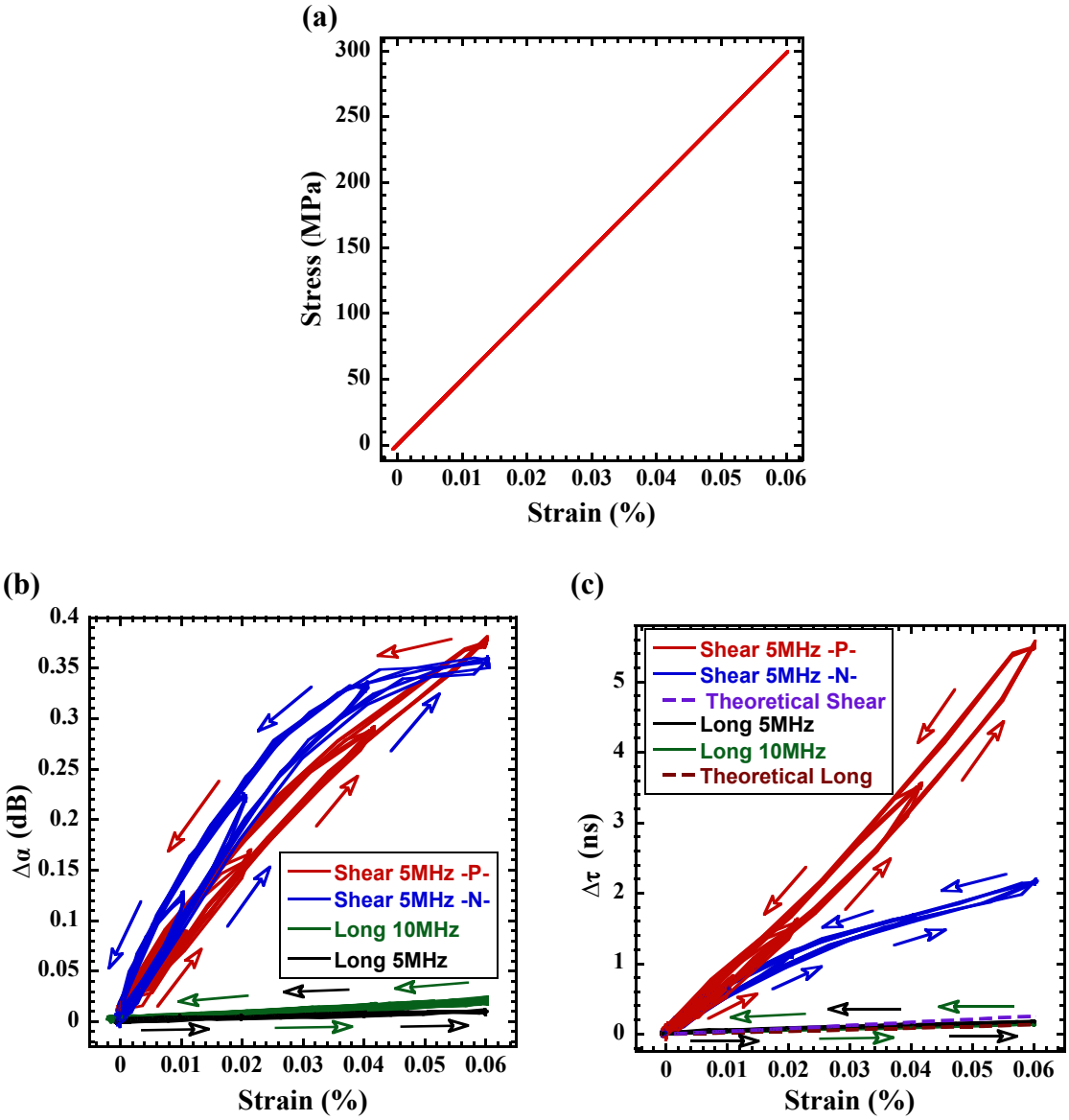

Figure C-12: (a) Macroscopic stress-strain response of sapphire during UBS experimentation. (b) and (c) show the Δα(ε) and Δτ(ε) ultrasonic response of sapphire from longitudinal: 10MHz (green), 5MHz (black); and shear 5MHz: P-(red) and N-(blue) ultrasonic wave modes, respectively. The purple and brown dashed lines represent the theoretical shear and longitudinal response assuming an ideal material without any defects interfering the ultrasonic wave.

C2.3 FG and CG alumina UBS results

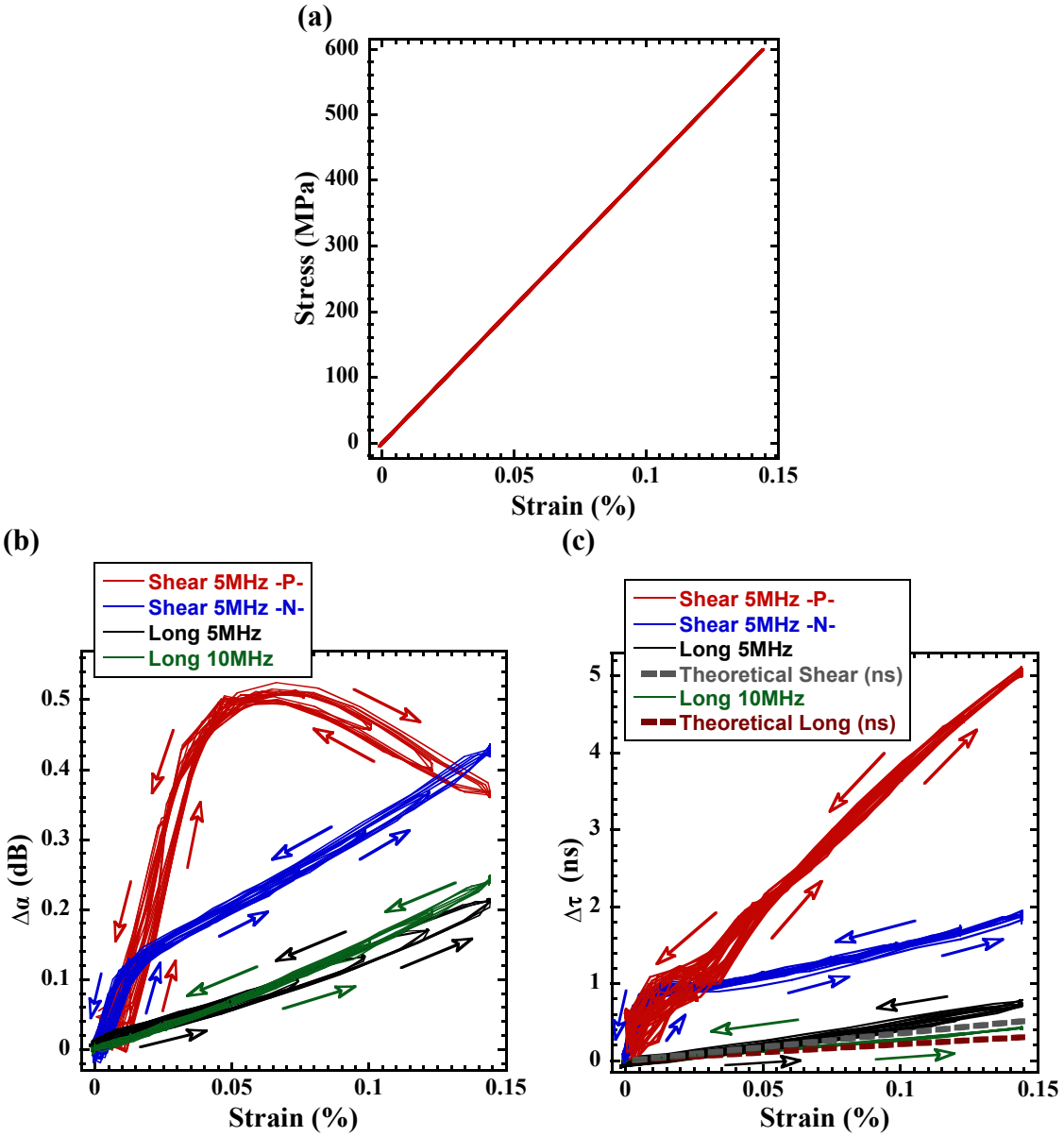

Figure C-13: (a) Macroscopic stress-strain response of FG alumina during UBS experimentation. (b) and (c) show the Δα(ε) and Δτ(ε) ultrasonic response of FG alumina from longitudinal: 10MHz (green), 5MHz (black); and shear 5MHz: P-(red) and N-(blue) ultrasonic wave modes, respectively. The grey and brown dashed lines represent the theoretical shear and longitudinal response assuming an ideal material without any defects interfering the ultrasonic wave. A holding time of 10 s at stress levels of 600, 500, 400, 300, 200, 100 & 50 MPa were performed.

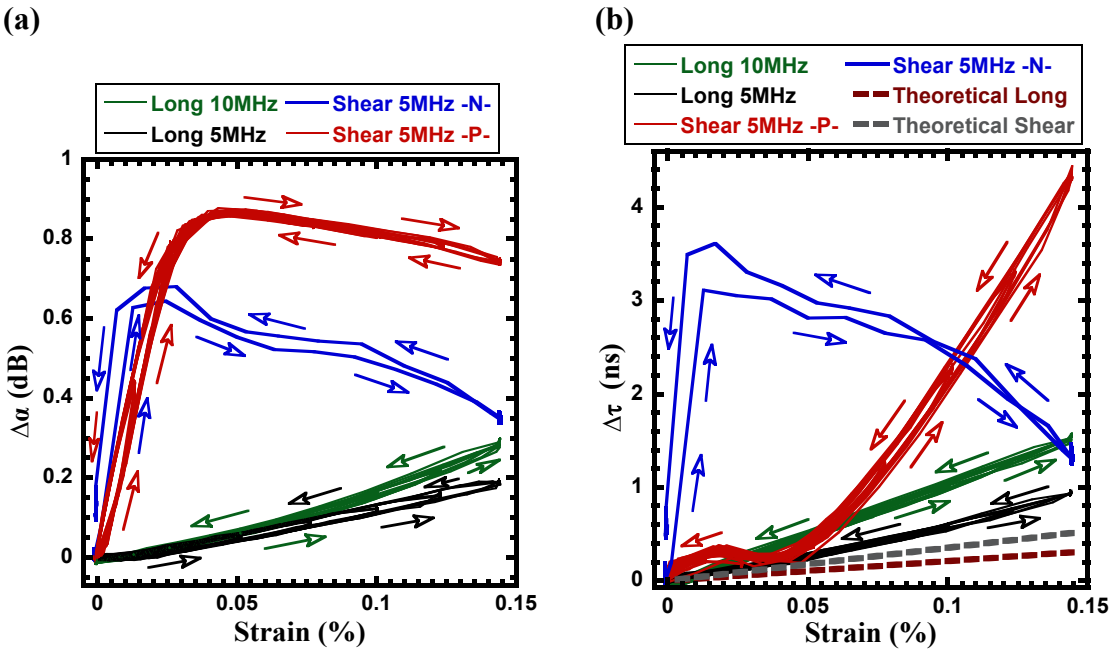

Figure C-14: Macroscopic stress-strain response of CG alumina during UBS experimentation is the same as that in Fig. C-13 (a). (a) and (b) show the $\Delta\alpha(\varepsilon)$ and $\Delta\tau(\varepsilon)$ ultrasonic response of CG alumina from longitudinal: 10MHz (green), 5MHz (black); and shear 5MHz: P-(red) and N-(blue) ultrasonic wave modes, respectively. The grey and brown dashed lines represent the theoretical shear and longitudinal response assuming an ideal material without any defects interfering the ultrasonic wave. A holding time of 10 s at stress levels of 600, 500, 400, 300, 200, 100 & 50 MPa were performed.

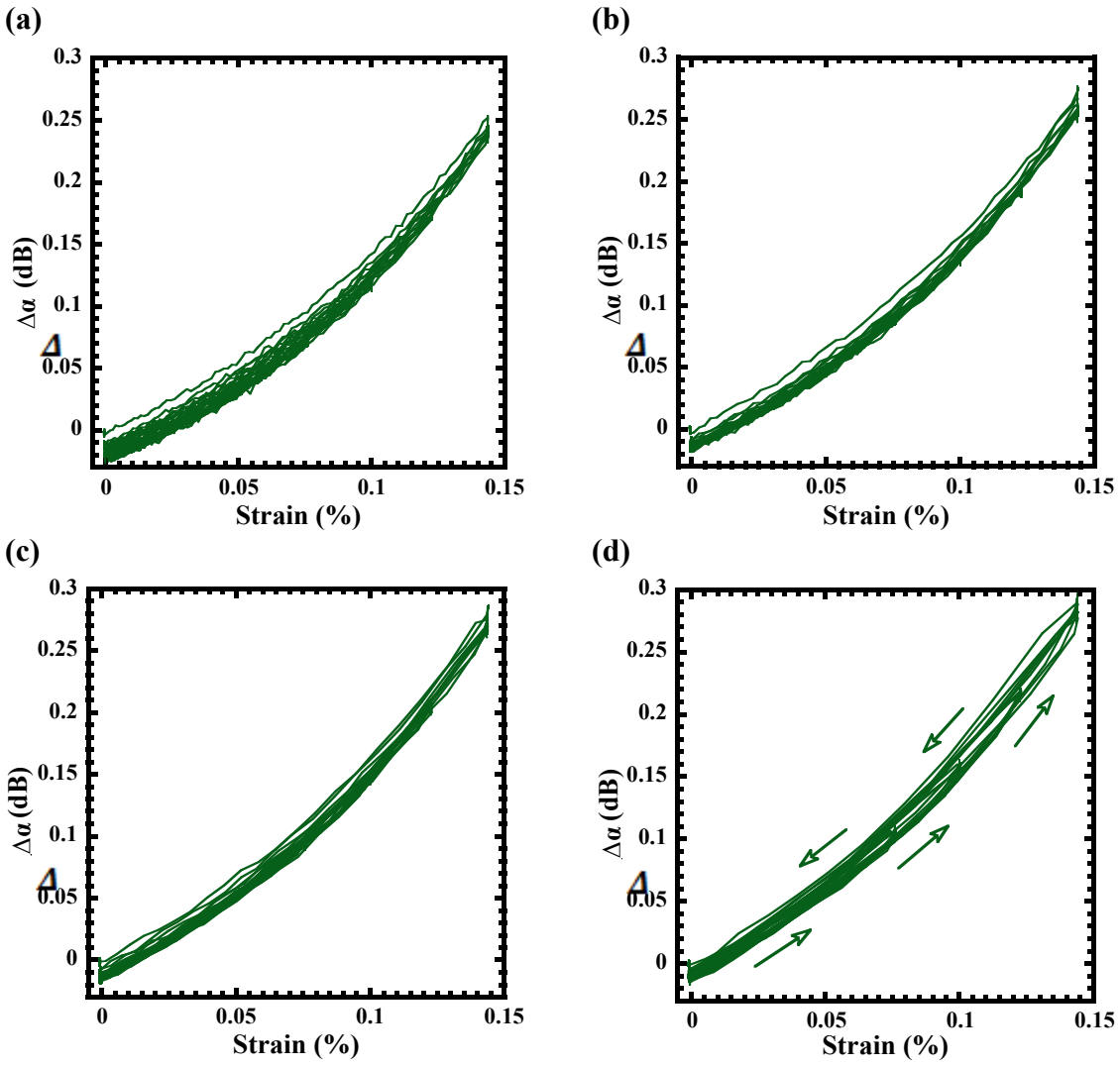

Figure C-15: CG alumina Δα results for the longitudinal 10 MHz ultrasonic wave mode at different strain rates. (a) 1.65×10^{-4} s^{-1}, (b) 3.3×10^{-4} s^{-1}, (c) 6.6×10^{-4} s^{-1}, and (d) 13.2×10^{-4} s^{-1}. A holding time of 10 s at stresses 600, 500, 400, 300, 200, 100 & 50 MPa was performed.

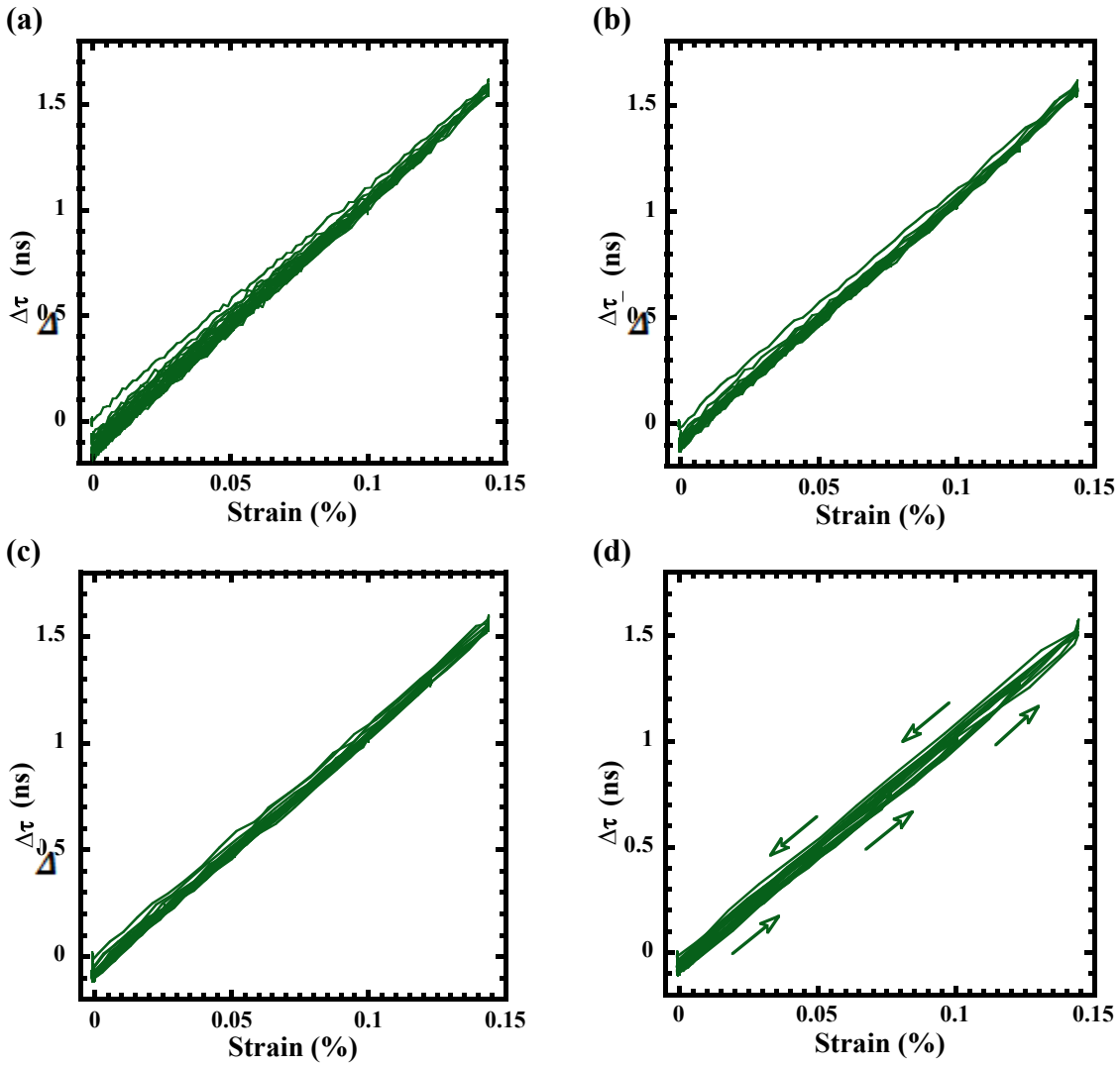

Figure C-16: CG alumina Δτ results for the longitudinal 10 MHz ultrasonic wave mode at different strain rates. (a) $1.65x10^{-4}s^{-1}$, (b) $3.3x10^{-4}s^{-1}$, (c) $6.6x10^{-4}s^{-1}$, and (d) $13.2x10^{-4}s^{-1}$. A holding time of 10 s at stresses 600, 500, 400, 300, 200, 100 & 50MPa was performed

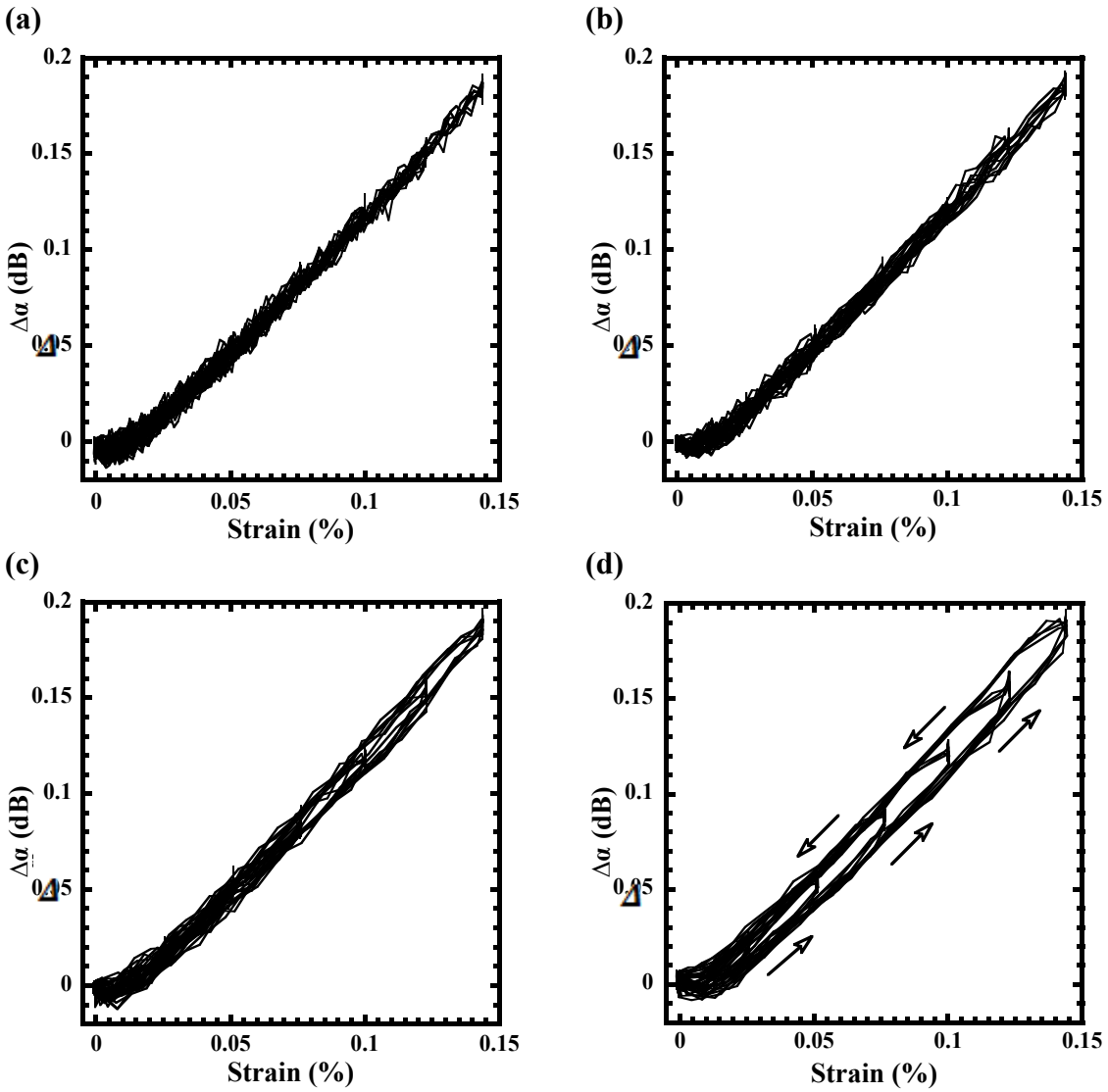

Figure C-17: CG Alumina Δα results for the longitudinal 5 MHz ultrasonic wave mode at different strain rates. (a) $1.65x10^{-4}s^{-1}$, (b) $3.3x10^{-4}s^{-1}$, (c) $6.6x10^{-4}s^{-1}$, and (d) $13.2x10^{-4}s^{-1}$. A holding time of 10 s at stresses 600, 500, 400, 300, 200, 100 & 50MPa was performed.

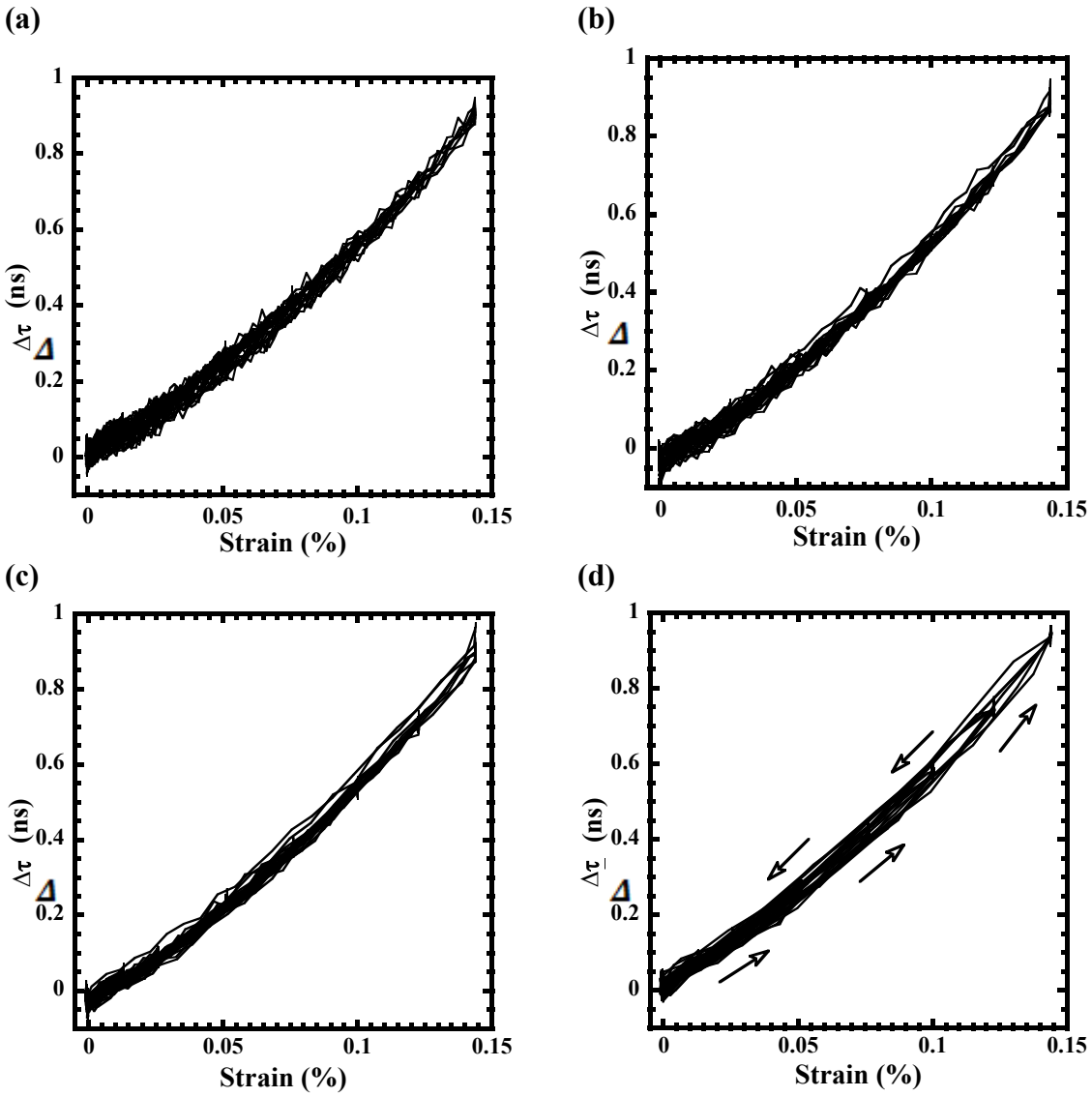

Figure C-18: CG alumina Δτ results for the longitudinal 5MHz ultrasonic wave mode at different strain rates. (a) 1.65x10^{-4}s^{-1}, (b) 3.3x10^{-4}s^{-1}, (c) 6.6x10^{-4}s^{-1}, and (d) 13.2x10^{-4}s^{-1}. A holding time of 10 s at stresses 600, 500, 400, 300, 200, 100 & 50 MPa was performed.

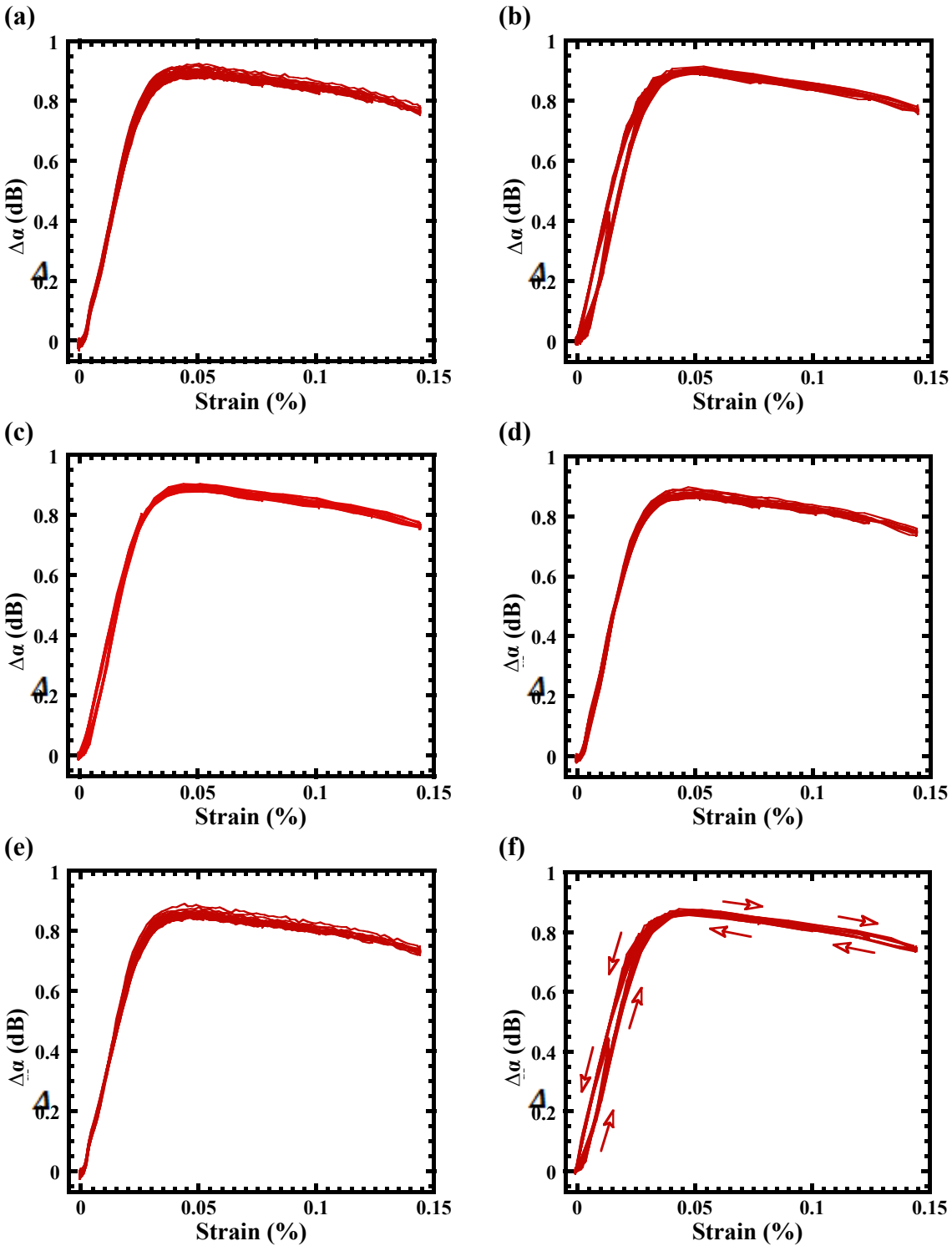

Figure C-19: CG alumina Δα results for the Shear-P 5MHz ultrasonic wave mode at different strain rates. (a) $1.65x10^{-4}s^{-1}$, (b) $13.2x10^{-4}s^{-1}$, (c) $6.6x10^{-4}s^{-1}$, (d) $3.3x10^{-4}s^{-1}$, (e) $1.65x10^{-4}s^{-1}$ and (f) $13.2x10^{-4}s^{-1}$. A holding time of 10 s at stresses 600, 500, 400, 300, 200, 100 & 50MPa was performed.

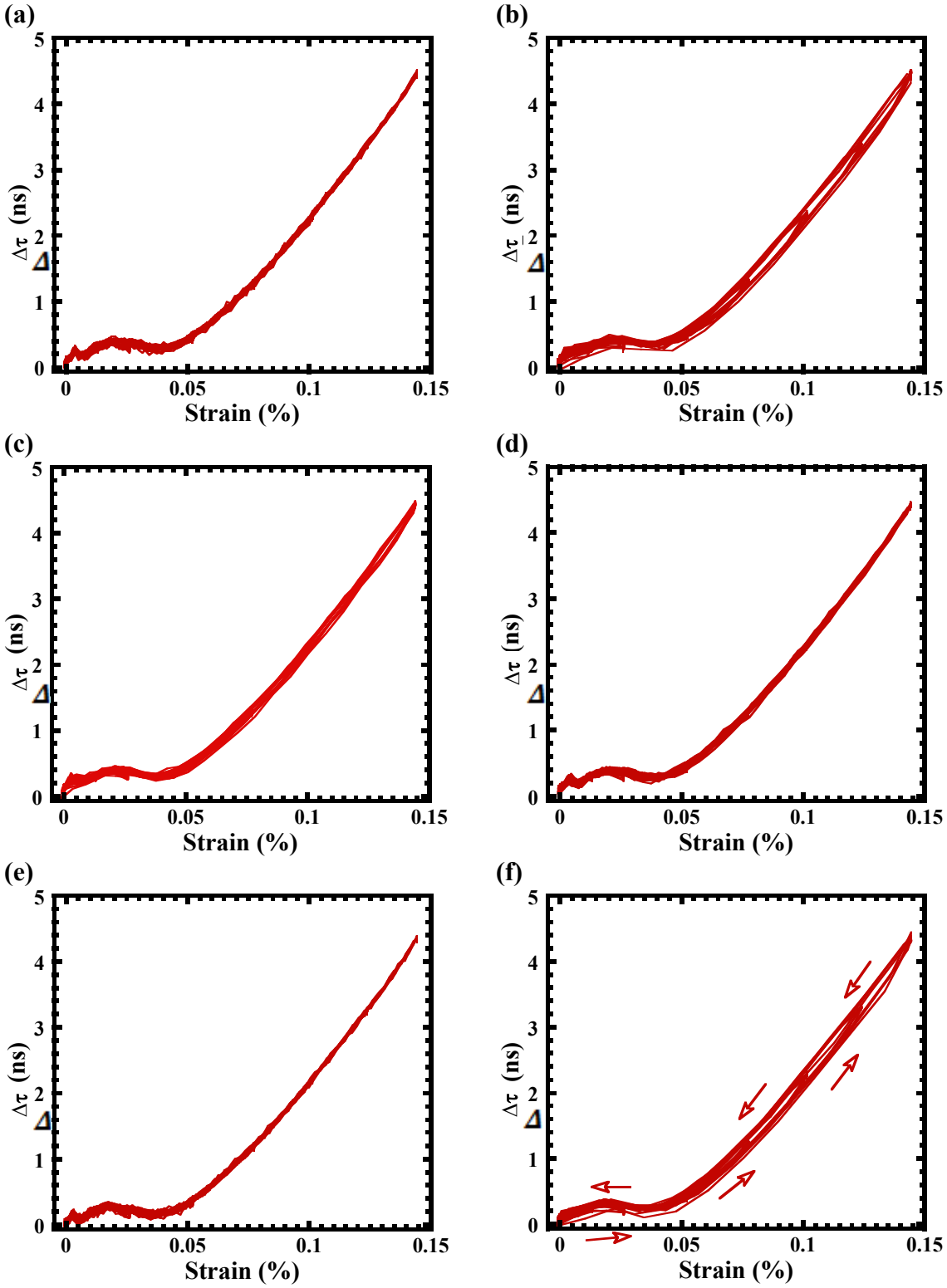

Figure C-20: Coarse Grained Alumina Δτ results for the Shear-P 5MHz ultrasonic wave mode at different strain rates. (a) $1.65x10^{-4}s^{-1}$, (b) $13.2x10^{-4}s^{-1}$, (c) $6.6x10^{-4}s^{-1}$, (d) $3.3x10^{-4}s^{-1}$, (e) $1.65x10^{-4}s^{-1}$ and (f) $13.2x10^{-4}s^{-1}$. A holding time of 10 s at stresses 600, 500, 400, 300, 200, 100 & 50MPa was performed.

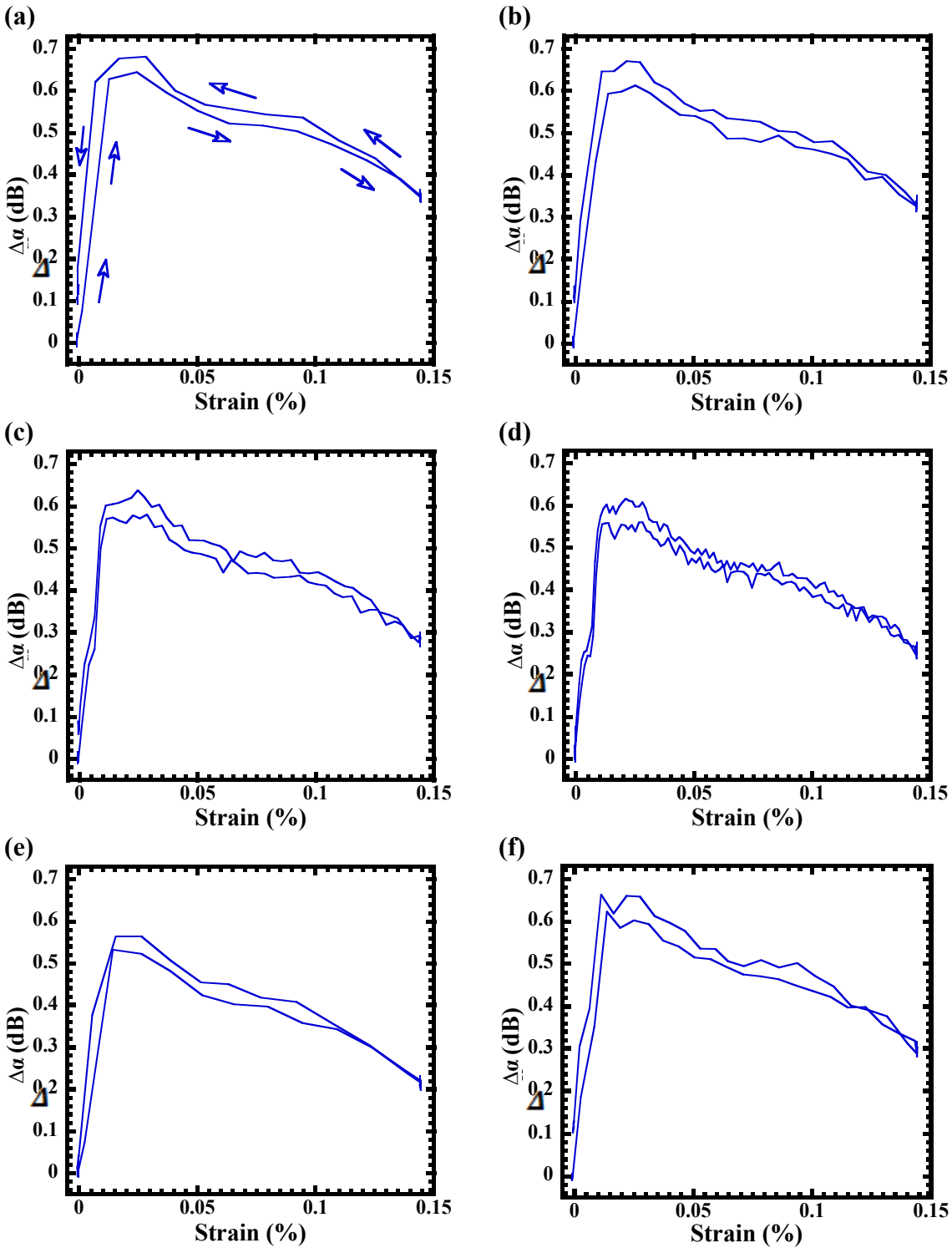
(a)
(b)
(c)
(d)
(e)
(f)
Δα (dB)
Strain (%)
0
0.1
0.2
0.3
0.4
0.5
0.6
0.7
0.05
0.15

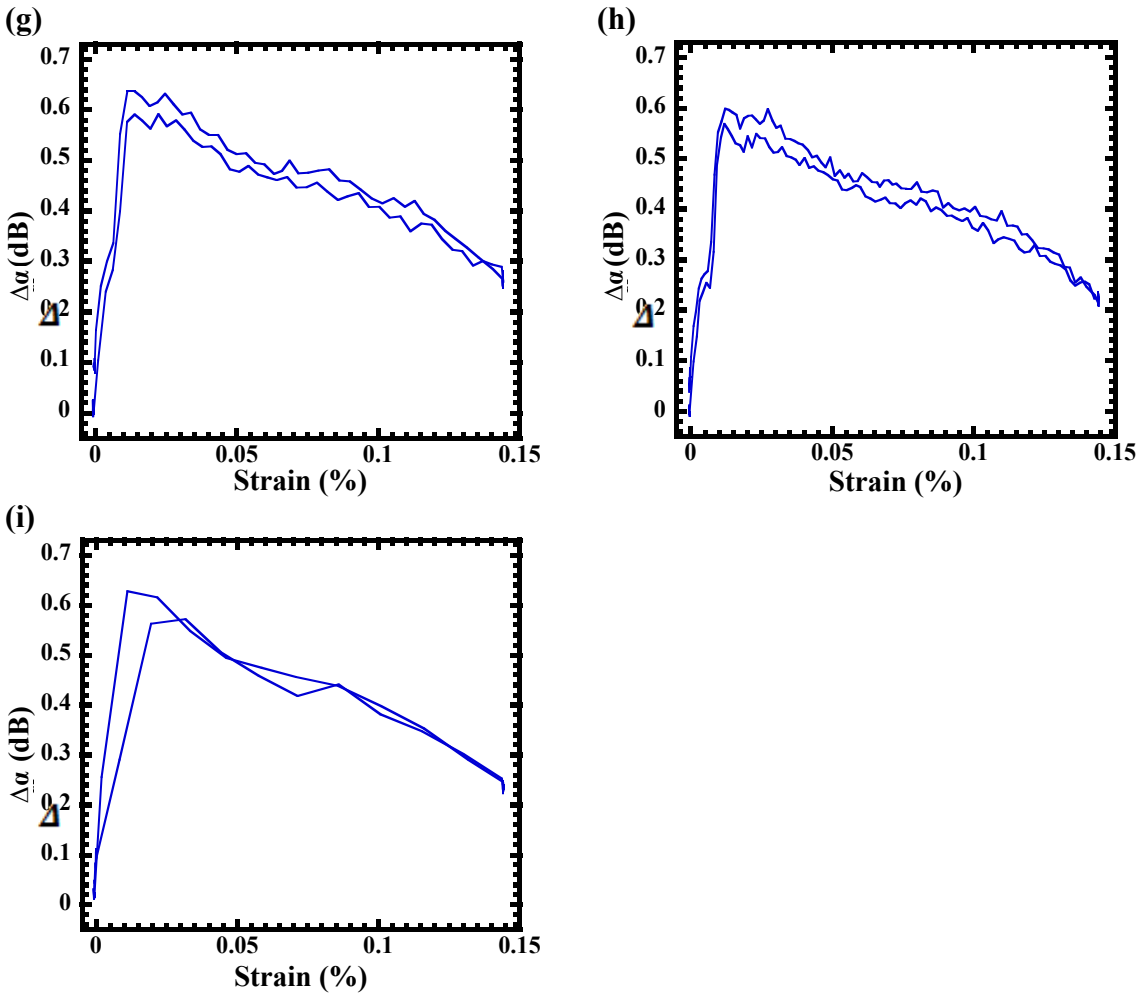

Figure C-21: Coarse Grained Alumina Δα results for the Shear-N 5MHz ultrasonic wave mode at different strain rates. (a) $13.2x10^{-4}s^{-1}$, (b) $6.6x10^{-4}s^{-1}$, (c) $3.3x10^{-4}s^{-1}$, (d) $1.65x10^{-4}s^{-1}$, (e) $13.2x10^{-4}s^{-1}$, (f) $6.6x10^{-4}s^{-1}$, (g) $3.3x10^{-4}s^{-1}$, (h) $1.65x10^{-4}s^{-1}$ and (i) $13.2x10^{-4}s^{-1}$. A holding time of 10 s at stresses 600, 500, 400, 300, 200, 100 & 50MPa was performed.

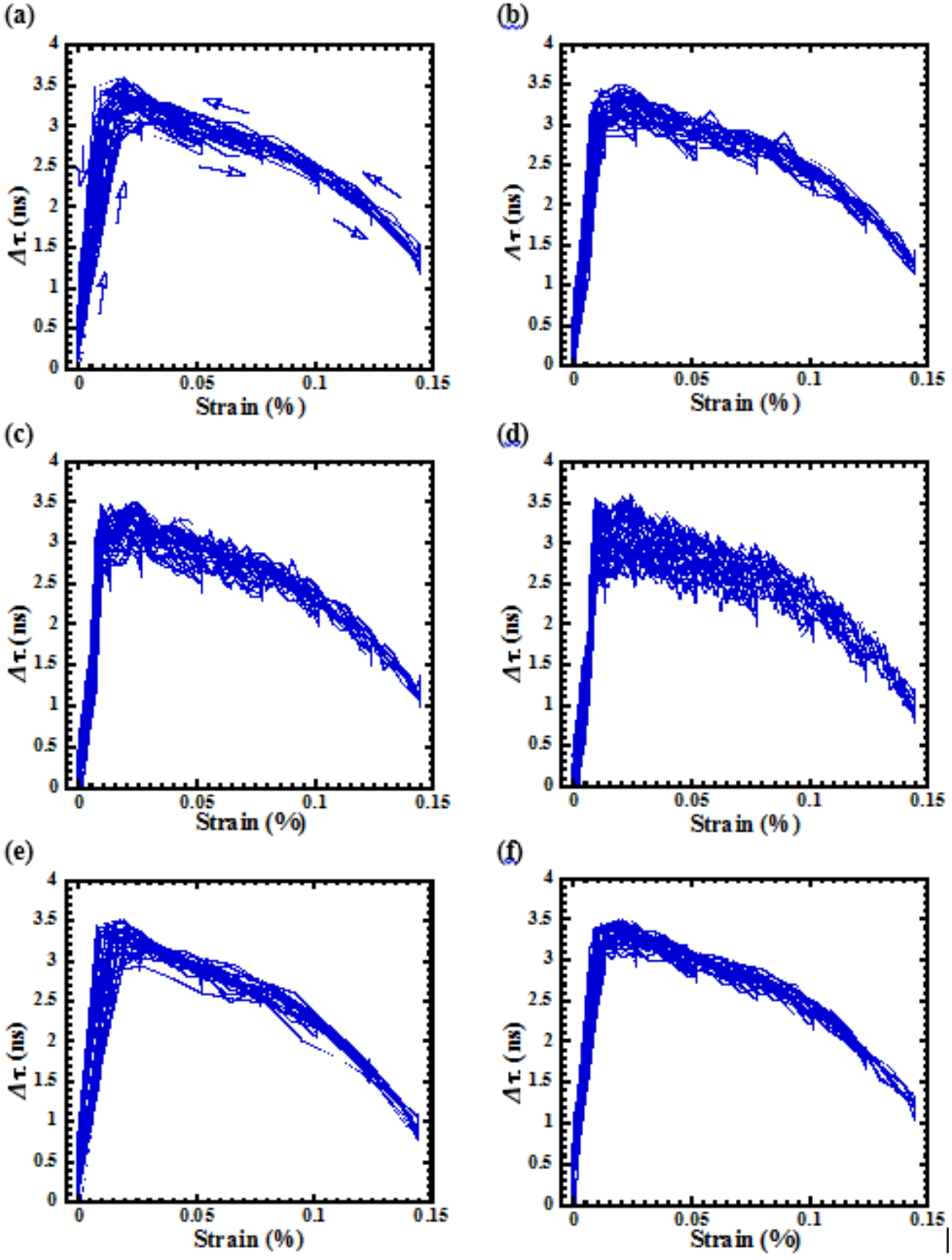
(a)
(b)
(c)
(d)
(e)
(f)
Δτ (ns)
Strain (%)
0
0.5
1
1.5
2
2.5
3
3.5
4
0.05
0.1
0.15

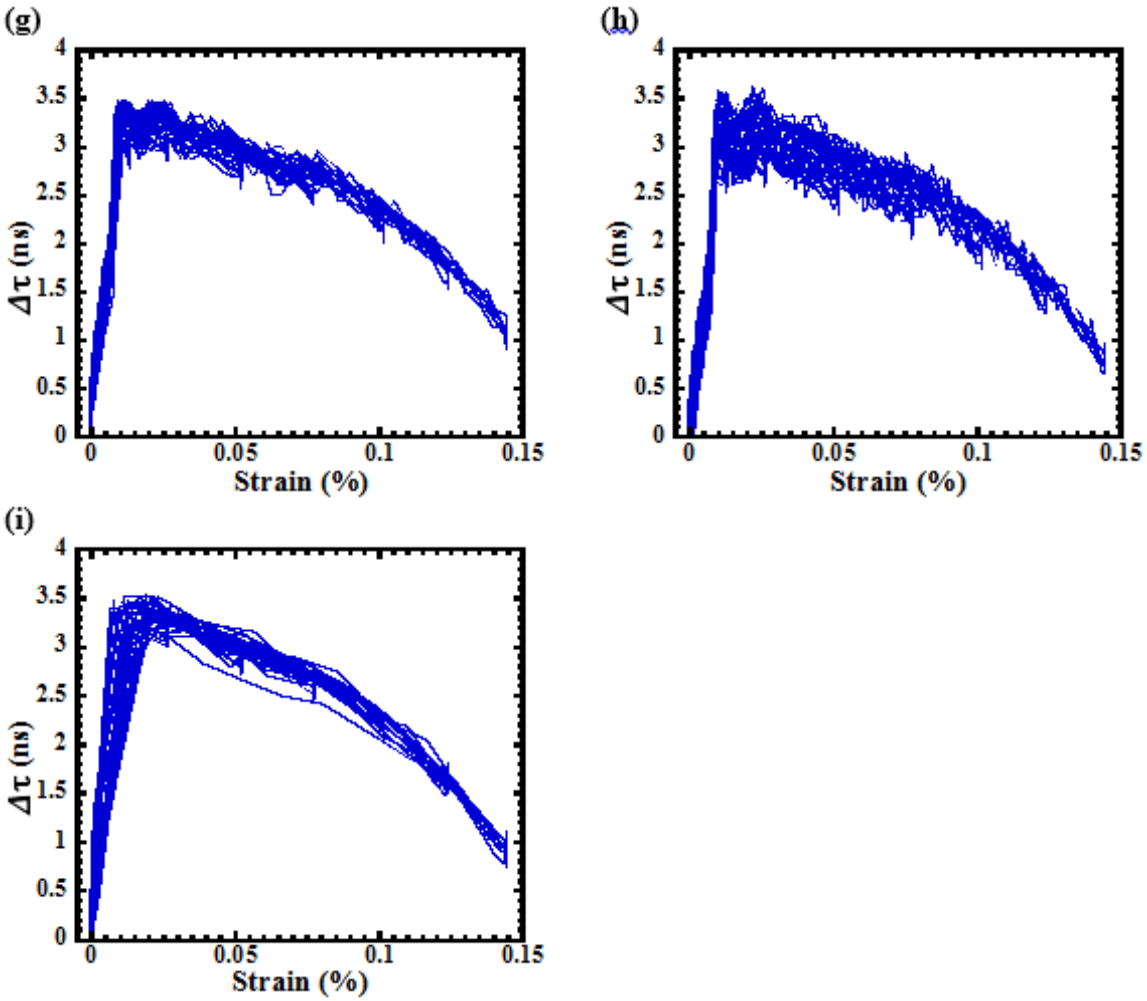

Figure C-22: Coarse Grained Alumina Δτ results for the Shear-N 5MHz ultrasonic wave mode at different strain rates. (a) $13.2x10^{-4}s^{-1}$, (b) $6.6x10^{-4}s^{-1}$, (c) $3.3x10^{-4}s^{-1}$, (d) $1.65x10^{-4}s^{-1}$, (e) $13.2x10^{-4}s^{-1}$, (f) $6.6x10^{-4}s^{-1}$, (g) $3.3x10^{-4}s^{-1}$, (h) $1.65x10^{-4}s^{-1}$ and (i) $13.2x10^{-4}s^{-1}$. A holding time of 10 s at stresses 600, 500, 400, 300, 200, 100 & 50MPa was performed.

Table C-1. Longitudinal and shear velocities of borosilicate glass, sapphire and alumina and corresponding wavelengths at 5 MHz and 10 MHz frequencies.

		Frequency		
		5MHz		10MHz
		Longitudinal	Shear	Longitudinal
Borosilicate Glass	Velocity (m/s)	5529	3415	5529
	Wavelength (μm)	1105.8	683.0	552.9
Sapphire	Velocity (m/s)	11223	5935	11223
	Wavelength (μm)	2244.6	1187.0	1122.3
Alumina (Al_2O_3)	Velocity (m/s)	10619	6568	10619
	Wavelength (μm)	2123.8	1313.6	1061.9

C3: UBS Results of MAX phases

C3.1 Ti_2SC UBS results

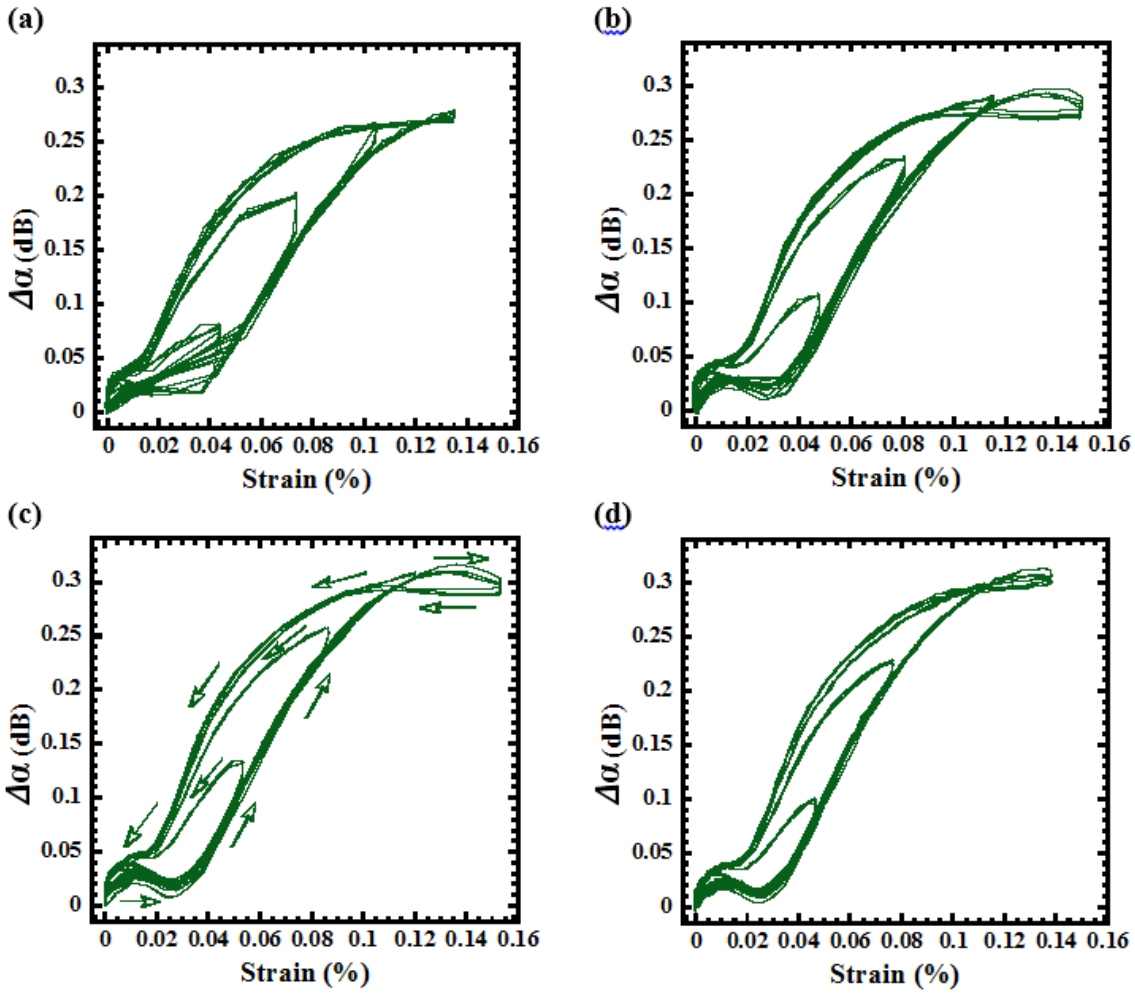

Figure C-23: Ti_2SC (8µm) Δα results for the longitudinal 10MHz ultrasonic wave mode at different strain rates. (a) $13.2x10^{-4}s^{-1}$, (b) $6.6x10^{-4}s^{-1}$, (c) $3.3x10^{-4}s^{-1}$ and (d) $1.65x10^{-4}s^{-1}$. A holding time of 10 s at stresses 500, 400, 300, 200, 100 & 50MPa was performed.

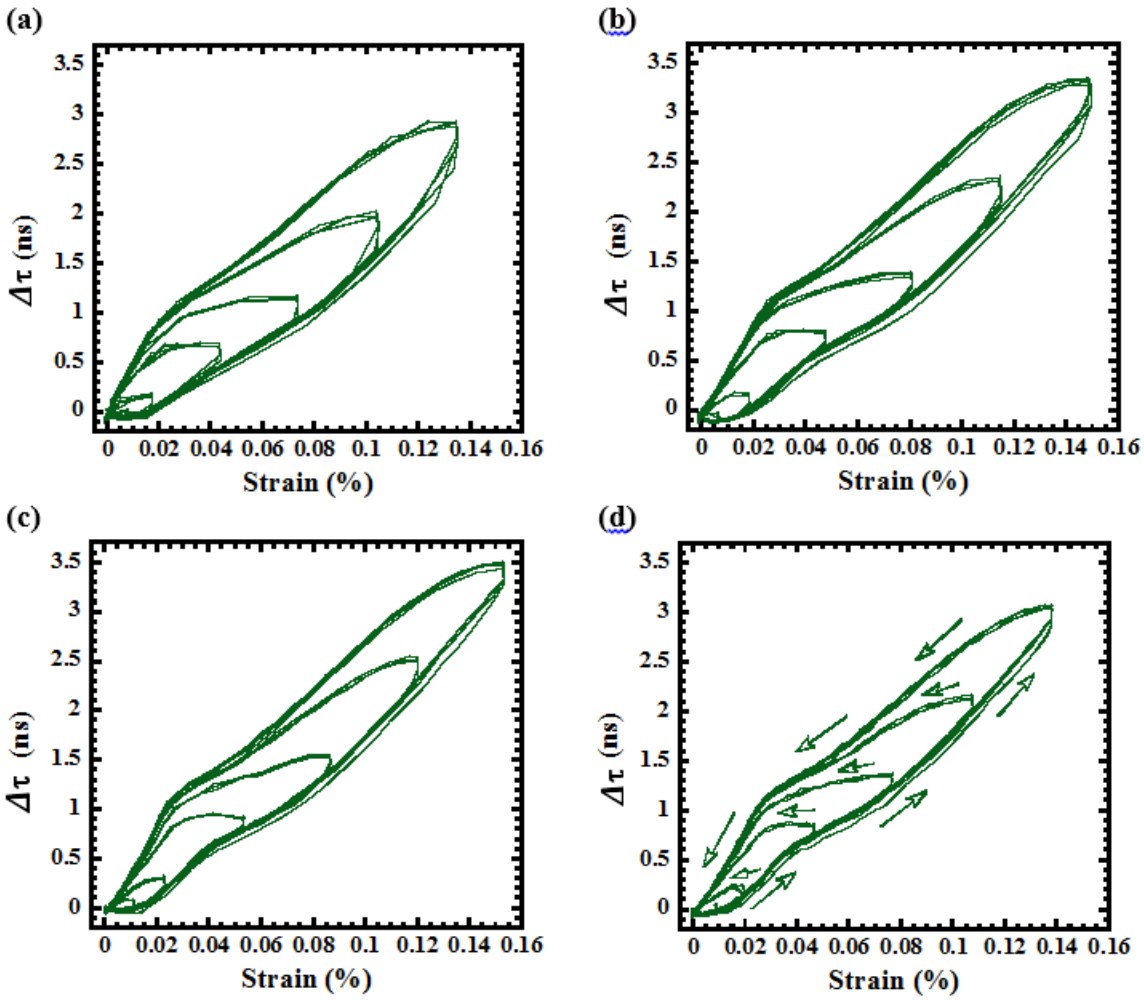

Figure C-24: Ti_2SC (8µm) Δτ results for the longitudinal 10MHz ultrasonic wave mode at different strain rates. (a) $13.2x10^{-4}s^{-1}$, (b) $6.6x10^{-4}s^{-1}$, (c) $3.3x10^{-4}s^{-1}$ and (d) $1.65x10^{-4}s^{-1}$. A holding time of 10 s at stresses 500, 400, 300, 200, 100 & 50MPa was performed.

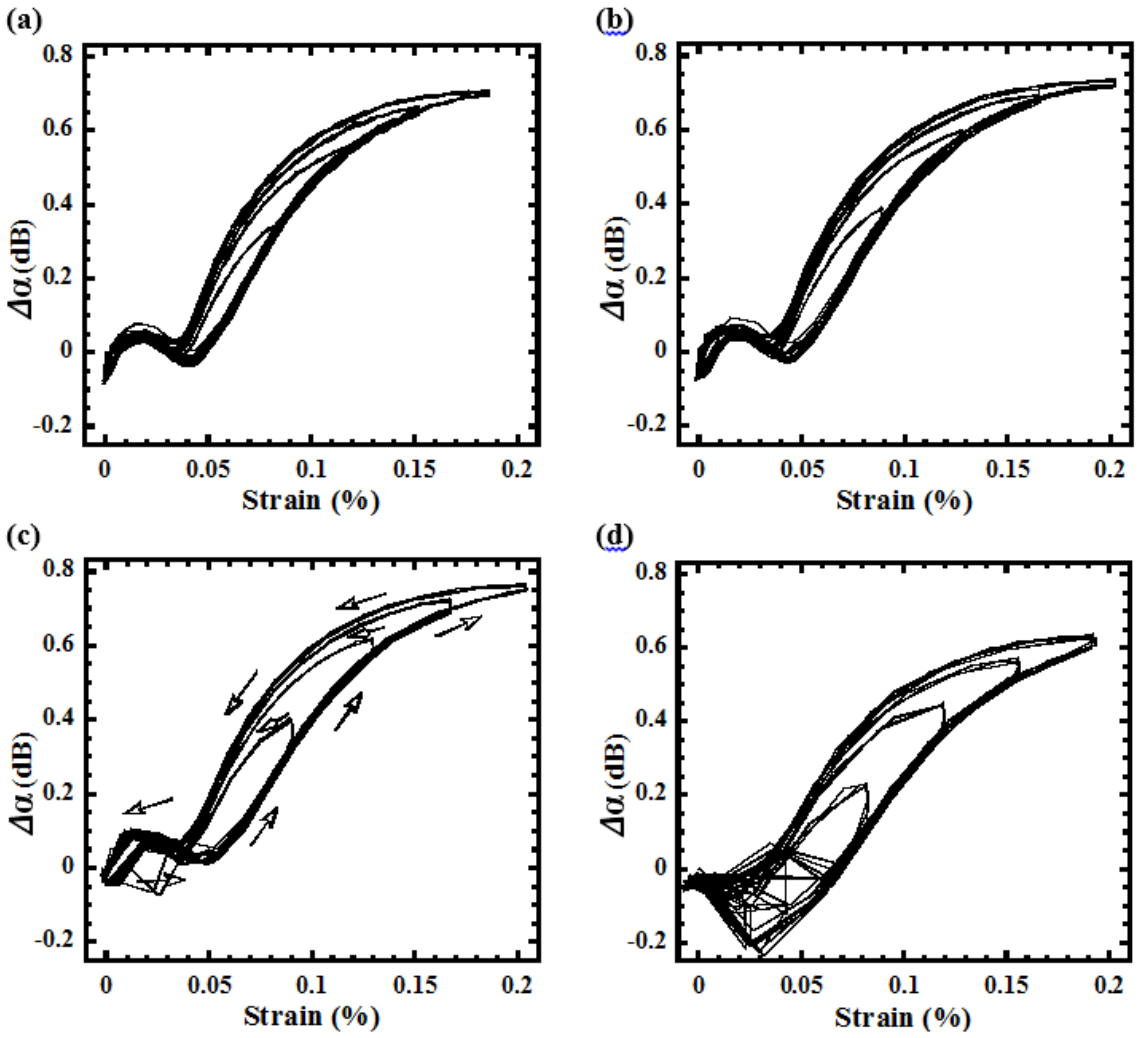

Figure C-25: Ti_2SC (8µm) Δα results for the longitudinal 5MHz ultrasonic wave mode at different strain rates. (a) $1.65x10^{-4}s^{-1}$, (b) $3.3x10^{-4}s^{-1}$, (c) $6.6x10^{-4}s^{-1}$ and (d) $13.2x10^{-4}s^{-1}$. A holding time of 10 s at stresses 500, 400, 300, 200, 100 & 50MPa was performed.

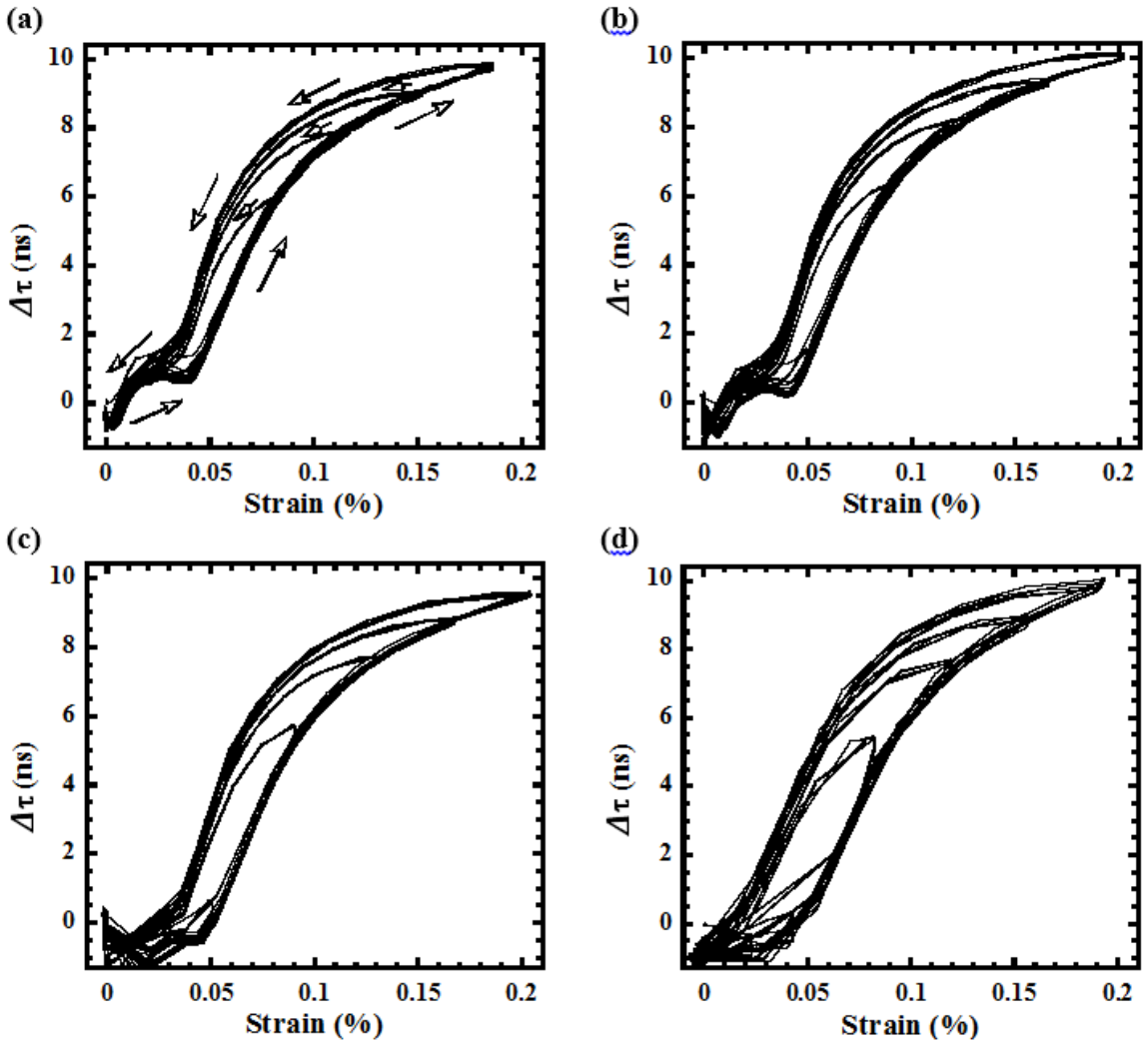

Figure C-26: Ti_2SC (8µm) $\Delta\tau$ results for the longitudinal 5MHz ultrasonic wave mode at different strain rates. (a) $1.65x10^{-4}s^{-1}$, (b) $3.3x10^{-4}s^{-1}$, (c) $6.6x10^{-4}s^{-1}$ and (d) $13.2x10^{-4}s^{-1}$. A holding time of 10 s at stresses 500, 400, 300, 200, 100 & 50MPa was performed.

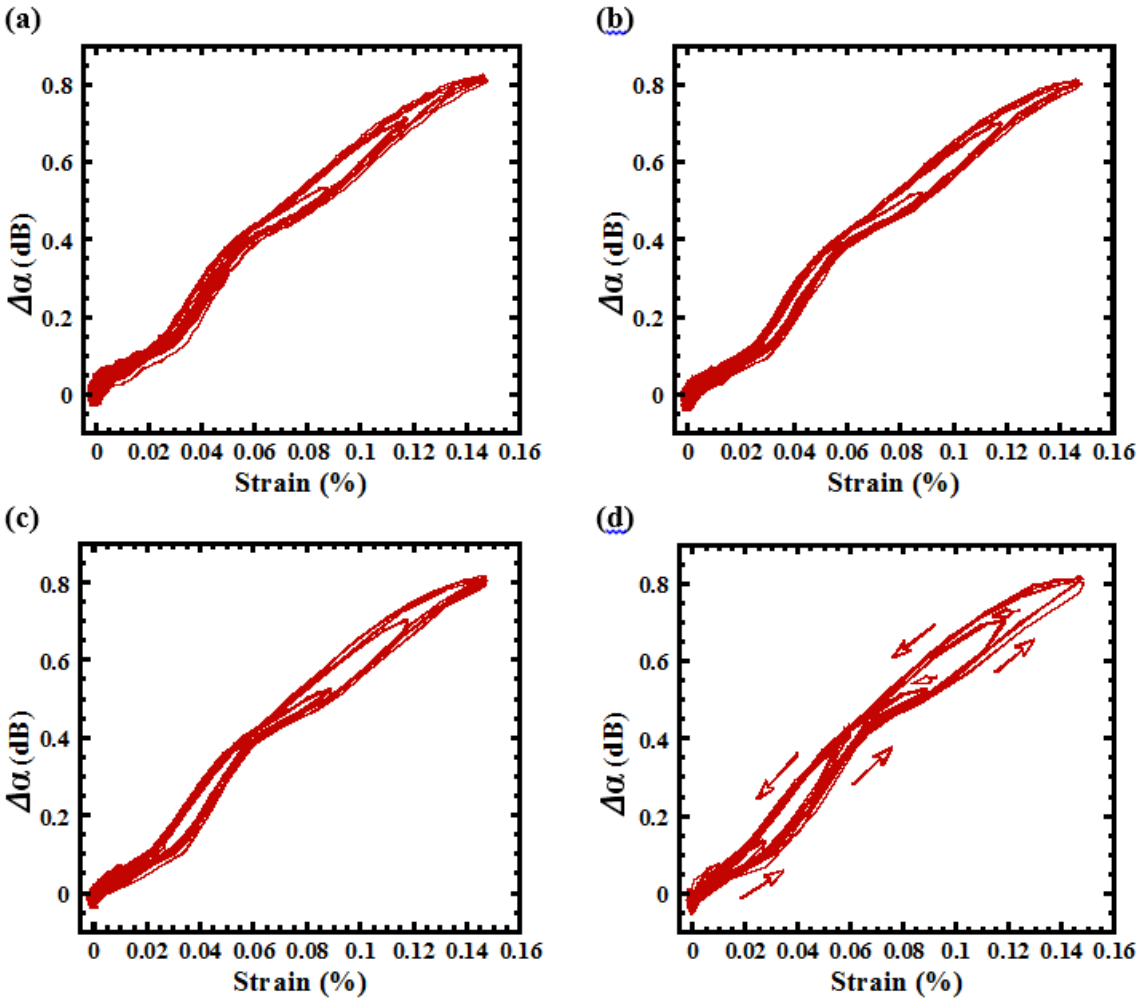

Figure C-27: Ti_2SC (8µm) Δα results for the shear-P 5MHz ultrasonic wave mode at different strain rates. (a) $1.65x10^{-4}$ s^{-1}, (b) $3.3x10^{-4}$ s^{-1}, (c) $6.6x10^{-4}s^{-1}$ and (d) $13.2x10^{-4}$ s^{-1}. A holding time of 10 s at stresses 500, 400, 300, 200, 100 & 50 MPa was performed.

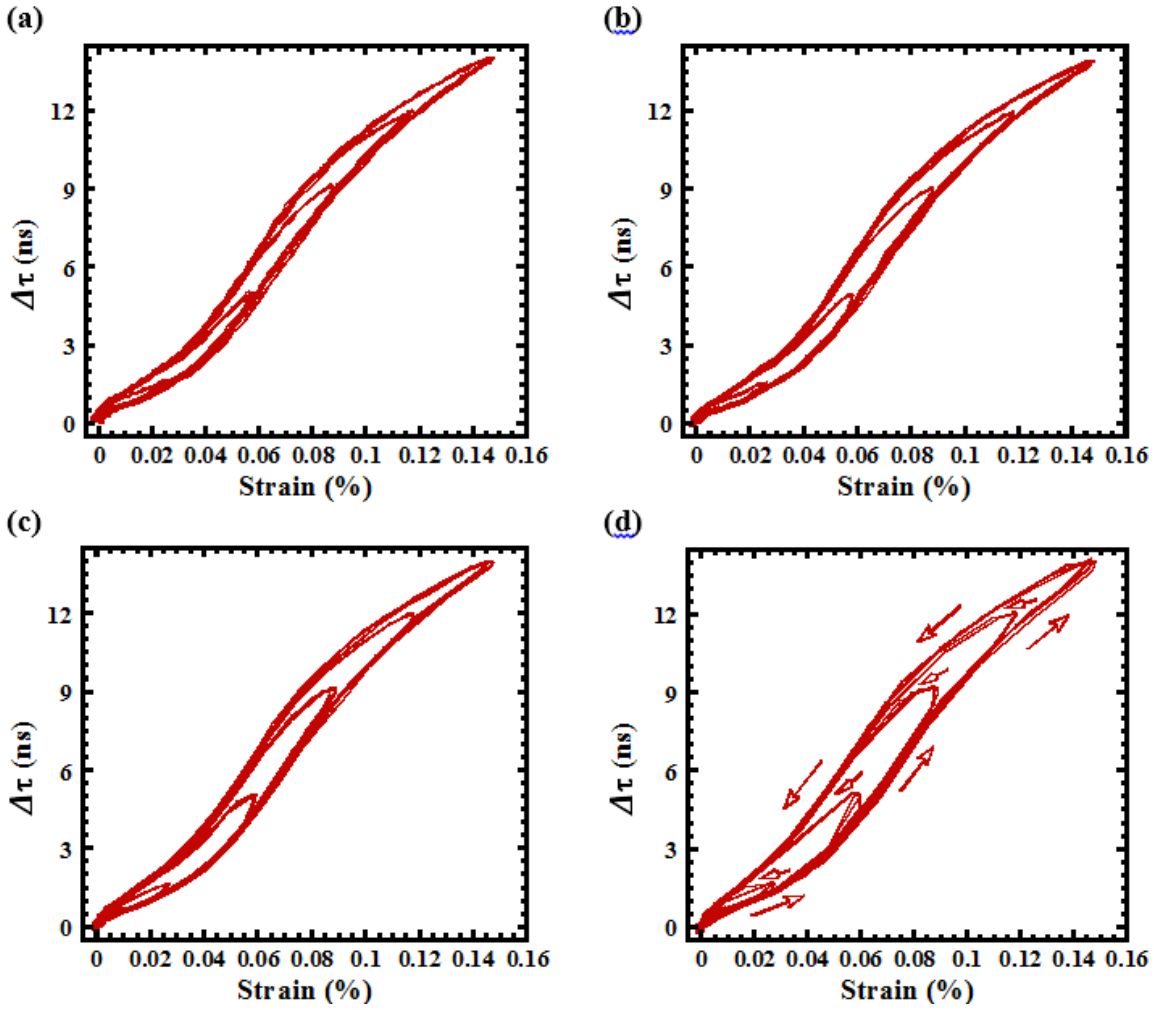

Figure C-28: Ti_2SC (8µm) Δτ results for the Shear-P 5MHz ultrasonic wave mode at different strain rates. (a) $1.65x10^{-4}s^{-1}$, (b) $3.3x10^{-4}s^{-1}$, (c) $6.6x10^{-4}s^{-1}$ and (d) $13.2x10^{-4}s^{-1}$. A holding time of 10 s at stresses 500, 400, 300, 200, 100 & 50MPa was performed.

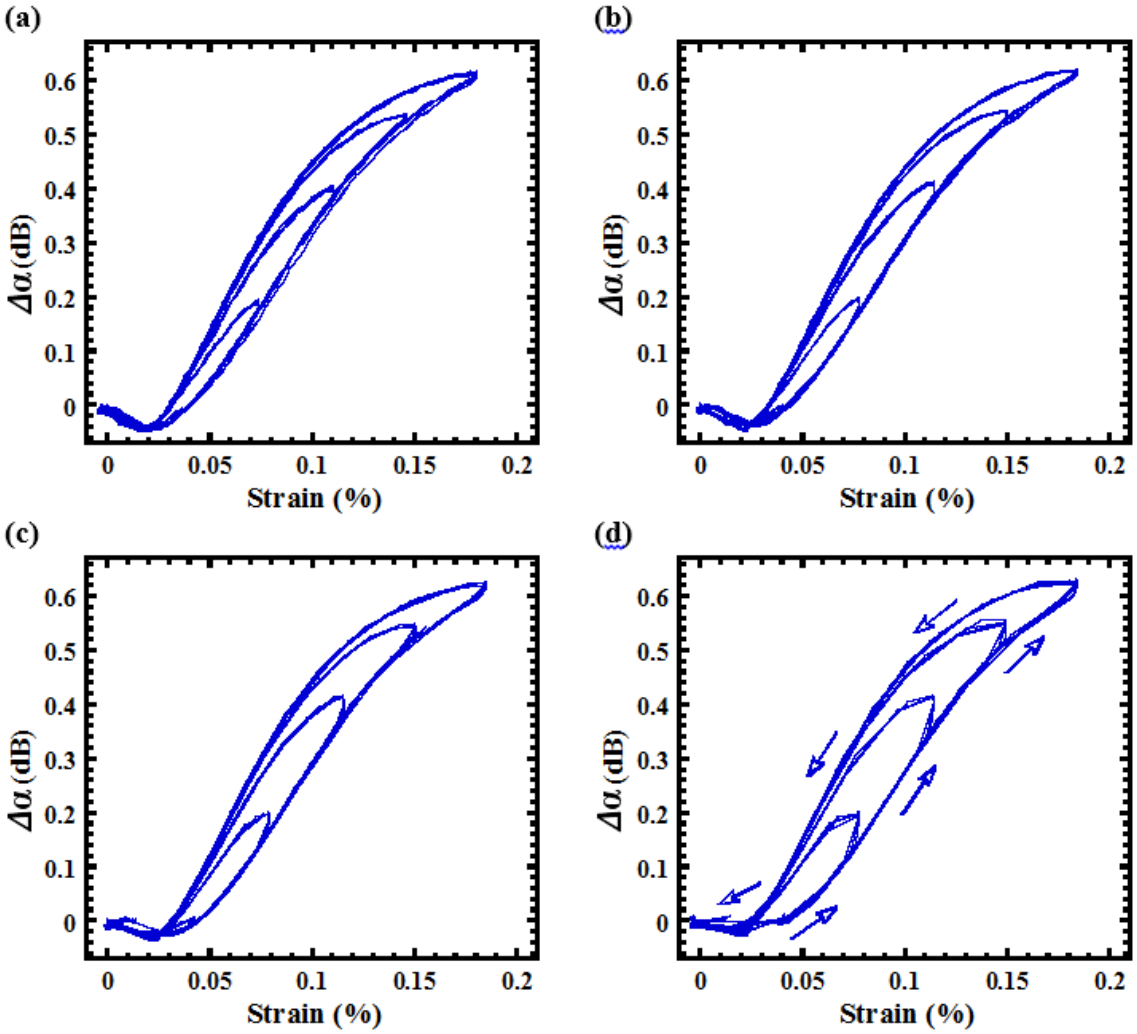

Figure C-29: Ti_2SC (8µm) Δα results for the Shear-N 5MHz ultrasonic wave mode at different strain rates. (a) $1.65x10^{-4}s^{-1}$, (b) $3.3x10^{-4}s^{-1}$, (c) $6.6x10^{-4}s^{-1}$ and (d) $13.2x10^{-4}s^{-1}$. A holding time of 10 s at stresses 500, 400, 300, 200, 100 & 50MPa was performed.

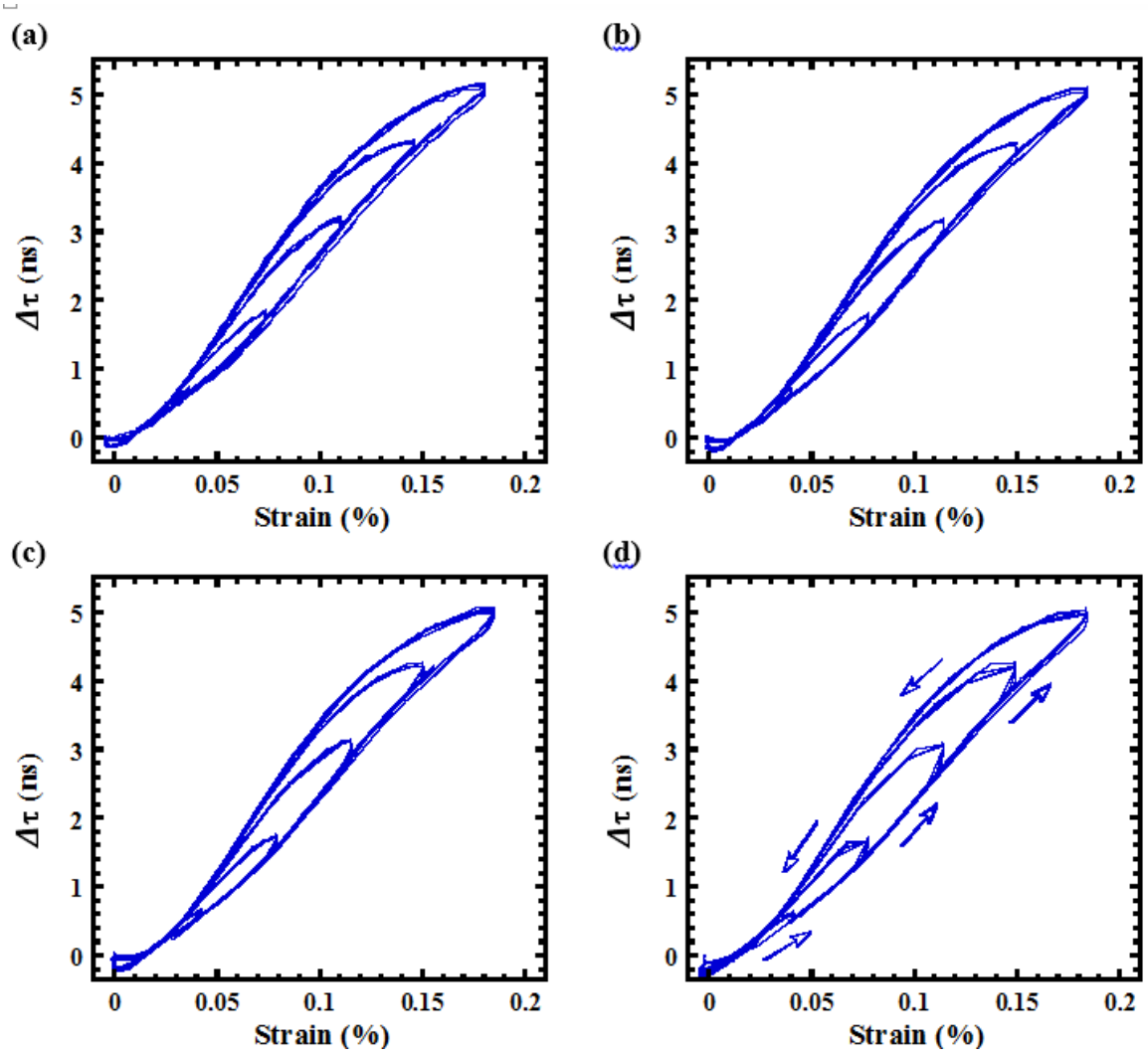

Figure C-30: Ti_2SC (8µm) Δτ results for the Shear-N 5MHz ultrasonic wave mode at different strain rates. (a) $1.65x10^{-4}s^{-1}$, (b) $3.3x10^{-4}s^{-1}$, (c) $6.6x10^{-4}s^{-1}$ and (d) $13.2x10^{-4}s^{-1}$. A holding time of 10 s at stresses 500, 400, 300, 200, 100 & 50MPa was performed.

C3.2 FG and CG Ti_3SiC_2 UBS results

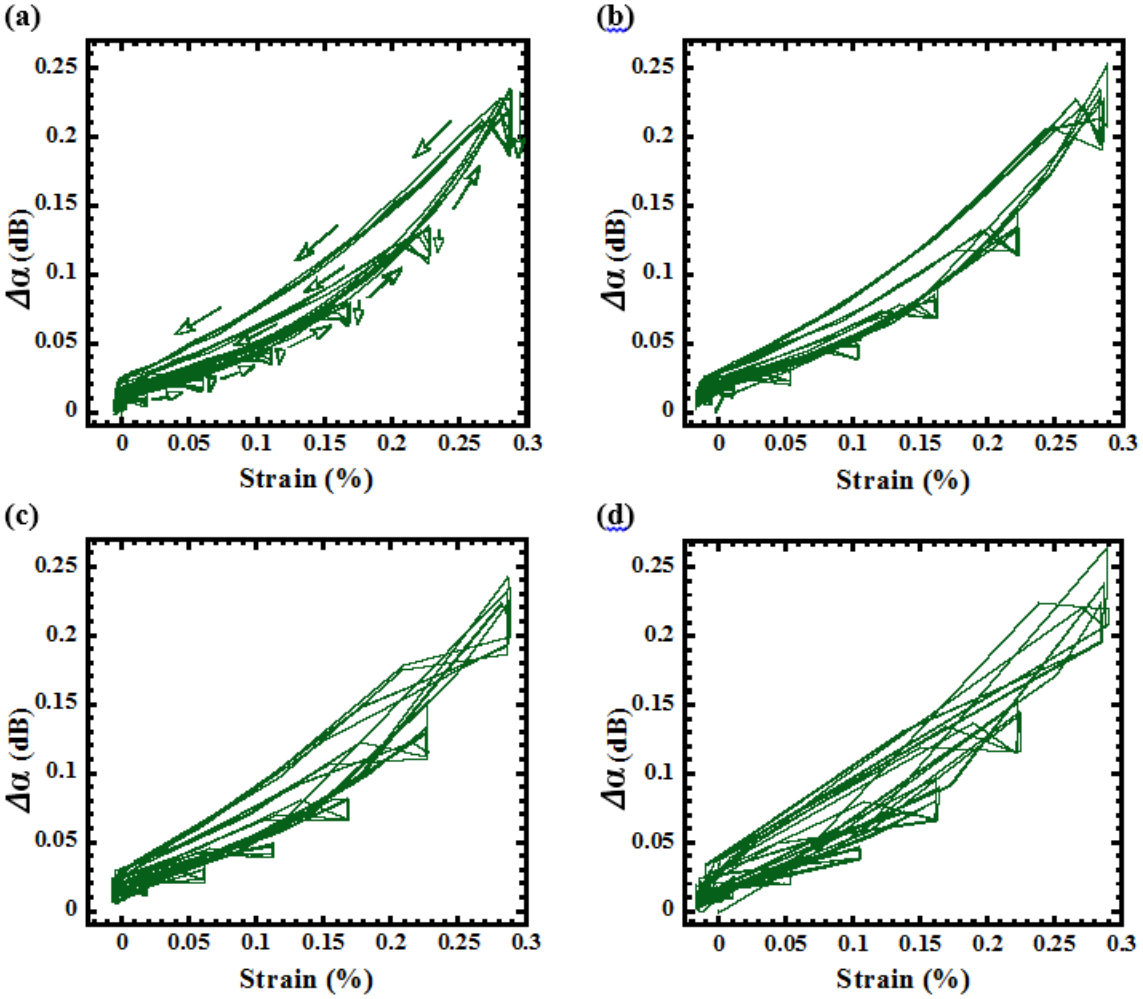

Figure C-31: FG Ti_3SiC_2 Δα results for the longitudinal 10MHz ultrasonic wave mode at different strain rates. (a) $1.65x10^{-4}s^{-1}$, (b) $3.3x10^{-4}s^{-1}$, (c) $6.6x10^{-4}s^{-1}$ and (d) $13.2x10^{-4}s^{-1}$. A holding time of 10 s at stresses 600, 500, 400, 300, 200, 100 & 50MPa was performed.

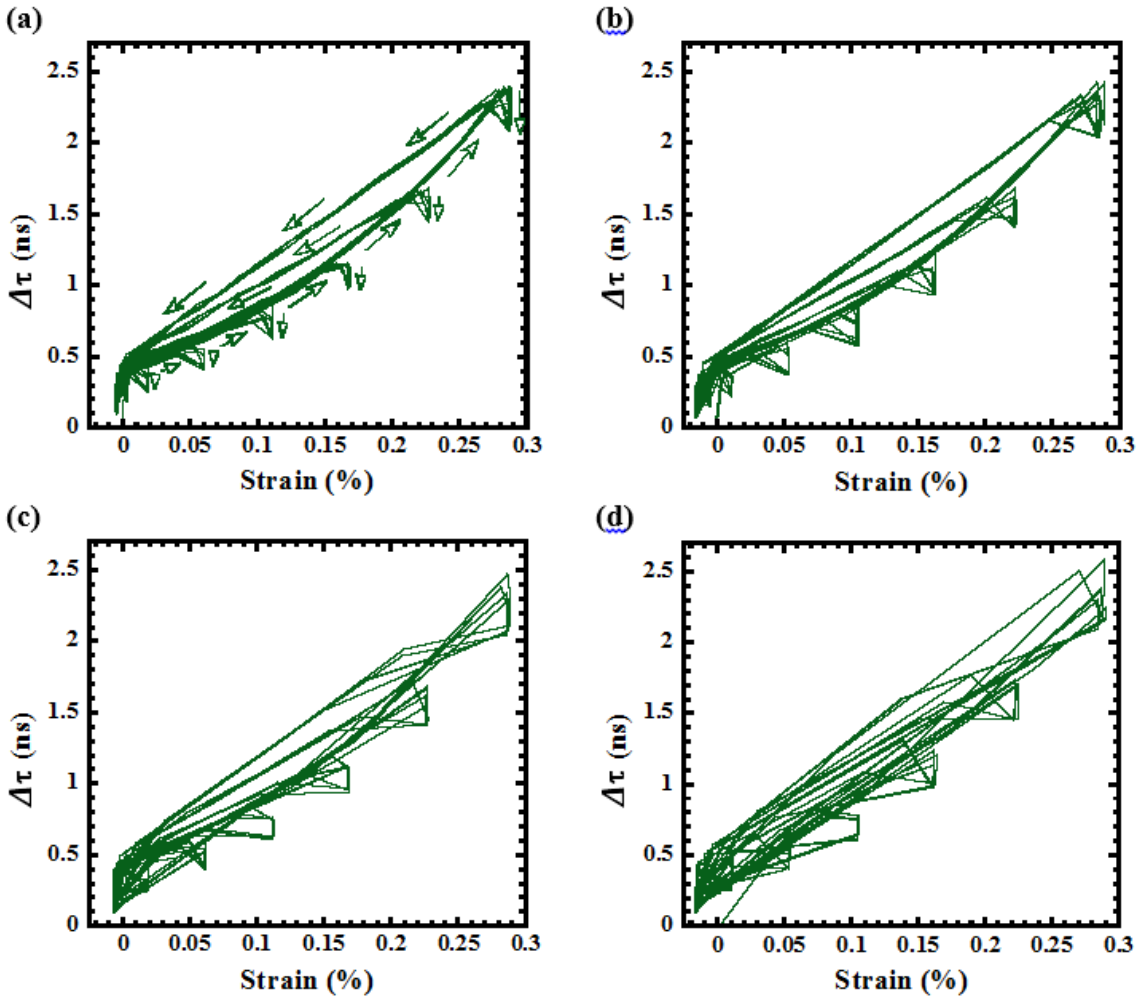

Figure C-32: FG Ti_3SiC_2 $\Delta\tau$ results for the longitudinal 10MHz ultrasonic wave mode at different strain rates. (a) $1.65x10^{-4}s^{-1}$, (b) $3.3x10^{-4}s^{-1}$, (c) $6.6x10^{-4}s^{-1}$ and (d) $13.2x10^{-4}s^{-1}$. A holding time of 10 s at stresses 600, 500, 400, 300, 200, 100 & 50MPa was performed.

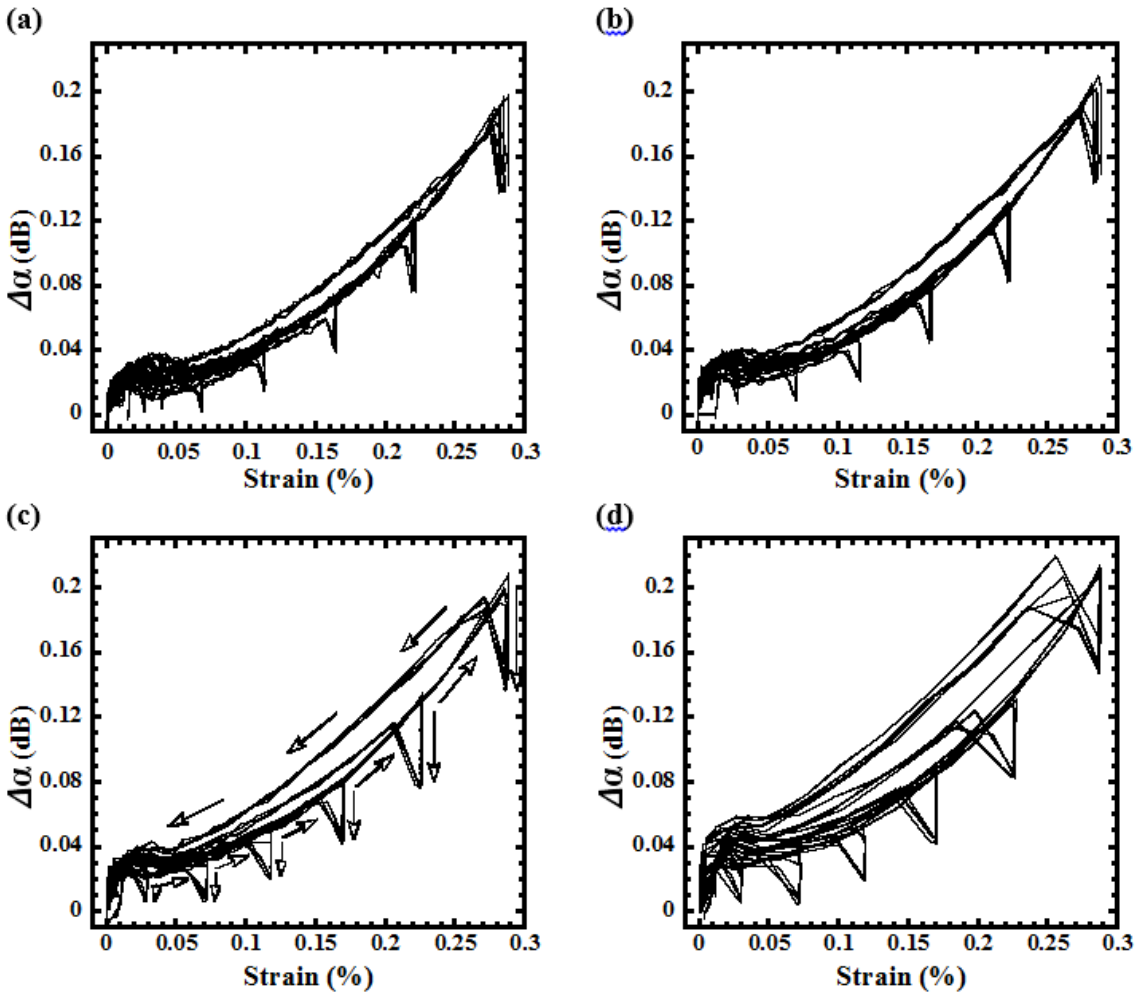

Figure C-33: FG Ti_3SiC_2 $\Delta\alpha$ results for the longitudinal 5MHz ultrasonic wave mode at different strain rates. (a) $1.65x10^{-4}s^{-1}$, (b) $3.3x10^{-4}s^{-1}$, (c) $6.6x10^{-4}s^{-1}$ and (d) $13.2x10^{-4}s^{-1}$. A holding time of 10 s at stresses 600, 500, 400, 300, 200, 100 & 50MPa was performed.

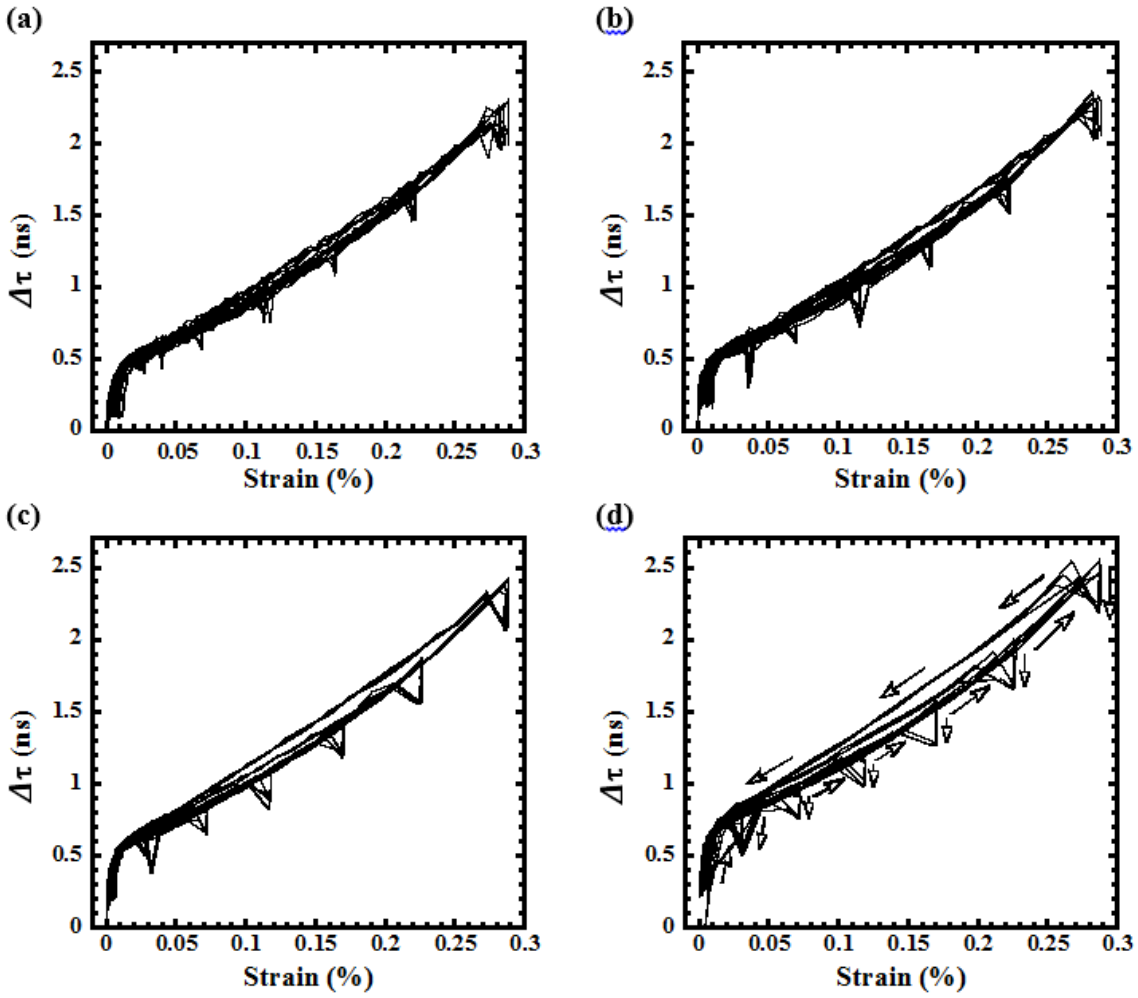

Figure C-34: FG Ti_3SiC_2 $\Delta\tau$ results for the longitudinal 5MHz ultrasonic wave mode at different strain rates. (a) $1.65x10^{-4}s^{-1}$, (b) $3.3x10^{-4}s^{-1}$, (c) $6.6x10^{-4}s^{-1}$ and (d) $13.2x10^{-4}s^{-1}$. A holding time of 10 s at stresses 600, 500, 400, 300, 200, 100 & 50MPa was performed.

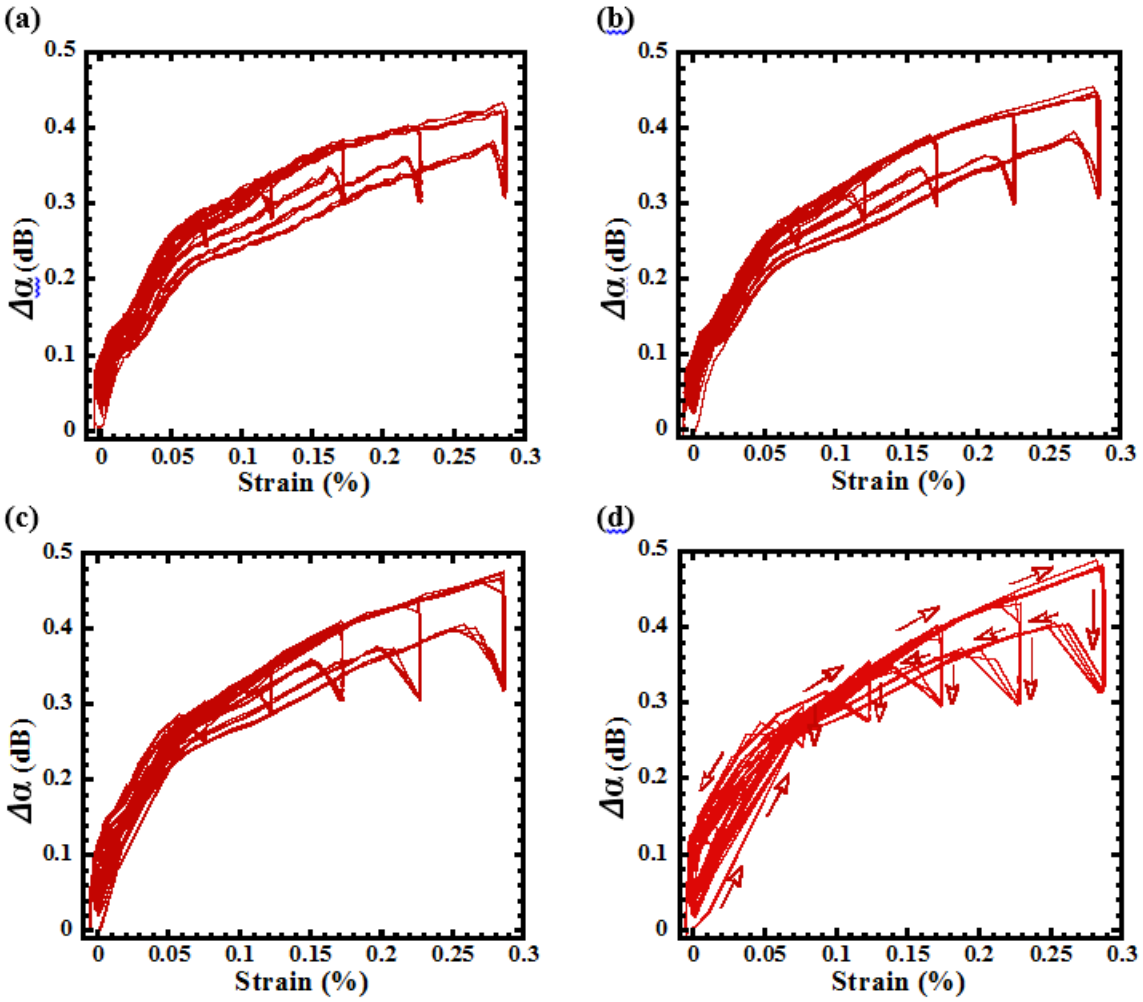

Figure C-35: FG Ti_3SiC_2 Δα results for the Shear-P 5MHz ultrasonic wave mode at different strain rates. (a) $1.65x10^{-4}s^{-1}$, (b) $3.3x10^{-4}s^{-1}$, (c) $6.6x10^{-4}s^{-1}$ and (d) $13.2x10^{-4}s^{-1}$. A holding time of 10 s at stresses 600, 500, 400, 300, 200, 100 & 50MPa was performed.

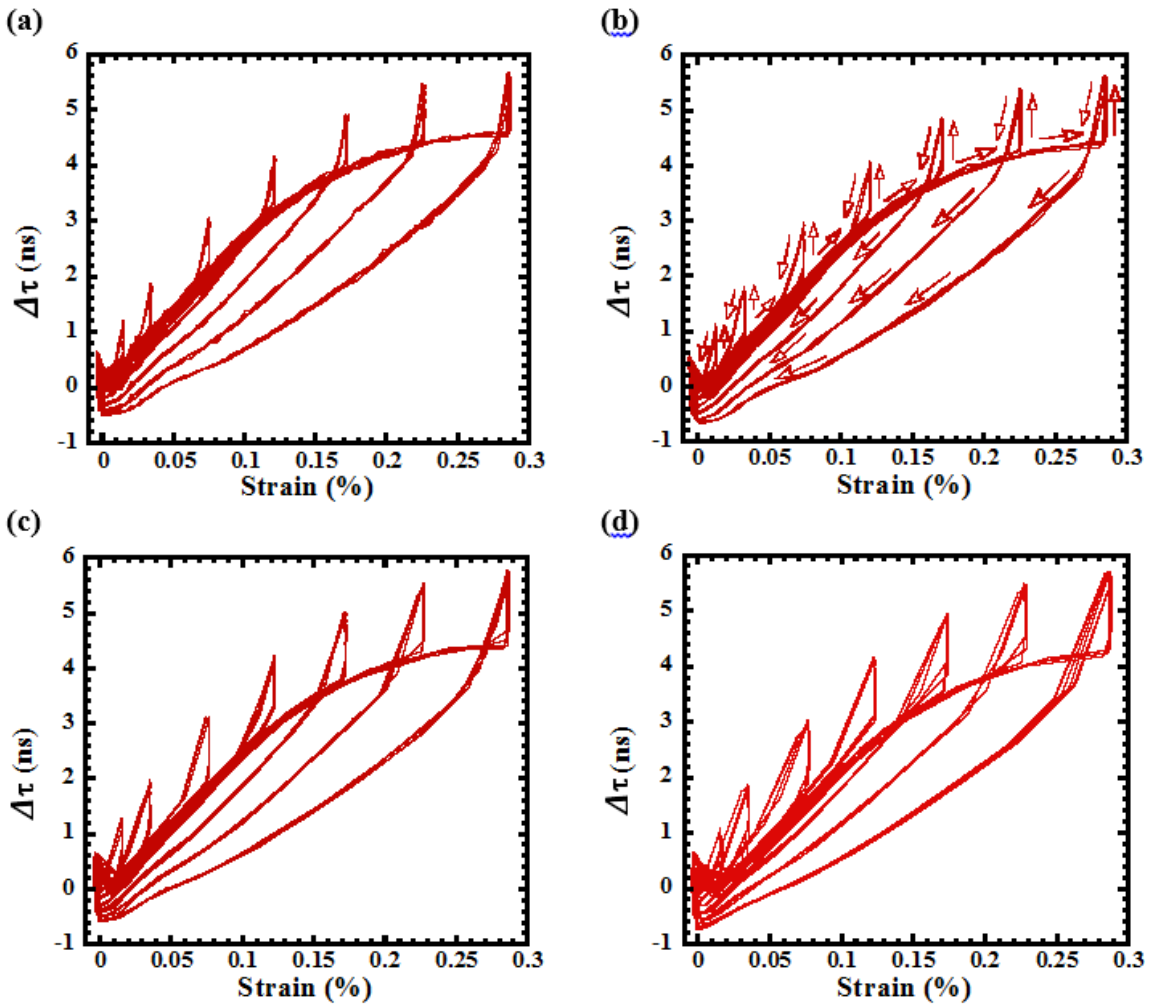

Figure C-36: FG Ti_3SiC_2 $\Delta\tau$ results for the Shear-P 5MHz ultrasonic wave mode at different strain rates. (a) $1.65x10^{-4}s^{-1}$, (b) $3.3x10^{-4}s^{-1}$, (c) $6.6x10^{-4}s^{-1}$ and (d) $13.2x10^{-4}s^{-1}$. A holding time of 10 s at stresses 600, 500, 400, 300, 200, 100 & 50MPa was performed.

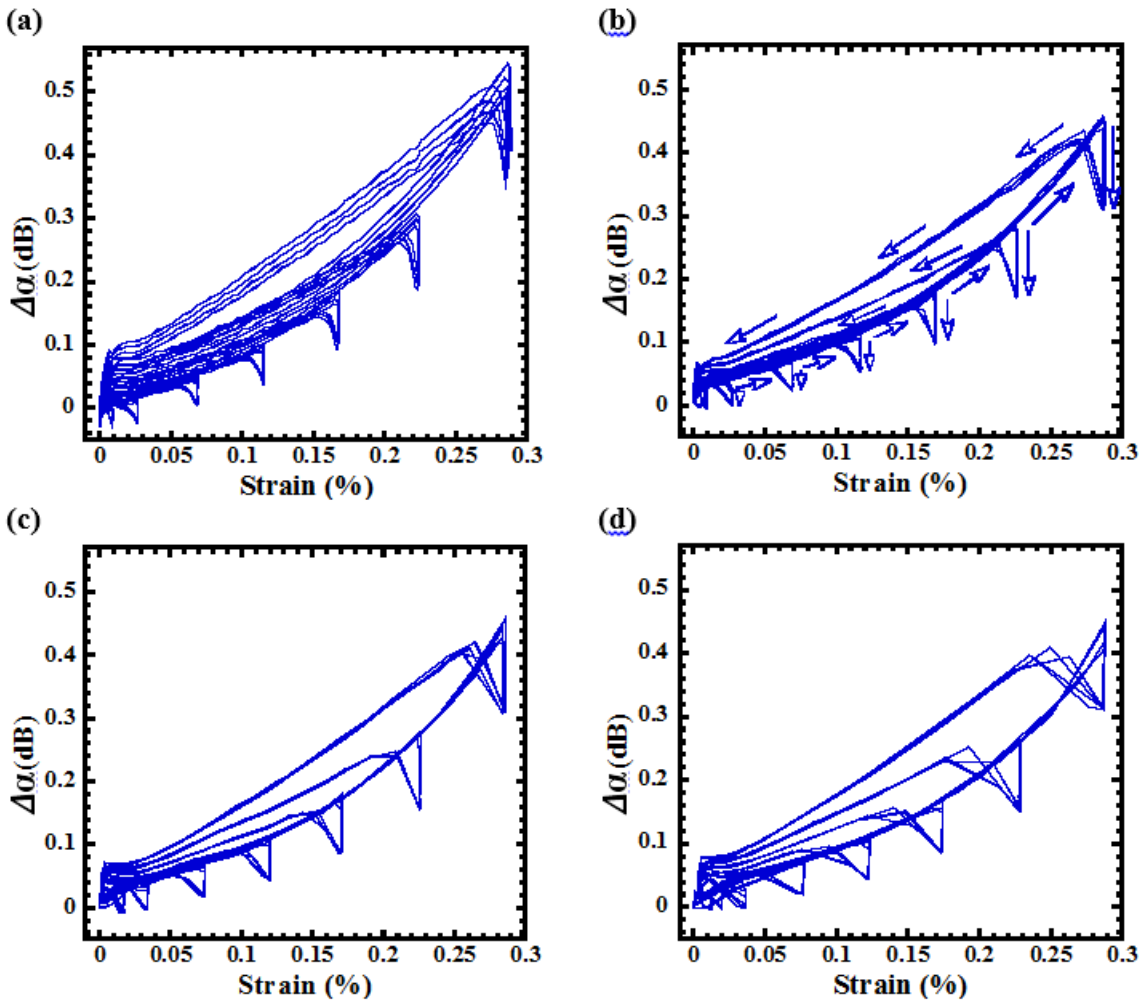

Figure C-37: FG Ti_3SiC_2 Δα results for the Shear-N 5MHz ultrasonic wave mode at different strain rates. (a) $1.65x10^{-4}s^{-1}$, (b) $3.3x10^{-4}s^{-1}$, (c) $6.6x10^{-4}s^{-1}$ and (d) $13.2x10^{-4}s^{-1}$. A holding time of 10 s at stresses 600, 500, 400, 300, 200, 100 & 50MPa was performed.

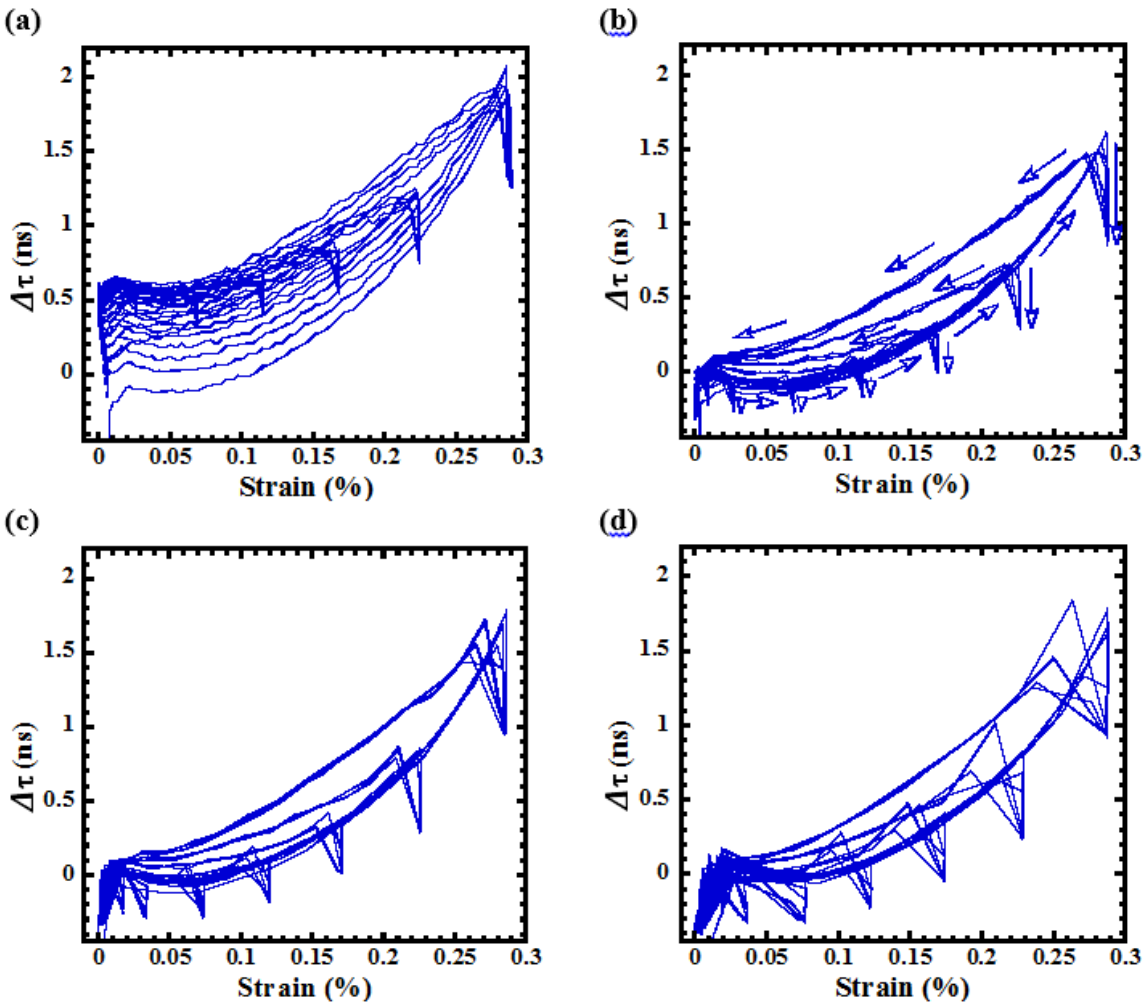

Figure C-38: FG Ti_3SiC_2 Δτ results for the Shear-N 5MHz ultrasonic wave mode at different strain rates. (a) $1.65x10^{-4}s^{-1}$, (b) $3.3x10^{-4}s^{-1}$, (c) $6.6x10^{-4}s^{-1}$ and (d) $13.2x10^{-4}s^{-1}$. A holding time of 10 s at stresses 600, 500, 400, 300, 200, 100 & 50MPa was performed.

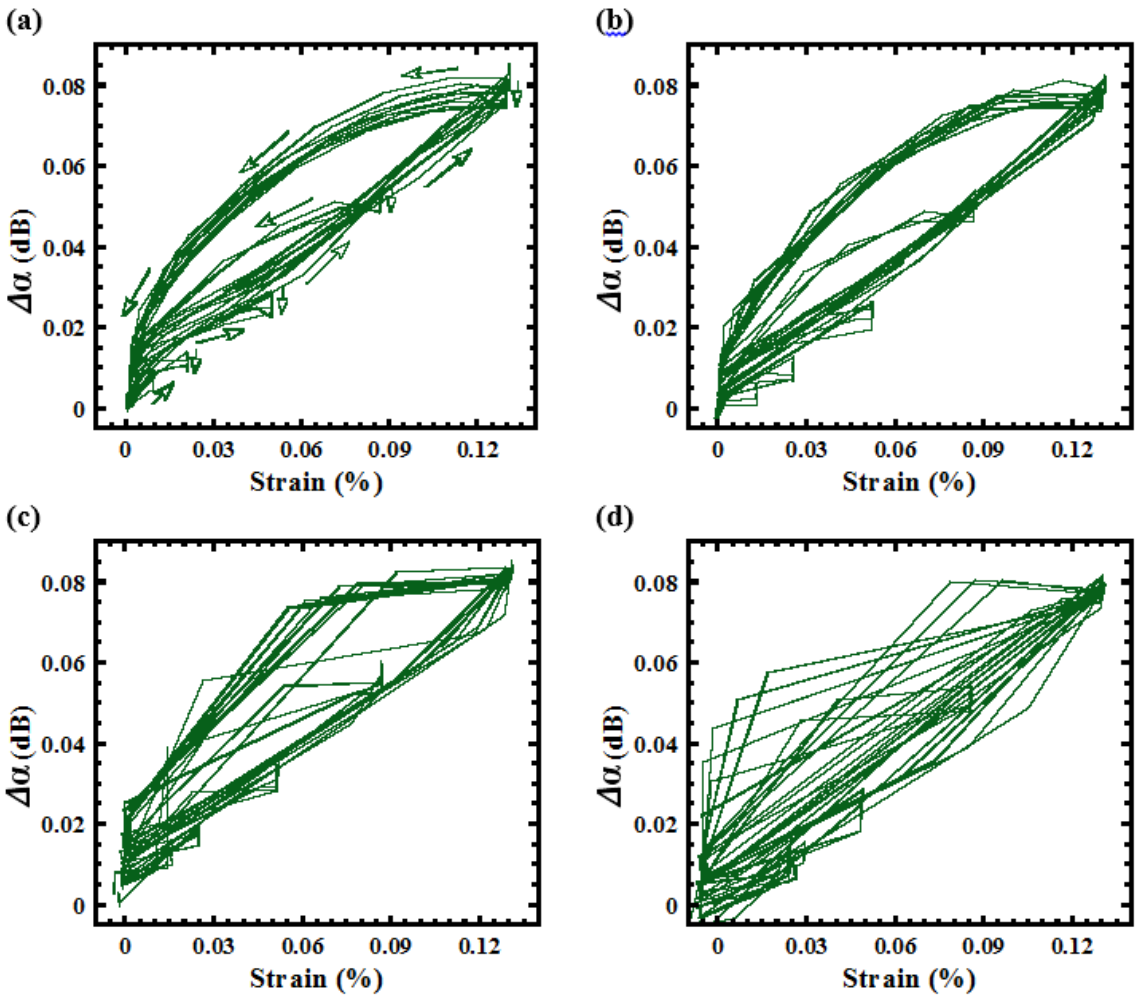

Figure C-39: CG Ti_3SiC_2 Δα results for the longitudinal 10MHz ultrasonic wave mode at different strain rates. (a) $1.65x10^{-4}s^{-1}$, (b) $3.3x10^{-4}s^{-1}$, (c) $6.6x10^{-4}s^{-1}$ and (d) $13.2x10^{-4}s^{-1}$. A holding time of 10 s at stresses 200, 150, 100 & 50MPa was performed.

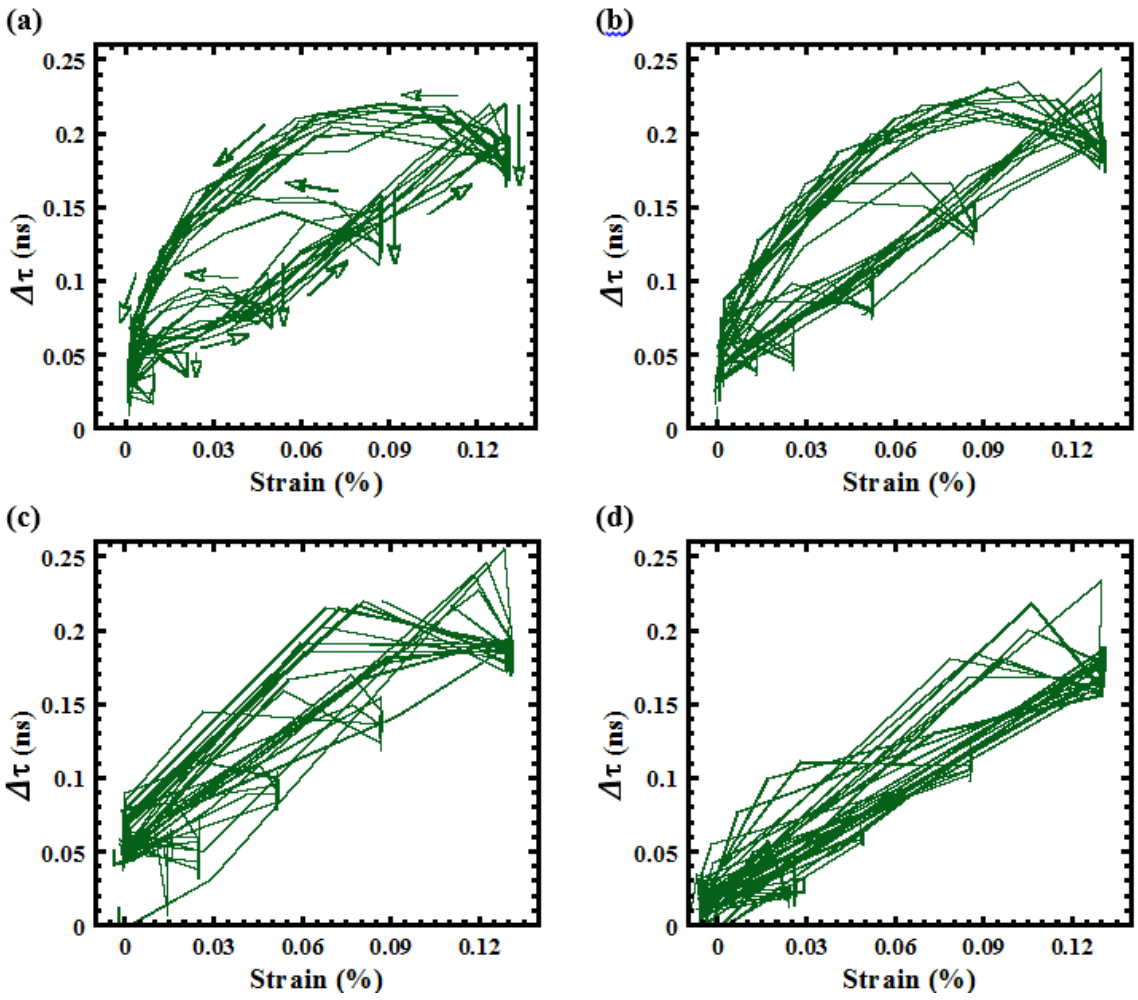

Figure C-40: CG Ti_3SiC_2 Δτ results for the longitudinal 10MHz ultrasonic wave mode at different strain rates. (a) $1.65x10^{-4}s^{-1}$, (b) $3.3x10^{-4}s^{-1}$, (c) $6.6x10^{-4}s^{-1}$ and (d) $13.2x10^{-4}s^{-1}$. A holding time of 10 s at stresses 200, 150, 100 & 50MPa was performed.

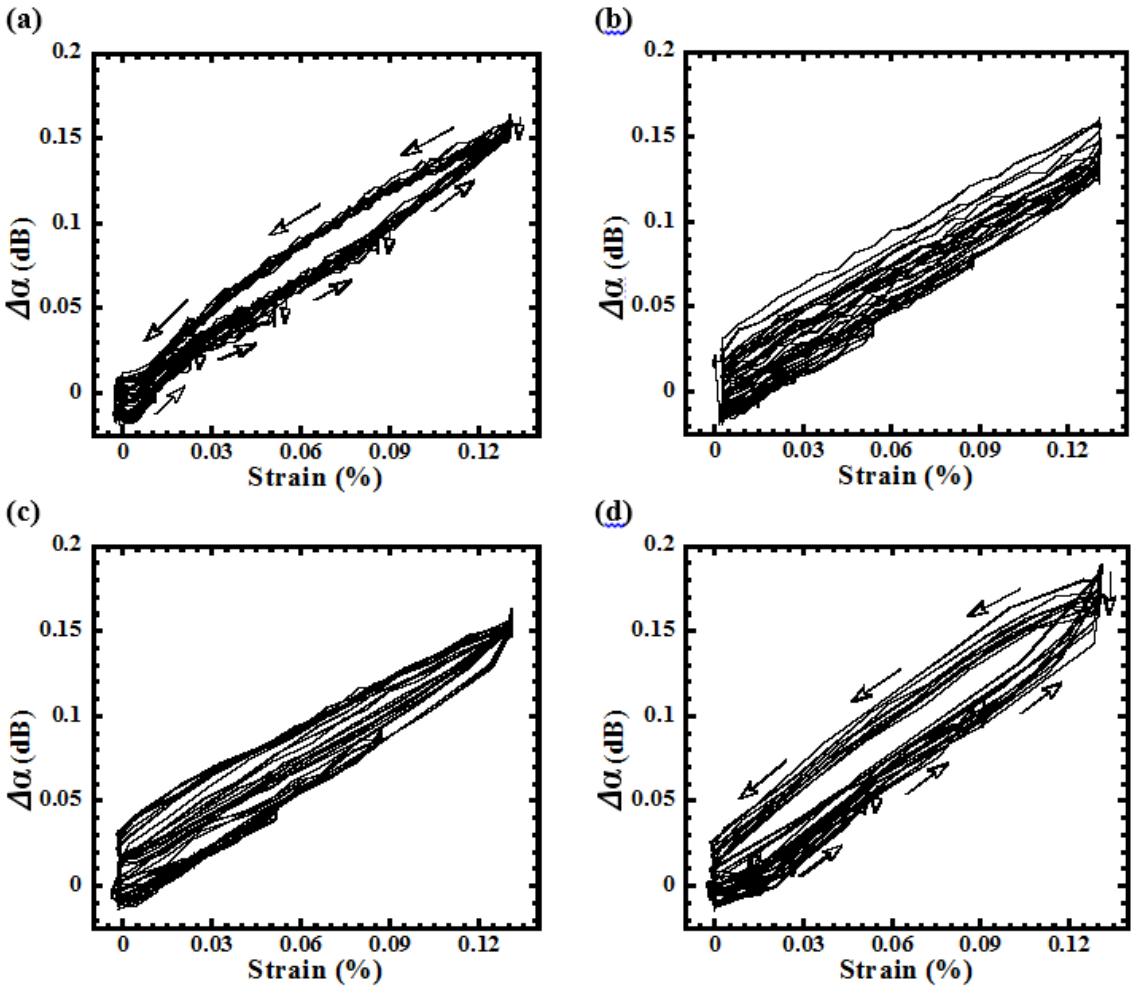

Figure C-41: CG Ti_3SiC_2 Δα results for the longitudinal 5MHz ultrasonic wave mode at different strain rates. (a) $1.65x10^{-4}s^{-1}$, (b) $3.3x10^{-4}s^{-1}$, (c) $6.6x10^{-4}s^{-1}$ and (d) $13.2x10^{-4}s^{-1}$. A holding time of 10 s at stresses 200, 150, 100 & 50MPa was performed.

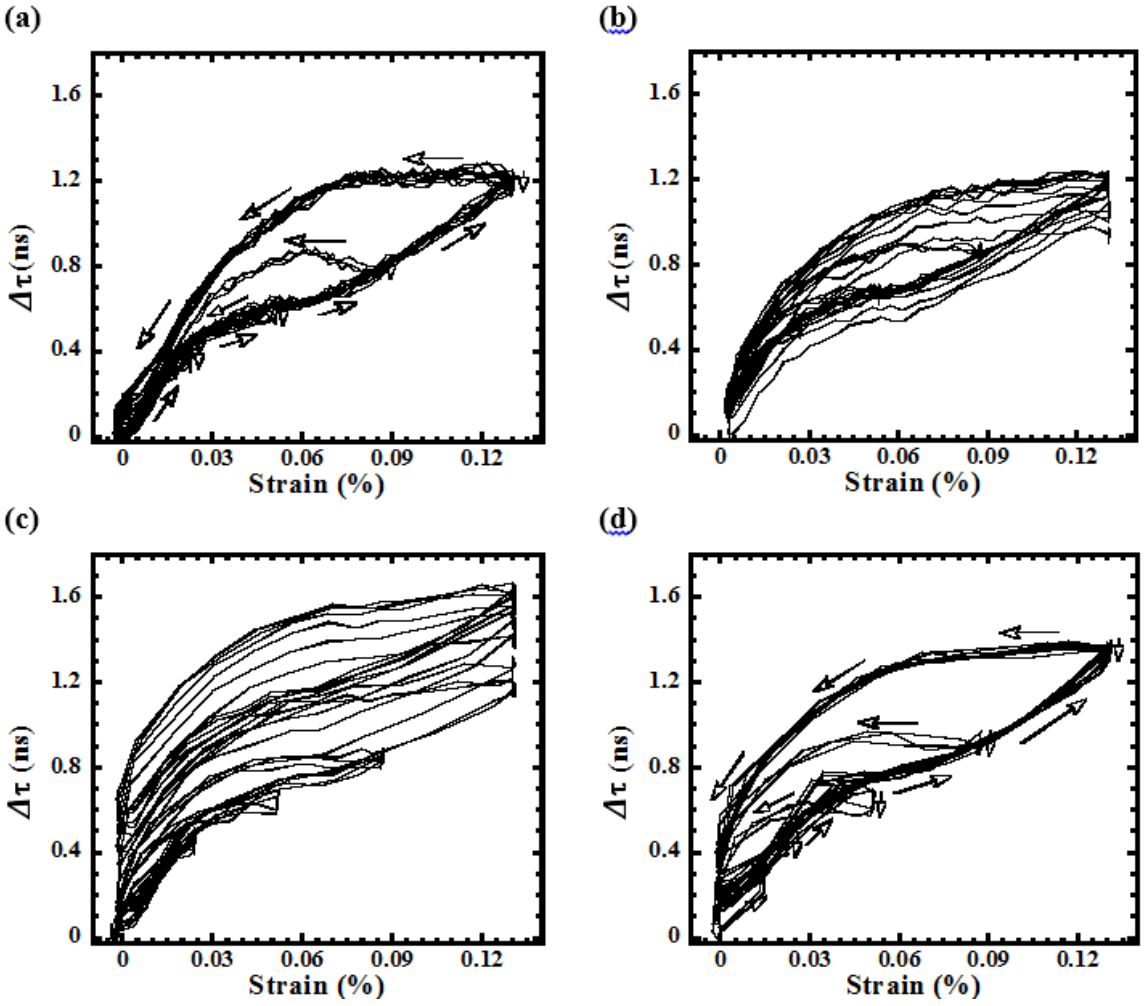

Figure C-42: CG Ti_3SiC_2 $\Delta\tau$ results for the longitudinal 5MHz ultrasonic wave mode at different strain rates. (a) $1.65x10^{-4}s^{-1}$, (b) $3.3x10^{-4}s^{-1}$, (c) $6.6x10^{-4}s^{-1}$ and (d) $13.2x10^{-4}s^{-1}$. A holding time of 10 s at stresses 200, 150, 100 & 50MPa was performed.

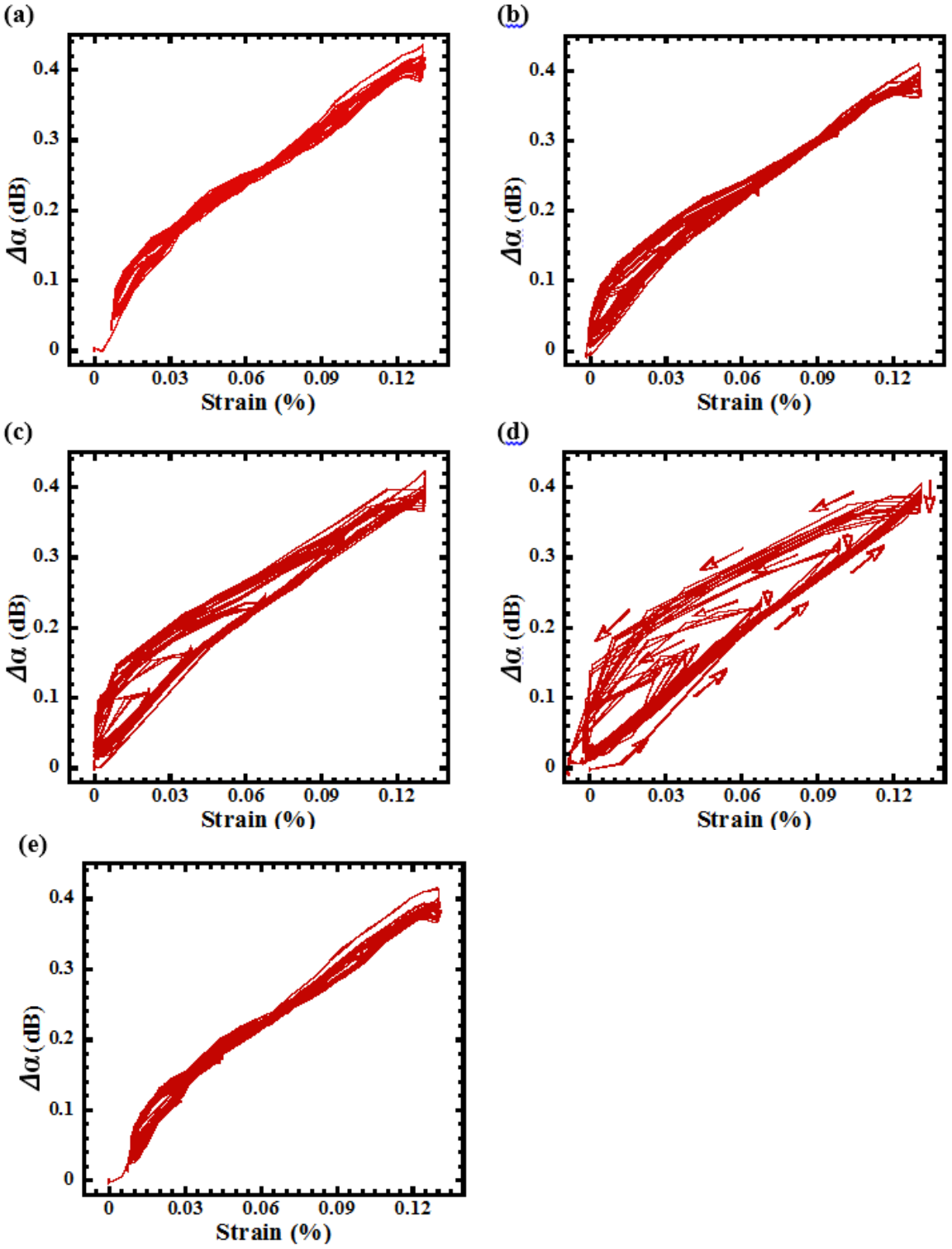

Figure C-43: CG Ti_3SiC_2 Δα results for the Shear-P 5MHz ultrasonic wave mode at different strain rates. (a) $1.65x10^{-4}s^{-1}$, (b) $3.3x10^{-4}s^{-1}$, (c) $6.6x10^{-4}s^{-1}$, (d) $13.2x10^{-4}s^{-1}$ and (e) $1.65x10^{-4}s^{-1}$. A holding time of 10 s at stresses 200, 150, 100 & 50MPa was performed.

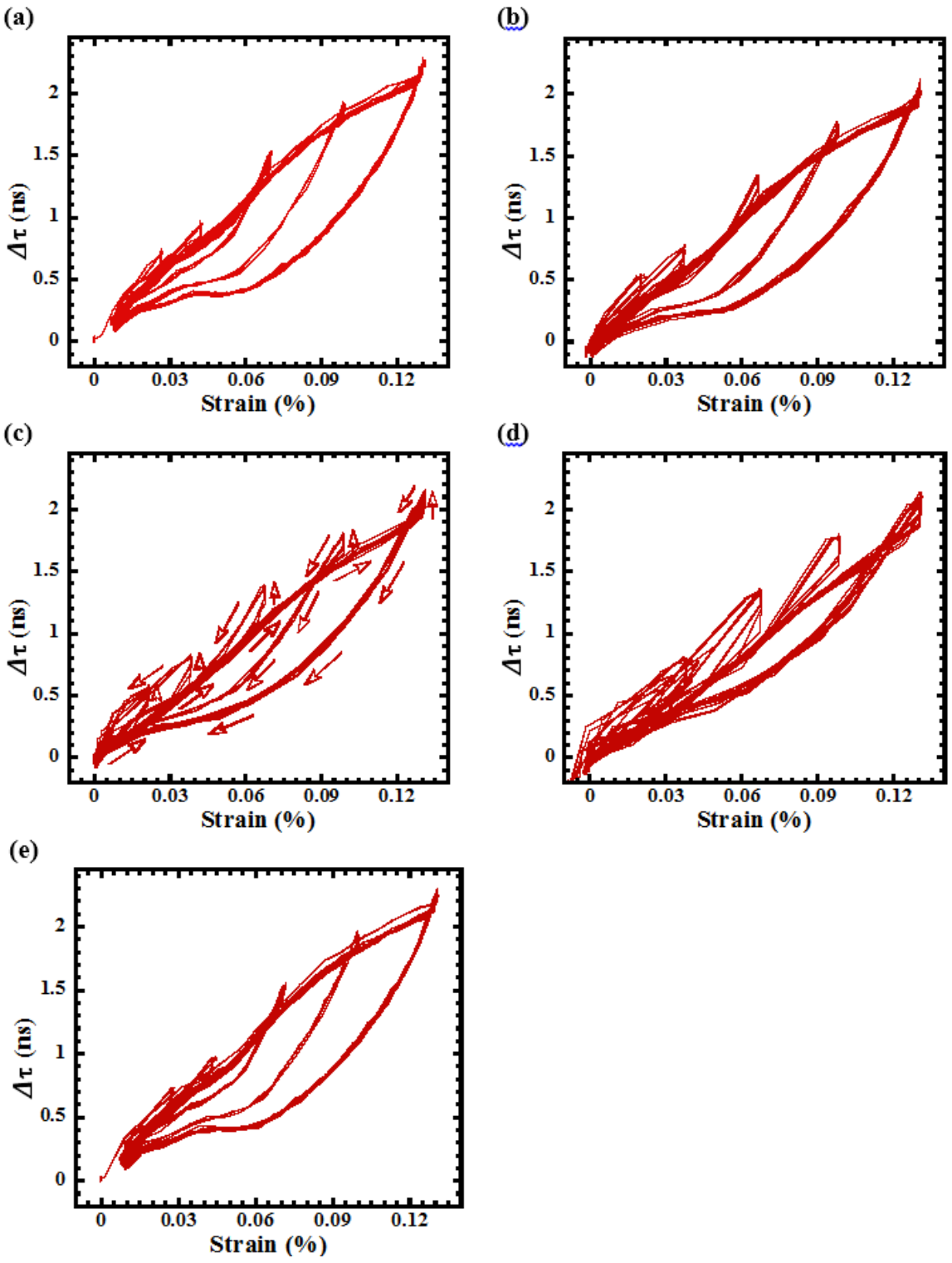

Figure C-44: CG Ti_3SiC_2 Δτ results for the Shear-P 5MHz ultrasonic wave mode at different strain rates. (a) $1.65x10^{-4}s^{-1}$, (b) $3.3x10^{-4}s^{-1}$, (c) $6.6x10^{-4}s^{-1}$, (d) $13.2x10^{-4}s^{-1}$ and (e) $1.65x10^{-4}s^{-1}$. A holding time of 10 s at stresses 200, 150, 100 & 50MPa was performed.

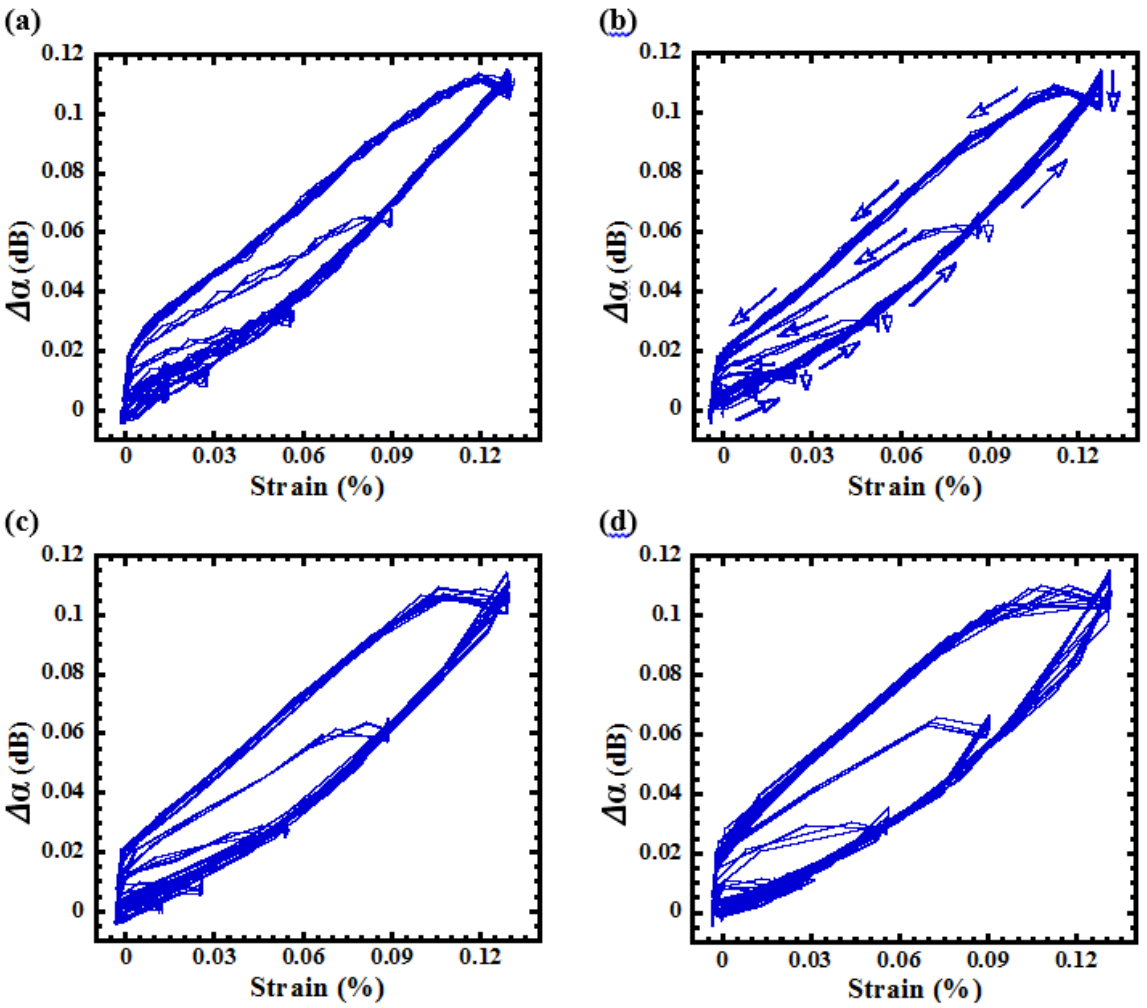

Figure C-45: CG Ti_3SiC_2 Δα results for the Shear-N 5MHz ultrasonic wave mode at different strain rates. (a) $1.65x10^{-4}s^{-1}$, (b) $3.3x10^{-4}s^{-1}$, (c) $6.6x10^{-4}s^{-1}$ and (d) $13.2x10^{-4}s^{-1}$. A holding time of 10 s at stresses 200, 150, 100 & 50MPa was performed.

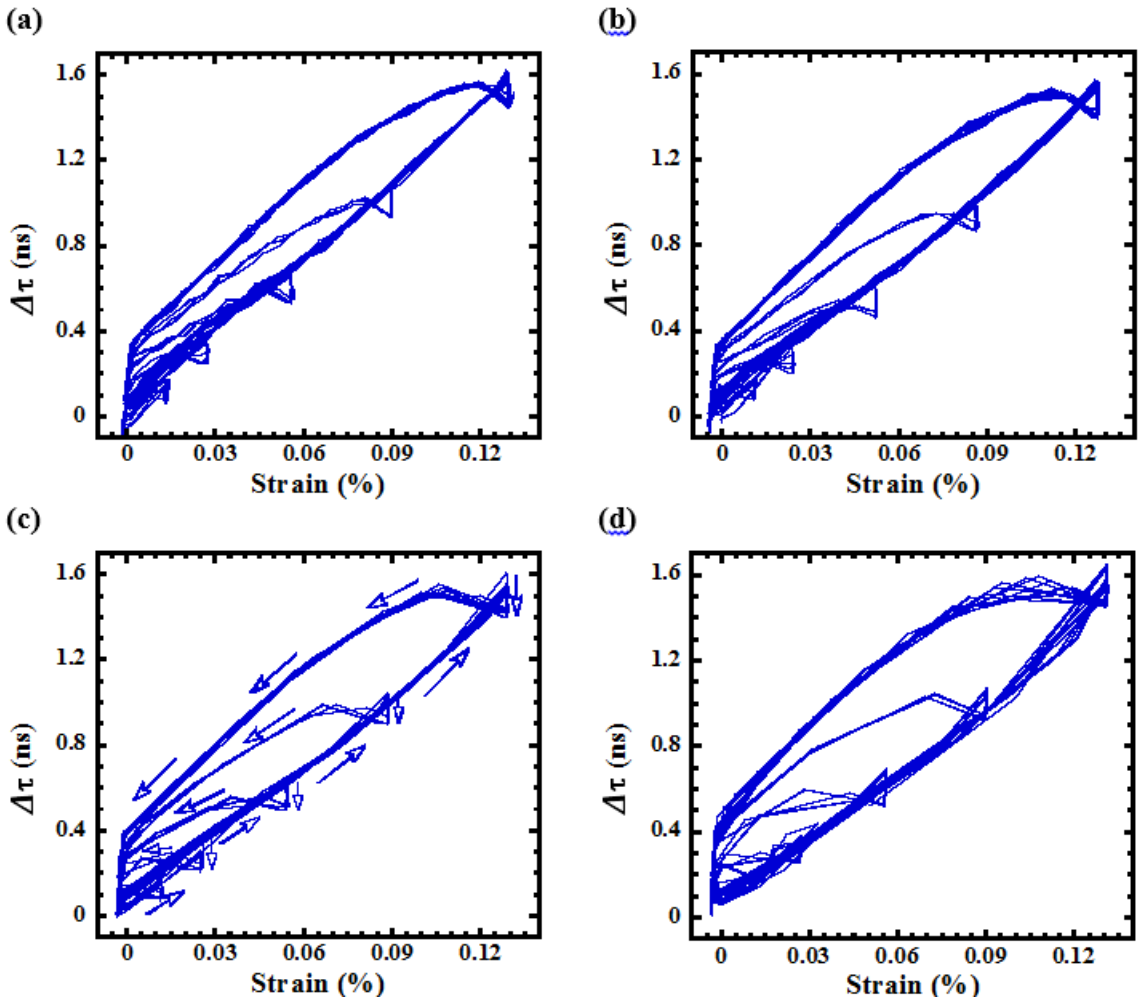

Figure C-46: CG Ti_3SiC_2 Δτ results for the Shear-N 5MHz ultrasonic wave mode at different strain rates. (a) $1.65x10^{-4}s^{-1}$, (b) $3.3x10^{-4}s^{-1}$, (c) $6.6x10^{-4}s^{-1}$ and (d) $13.2x10^{-4}s^{-1}$. A holding time of 10 s at stresses 200, 150, 100 & 50MPa was performed.

C3.3 CG Ti_2AlC-N &-P UBS results

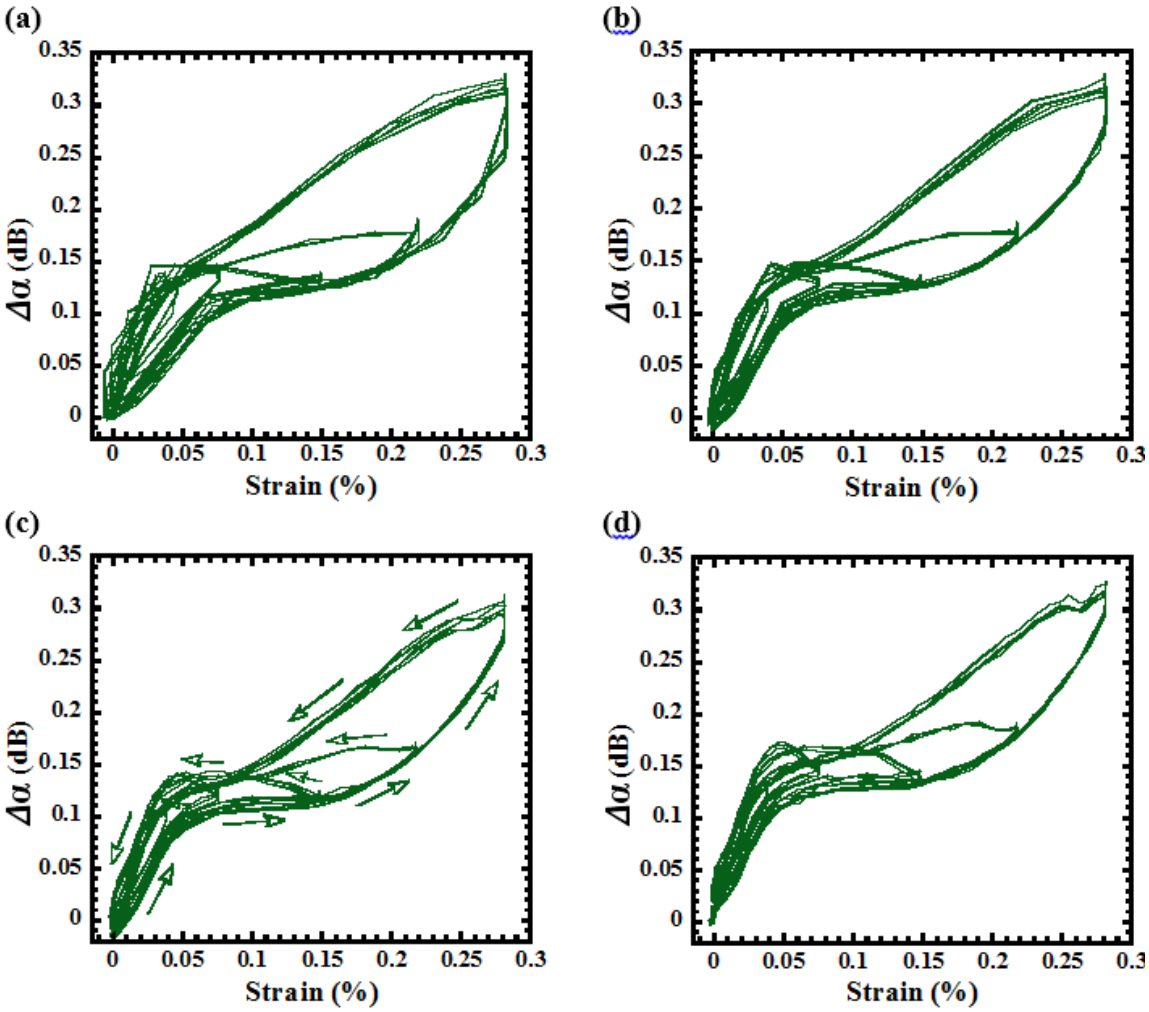

Figure C-47: Ti_2AlC-N texture $\Delta\alpha$ results for the longitudinal 10MHz ultrasonic wave mode at different strain rates. (a) $13.2x10^{-4}s^{-1}$, (b) $6.6x10^{-4}s^{-1}$, (c) $3.3x10^{-4}s^{-1}$ and (d) $1.65x10^{-4}s^{-1}$. A holding time of 10 s at stresses 400, 300, 200, 100 & 50MPa was performed.

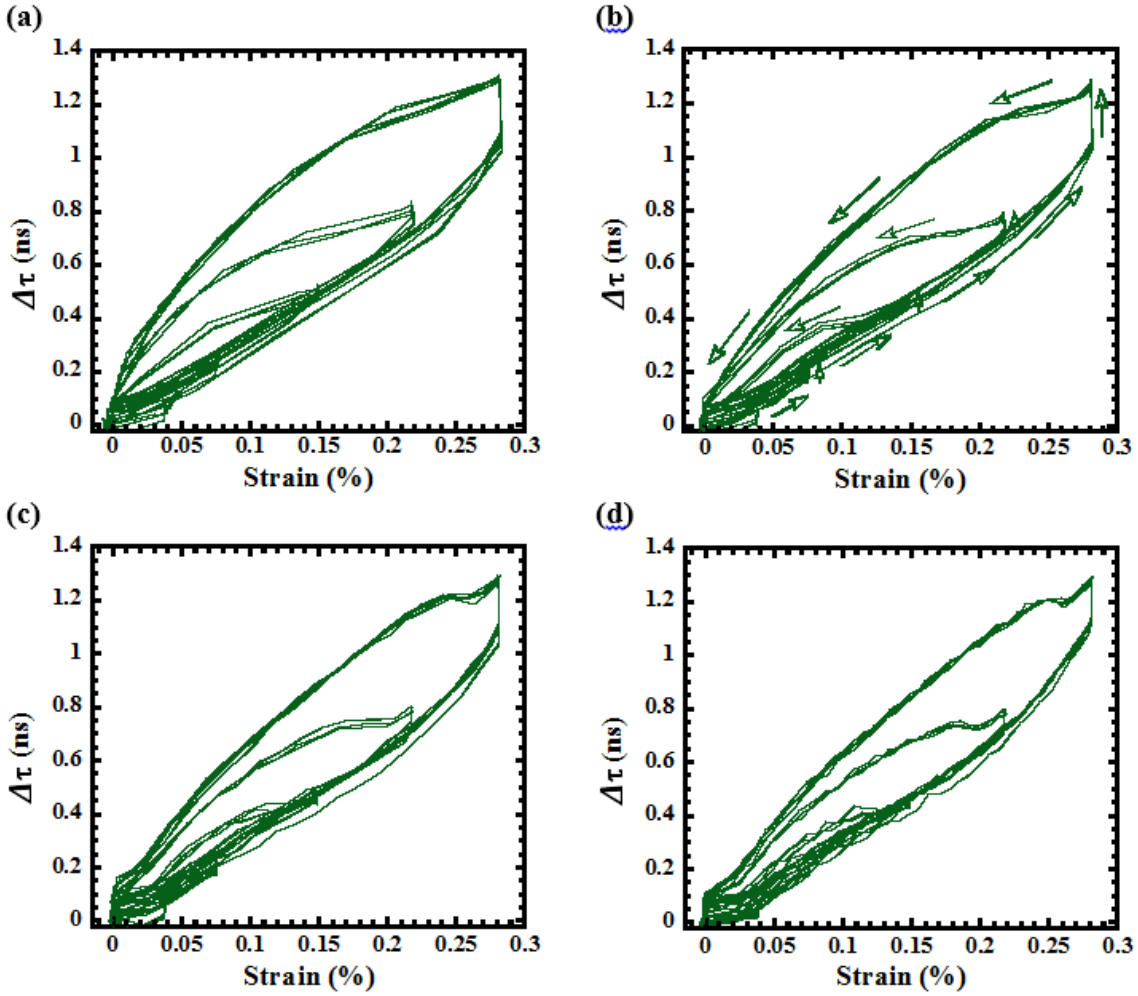

Figure C-48: Ti_2AlC-N texture $\Delta\tau$ results for the longitudinal 10MHz ultrasonic wave mode at different strain rates. (a) $13.2x10^{-4}s^{-1}$, (b) $6.6x10^{-4}s^{-1}$, (c) $3.3x10^{-4}s^{-1}$ and (d) $1.65x10^{-4}s^{-1}$. A holding time of 10 s at stresses 400, 300, 200, 100 & 50MPa was performed.

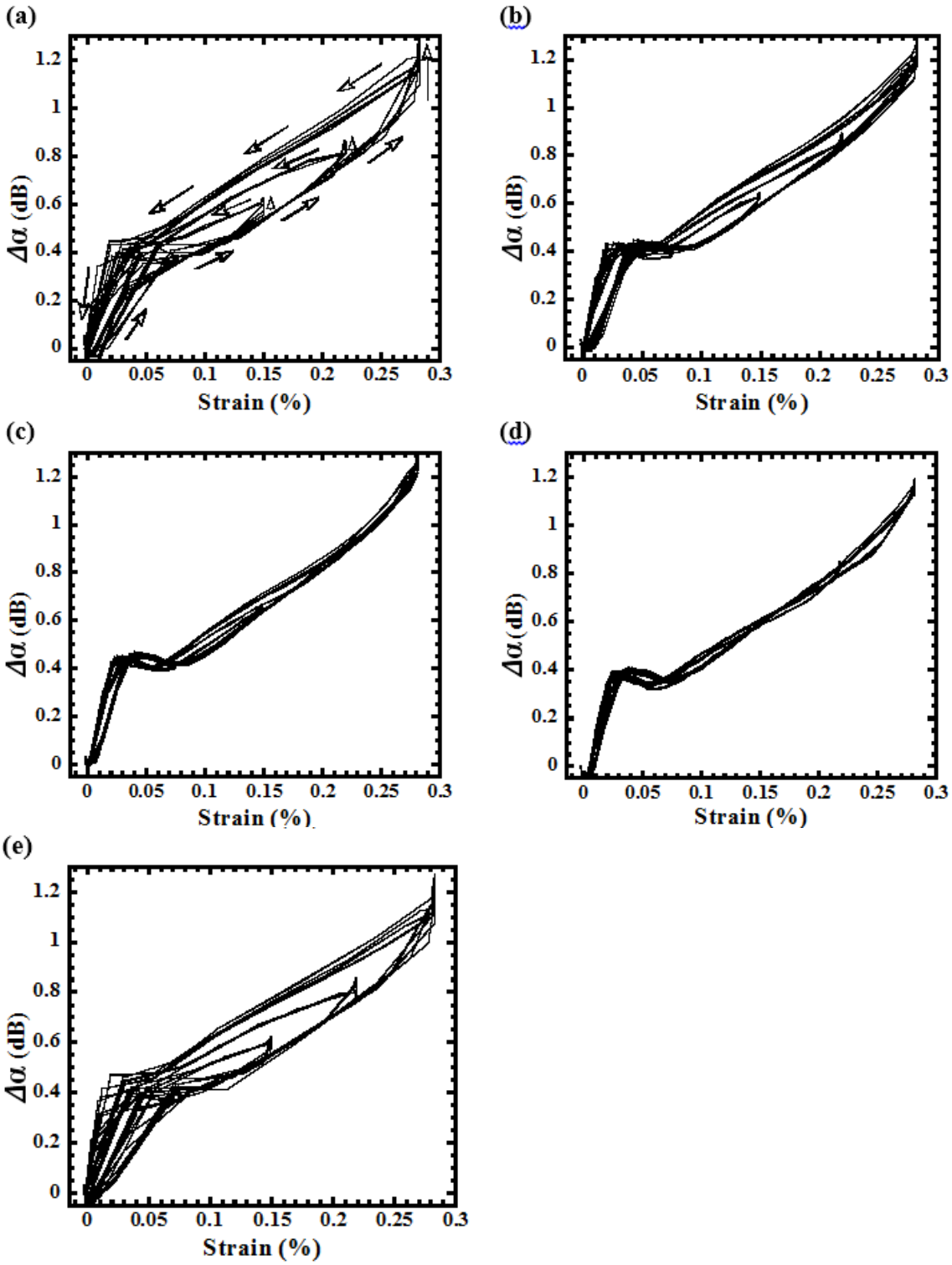

Figure C-49: Ti_2AlC-N texture $\Delta\alpha$ results for the longitudinal 5MHz ultrasonic wave mode at different strain rates. (a) $13.2x10^{-4}s^{-1}$, (b) $6.6x10^{-4}s^{-1}$, (c) $3.3x10^{-4}s^{-1}$, (d) $1.65x10^{-4}s^{-1}$ and (e) $13.2x10^{-4}s^{-1}$. A holding time of 10 s at stresses 400, 300, 200, 100 & 50MPa was performed.

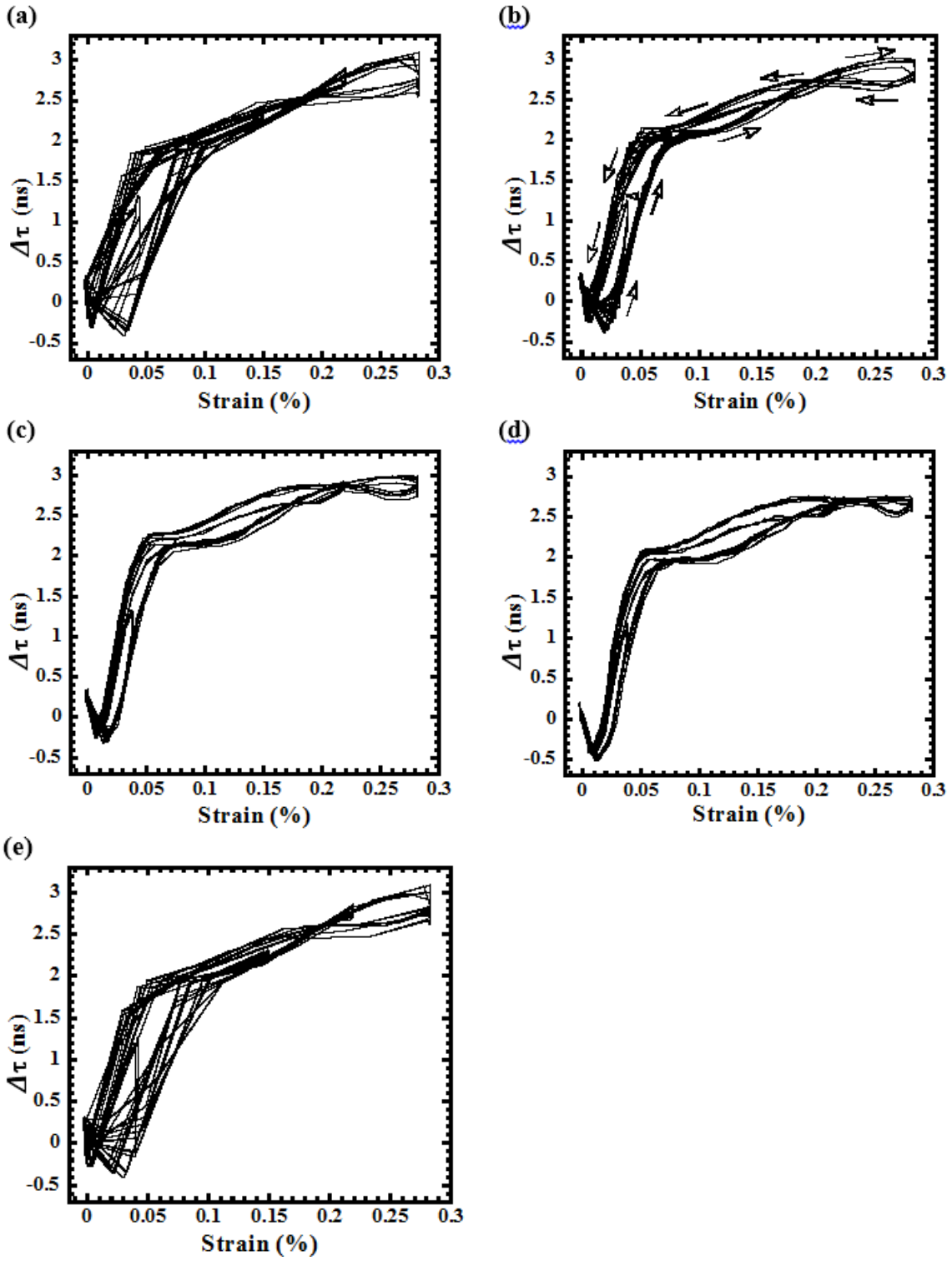

Figure C-50: Ti_2AlC-N texture $\Delta\tau$ results for the longitudinal 5MHz ultrasonic wave mode at different strain rates. (a) $13.2x10^{-4}s^{-1}$, (b) $6.6x10^{-4}s^{-1}$, (c) $3.3x10^{-4}s^{-1}$, (d) $1.65x10^{-4}s^{-1}$ and (e) $13.2x10^{-4}s^{-1}$. A holding time of 10 s at stresses 400, 300, 200, 100 & 50MPa was performed.

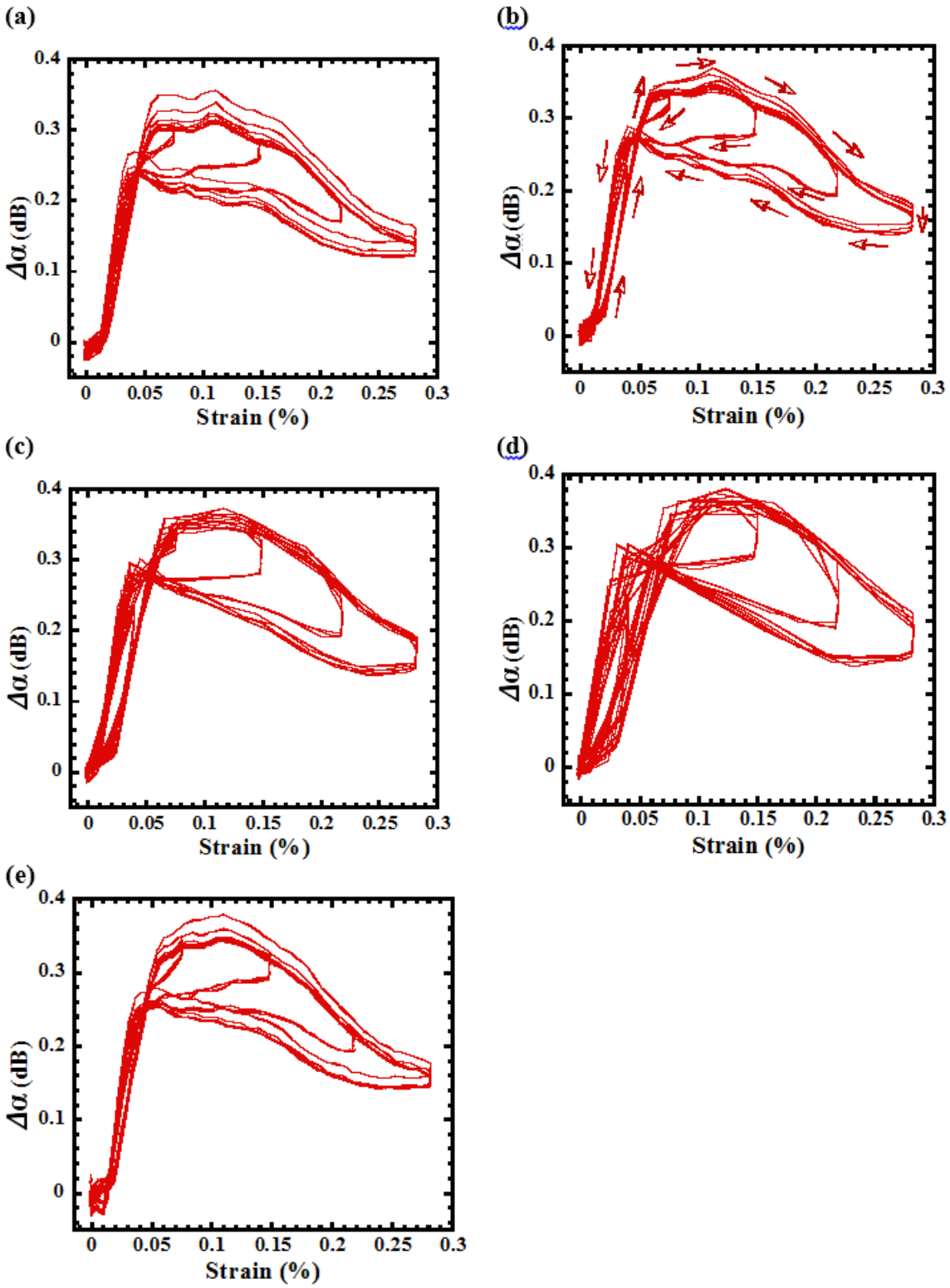

Figure C-51: Ti_2AlC-N texture Δα results for the Shear-P 5MHz ultrasonic wave mode at different strain rates. (a) $1.65x10^{-4}s^{-1}$, (b) $3.3x10^{-4}s^{-1}$, (c) $6.6x10^{-4}s^{-1}$, (d) $13.2x10^{-4}s^{-1}$ and (e) $1.65x10^{-4}s^{-1}$. A holding time of 10 s at stresses 400, 300, 200, 100 & 50MPa was performed.

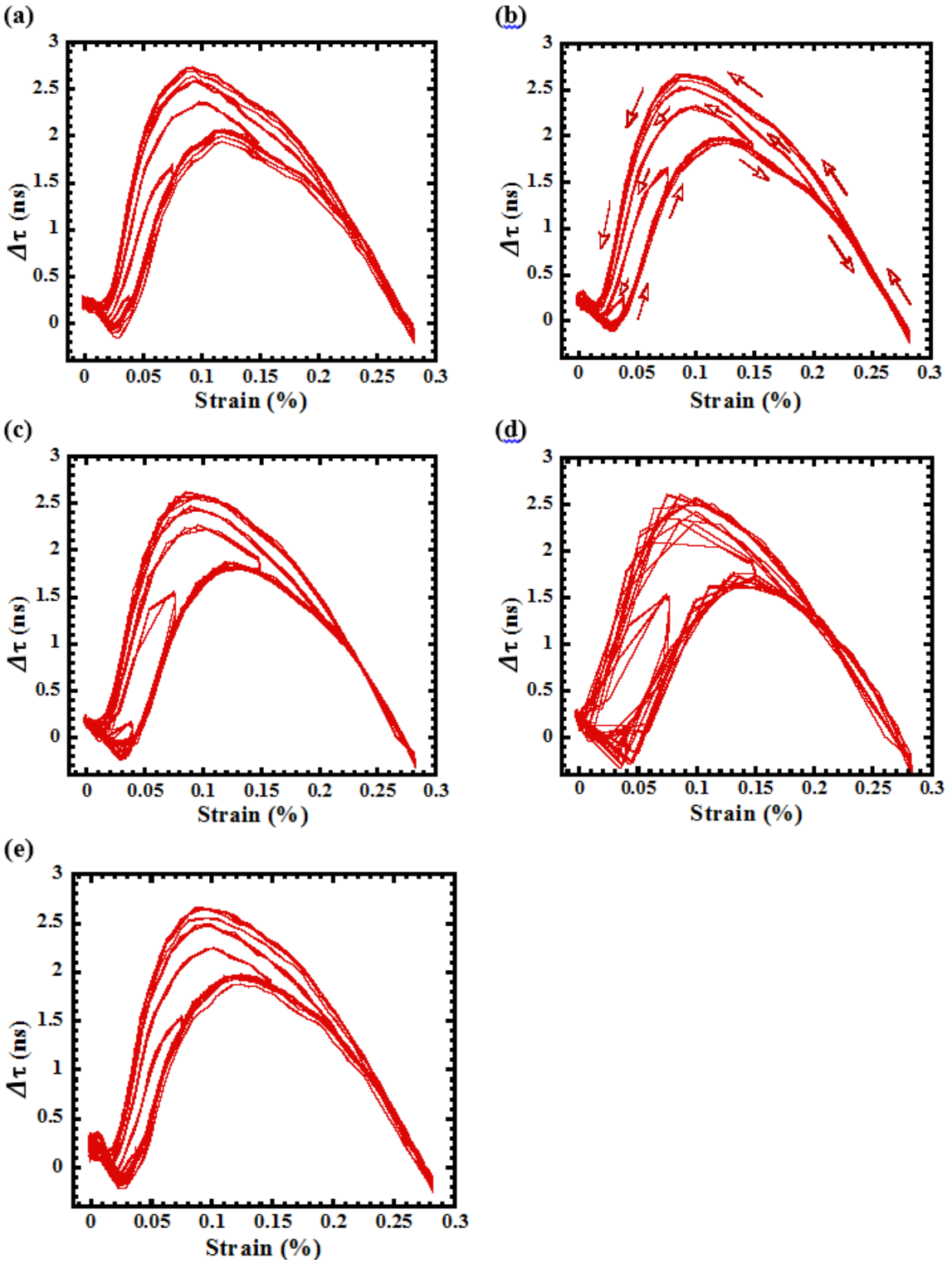

Figure C-52: Ti_2AlC-N texture $\Delta\tau$ results for the Shear-P 5MHz ultrasonic wave mode at different strain rates. (a) $1.65x10^{-4}s^{-1}$, (b) $3.3x10^{-4}s^{-1}$, (c) $6.6x10^{-4}s^{-1}$, (d) $13.2x10^{-4}s^{-1}$ and (e) $1.65x10^{-4}s^{-1}$. A holding time of 10 s at stresses 400, 300, 200, 100 & 50MPa was performed.

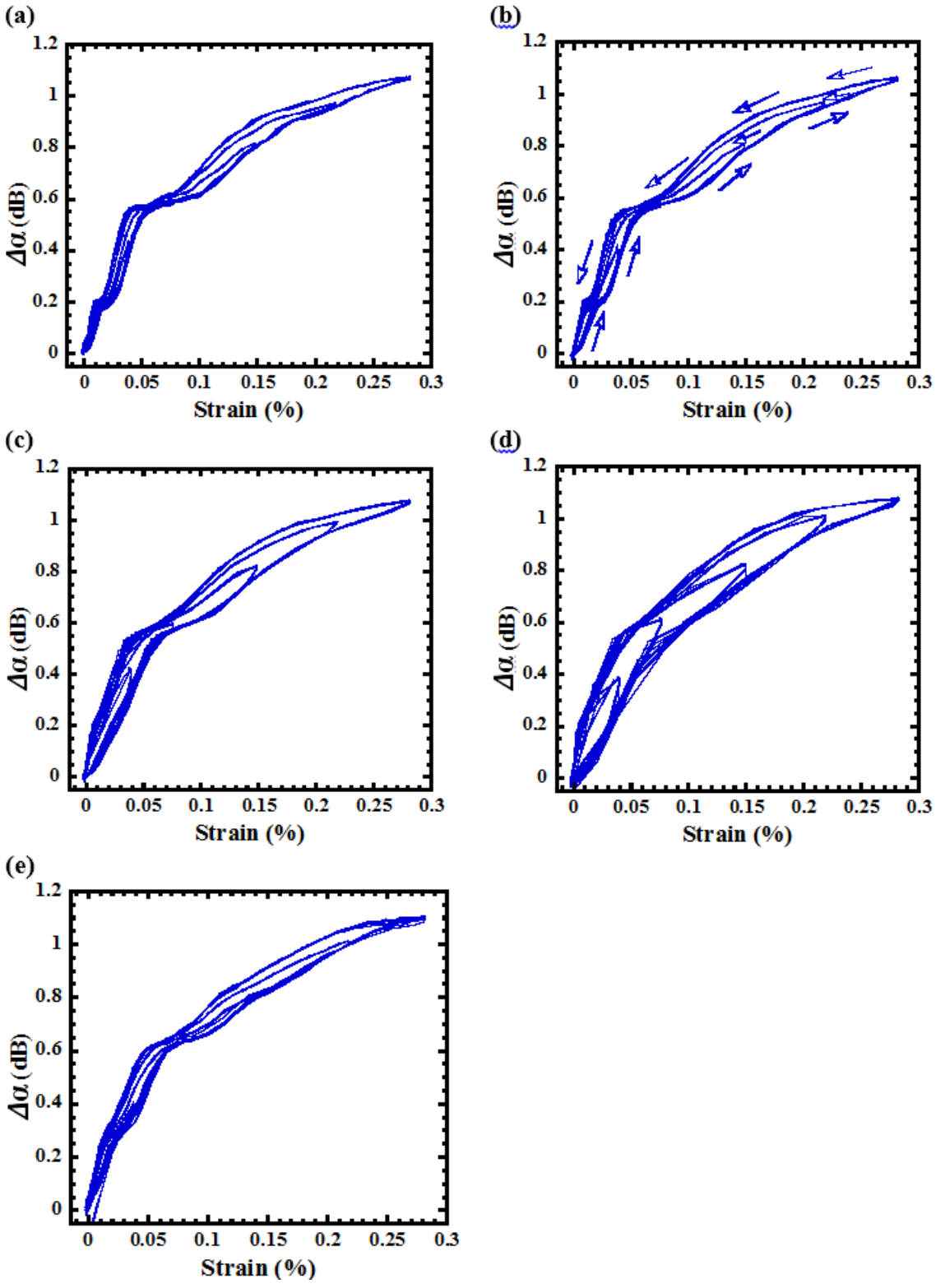

Figure C-53: Ti_2AlC-N texture Δα results for the Shear-N 5MHz ultrasonic wave mode at different strain rates. (a) $1.65x10^{-4}s^{-1}$, (b) $3.3x10^{-4}s^{-1}$, (c) $6.6x10^{-4}s^{-1}$, (d) $13.2x10^{-4}s^{-1}$ and (e) $1.65x10^{-4}s^{-1}$. A holding time of 10 s at stresses 400, 300, 200, 100 & 50MPa was performed.

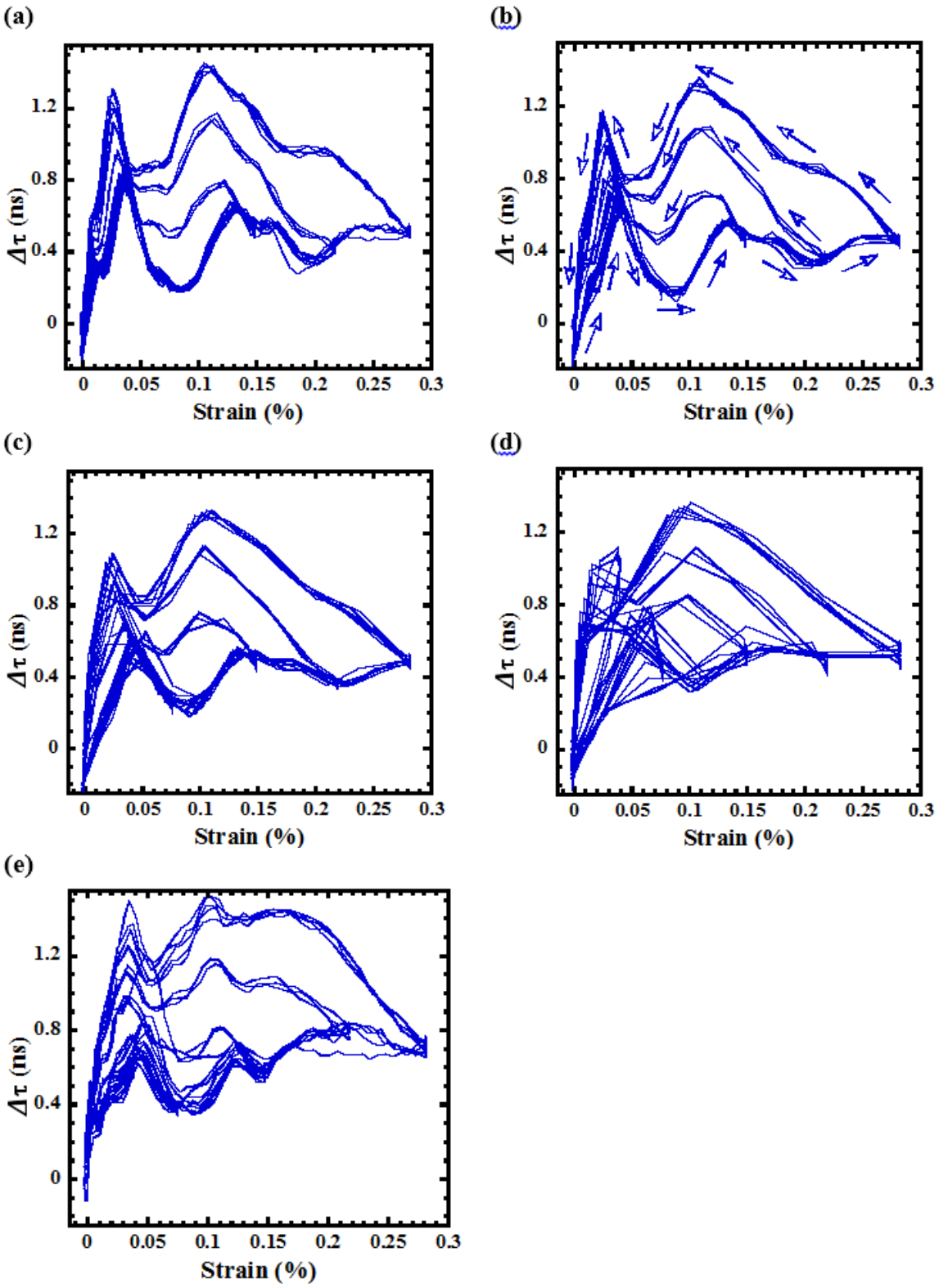

Figure C-54: Ti_2AlC-N texture $\Delta\tau$ results for the Shear-N 5MHz ultrasonic wave mode at different strain rates. (a) $1.65x10^{-4}s^{-1}$, (b) $3.3x10^{-4}s^{-1}$, (c) $6.6x10^{-4}s^{-1}$, (d) $13.2x10^{-4}s^{-1}$ and (e) $1.65x10^{-4}s^{-1}$. A holding time of 10 s at stresses 400, 300, 200, 100 & 50MPa was performed.

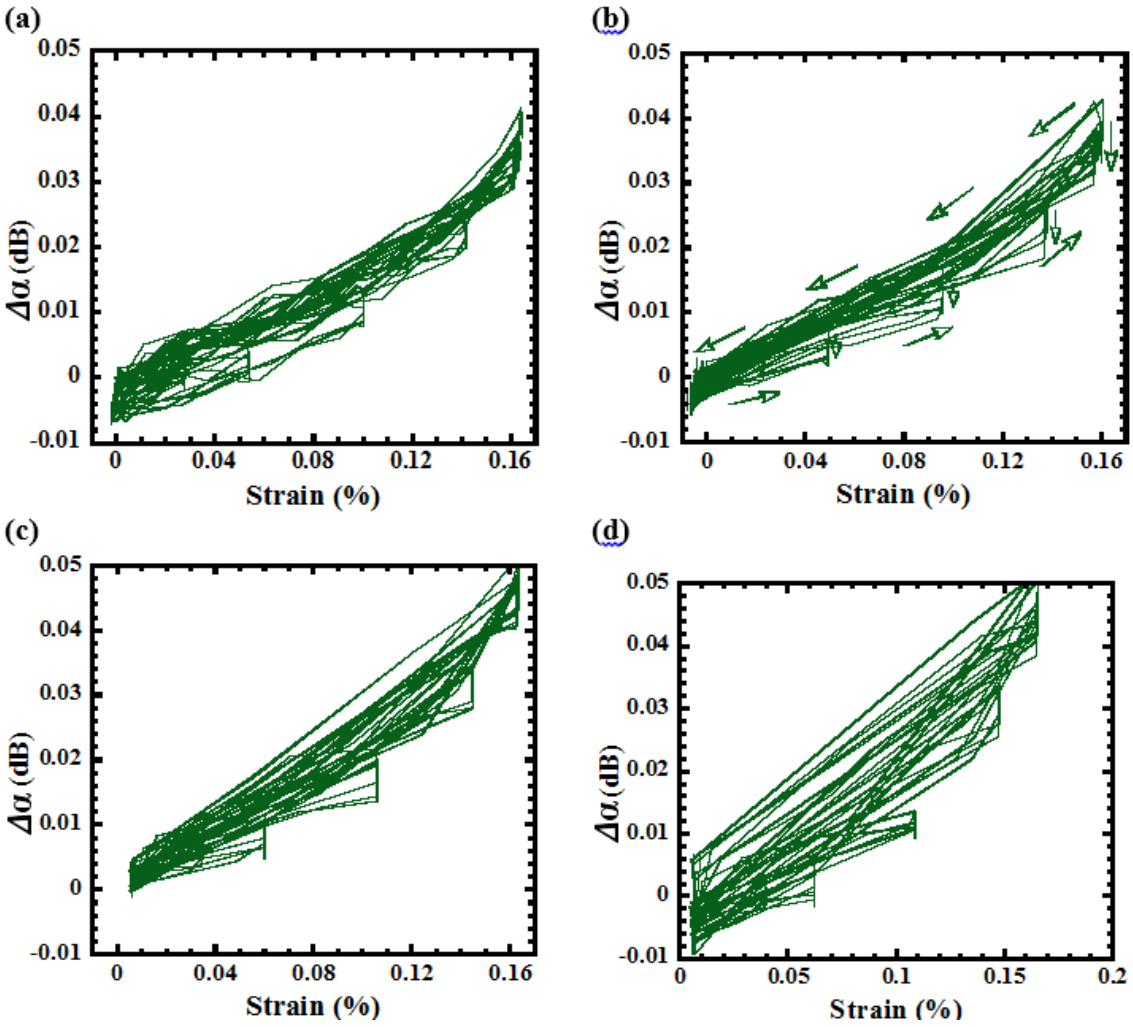

Figure C-55: Ti_2AlC-P texture Δα results for the longitudinal 10MHz ultrasonic wave mode at different strain rates. (a) $1.65x10^{-4}s^{-1}$, (b) $3.3x10^{-4}s^{-1}$, (c) $6.6x10^{-4}s^{-1}$ and (d) $13.2x10^{-4}s^{-1}$. A holding time of 10 s at stresses 350, 300, 200, 100 & 50MPa was performed.

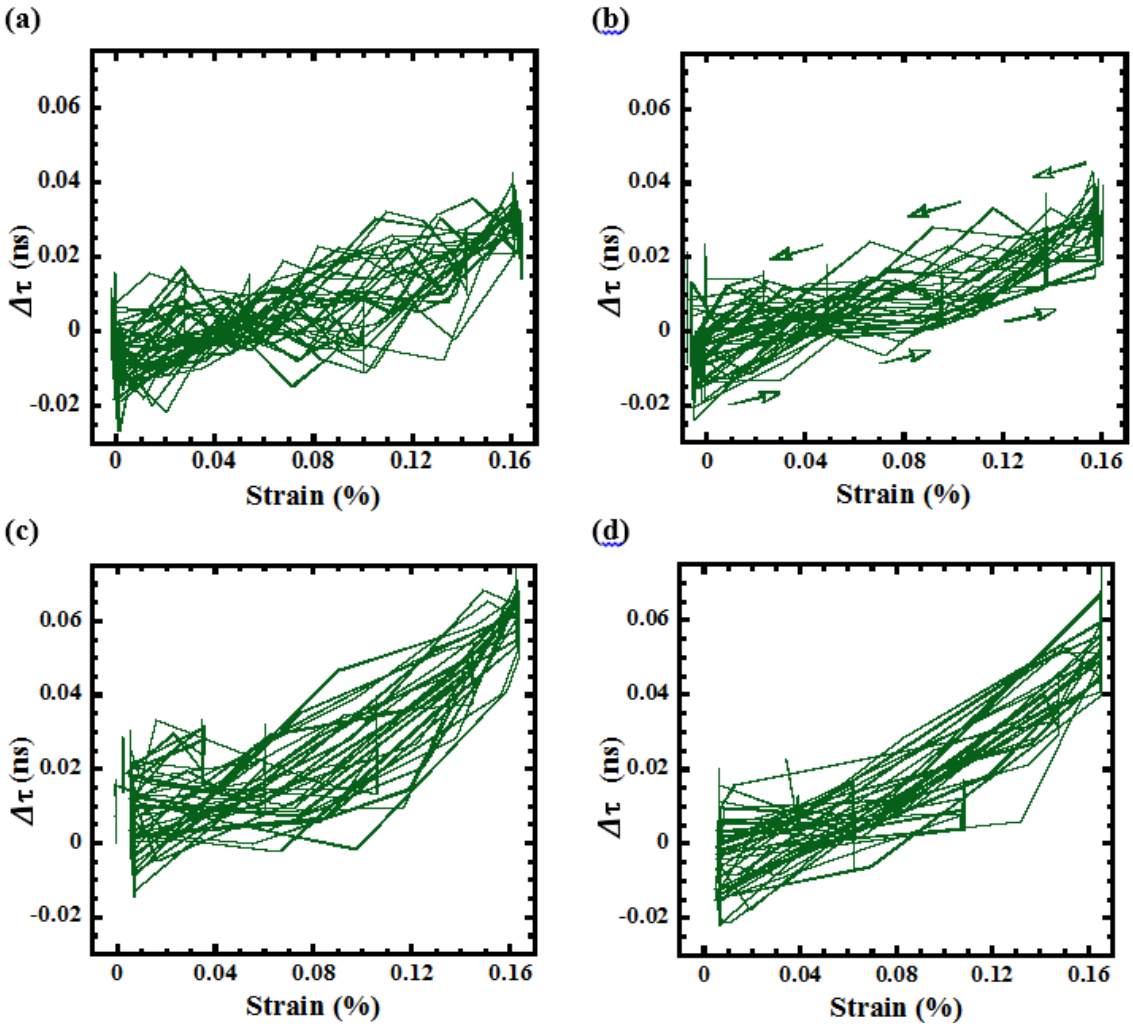

Figure C-56: Ti_2AlC-P texture Δτ results for the longitudinal 10MHz ultrasonic wave mode at different strain rates. (a) $1.65x10^{-4}s^{-1}$, (b) $3.3x10^{-4}s^{-1}$, (c) $6.6x10^{-4}s^{-1}$ and (d) $13.2x10^{-4}s^{-1}$. A holding time of 10 s at stresses 350, 300, 200, 100 & 50MPa was performed.

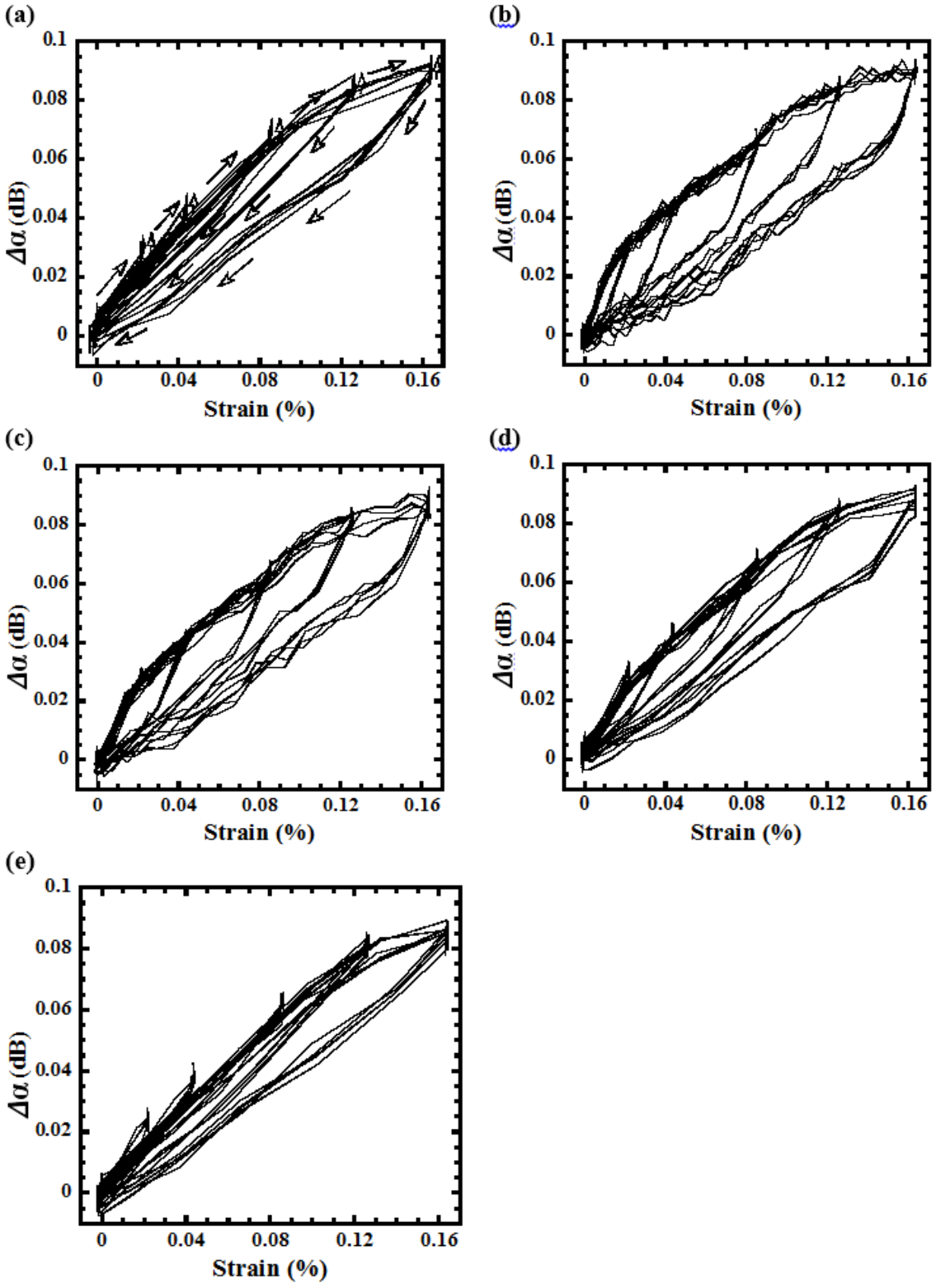

Figure C-57: Ti_2AlC-P texture Δα results for the longitudinal 5MHz ultrasonic wave mode at different strain rates. (a) $13.2x10^{-4}s^{-1}$, (b) $1.65x10^{-4}s^{-1}$, (c) $3.3x10^{-4}s^{-1}$, (d) $6.6x10^{-4}s^{-1}$ and (e) $13.2x10^{-4}s^{-1}$. A holding time of 10 s at stresses 350, 300, 200, 100 & 50MPa was performed.

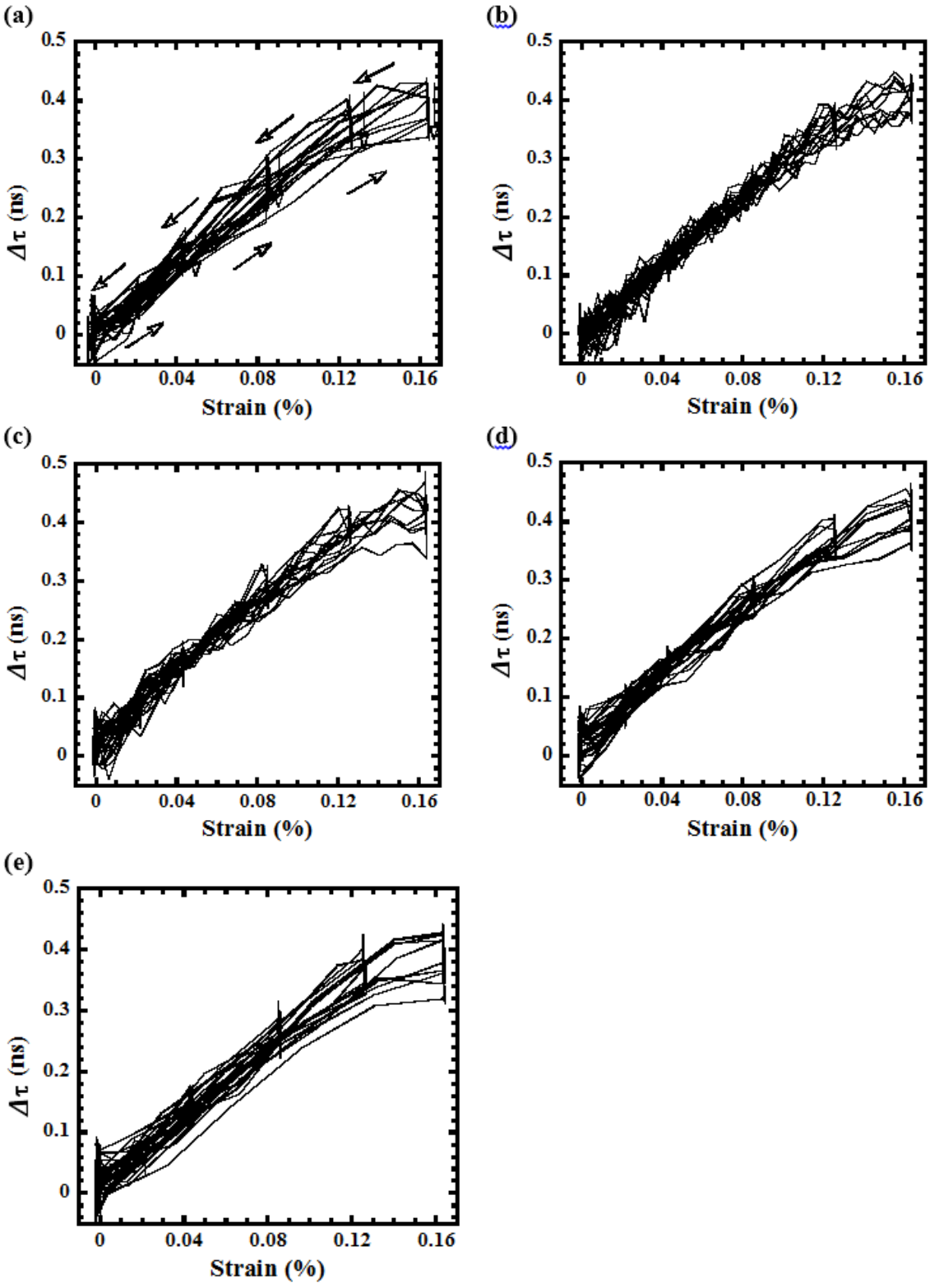

Figure C-58: Ti_2AlC-P texture $\Delta\tau$ results for the longitudinal 5MHz ultrasonic wave mode at different strain rates. (a) $13.2x10^{-4}s^{-1}$, (b) $1.65x10^{-4}s^{-1}$, (c) $3.3x10^{-4}s^{-1}$, (d) $6.6x10^{-4}s^{-1}$ and (e) $13.2x10^{-4}s^{-1}$. A holding time of 10 sat stresses 350, 300, 200, 100 & 50MPa was performed.

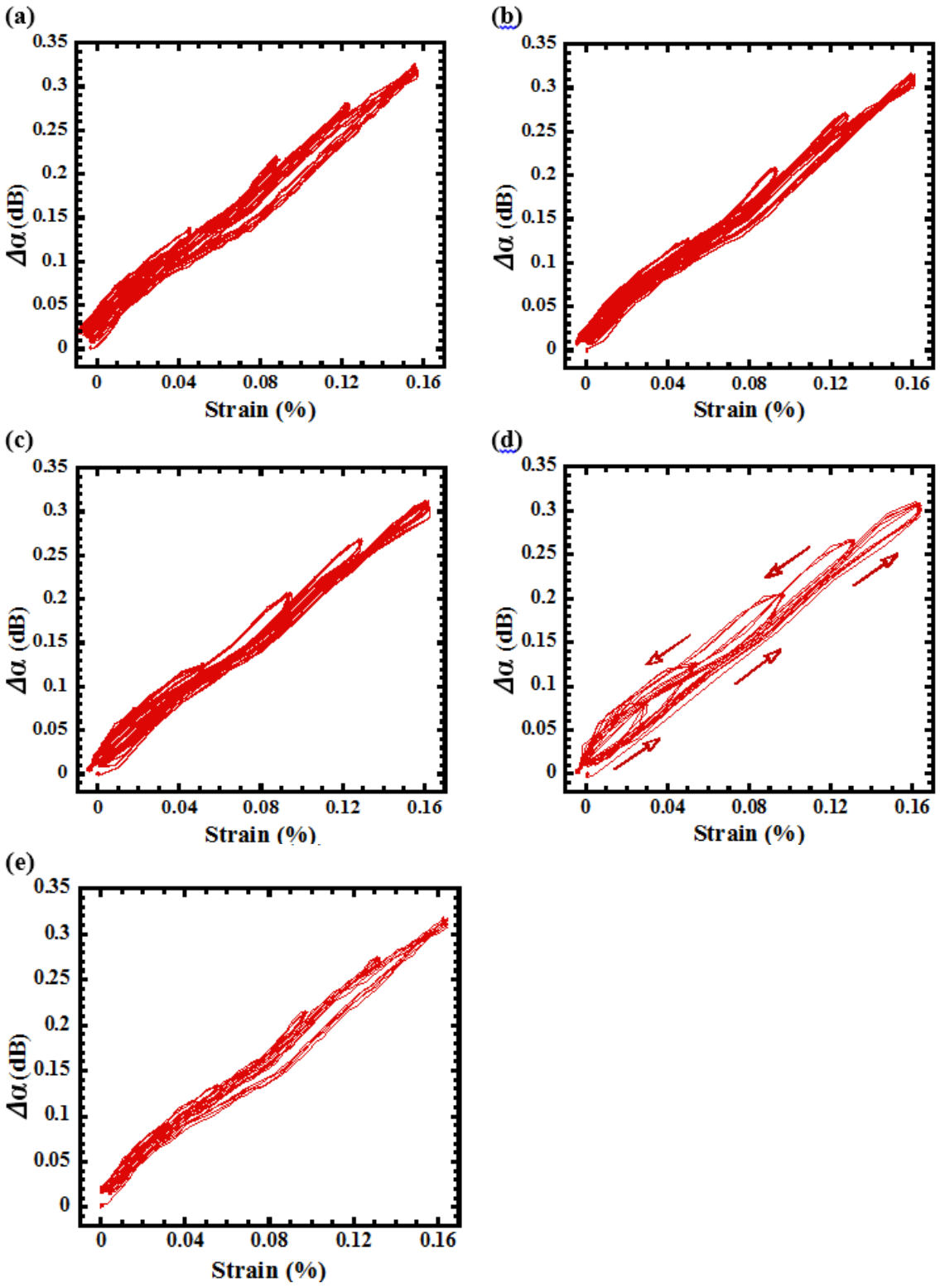

Figure C-59: Ti_2AlC-P texture Δα results for the Shear-P 5MHz ultrasonic wave mode at different strain rates. (a) $1.65x10^{-4}s^{-1}$, (b) $3.3x10^{-4}s^{-1}$, (c) $6.6x10^{-4}s^{-1}$, (d) $13.2x10^{-4}s^{-1}$ and (e) $1.65x10^{-4}s^{-1}$. A holding time of 10 s at stresses 350, 300, 200, 100 & 50MPa was performed.

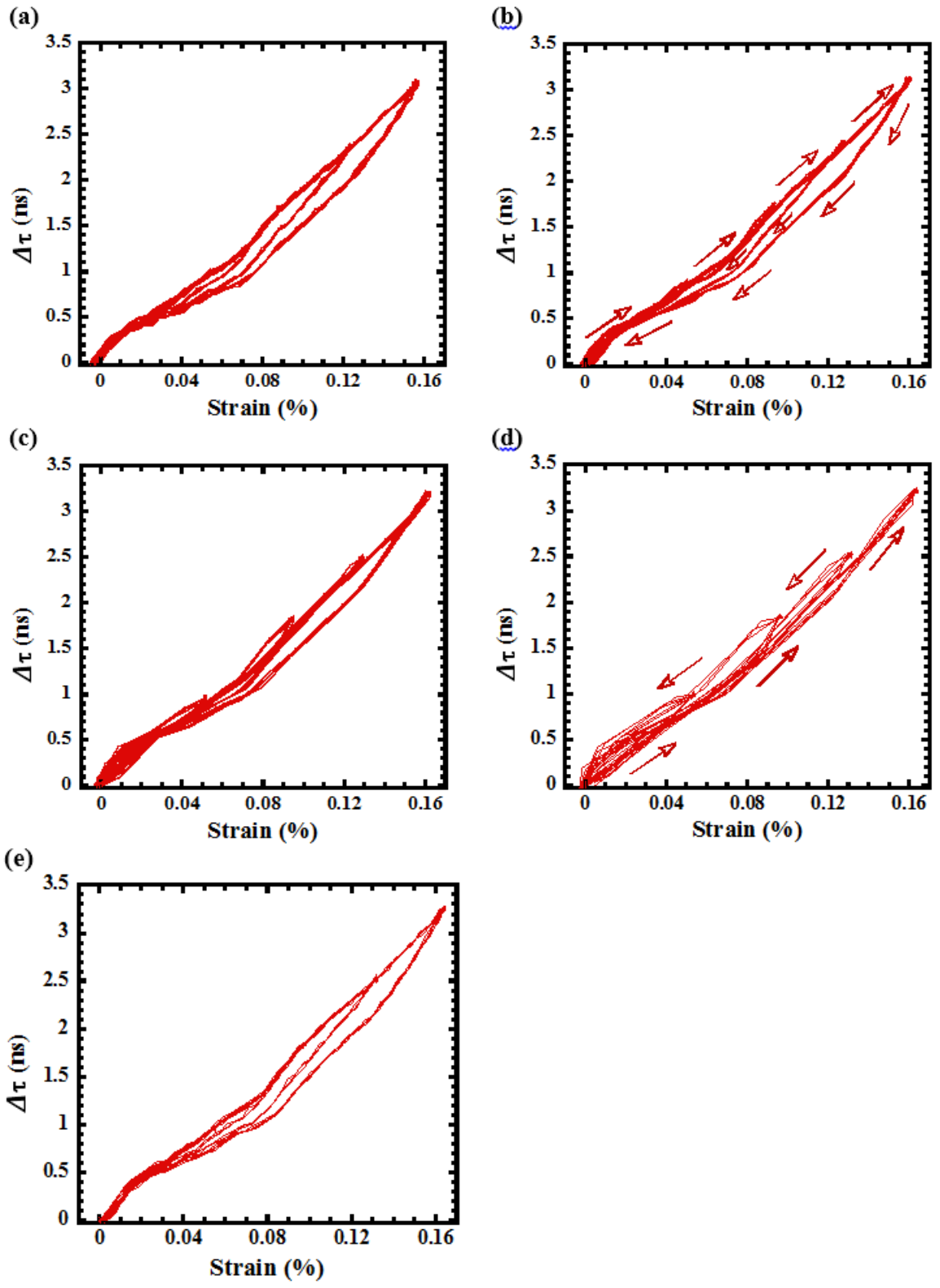

Figure C-60: Ti_2AlC-P texture $\Delta\tau$ results for the Shear-P 5MHz ultrasonic wave mode at different strain rates. (a) $1.65x10^{-4}s^{-1}$, (b) $3.3x10^{-4}s^{-1}$, (c) $6.6x10^{-4}s^{-1}$, (d) $13.2x10^{-4}s^{-1}$ and (e) $1.65x10^{-4}s^{-1}$. A holding time of 10 s at stresses 350, 300, 200, 100 & 50MPa was performed.

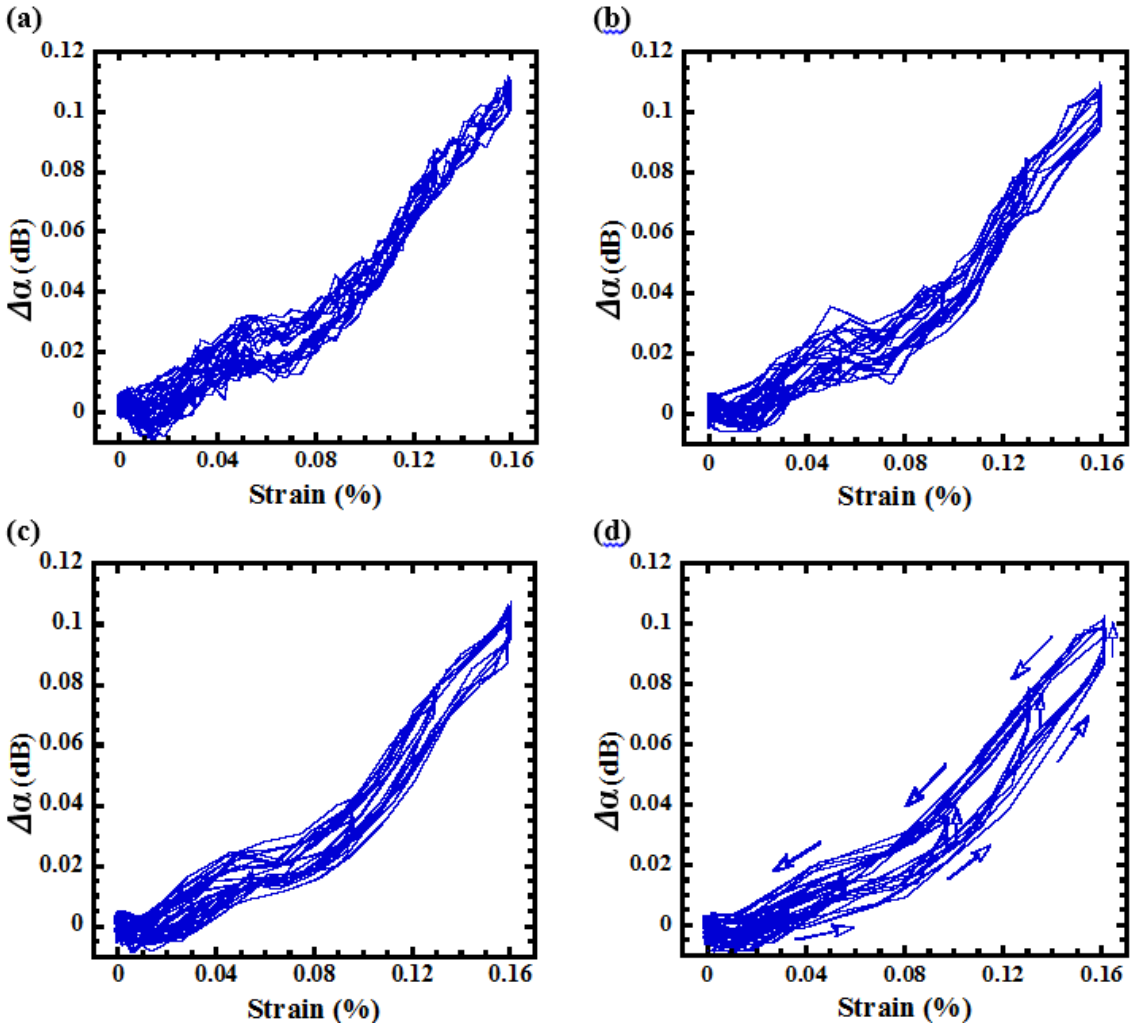

Figure C-61: Ti_2AlC-P texture Δα results for the Shear-N 5MHz ultrasonic wave mode at different strain rates. (a) $1.65x10^{-4}s^{-1}$, (b) $3.3x10^{-4}s^{-1}$, (c) $6.6x10^{-4}s^{-1}$ and (d) $13.2x10^{-4}s^{-1}$. A holding time of 10 s at stresses 350, 300, 200, 100 & 50MPa was performed.

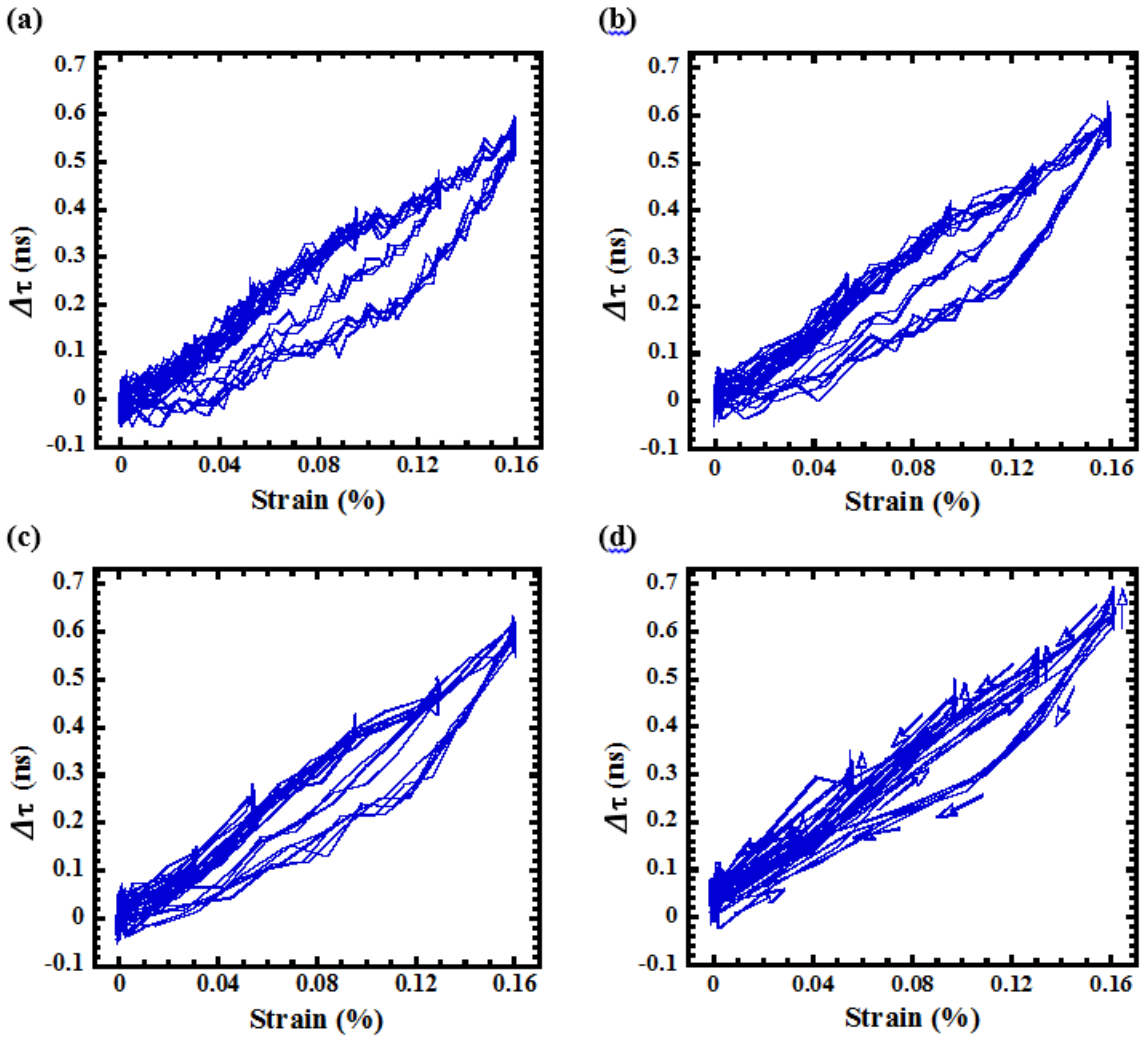

Figure C-62: Ti_2AlC-P texture $\Delta\tau$ results for the Shear-N 5MHz ultrasonic wave mode at different strain rates. (a) $1.65x10^{-4}s^{-1}$, (b) $3.3x10^{-4}s^{-1}$, (c) $6.6x10^{-4}s^{-1}$ and (d) $13.2x10^{-4}s^{-1}$. A holding time of 10 s at stresses 350, 300, 200, 100 & 50MPa was performed.

References

1. Tarr, M. *Stress and its effect on materials*. 2013 [cited 2013; Available from: http://www.ami.ac.uk/courses/topics/0124_seom/.
2. Barsoum, M.W., et al., *Fully reversible, dislocation-based compressive deformation of Ti3SiC2 to 1 GPa.* Nat Mater, 2003. **2**(2): p. 107-111.
3. Wadee, A. *Kink banding in layered structures and materials*. 2007 [cited 2013 21.9.2013]; Available from: http://www3.imperial.ac.uk/structuralengineering/research/mechanics/stability/kinks.
4. Ford, M. *Cliff on NE side of Millook Haven*. 2005 [cited 2013 21.9.2013]; Available from: http://www.geograph.org.uk/photo/63892.
5. Dodwell, T.J., et al., *Multi-layered folding with voids.* Philosophical Transactions of the Royal Society A: Mathematical, Physical and Engineering Sciences, 2012. **370**(1965): p. 1740-1758.
6. Benabou, L., *Kink Band Formation in Wood Species Under Compressive Loading.* Experimental Mechanics, 2008. **48**(5): p. 647-656.
7. Barsoum, M. and T. El-Raghy, *Room-temperature ductile carbides.* Metallurgical and Materials Transactions A, 1999. **30**(2): p. 363-369.
8. Orowan, E., *A TYPE OF PLASTIC DEFORMATION NEW IN METALS.* Nature, 1942. **149**(3788): p. 2.
9. Mugge, O., *Ueber Translationen und verwandte Erscheinungen in Krystallen [On translation and related phenomena in crystals].* Neues Jahrb. Mineral. Geol. Palaeontol. Jahrg, 1898. **1**: p. 71-186.
10. Nespolo, M., B. Souvignier, and D.B. Litvin, *About the concept and definition of "noncrystallographic symmetry".* Zeitschrift für Kristallographie - Crystalline Materials, 2008. **223**(9): p. 605-606.
11. Spowart, J.E. and T.W. Clyne, *The axial compressive failure of titanium reinforced with silicon carbide monofilaments.* Acta Materialia, 1999. **47**(2): p. 671-687.
12. Barrett, J.B.H.a.C.S., *Structure and nature of kink bands in zinc.* Trans . Metall. Soc. AIME 1949. **185**: p. 8.
13. Barsoum, M., L. Farber, and T. El-Raghy, *Dislocations, kink bands, and room-temperature plasticity of Ti3SiC2.* Metallurgical and Materials Transactions A, 1999. **30**(7): p. 1727-1738.
14. Barsoum, M.W., *The MN+1AXN phases: A new class of solids : Thermodynamically stable nanolaminates.* Progress in Solid State Chemistry, 2000. **28**(1-4): p. 201-281.
15. Moore, A.J.W., *Accommodation Kinking Associated with the Twinning of Zinc.* Proceedings of the Physical Society. Section B, 1952. **65**(12): p. 956.
16. Jillson, D.C., *Quantitative stress—strain studies on zinc single crystals in tension.* Transactions of the American Institute of Mining and Metallurgical Engineers; [Trans (A.I.M.E)], 1950. **188**: p. 5.
17. Moore, A.J.W., *Twinning and accommodation kinking in zinc.* Acta Metallurgica, 1955. **3**(2): p. 163-169.
18. Pratt, P.L. and S.F. Pugh, *The movement of twins, kinks, and mosaic walls in zinc.* Acta Metallurgica, 1953. **1**(2): p. 218-222.
19. Barsoum, M.W., et al., *Microscale modeling of kinking nonlinear elastic solids.* Physical Review B, 2005. **71**(13): p. 134101.

20. Timothy Dodwell, M.P., Christopher Budd, Giles Hunt. *DIC experiments - Buckling of Paper into nonlinear foundation*. 2011 [cited 2011 March 23, 2011]; Videos shows Digital Image Correlation (DIC) technology, when investigating the buckling of 1000 half sheets of A4 into a nonlinear foundation (sponge + ply wood).]. Available from: http://www.youtube.com/watch?v=T8oshIuDV5Y.
21. Dodwell, T., et al., *Self-Similar Voiding Solutions of a Single Layered Model of Folding Rocks.* SIAM Journal on Applied Mathematics, 2012. **72**(1): p. 444-463.
22. Crocker, A.G. and J.S. Abell, *The crystallography of deformation kinking.* Philosophical Magazine, 1976. **33**(2): p. 305-310.
23. Hosford, W.F., *Mechanical Behavior of Materials*. 2005: Cambridge University Press.
24. Gramoll, K. *MECHANICS - THEORY, Column Buckling*. eCourses 2014 [cited 2014 February 17th]; Available from: https://ecourses.ou.edu/cgi-bin/ebook.cgi?doc=..&topic=me&chap_sec=09.1&page=theory.
25. *Buckling*. 2014 [cited 2014 February 8th]; Buckling phenomena]. Available from: http://en.wikipedia.org/wiki/Buckling.
26. Tutelman, D. *All About Spines, What spine is -- and isn't*. The Tutelman Site 2008 [cited 2014 March 23rd]; Available from: http://www.tutelman.com/golf/shafts/allAboutSpines1.php.
27. one-school.net. *Malaysia SPM Form 5 Physics: Wave*. 2014 [cited 2014 March 21]; Available from: http://www.one-school.net/Malaysia/UniversityandCollege/SPM/Workbook/Physics/f5chp1/wave.html.
28. Tallman, D.J., et al., *Tensile creep of Ti2AlC in air in the temperature range 1000–1150°C.* Scripta Materialia, 2012. **66**(10): p. 805-808.
29. Pumpelly. R , N.D.T., *Geology of the Green Mountains in Massachusetts*. 1894, USGS Monograph, USA: United States Geological Survey. 34.
30. Hariri, M.M. *King Fahd University of Petroleum & Minerals (Welcome to Dr. Mustafa M. Hariri Page)*. 2011 10/01/2010 [cited 2014 12/8/2014]; Structural Geology]. Available from: http://faculty.kfupm.edu.sa/es/mmhariri/Teaching.htm.
31. Allison, D.T. *Structural Geology (Lecture 9 : Folding)*. 2014 [cited 2014 12/8/2014]; Available from: http://www.usouthal.edu/geography/allison/

http://www.usouthal.edu/geography/allison/GY403/GY403_Folding.pdf.
32. Lauren. *Geological Musings (Ramsay Fold Classifications)*. 2014; Available from: http://thinkgeogeek.blogspot.com/2012/06/ramsay-fold-classifications.html.
33. Prof. B. Clark Burchfiel, C.S.-G.T.A.a.L.I. *Structural Geology: Ductile deformation, folds and fabrics*. 2005 [cited 2014; Available from: http://ocw.mit.edu/courses/earth-atmospheric-and-planetary-sciences/12-113-structural-geology-fall-2005/lecture-notes/part6_dctl_fldfb.pdf

http://ocw.mit.edu/courses/earth-atmospheric-and-planetary-sciences/12-113-structural-geology-fall-2005/.
34. Eby, N. *Folds and Folding*. 2014 [cited 2014; Available from: http://faculty.uml.edu/Nelson_Eby/89.322/Instructor pdfs/Chapter 11. Folds and Folding.pdf

http://faculty.uml.edu/Nelson_Eby/.
35. Rubin, C.M. *Folding Mechanisms*. 2014 [cited 2014 12/8/2014]; Available from: http://www.geology.cwu.edu/facstaff/charlier/courses/g360/ppt/old/2007/lecture19_folds2.ppt

http://www.geology.cwu.edu/facstaff/charlier/.
36. Anderson, T.B., *Kink-Bands and Related Geological Structures.* Nature, 1964. **202**(4929): p. 272-274.
37. Hills, E.S., Elements of Structural Geology, 1963. **239**.
38. Flinn, D., Geological Magazine, 1952. **89**: p. 263.
39. Biot, M.A., *Theory of folding of stratified vis- coelastic media and its implications in tectonics and orogenesis.* Geolgy Society of America Bulliten, 1961. **72**: p. 1595- 1620.
40. WEISS, M.S.P.a.L.E., *Experimental Deformation and Folding in Phyllite.* Geological Society of America Bulletin, 1966. **77**: p. 32.
41. Paterson, M.S. and L.E. Weiss, *Experimental Folding in Rocks.* Nature, 1962. **195**(4846): p. 1046-1048.
42. Rosen, B.W., *Mechanics of composite strengthening.* Fiber Composite Materials. American Society of Metals, 1965. **chapter 3**: p. 37–75.
43. Argon, A.S., *Fracture of Composites*, in *Treatise on Materials Science & Technology*, H. Herbert, Editor. 1972, Elsevier. p. 79-114.
44. Budiansky, B., *Micromechanics.* Computers and Structures, 1983. **16**: p. 3–12.
45. Vogler, T.J., S.Y. Hsu, and S. Kyriakides, *On the initiation and growth of kink bands in fiber composites. Part II: analysis.* International Journal of Solids and Structures, 2001. **38**(15): p. 2653-2682.
46. Budiansky, B., N.A. Fleck, and J.C. Amazigo, *On kink-band propagation in fiber composites.* Journal of the Mechanics and Physics of Solids, 1998. **46**(9): p. 1637-1653.
47. Wadee, M.A. and R. Edmunds, *Kink band propagation in layered structures.* Journal of the Mechanics and Physics of Solids, 2005. **53**(9): p. 2017-2035.
48. Wadee, M.A., G.W. Hunt, and M.A. Peletier, *Kink band instability in layered structures.* Journal of the Mechanics and Physics of Solids, 2004. **52**(5): p. 1071-1091.
49. Zabaras, N. *MAE 212: Spring 2001, Lecture 12, DISLOCATIONS*. 2001 [cited 2009 July 7th]; Available from: http://mpdc.mae.cornell.edu/Courses/MAE212/Lecture12.pdf.
50. *Buckling of Columns 13.1-13.3, Buckling & Stability Critical Load*. 2014 [cited 2014 25 February 2014]; Available from: http://www.google.com/url?sa=t&rct=j&q=&esrc=s&source=web&cd=1&ved=0CCkQFjAA&url=http%3A%2F%2Fweb.clark.edu%2Fbwheeler%2FEngr%2520233%2FLectures%2520pp%2FWeek%252010%2F13.1-13.3.ppt&ei=7_6DU7enKtWnsQT544GoDQ&usg=AFQjCNE73s4bdovD47hi0RHqUJxmiDuAgw&sig2=Wy5C5UQzVKFAFV79ndUAcA.
51. Amini, S., M.W. Barsoum, and T. El-Raghy, *Synthesis and Mechanical Properties of Fully Dense Ti2SC.* Journal of the American Ceramic Society, 2007. **90**(12): p. 3953-3958.
52. Shamma, M., et al., *On the response of titanium sulfocarbide to stress studied by in situ neutron diffraction and the elastoplastic self-consistent approach.* Scripta Materialia, 2011. **65**(7): p. 573-576.
53. Fraczkiewicz, M., A.G. Zhou, and M.W. Barsoum, *Mechanical damping in porous Ti3SiC2.* Acta Materialia, 2006. **54**(19): p. 5261-5270.
54. El-Raghy, T. and M.W. Barsoum, *Processing and Mechanical Properties of Ti3SiC2: I, Reaction Path and Microstructure Evolution.* Journal of the American Ceramic Society, 1999. **82**(10): p. 2849-2854.
55. *The Official Website of the Nobel Prize*. 2013 [cited 2013; Available from: http://www.nobelprize.org/nobel_prizes/physics/laureates/1994/illpres/neutrons.html.
56. Paul Barnes, S.J., Martin Vickers. *Sources of Peak Broadening*. 2006 [cited 2014 11.17.2014]; Available from: http://pd.chem.ucl.ac.uk/pdnn/peaks/broad.htm.

57. Philips, R. *X-Ray Diffraction (XRD)*. 2014 [cited 2014 11.17.2014]; XRD Theory]. Available from: http://www.innovationservices.philips.com/sites/default/files/materials-analysis-xrd.pdf.
58. Bourke, M.A.M., D.C. Dunand, and E. Ustundag, *SMARTS - a spectrometer for strain measurement in engineering materials.* Applied Physics A: Materials Science & Processing, 2002. **74**(0): p. s1707-s1709.
59. Wenk, H.R., L. Lutterotti, and S. Vogel, *Texture analysis with the new HIPPO TOF diffractometer.* Nuclear Instruments & Methods in Physics Research Section a-Accelerators Spectrometers Detectors and Associated Equipment, 2003. **515**(3): p. 575-588.
60. Turner, P.A. and C.N. Tomé, *A study of residual stresses in Zircaloy-2 with rod texture.* Acta Metallurgica et Materialia, 1994. **42**(12): p. 4143-4153.
61. Clausen, B., T. Lorentzen, and T. Leffers, *Self-consistent modelling of the plastic deformation of f.c.c. polycrystals and its implications for diffraction measurements of internal stresses.* Acta Materialia, 1998. **46**(9): p. 3087-3098.
62. Clausen, B., et al., *Lattice strain evolution during uniaxial tensile loading of stainless steel.* Materials Science and Engineering A, 1999. **259**(1): p. 17-24.
63. Clausen, B., et al., *Reorientation and stress relaxation due to twinning: Modeling and experimental characterization for Mg.* Acta Materialia, 2008. **56**(11): p. 2456-2468.
64. Larsson, C., et al., *Measurements and predictions of strain pole figures for uniaxially compressed stainless steel.* Scripta Materialia, 2004. **51**(6): p. 571-575.
65. Kelly, E.J.F.a.A., *Twinning in Graphite.* Proceeding of the Royal Society A, 1961. **264**(1317): p. 8.
66. Bouhemadou, A. and R. Khenata, *Structural, electronic and elastic properties of M2SC (M = Ti, Zr, Hf) compounds.* Physics Letters A, 2008. **372**(42): p. 6448-6452.
67. Du, Y.L., et al., *First-principles study on electronic structure and elastic properties of Ti2SC.* Physics Letters A, 2008. **372**(31): p. 5220-5223.
68. Scabarozi, T.H., et al., *Thermal expansion of select M[sub n + 1]AX[sub n] (M = early transition metal, A = A group element, X = C or N) phases measured by high temperature x-ray diffraction and dilatometry.* Journal of Applied Physics, 2009. **105**(1): p. 013543-8.
69. Scabarozi, T.H., et al., *Electrical, thermal, and elastic properties of the MAX-phase Ti[sub 2]SC.* Journal of Applied Physics, 2008. **104**(3): p. 033502-5.
70. Cover, M.F., et al., *A comprehensive survey of M2AX phase elastic properties.* J. Phys.: Condens. Matter, 2009. **21**(305403 (9pp)).
71. Cui, S., et al., *Hexagonal Ti2SC with high hardness and brittleness: a first-principles study.* Scripta Materialia, 2009. **61**(6): p. 576-579.
72. Cover, M.F., et al., *Elastic properties of Tin+1AlCn and Tin+1AlNn MAX phases.* Advanced Engineering Materials, 2008. **10**(10): p. 935-938.
73. Barsoum, M.W., et al., *Fully Reversible, Dislocation-Based Compressive Deformation of Ti_3SiC_2 to 1 GPa.* Nature Materials, 2003. **2**: p. 107-111.
74. Barsoum, M.W. and S. Basu, *Kinking Nonlinear Elastic Solids*, in *Encyclopedia of Materials Science and Technology*, R.W.C. K. H. J. Buschow, M. C. Flemings, B. Ilschner, E. J. Kramer, S. Mahajan and P. Veyssiere, Editor. 2010, Elsevier: Oxford. p. 1-23.
75. Barsoum, M.W., et al., *Microscale modeling of kinking nonlinear elastic solids.* Physical Review B, 2005. **71**(13).
76. Zhou, A.G., et al., *Incipient and regular kink bands in fully dense and 10 vol.% porous Ti2AlC.* Acta Materialia, 2006. **54**(6): p. 1631-1639.

77. Zhou, A.G., S. Basu, and M.W. Barsoum, *Kinking nonlinear elasticity, damping and microyielding of hexagonal close-packed metals.* Acta Materialia, 2008. **56**(1): p. 60-67.
78. Zhou, A. and M. Barsoum, *Kinking Nonlinear Elasticity and the Deformation of Magnesium.* Metallurgical and Materials Transactions A, 2009. **40**(7): p. 1741-1756.
79. Zhou, A.G. and M.W. Barsoum, *Kinking nonlinear elastic deformation of Ti3AlC2, Ti2AlC, Ti3Al(C0.5,N0.5)2 and Ti2Al(C0.5,N0.5).* Journal of Alloys and Compounds, 2010. **498**(1): p. 62-70.
80. Wollmershauser, J.A., B. Clausen, and S.R. Agnew, *A slip system-based kinematic hardening model application to in situ neutron diffraction of cyclic deformation of austenitic stainless steel.* International Journal of Fatigue, 2012. **36**(1): p. 181-193.
81. Sun, Z., et al., *Calculated elastic properties of M2AlC (M = Ti, V, Cr, Nb and Ta).* Solid State Communications, 2004. **129**: p. 589-592.
82. Wang, J. and Y. Zhou, *Dependence of Elastic Stiffness on Electronic Band Structure of Nanolaminate M2AlC (M=Ti,V,Nb and Cr) Ceramics.* Phys. Rev. B, 2004. **69**: p. 214111.
83. Du, Y.L., et al., *Theoretical investigations on the elastic and thermodynamic properties of Ti2AlC0.5N0.5 solid solution.* Physics Letters A, 2009. **374**: p. 78–82.
84. Bouhemadou, A., R. Khenata, and M. Chegaar, *Structural and elastic properties of Zr2AlX and Ti2AlX (X = C and N) under pressure effect.* Eur. Phys. J. B, 2007. **56**: p. 209–215.
85. Rosen, J., et al., *Oxygen Incorporation in Ti2AlC: Tuning of Anisotropic Conductivity* Appl. Phys. Lett., 2010. **97**: p. 073103
86. Wang, X.H. and Y.C. Zhou, *Layered Machinable and Electrically Conductive Ti2AlC and Ti3AlC2 Ceramics: a Review.* Journal of Materials Science & Technology, 2010. **26**(5): p. 385-416.
87. Lane, N.J., et al., *Structure of a new bulk Ti5Al2C3 MAX phase produced by the topotactic transformation of Ti2AlC.* Journal of the European Ceramic Society, 2012. **32**(12): p. 3485-3491.
88. Barcelo, F., et al., *Electron-backscattered diffraction and transmission electron microscopy study of post-creep Ti3SiC2.* Journal of Alloys and Compounds, 2009. **488**(1): p. 181-189.
89. Roberts, J.M. and D.E. Hartman, Trans. AIME, 1964. **230**: p. 1125-1133.
90. Santisteban, J.R., *Time-of-flight neutron transmission of mosaic crystals.* Journal of Applied Crystallography, 2005. **38**: p. 934-944.
91. Santisteban, J.R., et al., *Tensile deformation of a Cu mosaic crystal along the 110 direction studied by time of flight neutron transmission.* Materials Science and Engineering a-Structural Materials Properties Microstructure and Processing, 2006. **437**(1): p. 151-156.
92. Muransky, O., et al., *In situ neutron diffraction investigation of deformation twinning and pseudoelastic-like behaviour of extruded AZ31 magnesium alloy.* International Journal of Plasticity, 2009. **25**(6): p. 1107-1127.
93. Lawn, B.R. and D.B. Marshall, *Nonlinear stress-strain curves for solids containing closed cracks with friction.* Journal of the Mechanics and Physics of Solids, 1998. **46**(1): p. 85-113.
94. Bruno, G., et al., *Connecting the macro- and microstrain responses in technical porous ceramics: modeling and experimental validations.* Journal of Materials Science, 2011. **46**(1): p. 161-173.

95. Darling, T.W., TenCate, J. A., Brown, D. W., Clausen, B., Vogel, S. C., *Neutron diffraction study of the contribution of grain contacts to nonlinear stress-strain behavior.* GEOPHYSICAL RESEARCH LETTERS, 2004. **31**: p. L16604.
96. Christien, F., M.T.F. Telling, and K.S. Knight, *Neutron diffraction in situ monitoring of the dislocation density during martensitic transformation in a stainless steel.* Scripta Mater., 2013. **68**: p. 506–509.
97. Best, B. *Lessons for Cryonics from Metallurgy and Ceramics*. 1990 [cited 2014 7/3/2014]; Available from: http://www.benbest.com/cryonics/lessons.html.
98. Dadaah, D. *A simple monochrome sphere*. 2005 [cited 2014 3/7/2014]; Sphere]. Available from: http://commons.wikimedia.org/wiki/File:Sphere_-_monochrome_simple.svg.
99. El-Raghy, T., et al., *Processing and Mechanical Properties of Ti3SiC2: II, Effect of Grain Size and Deformation Temperature.* Journal of the American Ceramic Society, 1999. **82**(10): p. 2855-2860.
100. Holm, B., R. Ahuja, and B. Johansson, *Ab initio calculations of the mechanical properties of Ti[sub 3]SiC[sub 2].* Applied Physics Letters, 2001. **79**(10): p. 1450-1452.
101. R. Yu, X.F.Z., L.L. He and H.Q. Ye, *Topology of charge density and elastic anisotropy of Ti3SiC2 polymorphs.* Journal of Matterials Research, 2006. **20**(5): p. 6.
102. Nabarro, F.R.N., *Theory of Crystal Dislocations* 1967, Oxford: Oxford University Press.
103. Blanter, M.S., I.S. Golovin, and H. Neuhäuser, *Internal Friction in Metallic Materials: A Handbook*. 2007: Springer London, Limited.
104. Hull, D.B., D.J., *Introduction to Dislocations*. 2001: Elsevier Science.
105. Lücke, K. and A.V. Granato, *Simplified theory of dislocation damping including point-defect drag. I. Theory of drag by equidistant point defects.* Physical Review B, 1981. **24**(12): p. 6991-7006.
106. Granato, A.V. and K. Lücke, *Simplified theory of dislocation damping including point-defect drag. II. Superposition of continuous and pinning-point-drag effects.* Physical Review B, 1981. **24**(12): p. 7007-7017.
107. Granato, A.V., *Viscosity effects in plastic flow and internal friction.* Scripta Metallurgica, 1984. **18**(7): p. 663-668.
108. Zener, C., *Elasticity and Inelasticity of Metals*. 1960: University of Chic. Press.
109. Schaller, R., G. Fantozzi, and G. Gremaud, *Mechanical spectroscopy Q-¹ 2001 : with applications to materials science*. 2001, Zuerich-Uetikon, Switzerland; Enfield, NH: Trans Tech Publications.
110. Hirao, M., et al., *Ultrasonic attenuation peak during fatigue of polycrystalline copper.* Acta Materialia, 2000. **48**(2): p. 517-524.
111. Gremaud, G.B., W., *THE INTERACTIONS BETWEEN DISLOCATIONS AND POINT DEFECTS STUDIED BY ULTRASONIC MEASUREMENTS DURING A CYCLIC DEFORMATION.* J. Phys. Colloques, 1981. **42**(C5): p. C5-369-C5-374.
112. Couteau, O. and R. Schaller, *Étude par spectroscopie mécanique de l'interface dans des composites à matrice magnésium.* J. Phys. IV France, 2003. **106**: p. 63-68.
113. Bremnes, Ø., B. Carreño-Morelli, and G. Gremaud, *Influence of the interaction between dislocations and mobile point-defects on the damping spectrum of aluminium.* Journal of Alloys and Compounds, 2000. **310**(1–2): p. 62-67.
114. Bujard, M., G. Gremaud, and W. Benoit, *Study of the dislocation mechanism responsible for the Bordoni relaxation in aluminum by the two-wave acoustic coupling method.* Journal of Applied Physics, 1987. **62**(8): p. 3173-3183.

115. Mason, W.P. and H.J. McSkimin, *Energy Losses of Sound Waves in Metals Due to Scattering and Diffusion.* Journal of Applied Physics, 1948. **19**(10): p. 940-946.
116. Meisner, N.B., et al., *Ultrasonic detection of the pinning of dislocations by point defects in lead—II. Model for dislocation defect interaction.* Journal of Physics and Chemistry of Solids, 1973. **34**(8): p. 1409-1416.
117. Attia, E.A., *Low-temperature internal friction of plastically deformed aluminium.* Journal of Physics D: Applied Physics, 1968. **1**(11): p. 1431.
118. Ogi, H., T. Hamaguchi, and M. Hirao, *Ultrasonic attenuation peak in steel and aluminum alloy during rotating bending fatigue.* Metallurgical and Materials Transactions A, 2000. **31**(4): p. 1121-1128.
119. Bremnes, O., et al., *Complex Interaction Mechanisms between Dislocations and Point Defects Studied in Pure Aluminium by a Two-Wave Acoustic Coupling Technique.* physica status solidi (a), 1997. **160**(2): p. 395-402.
120. Min, X.H. and H. Kato, *Change in ultrasonic parameters with loading/unloading process in cyclic loading of aluminium alloy.* Materials Science and Engineering: A, 2004. **372**(1–2): p. 269-277.
121. Feltham, P., *On low temperature internal friction peaks in deformed metals.* Philosophical Magazine, 1966. **13**(125): p. 913-919.
122. Marchesoni, F., *Internal Friction by Pinned Dislocations: Theory of the Bordoni Peak.* Physical Review Letters, 1995. **74**(15): p. 2973-2976.
123. Granato, A. and K. Lucke, *Application of Dislocation Theory to Internal Friction Phenomena at High Frequencies.* Journal of Applied Physics, 1956. **27**(7): p. 789-805.
124. Zener, C., *Stress Induced Preferential Orientation of Pairs of Solute Atoms in Metallic Solid Solution.* Physical Review, 1947. **71**(1): p. 34-38.
125. Fantozzi, G., et al., *Internal friction and microdeformation due to the intrinsic properties of dislocations: The Bordoni relaxation.* Progress in Materials Science, 1982. **27**(3–4): p. 311-451.
126. Gramaud, G., *A NEW TECHNIQUE OF MEASUREMENT BY COUPLING OF A CYCLIC LOW FREQUENCY STRESS WITH AN ULTRASONIC WAVE.* Journal de Physique Colloques, 1981. **42**(C5): p. C5-1141-C5-1146.
127. Gremaud, G., M. Bujard, and W. Benoit, *The coupling technique: A two-wave acoustic method for the study of dislocation dynamics.* Journal of Applied Physics, 1987. **61**(5): p. 1795-1805.
128. Rosen, M., et al., *An investigation of the precipitation-hardening process in aluminum alloy 2219 by means of sound wave velocity and ultrasonic attenuation.* Materials Science and Engineering, 1982. **53**(2): p. 163-177.
129. McSkimin, H.J.A., P., *Analysis of the Pulse Superposition Method for Measuring Ultrasonic Wave Velocities as a Function of Temperature and Pressure.* The Journal of the Acoustical Society of America, 1962. **34**(5): p. 609-615.